

NASA

N66-1-506

N66-19586

FACILITY FORM 507

ACCESSION NUMBER	(THRU)
179	1
(PAGES)	(CODE)
	32
(NASA CR OR TMX OR AD NUMBER)	(CATEGORY)

INVESTIGATION OF PLANE-STRAIN FLAW GROWTH IN THICK-WALLED TANKS

by

C.F.Tiffany, P.M.Lorenz, L.R.Hall

prepared for

NATIONAL AERONAUTICS AND SPACE ADMINISTRATION

CONTRACT NAS 3-4194

GPO PRICE \$ _____

CFSTI PRICE(S) \$ _____

Hard copy (HC) 5.00Microfiche (MF) 1.00

N 853 July 65

AEROSPACE GROUP

THE **BOEING** COMPANY

SEATTLE, WASHINGTON

NOTICE

This report was prepared as an account of Government sponsored work. Neither the United States, nor the National Aeronautics and Space Administration (NASA), nor any person acting on behalf of NASA:

- A.) Makes any warranty or representation, expressed or implied, with respect to the accuracy, completeness, or usefulness of the information contained in this report, or that the use of any information, apparatus, method, or process disclosed in this report may not infringe privately owned rights; or
- B.) Assumes any liabilities with respect to the use of, or for damages resulting from the use of any information, apparatus, method or process disclosed in this report.

As used above, "person acting on behalf of NASA" includes any employee or contractor of NASA, or employee of such contractor, to the extent that such employee or contractor of NASA, or employee of such contractor prepares, disseminates, or provides access to, any information pursuant to his employment or contract with NASA, or his employment with such contractor.

Requests for copies of this report should be referred to

National Aeronautics and Space Administration
Office of Scientific and Technical Information

Attention: AFSS-A
Washington, D.C. 20546

NASA CR-54837
D2-24078-1

Final Report

INVESTIGATION OF PLANE-STRAIN FLAW GROWTH
IN THICK-WALLED TANKS

By

C.F. Tiffany, P.M. Lorenz, L.R. Hall

Prepared for

National Aeronautics and Space Administration

February 1966

Contract NAS3-4194

Technical Management
NASA Lewis Research Center
Cleveland, Ohio
Liquid Rocket Technology Branch
Gordon T. Smith

Aerospace Group
THE BOEING COMPANY
Seattle, Washington

FOREWORD

This document reports on an investigation by The Boeing Company from June 26, 1964 to October 26, 1965 of plane-strain flaw growth in thick-walled tanks under Contract NAS3-4194. The work was administered under the direction of Mr. Gordon Smith of the NASA Lewis Research Center.

Boeing personnel who participated in the investigation described herein include C.F. Tiffany, project supervisor; P.M. Lorenz, technical leader; and L.R. Hall, research engineer. Structural testing of specimens and cryogenic tanks was conducted by A.A. Ottlyk and J.R. Hughes. Manufacturing support was provided by M.W. Schoeggl.

The information contained in this document is also released as Boeing Document D2-24078-1.

INVESTIGATION OF PLANE-STRAIN FLAW GROWTH IN THICK-WALLED TANKS

By

C. F. Tiffany, P. M. Lorenz, L. R. Hall

ABSTRACT

Plane-strain cyclic flaw-growth rates and fracture-toughness values were obtained for 2219-T87 aluminum and 5Al-2.5Sn (ELI) titanium. Investigations were conducted at room temperature, -320°F , and -423°F , and under zero-to-tension and half-tension-to-tension loading profiles. The experimental approach used linear elastic fracture mechanics. Results from surface-flawed uniaxial specimens and cylindrical tanks were obtained and compared. It was concluded that, within limitations, the uniaxial data can be usefully applied in the design of cryogenic pressure vessels.

CONTENTS

	<u>Page</u>
SUMMARY	1
1.0 INTRODUCTION	3
2.0 BACKGROUND	5
2.1 Technical	5
2.1.1 Stress Intensity Analyses	5
2.1.2 Evaluation of Subcritical Flaw Growth in Terms of Stress Intensity	7
2.2 Fractography	10
3.0 MATERIALS AND FABRICATION PROCEDURES	11
3.1 Materials	11
3.2 Fabrication Procedures	12
3.2.1 Uniaxial Test Specimens	12
3.2.2 Biaxial Test Specimens (Cylindrical Tanks)	12
4.0 EXPERIMENTAL PROCEDURE	15
4.1 Uniaxial Specimens	15
4.2 Biaxial Specimens (Cylindrical Tanks)	15
4.3 Fractographic Technique	17
5.0 TEST RESULTS	19
5.1 Mechanical Properties	19
5.2 5Al-2.5Sn (ELI) Titanium Uniaxial Specimen Results	19
5.2.1 Plane-Strain Fracture Toughness	19
5.2.2 Cyclic Life — Stress-Intensity Relationships	20
5.2.3 Flaw Growth Rates Computed from End-Point Analysis	20
5.2.4 Microscopically Determined Flaw Growth Rates	21
5.3 5Al-2.5Sn (ELI) Titanium Cylindrical Tank Results	23
5.4 2219-T87 Aluminum Uniaxial Specimen Results	24
5.4.1 Plane-Strain Fracture Toughness	24
5.4.2 Cyclic Life — Stress-Intensity Relationships	25

	<u>Page</u>
5.4.3 Flaw Growth Rates Computed from End-Point Analysis	25
5.4.4 Microscopically Determined Flaw Growth Rates	25
5.5 2219-T87 Aluminum Cylindrical Tank Results	26
6.0 DISCUSSION OF RESULTS	29
6.1 Discussion of 5Al-2.5Sn (ELI) Titanium Results	29
6.1.1 Plane-Strain Fracture Toughness	29
6.1.2 Cyclic Life — Stress-Intensity Relationships	30
6.1.3 Flaw Growth Rates Computed from End-Point Analysis	30
6.1.4 Microscopically Determined Flaw Growth Rates	32
6.1.5 Cylindrical Tank Results	33
6.2 2219-T87 Aluminum Test Results	33
6.2.1 Effect of Laminations on Test Results	33
6.2.2 Plane-Strain Fracture Toughness	34
6.2.3 Cyclic Life — Stress-Intensity Relationships	35
6.2.4 Flaw Growth Rates Computed from End-Point Analysis	35
6.2.5 Microscopic Flaw Growth Rates	35
6.2.6 2219-T87 Aluminum Tank Tests	36
7.0 APPLICATIONS AND LIMITATIONS	41
7.1 Applications	41
7.2 Limitations	42
8.0 CONCLUSIONS	45
REFERENCES	47
APPENDIX: ILLUSTRATIVE TANK DESIGNS USING CYCLIC-LIFE AND FRACTURE-TOUGHNESS DATA	49

ILLUSTRATIONS

<u>Figure</u>		<u>Page</u>
1	Variation of Stress Intensity Along Flaw Periphery	55
2a	Basic Crack Growth Curve	56
2b	Crack Growth-Rate Data	56
3	Flaw-Growth Measurement from a Single Specimen	57
4a	Initial Flaw Size vs Life Span	58
4b	K-N Curve Describing Cyclic Life Span	58
5	Sustained Flaw Growth	59
6	Combined Cyclic and Sustained-Stress Flaw Growth	59
7a	Electron Fractograph of Cyclic Crack Growth in 2219-T87 Aluminum	60
7b	Electron Fractograph of Cyclic Crack Growth in 6Al-4V Titanium	60
8a	Optical Micrograph of Cyclic Crack Growth in 7075-T6 Aluminum	61
8b	Electron Micrograph of Cyclic Crack Growth in 7075-T6 Aluminum	61
9	Tensile Specimen (Titanium)	62
10	Through-the-Thickness Centrally Cracked Fracture Tough- ness Specimen	63
11	Surface-Flawed Titanium Specimen	64
12	Tensile Specimen (Aluminum)	65
13	Surface-Flawed Specimen for 1.2 in. Aluminum	66
14	Surface-Flawed Specimen for 0.6 in. Aluminum	67
15	5Al-2.5Sn (ELI) Titanium Test Cylinder	69
16	Fractographs Showing Typical Initial Flaw Extension in Titanium Specimens and Tanks	71
17	2219-T87 Aluminum Test Tank for Room Temperature and -320°F Testing	73
18	2219-T87 Aluminum Test Tank for -423°F Testing	75
19	Initial Flaw Extension in Aluminum Shell	77

<u>Figure</u>		<u>Page</u>
20	Fractographs Showing Typical Initial Flaw Extension in Aluminum Specimens and Tanks	78
21	Location of Strain Gages on 2219-T87 Test Tank	79
22	Schematic Diagram of Pressure and Control System Used for Room Temperature Tank Tests	80
23	Schematic Diagram of Pressure and Control System Used for -320°F Tank Tests	81
24	Schematic Diagram of Pressure and Control System Used for -423°F Test Tanks	82
25	Schematic Illustration of Fractographic Setup	83
26	Cross-Sections of Photographically Discrete Zones (300X) in Cyclically Tested 2219-T87 Aluminum Specimen	84
27	2219 Aluminum Fatigue Specimen	85
28a	Schematic Illustration of Grid and Replica Location on Fracture Face of Test Specimen	86
28b	Schematic Illustration of Sample Grid with Typical Replica	86
29	Mechanical Properties of 5Al-2.5Sn (ELI) Titanium Plate	87
30	Mechanical Properties of 2219-T87 Aluminum Plate	88
31	Plane Strain Fracture Toughness of 5Al-2.5Sn (ELI) Titanium	89
32	Stress Intensity vs Cycles-to-Failure Correlation for 5Al-2.5Sn (ELI) Titanium at Room Temperature	90
33	Stress Intensity vs Cycles-to-Failure Correlation for 5Al-2.5Sn (ELI) Titanium at -320°F	91
34	Stress Intensity vs Cycles-to-Failure Correlation for 5Al-2.5Sn (ELI) Titanium at -423°F	92
35	Cyclic Flaw Growth Data for 5Al-2.5Sn (ELI) Titanium at -320°F (0-100-0 Load Profile)	93
36	Cyclic Flaw Growth Data for 5Al-2.5Sn (ELI) Titanium at -320°F (50-100-50 Load Profile)	94
37	Cyclic Flaw Growth Data for 5Al-2.5Sn (ELI) Titanium at -423°F (0-100-0 Load Profile)	95
38	Cyclic Flaw Growth Data for 5Al-2.5Sn (ELI) Titanium at -423°F (50-100-50 Load Profile)	96
39	Flaw Growth Rates for 5Al-2.5Sn (ELI) Titanium at Room Temperature	97

<u>Figure</u>		<u>Page</u>
40	Flaw Growth Rates Computed from End Point Analyses for 5Al-2.5Sn (ELI) Titanium at -320°F	98
41	Flaw Growth Rates Computed from End Point Analyses for 5Al-2.5Sn (ELI) Titanium at -423°F	99
42	Fractographs of Striated Regions 5Al-2.5Sn (ELI) Titanium	100
43	Flaw Growth Rates for 5Al-2.5Sn (ELI) Titanium at -320°F (Maximum Cyclic Stress = 117.5 ksi)	101
44	Flaw Growth Rates for 5Al-2.5Sn (ELI) Titanium at -320°F (Maximum Cyclic Stress = 117.5 ksi)	102
45	Flaw Growth Rates for 5Al-2.5Sn (ELI) Titanium at -320°F (Maximum Cyclic Stress = 139 ksi)	103
46	Flaw Growth Rates for 5Al-2.5Sn (ELI) Titanium at -320°F (Maximum Cyclic Stress = 139 ksi)	104
47	Flaw Growth Rates for 5Al-2.5Sn (ELI) Titanium at -320°F (Maximum Cyclic Stress = 158 ksi)	105
48	Flaw Growth Rates for 5Al-2.5Sn (ELI) Titanium at -320°F (Maximum Cyclic Stress = 158 ksi)	106
49	Comparison of Microscopic Flaw Growth Rates at Three Different Maximum Cyclic Stresses: 5Al-2.5Sn (ELI) Titanium at -320°F	107
50	Fracture Appearance of 5Al-2.5Sn (ELI) Titanium Tanks	108
51	Microscopic Flaw Growth Rates for 5Al-2.5Sn (ELI) Titanium Tank 0009 Tested at Room Temperature	109
52	Plane Strain Fracture Toughness of 2219-T87 Aluminum	110
53	Stress Intensity vs Cycles-to-Failure Correlation for 2219-T87 Aluminum at Room Temperature	111
54	Stress Intensity vs Cycles-to-Failure Correlation for 2219-T87 Aluminum at -320°F	112
55	Stress Intensity vs Cycles-to-Failure Correlation for 2219-T87 Aluminum at -423°F	113
56	Cyclic Flaw Growth Data for 2219-T87 Aluminum at Room Temperature (0-100-0 Load Profile)	114
57	Cyclic Flaw Growth Data for 2219-T87 Aluminum at Room Temperature (50-100-50 Load Profile)	115
58	Cyclic Flaw Growth Data for 2219-T87 Aluminum at -320°F (0-100-0 Load Profile)	116

<u>Figure</u>		<u>Page</u>
59	Cyclic Flaw Growth Data for 2219-T87 Aluminum at -320°F (50-100-50 Load Profile)	117
60	Cyclic Flaw Growth Data for 2219-T87 Aluminum at -423°F (0-100-0 Load Profile)	118
61	Cyclic Flaw Growth Data for 2219-T87 Aluminum at -423°F (50-100-50 Load Profile)	119
62	Flaw Growth Rates Computed from End Point Analysis for 2219-T87 Aluminum	120
63	Fractographs of Striated Regions 2219-T87 Aluminum	121
64	Microscopic Flaw Growth Rates for 2219-T87 Aluminum at Room Temperature	122
65	Microscopic Flaw Growth Rates for 2219-T87 Aluminum at -320°F	123
66	Microscopic Flaw Growth Rates for 2219-T87 Aluminum at -423°F	124
67	Photographs of Fractured 2219-T87 Tanks	125
68	Microscopic Flaw Growth Rates for 2219-T87 Aluminum Tank II at -320°F	126
69	Effect of Relative Flaw Depth on Calculated K_{Ic} Values for 5Al-2.5Sn (ELI) Titanium at -320°F	127
70	Estimated* Cyclic Life Curves for 5Al-2.5Sn (ELI) Titanium at Room Temperature	128
71	Fracture Surface with Visible Delamination in 2219-T87 Aluminum	129
72	Effect of Laminations on Flaw Growth in 2219-T87 Aluminum	130
73	Comparisons of K_{Ic} Values in Layered and Nonlayered 2219-T87 Aluminum	131
74	Failure Origin of 2219-T87 Aluminum Tank No. III	132
75	Failure Origin of 2219-T87 Aluminum Tank No. IV	133
76	Critical Flaw Sizes at Operating Stress for 5Al-2.5Sn (ELI) Titanium and 2219-T87 Aluminum vs Temperature	134
77	Flaw Growth Rates at Operating Stress vs Flaw Size for 5Al-2.5Sn (ELI) Titanium (0-100-0 Load Profile)	135
78	Flaw Growth Rates at Operating Stress vs Flaw Size for 2219-T87 Aluminum (0-100-0 Load Profile)	136

<u>Figure</u>		<u>Page</u>
79	Cycles to Failure at Operating Stress vs Initial Flaw Size for 5Al-2.5Sn (ELI) Titanium (0-100-0 Load Profile)	137
80	Cycles to Failure at Operating Stress vs Initial Flaw Size for 2219-T87 Aluminum (0-100-0 Load Profile)	138
A1	Lower Bound Stress Intensity — Cyclic Life Curves at -423°F for Illustrative Design of Titanium Tank	139
A2	Schematic Representation of the Effect of K_{Ic} on Normalized Cyclic-Life Curves	140
A3	Composite Cyclic Flaw Growth Data 2219-T87 Aluminum at Room Temperature, -320°F, and -423°F	141
A4	Illustrative Design of 5Al-2.5Sn (ELI) Titanium Tank	142
A5	Illustrative Design of 2219-T87 Aluminum Tank	143

TABLES

	<u>Page</u>
I Chemical Composition of the Materials Used to Fabricate Specimens and Tanks	145
II Weld Settings Used for Fabrication of Aluminum and Titanium Tanks	146
III Mechanical Properties of 5Al-2.5Sn (ELI) Titanium Plate 0.188-Inch Thick, at R.T., -320°F, and -423°F Test Temperatures	147
IV Mechanical Properties of 2219-T87 Aluminum Plate 1.25 Inches Thick, at R.T., -320°F and -423°F Test Temperatures	148
V Static Fracture Toughness Test Results — 5Al-2.5Sn (ELI) Titanium	149
VI Cyclic Flaw Growth Data for 5Al-2.5Sn (ELI) Titanium, 0-100-0 Load Profile at Room Temperature	150
VII Cyclic Flaw Growth Data for 5Al-2.5Sn (ELI) Titanium, 50-100-50 Load Profile at Room Temperature	151
VIII Cyclic Flaw Growth Data for 5Al-2.5Sn (ELI) Titanium, 0-100-0 Load Profile at -320°F	152
IX Cyclic Flaw Growth Data for 5Al-2.5Sn (ELI) Titanium, 50-100-50 Load Profile at -320°F	153
X Cyclic Flaw Growth Data for 5Al-2.5Sn (ELI) Titanium, 0-100-0 Load Profile at -423°F	154
XI Cyclic Flaw Growth Data for 5Al-2.5Sn (ELI) Titanium, 50-100-50 Load Profile at -423°F	155
XII Titanium Tank Test Results	156
XIII Static Fracture Toughness Test Results — 2219-T87 Aluminum	157
XIV Cyclic Flaw Growth Data for 2219-T87 Aluminum, 0-100-0 Load Profile at Room Temperature	158
XI Cyclic Flaw Growth Data for 2219-T87 Aluminum, 50-100-50 Load Profile at Room Temperature	159
XVI Cyclic Flaw Growth Data for 2219-T87 Aluminum, 0-100-0 Load Profile at -320°F	160
XVII Cyclic Flaw Growth Data for 2219-T87 Aluminum, 50-100-50 Load Profile at -320°F	161

	<u>Page</u>
XVIII Cyclic Flaw Growth Data for 2219-T87 Aluminum, 0-100-0 Load Profile at -423°F	162
XIX Cyclic Flaw Growth Data for 2219-T87 Aluminum, 50-100-50 Load Profile at -423°F	163
XX Aluminum Tank Test Results	164

SUMMARY

9586

The objectives of this investigation were to: (1) generate plane-strain fracture toughness and cyclic flaw growth data for 2219-T87 aluminum and 5Al-2.5Sn (ELI) titanium from the testing of uniaxially loaded specimens; (2) establish how and under what conditions uniaxial data can be applied to cryogenic pressure vessel design; (3) verify the applicability of the uniaxial data to cryogenic pressure vessel design. Tests were conducted on uniaxially loaded surface-flawed specimens and on biaxially stressed surface-flawed tanks fabricated from each material. Tests were conducted at room temperature in air, at -320°F in the environment of liquid nitrogen, and at -423°F in the environment of liquid hydrogen. Both zero-to-tension and half-tension-to-tension loading profiles were investigated.

Plane-strain cyclic flaw growth rates and fracture toughness values were successfully determined for both 2219-T87 aluminum and 5Al-2.5Sn (ELI) titanium at all three test temperatures and for the two aforementioned loading profiles.

Replicas of some fracture surfaces were viewed through an electron microscope. Particular attention was given to striated areas. Flaw growth rates were computed from measured striation spacings.

The results of this test program showed that, within the limitations of application expressed in this report, uniaxial fracture specimen data can be used in the prediction of plane-strain subcritical flaw growth characteristics and critical flaw sizes in pressure vessels.

[Handwritten signature]

1.0 INTRODUCTION

Many failures in pressure vessels have originated at flaws. Some failures have occurred in proof tests of pressure vessels. Proof-test failures result when the size of a flaw is sufficiently large to become unstable before proof stress is attained. Other failures have occurred under normal operating conditions. Operational failures have often occurred after a flaw grew sufficiently in size to become unstable at the operating stress. An estimate of the performance capability of pressure vessels requires knowledge of initial flaw sizes, critical flaw size, and subcritical flaw growth characteristics of the vessel material.

In relatively thick-walled pressure vessels, internal or surface flaws take on a great deal of importance. Such flaws usually grow and cause fracture under conditions of plane strain. The growth and fracture characteristics of the flaws are governed by the plane-strain fracture toughness of the vessel material.

It is possible for catastrophic failures to originate from surface or embedded flaws without prior warning such as tank leakage. Furthermore, critical flaw sizes can be sufficiently small to demand severe nondestructive inspection requirements.

The investigation reported herein was undertaken to:

- 1) Generate fracture toughness and cyclic flaw growth data from the testing of uniaxially loaded surface-flawed specimens;
- 2) Establish how and under what conditions uniaxial data can be applied to cryogenic pressure vessel design;
- 3) Verify the applicability of the uniaxial data to cryogenic tank design by cyclically pressure testing surface-flawed cylindrical tanks.

Two materials were selected for testing in the program: 2219-T87 aluminum and 5Al-2.5Sn (ELI) titanium. The aluminum plate used was 1.25-inch thick. The titanium plate used was 0.188-inch thick. Tests were conducted on both materials at room temperature in air, at -320°F in the environment of liquid nitrogen, and at -423°F in the environment of liquid hydrogen. Flaw growth tests were conducted under cyclic loading. The cyclic testing of the uniaxial specimens was conducted using two different loading profiles: zero-to-tension (0-100-0) and half-tension-to-tension (50-100-50). The cyclic tank tests were conducted under only a 0-100-0 loading profile. A total of 100 tests were conducted in the program, including 43 uniaxial and 6 tank tests on 2219-T87 aluminum, and 45 uniaxial and 6 tank tests on the 5Al-2.5Sn (ELI) titanium.

The fracture surfaces of 19 titanium and 8 aluminum specimens were examined through an electron microscope. High-magnification photographs were taken of striated areas on the fracture surfaces. Flaw growth rates were computed from the measured striation spacings and compared with flaw growth rates determined by end-point analyses.

2.0 BACKGROUND

2.1 TECHNICAL

2.1.1 Stress Intensity Analyses

Relationships between stress intensity, crack size, and nominal stress field have been derived for a number of structural configurations. Two such solutions will be used in evaluating test results in the program described herein. One solution is for the stress intensity of a semielliptical surface flaw in a finite plate; the other solution is for the stress intensity of a through-the-thickness crack in a finite strip.

Stress Intensity of a Semielliptical Surface Flaw in Finite Plates — A rigorous three-dimensional elasticity solution has been derived by Green and Sneddon (Ref. 1) for the distribution of stress near a flat elliptical crack in a body of infinite extent. The body was assumed to be loaded perpendicularly to the crack and at infinity. Irwin (Ref. 2) used the Green and Sneddon solution to show that the expression for the stress intensity around the crack periphery for the embedded elliptical flaw is

$$K = \frac{\sqrt{\pi}}{\Phi} \sigma \sqrt{a} \left\{ \frac{1}{c^2} \left[a^2 \cos^2 \varphi + c^2 \sin^2 \varphi \right] \right\}^{1/4} \quad (1)$$

where σ is the uniform stress perpendicular to the crack. The parametric equations of the flaw periphery are $x = c \sin \varphi$, $y = a \cos \varphi$, where c is the semi-major and a is the semiminor axis of the ellipse, and Φ is the complete elliptical integral of the second kind corresponding to the modulus $k = [(c^2 - a^2)/c^2]^{1/2}$, i.e.,

$$\Phi = \int_0^{\pi/2} \left[1 - \left(\frac{c^2 - a^2}{c^2} \right) \sin^2 \theta \right]^{1/2} d\theta$$

Irwin also showed that the state of deformation at any point on the flaw periphery was one of plane strain. Hence, values of K computed from Equation 1 are plane strain or opening mode values of K , i.e., K_I .

In seeking an expression for the stress intensity for a semielliptical surface flaw in a finite thickness plate, Equation 1 led Irwin to assume the functional form

$$K_I = \alpha \frac{\sqrt{\pi}}{\Phi} \sigma \sqrt{a} \gamma \left\{ \frac{1}{c^2} \left[a^2 \cos^2 \varphi + c^2 \sin^2 \varphi \right] \right\}^{1/4} \quad (2)$$

where α is a correction factor to account for the effect on stress intensity of the stress-free surface from which the flaw emanates, γ is a correction factor to account for the effect on stress intensity of the plastic yielding around the flaw periphery.

Values of α and γ were estimated by Irwin (Ref. 3) and were considered valid for surface flaws with a/c ratios less than 1 and flaw depths not exceeding 50 percent of the plate thickness. The resulting expression for the stress intensity was

$$K_I = 1.1 \sqrt{\pi} \sigma \left(\frac{a}{Q}\right)^{1/2} \left\{ \frac{1}{c^2} [a^2 \cos^2 \varphi + c^2 \sin^2 \varphi] \right\}^{1/4} \quad (3)$$

where $Q = \Phi^2 - 0.212 (\sigma/\sigma_{ys})^2$, and σ_{ys} is the uniaxial yield strength of the material.

The maximum value of K_I occurs at the end of the semiminor axis of the ellipse and has a value of

$$K_I = 1.1 \sqrt{\pi} \sigma \left(\frac{a}{Q}\right)^{1/2} \quad (4)$$

If a specimen with a surface flaw is subjected to a monotonously increasing value of σ , the flaw size becomes unstable and propagates rapidly at some particular value of σ . The value of K_I computed from Equation 4 at the inception of this instability is called the critical value of K_I and is designated by the symbol K_{IC} .

If Equation 3 is normalized by the maximum value of K_I from Equation 4, the ratio of the K_I at any point on the flaw periphery described by the angle φ to the maximum value of K_I is obtained. This value is

$$\frac{(K_I)_{\varphi}}{(K_I)_{\max}} = \frac{1}{\sqrt{c}} \left\{ a^2 \cos^2 \varphi + c^2 \sin^2 \varphi \right\}^{1/4} \quad (5)$$

and is plotted as a function of the circular angle of the ellipse $\psi = \tan^{-1}(a/c \tan \varphi)$ in Figure 1.

Stress Intensity for Through-the-Thickness Cracks in Finite Plates — Several investigators have derived solutions for the stress intensity at the tips of a through-the-thickness crack symmetrically located in a finite strip. Irwin (Ref. 3) first provided an approximate closed-form solution by making use of a Westergaard (Ref. 4) stress function. Some other solutions were later provided in References 5, 6, and 7. However, for crack lengths that are not large with respect to the width of the plate, the closed-form Irwin solution is quite accurate; its use has been recommended by the ASTM Committee on Fracture Testing (ASTM committee E-24).

The stress intensity resulting from Irwin's approximate elastic analysis of a central crack in a finite strip subjected to a uniaxial stress σ is

$$K = \sigma \left\{ W \tan \frac{\pi a}{W} \right\}^{1/2} \quad (6)$$

where W = strip width, and $2a$ = crack length.

In real materials, plastic zones surround the crack tip. If no account is taken of these yielded zones, the K value computed from elastically derived formulae such as Equation 6 are generally too low. An approximate method of altering Equation 6 to account for the effect of the plastic zones is outlined in Reference 8.

The resulting formula is

$$K = \sigma W^{1/2} \left\{ \tan \left(\frac{\pi a}{W} + \frac{K^2}{2W \sigma_{ys}^2} \right) \right\}^{1/2}. \quad (7)$$

It has been observed that the initial extension of cracks in center-cracked specimens sometimes occurs as a distinct burst or "pop-in." The pop-in is followed by a stage of gradual crack extension until, at some given crack length, the rate of crack growth suddenly becomes very rapid. It has been shown (Ref. 9) that the value of K computed from Equation 7 at the inception of pop-in is equivalent to K_{Ic} — the critical opening mode value of K . The state of stress at the crack tip when the second instability occurs is often one of plane stress when the sheet is sufficiently thin. Hence the value of K at which the second abrupt change in crack growth rate occurs can be called the critical plane-stress K value and is designated as K_c .

2.1.2 Evaluation of Subcritical Flaw Growth in Terms of Stress Intensity

Cyclic Flaw Growth — Observations of crack growth due to a fluctuating load indicate that a certain amount of growth usually occurs in each load cycle. Hence, it is reasonable to regard crack growth as a continuous process (Ref. 10). Experimental observations of crack length, a , can be made at given numbers of cycles, N , and the data can be represented by a smooth, continuous a versus N curve. The slope (da/dN) of the a versus N curve at any point is taken to be the crack growth rate at that point.

For through-the-thickness cracks growing under conditions of plane stress, a versus N curves can be generated by cycling center-cracked fracture specimens under given loading conditions. Periodic measurements of crack length are made after given numbers of load applications. A typical, a versus N curve generated by means of the above method is schematically illustrated in Figure 2a.

Plane stress crack growth tests (Refs. 11 and 12) have shown that the crack growth rate for a given material is dependent primarily on the maximum stress intensity (K_{max}) and on the ratio of minimum stress intensity to maximum stress intensity, R . The growth rates are influenced to a lesser extent by cyclic speed and test temperature. A typical da/dN versus K_{max} curve is illustrated in Figure 2b for two different R values.

After looking at the overall trends exhibited by a significant amount of data, Paris (Ref. 10) concluded that plane stress crack growth rates could be adequately represented for sinusoidally loaded metal specimens by the expression

$$da/dN = C \cdot \Delta K^4 \quad (8)$$

where C is a coefficient that incorporates effects of mean load level, frequency, and environment; and ΔK is the value of $K_{max} - K_{min}$ for the loading cycle.

A value of C has been estimated by Krafft (Ref. 13), who has proposed the crack growth rate formula

$$\frac{da}{dN} = \frac{16 \times 10^6 f(\gamma)}{7 E^3 K_{Ic}^2 n} K_{max}^4 \quad (9)$$

where E is the Young's modulus of the material, n is the tensile strain that can be applied before plastic instability ensues, K_{max} is the maximum value of K during the loading sequence, $\gamma = (K_{max} - K_{min})/K_{max}$ where K_{min} is the minimum value of K during the loading sequence, and

$$f(\gamma) = [1 - (1 - \gamma)^2] [1 + \gamma]^4$$

The experimental determination of flaw growth rate data for surface or embedded flaws is more complex than for through-the-thickness cracks. A surface flaw grows along its entire periphery and continually changes, not only in size but also in shape. Furthermore, the inaccessibility of the flaw prevents direct visual measurements of the flaw shape and size during the test.

The effect of change in flaw shape can be accounted for by using the parameter (a/Q) to describe flaw size. Theoretically, elliptical flaws with identical (a/Q) values develop identical maximum K_I values in a uniaxial stress field acting perpendicularly to the flaw. Hence, the (a/Q) value of a flaw provides a single parameter with which to correlate fracture and flaw growth data obtained from surface-flawed specimens with different flaw shapes as well as different flaw depths. To date, no systematic experimental program has been conducted specifically to determine the general validity of the use of Q as a correlative factor over a wide range of flaw shapes and sizes. However, fracture toughness tests of surface-flawed specimens (Ref. 14) with widely varying flaw shapes and depths have yielded very consistent fracture toughness values for given materials. The flaw growth rate of a surface or embedded flaw whose size is described by the parameter (a/Q) is $d(a/Q)dN$.

The requirement for subcritical flaw shape and size measurements can be circumvented. For example, suppose that the flaw size in a surface flawed specimen could be continuously monitored. Further suppose that the results show that after A loading cycles, the flaw depth had increased from a_1 to a_2 and the flaw shape parameter had changed from Q_1 to Q_2 ; after B loading cycles, the flaw had grown to depth a_3 , and the shape parameter had changed to Q_3 ; after C loading cycles, the flaw had reached the critical depth and become unstable. The flaw size versus cycle relationship for the specimen is given in Figure 3. If a series of specimens were to be fabricated with flaw depth a_1 , a_2 , and a_3 , and with shape parameters Q_1 , Q_2 , and Q_3 , and tested under the same maximum cycle stress and test conditions as the aforementioned single specimen, the specimen with flaw depth a_1 should take about C cycles, the specimen with flaw depth a_2 (C-A) cycles and the specimen with flaw depth a_3 (C-B) cycles to grow to the critical size, a_{cr} , and fail. Hence, the three specimens can be used to define the same flaw growth curve as the single continuously monitored specimen.

The slope of the curve at any given flaw size is the flaw growth rate $d(a/Q)/dN$ at that point.

It has been shown in Reference 14 that the cyclic life of surface flawed specimens under given test conditions correlates well with the maximum initial stress intensity (K_{Ii}) at the tip of the surface flaw. Since K_{Ii} is a function of both flaw size and maximum cyclic stress, the initial stress intensities for a number of surface-flawed specimens can be varied by changing either or both the initial flaw size and maximum cyclic stress. Hence, it is not necessary to test specimens under a single maximum cyclic stress to generate a cyclic life curve similar to that in Figure 4a.

Cyclic life data can be plotted in a number of ways. For instance, the data of Figure 3 can be plotted in terms of initial flaw size versus the corresponding cycles to failure as schematically illustrated in Figure 4a. The maximum stress intensities for the initial flaw can also be plotted against the corresponding cycles to failure as schematically illustrated in Figure 4b.

Flaw growth rates that correspond to a given K_{Ii} versus N curve can be computed. For an assumed maximum cyclic stress level, say σ_1 , the given K_{Ii} versus N curve can be converted to an $(a/Q)_i$ versus N curve by means of Equation 4, i.e.,

$$(a/Q) = \frac{1}{1.21 \pi} \left[\frac{K_{Ii}}{\sigma_1} \right]^2$$

The slope of the (a/Q) versus N curve at any given (a/Q) value is the flaw growth rate for that particular (a/Q) and assumed maximum cyclic stress (σ_1). If a different maximum cyclic stress (σ_2) is used in the computations, the above relationship between (a/Q) and K_{Ii} changes and a different (a/Q) versus N curve is derived from the given K_{Ii} versus N curve. Hence, the computed flaw growth rates at any given K_I value vary with applied stress level.

The foregoing method of computing flaw growth rates will hereafter be referred to as the "end point analysis."

Sustained Stress Flaw Growth — It has been shown experimentally (Refs. 16 and 17) that if the stress intensity at the tip of a flaw is elevated beyond a certain value, called the apparent threshold stress intensity (Figure 5), the flaw will begin to grow. If the stress level in the specimen is kept constant, the flaw will continue to grow until it reaches the critical size and becomes unstable. This type of growth is called sustained stress flaw growth and has been observed both under plane stress conditions (Ref. 16) and under plane strain conditions (Ref. 17).

Combined Sustained-Stress and Cyclic Flaw Growth — Sustained stress flow growth can have an effect on the total cyclic life of a structure that is subjected to both cyclic and sustained stresses. To illustrate this statement, a qualitative K_I versus N curve is included in Figure 6. Superimposed on this curve is a horizontal line at $0.80 K_{IC}$. This value is assumed to be the threshold stress intensity of the material under the given environment. Consider the situation in which the initial flaw and applied cyclic stress result in an initial stress intensity equal to 50 percent of the critical stress intensity. It would take A loading cycles to grow the initial flaw to critical size if there were no sustained stress flow growth. However, in B cycles, the initial flaw would have increased in size a sufficient amount to elevate the stress intensity to the assumed threshold value of $0.80 K_{IC}$. If the applied loading cycles include a long period of time at maximum load, it appears possible that the flaw could continue to grow under the sustained maximum stress and fail in $(B + 1)$ loading cycles. If, on the other hand, the loading cycles included very little time at maximum stress, it appears that the life of the structure could approach A cycles.

In the tests described herein, the load cycles will involve only a short time at maximum stress. Consequently, it will be assumed that the sustained stress flow growth in the specimens is sufficiently small to be of no importance. In applying the cyclic flow growth data, consideration must be given to the type of loading sequence to which the structure is subjected to determine if the cyclic flow growth data is applicable at stress intensities above the threshold value.

2.2 FRACTOGRAPHY

The examination of surfaces of fatigue fractures by means of electron or optical microscopes often reveals zones characterized by a series of regular striations. Figures 7a and 7b show electron microscope fractographs of fatigued fracture surfaces in 2219-T87 aluminum and 6Al-4V titanium. Figures 8a and 8b illustrate optical and electron micrographs of a fatigued fracture surface in 7075-T6 aluminum. Examination of program-loaded fatigue fractures has shown that each of the characteristic fatigue striations is produced by a single cycle of stress (Ref. 18). It has been concluded from this observation that the striations represent successive positions of a local flow front at each load cycle.

Under uniform loading conditions, the height and spacing of the striations have been observed to increase with increasing crack length. Striation spacing is also markedly dependent on applied load, i.e., the larger the applied load the larger the striation spacing. However, as discussed in Reference 19, the spacing of striations as measured by electron microscopy is not always equal to the calculated spacing or crack growth rate derived from macroscopic measurements of crack length versus number of cycles.

To date, almost all experimental correlations between striation spacing and macroscopic flow growth rate have been derived for through-the-thickness cracks. To gain information on the same relationships for surface flaws subjected to fatigue loadings, the fracture surfaces of some specimens tested in this program have been examined by an electron microscope.

3.0 MATERIALS AND FABRICATION PROCEDURES

3.1 MATERIALS

The 5Al-2.5Sn (ELI) titanium plate, 0.188 by 20 by 60 inches, was purchased in annealed condition per AMS 4910 (except the interstitial elements content, which was required not to exceed the following limits: C = 0.88 max; N₂ = 0.05 max; O₂ = 0.12 max; H₂ = 0.0175 max; and Fe = 0.25 max). The minimum yield strength of the annealed material was set at 100 ksi. The deviations from the standard AMS 4910 specification were necessary because there is no approved aeronautical or military specification for extra-low interstitial (ELI) titanium plate. The 5Al-2.5Sn (ELI) titanium plates were stipulated to be of the same melting heat and the same rolling batch.

All 5Al-2.5Sn (ELI) titanium specimens were fabricated and tested in the annealed condition. No heat treatment of any kind was given to specimens. However, the fabricated tanks were stress relieved for 1 hour at 1200°F in an argon atmosphere. The tank end-closures (heads) were machined from 5Al-2.5Sn (ELI) titanium forged hemispheres purchased per AMS 4966. Maximum limits for interstitial elements were required to be the same as those used for the plate. Weld filler wire used for welding titanium tanks was purchased per AMS 4953 (except that maximum limits for the interstitial elements were set to be lower than those of the plate material: C = 0.01 max; N₂ = 0.007 max; O₂ = 0.063 max; H₂ = 0.005 max; Fe = 0.09 max). Chemical composition of 5Al-2.5Sn (ELI) titanium weld filler wire as well as 5Al-2.5Sn (ELI) titanium plate material is shown in Table I.

The 2219 aluminum plate, 1.25 by 72 by 120 inches, was purchased per BMS 7-105C (equivalent to MIL-A-8920A (ASG) military specifications for 2219 aluminum alloy plate and sheet). All plates were required to be of the same melting heat and rolling batch. Aluminum plates used for fabrication of test specimens were cut into specimen blanks and heat treated from T37 to T87 condition per BAC 5602 (equivalent to MIL-H-6088D Military Specification of Heat Treatment of Aluminum Alloys). Aluminum plates used for fabrication of 35-inch-diameter test tanks were first machined to reduce the plate thickness from 1.25 to 0.60 inches at the test section, then rolled and heat treated to T87 condition prior to welding. The aluminum tank heads were fabricated from 2219 aluminum plate, 1.00 by 48 by 48 inches, which was purchased in the fully annealed condition. The heads were explosively formed, heat treated to a T62 condition, then finish machined and welded. All welding was done using 2319 weld filler wire. The 2319 weld filler wire was 0.062 inch in diameter and was purchased per BMS 7-75B Type II (equivalent to ASTM B-285-21T "Tentative Specification for Aluminum and Aluminum-Alloy Welding Rods and Bare Electrodes"). Chemical composition of 2219 aluminum plate and 2319 aluminum weld filler wire is given in Table I.

3.2 FABRICATION PROCEDURES

3.2.1 Uniaxial Test Specimens

Three different types of uniaxial test specimens were fabricated from 5Al-2.5Sn (ELI) titanium. Smooth tensile specimens used for determining mechanical properties are shown in Figure 9. The through-the-thickness cracked specimens that were used to determine the plane-strain fracture toughness of titanium at room temperature are shown in Figure 10. Surface flawed specimens that were used to determine cyclic flaw growth characteristics of titanium at room temperature, -320, and -423°F are shown in Figure 11.

Three different types of uniaxial test specimens were fabricated from 2219-T87 aluminum. Smooth uniaxial test specimens used for the determination of mechanical properties are shown in Figure 12. Surface flawed specimens with 1.2- and 0.6-inch thicknesses are shown in Figures 13 and 14, respectively. The 0.60-inch-thick specimens were fabricated from the 1.25-inch-thick plate to provide uniaxial test specimens with the same thickness as the wall thickness of the test tanks.

All initial flaws in titanium and aluminum surface-flawed specimens were prepared by using an electric discharge machine (EDM) to introduce an initial flaw with a terminating radius of less than 0.003 inch. The EDM flaw was then extended under low stress fatigue. Maximum cyclic stress levels using low stress fatigue of 5Al-2.5Sn (ELI) titanium varied from 40 to 50 ksi and for the surface-flawed 2219-T87 aluminum from 20 to 25 ksi. The number of cycles required to extend the initial flaws varied from specimen to specimen, depending upon the initial flaw size, but usually between 4000 and 20,000 cycles. The specimens were cycled at the rate of 700 to 1200 cycles per minute. Low stress fatigue extension is considered part of specimen preparation for testing and is assumed not to have any effect (Ref. 20) upon measured fracture toughness or cyclic flaw growth characteristics of either material.

3.2.2 Biaxial Test Specimens (Cylindrical Tanks)

Cyclic flaw growth characteristics of 5Al-2.5Sn (ELI) titanium under biaxial loading conditions were determined at room temperature, -320°F, and -423°F using 15-inch-diameter cylindrical pressure vessels shown in Figure 15. Extension of the initial EDM flaws was initially scheduled to use low-stress cyclic pressurization of a complete tank at room temperature. However, the first tank that was subjected to such cyclic pressurization (40 to 50 ksi maximum hoop stress) sprung a leak in the weld fusion line along a longitudinal weldment after 5500 cycles. The tank had been pressure cycled with water. As a precaution against possible stress-corrosive influences of water, the remaining tanks were pressurized with hydraulic oil. In addition, the remaining tanks were stress relieved at 1200°F for 1 hour.

These precautions did not eliminate the longitudinal weldment failures. Other tanks failed in the weld fusion zone, during both low-stress pressurization and actual testing at cryogenic temperatures. Eventually, by sectioning and re-welding prematurely fractured tanks, and by flexing shell components before welding to extend the initial flaw, it was possible to obtain test data at each test temperature, and thus bring biaxial testing of 5Al-2.5Sn (ELI) titanium to a successful conclusion.

All titanium tanks were welded using the gas tungsten arc (GTA) process. Basic weld settings used for welding titanium test tanks are shown in Table II. Sample fractographs of the uniaxial test specimen and titanium tank are shown in Figure 16.

The 2219-T87 aluminum tank that was tested is shown in Figures 17 and 18. The -423°F tests were conducted using a volume filler (slightly smaller tank) placed inside the test tank to reduce internal volume. This was needed to compensate for higher compressibility of liquid hydrogen, yet maintain the same pressurization rate as was used in -320°F and room-temperature test tanks. All 2219-T87 test tanks and volume fillers were welded using the gas tungsten arc (GTA) welding process. The basic weld settings are shown in Table II. Weld edge preparations are shown in detailed views in Figures 17 and 18.

Initial EDM flaws in 2219-T87 test tanks were extended by flexing the entire tank shell in the manner shown in Figure 19. The flexing was done before the end closures (heads) were welded to the shells. Figure 20 shows a fractograph of a uniaxial surface-flawed specimen and a tank.

BLANK PAGE

4.0 EXPERIMENTAL PROCEDURE

4.1 UNIAXIAL SPECIMENS

All room-temperature test specimens were tested in the ambient atmosphere in an enclosed building with temperatures ranging between 65 and 75° F. A strain rate of 0.005 in/in/minute was used on all smooth tensile specimens until the material yield strength was reached. A strain rate of 0.02 in/in/minute was then used for the remaining portion of the loading sequence until failure. Static fracture toughness specimens were pulled at a rate needed to precipitate a complete fracture within 1 to 3 minutes after initial application of load.

Cyclically tested specimens were subjected to 0-100-0 and 50-100-50 trapezoidal loading profiles with the frequency of 1 cycle per minute. The 0-100-0 trapezoidal loading profile was generated by dividing each cyclic period of 1 minute into four equal parts. The first part was spent in going from zero load to maximum load; the second in holding the specimen at maximum load; the third in unloading; and the fourth part at zero load. Cyclic flaw growth data for 50-100-50 cyclic loading profiles were obtained in a manner similar to that for the 0-100-0 profile, except that minimum load was 50 percent of maximum instead of being zero.

The -320° F and -423° F tests were conducted in the environments of liquid nitrogen and liquid hydrogen, respectively. The liquid nitrogen was introduced into a wrap-around cryostat to keep the gage area of each specimen completely submerged during the entire test sequence. The -423° F tests were conducted in a similar manner, except that large aluminum specimens were kept at -423° F by a direct liquid hydrogen spray upon the specimen gage area.

The direct spray approach, rather than complete submergence, was necessitated by safety regulations limiting the amount of liquid hydrogen in the test area to 10 pounds maximum. The allowable quantity of hydrogen was sufficient for the smaller wrap-around cryostat used for titanium specimens, but was too small for the larger cryostat used for aluminum specimens. A survey specimen of a configuration similar to the aluminum specimens was instrumented with embedded thermocouples to check temperature distribution within the specimen gage area. The temperature survey test showed that the temperature of the test specimen was -423° F, within a few degrees of experimental accuracy. In all cases of cryogenic specimen testing, the load was applied only after temperature was stabilized in the gage area. Upon failure, each specimen was dried with hot air and protectively wrapped to preserve fractured surfaces for fractographic analysis and flaw size measurements.

4.2 BIAXIAL SPECIMENS (CYLINDRICAL TANKS)

Cyclic testing of 5Al-2.5Sn (ELI) titanium and 2219-T87 aluminum tanks at room temperature was done only under 0-100-0 trapezoidal loading profile. Cyclic

frequency, as in uniaxial test specimens, was 1 cycle per minute. A closed-loop servo system used an electronic programmer, a servo-valve, and pressure transducers in conjunction with a hydraulic bench to generate pressure cycles. Demineralized water was used to pressurize 2219-T87 aluminum test tanks. In the case of 5Al-2.5Sn (ELI) titanium tanks, water was replaced with hydraulic oil as a precaution against possible stress-corrosive cracking of weldments.

During room-temperature testing, the temperature of the pressurizing media usually rose to about 80 to 85°F. One of the aluminum tanks was instrumented with strain gages to check the biaxial stress ratio. Figure 21 shows the location of strain gages on the tank shell. A load history of pressure versus time was recorded during the entire cyclic pressurization of each tank. Each tank was photographed, upon fracture, to show the fracture origin. Fracture faces were removed and subjected to fractographic analysis. A schematic diagram of the hydraulic pressure and control system for room-temperature testing is shown in Figure 22.

Cyclic testing of aluminum and titanium tanks at -320°F was done in the environment of liquid nitrogen using closed-loop servo system in conjunction with a cryogenic pump. A schematic diagram of the cryogenic test pressure system for liquid nitrogen is shown in Figure 23. Tank testing began only after the entire tank was submerged in liquid nitrogen. A complete load-time history was recorded. After failure, fracture faces were dried with hot air, each tank was photographed showing fracture origin, and fracture faces were removed for fractographic analysis and flaw size measurements.

Cyclic testing of tanks at -423°F was done in the environment of liquid hydrogen. The same basic cryogenic pressurization system was used, with the exception of a modification to permit helium purge of the entire system before and after the test. A schematic diagram of the -423°F tank test setup is shown in Figure 24. The loading profile for the 2219-T87 aluminum tanks was 0-100-0 and very nearly trapezoidal. Departure from a purely trapezoidal profile was brought about by the fact that maximum pressure could not be reached in less than 20 seconds. The time at maximum load was correspondingly reduced to some 10 rather than 15 seconds as initially programmed. The 0-100-0 loading profile for -423°F testing of titanium tanks was modified still further by allowing 45 seconds to reach maximum load. The programmer was adjusted to keep the tank at maximum pressure for a full 15 seconds. During the -423°F testing, each tank was submerged in liquid hydrogen. Upon failure, fracture faces were dried with hot air and each tank was photographed showing the fracture origin. Fracture faces were removed and subjected to fractographic examination for determination and measurement of initial and critical flaw sizes.

4.3 FRACTOGRAPHIC TECHNIQUE

Fatigue zones on fractured surfaces, while frequently visible to the naked eye in properly oriented light, are difficult to photograph under ordinary illumination. During the course of this program, attempts were made to improve fractographic resolution of cyclically tested specimens by utilizing polarized white light. The essential elements of the fractographic technique are illustrated schematically in Figure 25.

The developed fractographic setup consists of a beam of white light passing through the first polaroid filter, which is positioned so that its plane of polarization is parallel to the upper edge of an optical glass reflector. Light transmitted through the first filter is plane-polarized and is reflected from the glass plate vertically downward on fracture specimens without rotating the polarization plane. Upon striking the specimen surface, some of the plane-polarized rays of light are reflected under a shallow angle with respect to the horizontal plane and are scattered outside the optical axis of a camera. Others are reflected upward, pass through glass plate without rotation, and then are cross-polarized by the second polarizer screen. Still other rays strike the somewhat obliquely oriented flat surfaces and are reflected upward with resultant rotation of polarizing plane. These rays pass more readily through the second polarizing plate and are recorded on the film. The degree of shading or contrast attained is apparently a measure of relative density and distribution of reasonably flat and obliquely oriented surfaces.

One cyclically tested 2219-T87 aluminum specimen was sectioned and polished to show fracture profile and is pictured in Figure 26. It can be seen that profiles of the fracture faces bear distinct characteristics depending on mode of crack propagation. The low-stress initial extension region has numerous flat plateaus and appears to be dark in the picture. The region in which the fracture was under cyclic high-stress loading has a lesser amount of flat plateaus and is not as dark in the pictures. Finally, regions of rapidly propagating fracture are almost completely devoid of flat surfaces and appear to be quite light on the fractograph. An illustration that compares a fractograph taken with polarized light with a fractograph obtained from the same specimen using conventional illumination is shown in Figure 27.

Initial and critical surface flaw dimensions were determined directly from such fractographs showing outlines of initial and critical flaw regions. Depth of the flaws (a-dimensions) were measured directly from the fractograph. Flaw lengths due to flaw shape irregularities were calculated by first planimetering flaw area, then calculating the surface flaw length (2c-dimension), assuming the shape to be truly elliptical.

Cyclic flaw growth rates for 5Al-2.5Sn (ELI) titanium and 2219-T87 aluminum at room temperature, -320°F , and -423°F test temperatures were established by the end-point analysis of stress intensity versus cyclic life curves. The procedure

has been described in the section on technical background (Section 2.1.2). In addition, cyclic flaw growth rates were also determined in selected specimens and tanks using high-power electron-microscope fractography. The electron-microscope fractography procedure has been systemized to permit an exact determination of location and orientation with respect to flaw geometry of regions being analyzed.

Each fracture surface that was analyzed was gridded with fine scribe lines directly on the fracture face as shown schematically in Figure 28a. The imprint was then taken from the gridded region and shadowed and cut with a sharp scalpel forming individual replicas 0.06-inch deep and 0.09-inch wide. Simultaneously, a lower right-hand corner of each replica was clipped to identify the orientation. Next, each replica was treated with acetone (to dissolve the acetate film) and placed on a 0.118-inch-diameter sample grid for examination in the electron microscope. The replica's position on each sample grid was recorded photographically at low-power magnification as illustrated schematically in Figure 28b. Once the replica was placed on a sample grid, it remained permanently attached to the grid.

The examination of fracture replicas was conducted in two steps. First, the entire visible grid area was mapped on a separate, enlarged sketch of a grid sample. The mapping consisted of examining each grid window and symbolically recording the type of surface textures noted. In addition, a series of photographs were taken of the striated regions. The photographs were used to measure striation spacings throughout the entire region of flaw growth from initial to critical size. The magnification ratio (about 2800 times) in the photographs was selected so that the microstructure and at least a major portion of a grid window outline was visible. In this manner, the location and orientation of the region being analyzed were established to offer an opportunity to relate microscopic flaw growth indications to the overall growth of the entire flaw front.

5.0 TEST RESULTS

5.1 MECHANICAL PROPERTIES

The mechanical properties of the 5Al-2.5Sn (ELI) titanium and 2219-T87 aluminum materials that were tested in this program were determined, and were measured at the three test temperatures of room temperature, -320°F , and -423°F . The resulting properties of 5Al-2.5Sn (ELI) titanium and 2219-T87 aluminum are listed in Tables III and IV, respectively. The effect of temperature on ultimate strength, yield strength, and elongation for the two materials is illustrated in Figures 29 and 30.

5.2 5Al-2.5Sn (ELI) TITANIUM UNIAXIAL SPECIMEN RESULTS

5.2.1 Plane-Strain Fracture Toughness

Longitudinal-grain plane-strain fracture-toughness values were obtained for 5Al-2.5Sn (ELI) titanium at room temperature, -320°F , and -423°F in the environments of air, liquid nitrogen, and liquid hydrogen, respectively. Toughness values were computed for both statically and cyclically loaded uniaxial test specimens fabricated from 0.188-inch-thick material. The results of the static and cyclic tests are included in Tables V through XI.

At room temperature, a single K_{IC} value was determined from a center-cracked specimen. A distinct pop-in occurred at a K_I of 116 ksi $\sqrt{\text{in.}}$ as computed from Equation 7. A second center-cracked specimen was tested but no pop-in was detected. The crack reached final instability at a computed K value of 193 ksi $\sqrt{\text{in.}}$. In this report, the value of K_{IC} for 5Al-2.5Sn (ELI) titanium at room temperature is taken to be 116 ksi $\sqrt{\text{in.}}$.

Plane-strain fracture-toughness values computed at -320°F for both static and cyclic tests of uniaxially loaded 5Al-2.5Sn (ELI) titanium specimens are included in Tables V, VIII, and IX. The average of all the -320°F K_{IC} values in Tables V, VIII, and IX is 61 ksi $\sqrt{\text{in.}}$; this value is taken to represent the fracture toughness of 5Al-2.5Sn (ELI) titanium at -320°F .

Plane-strain fracture-toughness values for 5Al-2.5Sn (ELI) titanium at -423°F were computed only from statically tested specimens. Four specimens for which test results are given in Tables V, X, and XI failed under static loading conditions and yielded K_{IC} values of 45.4, 49.6, 57.4, and 57.4 ksi $\sqrt{\text{in.}}$. The specimens fractured at stress levels of 96.7, 116.1, 158.3, and 161.4 ksi, respectively.

The critical flaw sizes for the cyclically tested specimens listed in Tables X and XI could not be definitely measured. Neither the polarized-light technique nor the high-magnification fractograph provided a reliable means of identifying the critical flaw peripheries.

The effect of temperature on K_{IC} for 5Al-2.5Sn (ELI) titanium is illustrated in Figure 31.

5.2.2 Cyclic Life — Stress-Intensity Relationships

Surface-flawed 5Al-2.5Sn (ELI) titanium specimens were cyclically tested at room temperature, -320°F , and -423°F in the environments of air, liquid nitrogen, and liquid hydrogen. The resulting data are included in Tables VI through XI. The cyclic life of each specimen is related to its K_{II} value in Figures 32, 33, and 34.

In the titanium specimens that were cyclically tested at room temperature, the surface flaws grew through the thickness of each specimen before becoming unstable. The number of loading cycles required to grow the flaws through the specimen thickness have been taken as the lives of the room-temperature specimens. The specimen lives are related to the K_{II} values in Figure 32. The K_{II} values are presented as a decimal fraction of the K_{IC} value of $116 \text{ ksi}\sqrt{\text{in.}}$

The lives of the titanium specimens that were cyclically tested at -320°F are related to the individual K_{II} values in Figure 33. The K_{II} values are presented as a decimal fraction of the K_{IC} value of $61 \text{ ksi}\sqrt{\text{in.}}$. Four specimens were tested at a maximum cyclic stress of 97.5 percent of the uniaxial yield stress. Results from these specimens are indicated by data points that have an S beside them in Figure 33. The data points so indicated fall below the curves that were considered to represent the average results of specimens tested at lower maximum cyclic stress levels.

The lives of the titanium specimens that were cyclically tested at -423°F are related to the corresponding K_{II} values in Figure 34. The K_{II} values were determined for the initial flaw sizes that were visible on fractographs taken with polarized light. The same fractographs failed to give a definite indication of the critical flaw periphery. The results are represented by average curves in Figure 37 for both the 0-100-0 and 50-100-50 loading profiles.

The cyclic life data in Figures 33 and 34 can also be represented on σ versus a/Q plots. This has been done in Figures 35 through 38. Constant-cycles-to-failure curves were plotted to represent the average K_{II} versus N curves in Figures 33 and 34.

5.2.3 Flaw Growth Rates Computed from End-Point Analysis

Plane-strain flaw growth rates were obtained for 5Al-2.5Sn (ELI) titanium at room temperature, -320°F , and -423°F in the environments of air, liquid nitrogen, and liquid hydrogen. Flaw growth rates were computed from the average K_{II} versus N curves by means of the end-point analysis procedure outlined in Section 2.1.2 of this report.

The resulting flaw growth rates are presented in the form of $d(a/Q)/dN$ versus K_I curves in Figures 39, 40, and 41. Room-temperature flaw growth rate calculations are indicated by the open circles in Figure 39. The flaw growth rates have been extrapolated from the K_I values at which tests were conducted. Flaw growth rates at -320 and -423°F in Figures 40 and 41 were calculated for the entire range of K_{Ii} to K_{Ic} values.

5.2.4 Microscopically Determined Flaw Growth Rates

Replicas of the fracture surfaces of eighteen 5Al-2.5Sn (ELI) titanium test specimens were examined under an electron microscope. The procedure followed in the examination of the fracture surfaces is outlined in Section 4.0 of this report. Of the 18 specimens examined, two had been tested at room temperature, eight at -320°F , and eight at -423°F . The specimens examined at each temperature were equally divided between the 0-100-0 and 50-100-50 loading profiles.

Examining the fractures of the room-temperature specimens showed that there were many striated areas on the fracture surfaces. There were considerably fewer striated areas on the -320°F fracture surfaces. The -423°F fracture surfaces were essentially devoid of areas that contained recognizable striations. Sample fractographs of striated regions are shown in Figure 42.

The following observations were made during an investigation of characteristics of striated areas on the fracture surfaces:

- 1) There were very few areas that contained a large number of uniform striations. The striation formation appeared to be retarded by the grain boundaries. This apparent retardation resulted in curved striations of nonuniform width.
- 2) The striation spacings often increased monotonously over the surface of a single grain.
- 3) Striation spacings varied significantly from grain to grain at a given location.
- 4) There was no predominant striation orientation. Local orientations varied within ± 50 degrees with respect to the direction of macroscopic flaw propagation. Furthermore, there seemed to be no correlation between striation orientation and spacing.
- 5) As flaw depth became larger and approached the critical size, there were fewer and fewer discernible striations.

It was desired to compute flaw growth rates from the striation spacings on the basis of the belief that the striations represent the successive positions of the local flaw front at each loading cycle. The observed striation spacings accordingly represent localized flaw depth growth rates or da/dN . However, it was not obvious as to how the differences or variations of striation spacings should be interpreted. It was decided to record striation spacings where there were

two or more consecutive striations with a uniform spacing that was judged to be not greatly affected by the grain boundaries. No consideration was given to the orientation of the striations so that all measured spacings were given equal weight.

It was desired to compare the microscopic flow growth rates with rates calculated by end-point analyses, $d(a/Q)/dN$. Hence, not only the flaw depth, a , but also the flaw width, $2c$, was needed at each location of measured striation spacing. The flaw depth, a , values were measured directly from low-magnification fractographs. However, the flaw length, $2c$, values for only the initial flaw and the critical flaw were known. Intermediate values of $2c$ had to be estimated. To do so, it was assumed that for any given flaw depth

$$\frac{a - a_i}{a_{cr} - a_i} = \frac{2c - (2c)_i}{(2c)_{cr} - (2c)_i} \quad (11)$$

That is, both flaw depth and width growth simultaneously reached the same percentage of their total respective growths from initial to critical values.

The measured striation spacings are values of da/dN , which is the flaw depth growth rate. A relationship between da/dN and $d(a/Q)/dN$ can be derived by simple differentiation and is found to be

$$d(a/Q)/dN = \frac{da}{dN} \left(\frac{1}{Q} - \frac{a}{Q^2} \frac{dQ}{da} \right) \quad (12)$$

In the analysis of microscopic flow growth rates, values of $2c$ were computed from Equation 11; values of $d(a/Q)/dN$ were computed from Equation 12.

Flaw growth rates in 5Al-2.5Sn (ELI) titanium at room temperature were microscopically determined from striation spacing measurements made from two specimens tested at a maximum cyclic stress of 88 ksi. The one specimen had been subjected to a 0-100-0 loading profile and the other to a 50-100-50 loading profile. Each individual flaw growth rate determination is indicated by a solid data point in Figure 39. The flaw growth rates computed by the end-point analysis are indicated by the open data points in the same figure.

Flaw growth rates were microscopically determined for the 5Al-2.5Sn (ELI) titanium at -320°F from specimens that were tested at three different maximum cyclic stresses. The microscopically determined flaw growth rates are compared with corresponding end-point analysis flaw growth rates in Figures 43 through 48. Each figure represents results obtained for one maximum cyclic stress level and one loading profile. A comparison of microscopic flow growth rates at -320°F test temperature for the three test stress levels is made in Figure 49.

5.3 5Al-2.5Sn (ELI) TITANIUM CYLINDRICAL TANK RESULTS

A number of failures in the 5Al-2.5Sn (ELI) titanium cylindrical tanks occurred at longitudinal weldments rather than at the surface flaw in the cylinder wall. Notwithstanding the weld failures, four successful tests and one partially successful test were completed on the titanium tanks. The results of these five tests are included in Table XII.

In one cyclic room-temperature tank test (Tank 0009), the initial surface flaw grew through the thickness of the tank wall without becoming unstable. The number of cycles of loading required to grow the flaw through the wall thickness is related to the K_{II} value of the flaw in Figure 32. In the other cyclic room-temperature tank test, Tank 0008 withstood only five loading cycles before failure occurred at one of the longitudinal weldments. The initial and final flaw shapes for the five cycles of growth were identifiable on the flaw surface. An average flaw growth rate for the five loading cycles was computed by dividing the total change in the a/Q value of the flaw by the number of loading cycles over which the growth occurred. The computed growth rate is included in Figure 39.

One cyclic titanium tank test was completed at -320°F . Tank 0012 was subjected to 315 cycles of a 0-100-0 loading profile with a maximum cyclic stress of 80.4 ksi. The maximum cyclic stress was then increased to 115 ksi and, after an additional 81 loading cycles, the tank fractured. The fractured tank is pictured in Figure 50a. The failure originated at the artificial surface flaw. A fractograph of the fracture surface (Figure 50a) revealed both the critical flaw periphery and the location of the flaw periphery after the first 315 loading cycles. The K_{II} value for the 81 cycles of loading under the 115-ksi maximum cyclic stress was computed using the flaw dimensions that existed after the first 315 loading cycles. The cyclic life of the tank under the 115-ksi maximum cyclic stress is related to this computed K_{II} value in Figure 33. The computed K_{IC} value for this tank was $59 \text{ ksi} \sqrt{\text{in.}}$.

Two cyclic titanium tank tests were conducted at -423°F . Tank 0013 failed at a longitudinal weldment after being subjected to 75 cycles of a 0-100-0 loading profile with a maximum cyclic stress of 98 ksi. The failed tank is pictured in Figure 50b. The surface of the flaw in the parent metal was stained after the test; the final flaw size was readily identifiable on a fractograph of the fracture surface (Figure 50b). The K_I value at the flaw tip at failure was $56.5 \text{ ksi} \sqrt{\text{in.}}$. A comparison of this K_I value with the uniaxial K_{IC} values, which ranged from 45 to $57 \text{ ksi} \sqrt{\text{in.}}$, leads one to believe that failure at the base metal flaw must have been imminent at the time of the longitudinal weldment failure. Hence, the 75-cycle life of Tank 0013 is probably close to the life that would have been measured had failure occurred at the base metal flaw. The cyclic life of this tank is related to the K_{II} value for the flaw in Figure 34. Tank 0010 failed after being subjected to 28 cycles of a 0-100-0 loading profile with a maximum cyclic stress of 117.3 ksi. The data point from this tank test is also included in Figure 34.

The fracture surface of room-temperature Tank 0009 was investigated using an electron microscope. Striated areas were found that were very similar in appearance to the striated areas on the room-temperature uniaxial specimen fracture surfaces. Striation measurements were made over the flaw depth range of 0.13 to 0.17 inch in the 0.20-inch-thick tank wall. Hence, there presently is no generally accepted method to calculate the K_I values under which the striations were formed. The resulting flaw growth rates are therefore given as a function of the corresponding $(a/Q)^{1/2}$ values in Figure 51.

5.4 2219-T87 ALUMINUM UNIAXIAL SPECIMEN RESULTS

5.4.1 Plane-Strain Fracture Toughness

Transverse grain plane-strain fracture-toughness values for 2219-T87 aluminum were obtained at room temperature, -320°F , and -423°F in the environments of air, liquid nitrogen, and liquid hydrogen, respectively. Toughness values were obtained from both statically and cyclically loaded specimens of two different thicknesses, 0.6 and 1.2 inches. The results of the uniaxial specimen tests are included in Tables XIII through XIX.

At room temperature, K_{IC} values were computed from two statically and six cyclically tested uniaxial specimens. The values were computed from Equation 4 and are listed in Tables XIII, XIV, and XV. Toughness values have not been computed from some of the uniaxial test specimens. It was felt that the results from these specimens were affected by laminations in the 2219-T87 material. This matter will be discussed in Section 6.1 of this report. The average of all K_{IC} values for 2219-T87 at room temperature that are listed in Tables XIII, XIV, and XV is $33.4 \text{ ksi } \sqrt{\text{in.}}$.

An average K_{IC} was determined from the -320°F static and cyclic tests by the same procedure that was followed in evaluating the room-temperature tests. The individual K_{IC} 's for the statically tested specimens are given in Table XIII, and for the cyclically tested specimens in Tables XVI and XVII. No K_{IC} values are given for specimens in which the test results seemed to be affected by the laminations in the base material. The average K_{IC} for 2219-T87 aluminum at -320°F is $37.2 \text{ ksi } \sqrt{\text{in.}}$.

An average K_{IC} value for 2219-T87 aluminum at -423°F was determined from only cyclically tested specimens. An examination of the two statically tested specimens revealed delaminations at the tips of the initial flaws in both specimens. The K_{IC} values given in Tables XVIII and XIX were averaged to obtain a K_{IC} for the 2219-T87 aluminum at -423°F of $37.3 \text{ ksi } \sqrt{\text{in.}}$.

The effect of temperature on K_{IC} for 2219-T87 aluminum is illustrated in Figure 52. At -320°F , longitudinal-grain K_{IC} values determined in Reference 17 are included in the figure. The effect of temperature upon mechanical properties of 2219-T87 aluminum was shown earlier in Figure 30.

5.4.2 Cyclic Life — Stress-Intensity Relationships

Surface-flawed 2219-T87 aluminum specimens were cyclically tested at room temperature, -320°F , and -423°F in the environments of air, liquid nitrogen, and liquid hydrogen, respectively. The resulting data is included in Tables XIV through XIX. The cyclic life of each specimen is related to the corresponding K_{II} value in Figures 53 through 55.

The data for each test temperature and loading profile has been represented by an average test curve. In the drawing of the curves, data points for specimens in which the laminations seemed to have no effect were given more weight than were the data points for lamination-affected specimens.

The cyclic life data in Figures 53 through 55 can also be represented on σ versus a/Q plots. This has been done in Figures 56 through 61. Constant cycles-to-failure curves were plotted to represent the average K_{II} versus N curves. The σ versus a/Q plots show the range of maximum cyclic stresses over which tests were conducted.

5.4.3 Flaw Growth Rates Computed from End-Point Analysis

Plane-strain flaw growth rates were computed at room temperature, -320°F , and -423°F for the 2219-T87 aluminum. The rates were determined by applying the end-point analysis method described in Section 2.1.2 to the average K_{II} versus N curves of Figures 53 through 55. The results are summarized in Figure 62.

5.4.4 Microscopically Determined Flaw Growth Rates

Replicas of the fracture surfaces of one 2219-T87 aluminum uniaxial test specimen for each loading profile and test temperature were examined under an electron microscope. Striations were observed on the fracture surfaces of specimens tested at all three test temperatures. The striations were used to compute flaw growth rates by considering the striations to represent successive positions of the flaw front at each load cycle.

A large percentage of the flaw surfaces in the specimens that were tested at room temperature were striated. In contrast, the flaw surface of the -320°F and -423°F specimens were striated to a lesser percentage. Sample fractographs of observed striations are included in Figure 63.

During examination of striated areas, it was found that the same general observations enumerated in Section 5.2.4 for titanium also apply to 2219-T87 aluminum. In addition, it was also noted that in the 2219-T87 aluminum, there were locations at which striations radiated in all directions from an inclusion. The spacing of such striations increased with increasing radial distance from the inclusion.

The striations on the 2219-T87 fracture surfaces were interpreted in the same way as were the striations on the titanium specimens. Striation spacings were recorded where there were two or more striations with a uniform spacing that did not seem to be affected by grain boundaries. The striation spacings were taken as values of da/dN and were converted to flaw growth rates by means of Equations 11 and 12.

Three specimens that were examined exhibited flaw growth that did not seem to be affected by laminations. One specimen that was tested at -320°F failed after 47 cycles of a 0-100-0 loading profile. No recognizable striations were observed on the failure surface. The flaw growth rates computed from striation spacing measurements on specimens tested at room temperature, -320°F , and -423°F are indicated by the solid circles in Figures 64, 65, and 66. The corresponding macroscopic flaw growth rates are included in the same figures.

Flaw growth in the other specimens examined seemed to have been affected by laminations. These specimens were useful in observing the characteristics of striations but were not used to compute flaw growth rates.

5.5 2219-T87 ALUMINUM CYLINDRICAL TANK RESULTS

Six 2219-T87 aluminum tanks were tested under a 0-100-0 loading profile. Two tanks were tested at each of the three test temperatures of room temperature, -320°F , and -423°F . Surface flaws in the tanks were located in the tank wall in a 2:1 biaxial stress field with the plane of the flaw oriented perpendicularly to the maximum stress. Photographs of two fractured tanks are shown in Figure 67. The cyclic flaw growth data obtained from the tank tests are contained in Table XX and are plotted in Figures 53, 54, and 55.

All aluminum tank tests were continuous except for the Tank III test. Tank III was programmed for 20 to 40 cycles. The tank, however, withstood 80 cycles with a maximum cyclic stress of 46.5 ksi. This led to a suspicion that the flaw was delaminated. The load cycling was then halted and the pressure was slowly increased until a deliberate burst occurred at a computed membrane stress of 58 ksi.

In both tanks tested at -423°F (Tanks III and IV), the flaw growth was different from the type of growth that was observed in all other aluminum tanks and uniaxial specimens. The peculiar growth made it difficult to relate the test results from Tanks III and IV to the uniaxial specimen data. Interpretations of the -423°F aluminum-tank results will be discussed in Section 6.2.6 of this report.

Strain measurements were made on the outside surface of Tank V as described in Section 4.0 of this report. Maximum hoop and longitudinal stresses were calculated from strains measured at each of the three gage locations (see Figure 21 for gage location). The resulting stresses are included below.

<u>Gage</u>	<u>Hoop Stress, ksi</u>	<u>Longitudinal Stress, ksi</u>
1	42.8	21.6
2	40.1	18.6
3	39.7	19.7

Replicas of the fracture surface of Tanks II and VI were microscopically examined. A number of striated areas were observed within the critical flaw periphery of Tank II. The striations showed the same characteristics as did the striations on the uniaxial specimen fracture surfaces. The fracture surface of Tank VI revealed no recognizable striations.

Microscopic flaw growth rates were computed from striation spacing measurements for Tank II. The procedure used in calculating the flaw growth rates was the same as that used for uniaxial specimens, outlined in Section 5.1.4 of this report. The results are indicated by the solid circles in Figure 68.

BLANK PAGE

6.0 DISCUSSION OF RESULTS

6.1 DISCUSSION OF 5Al-2.5Sn (ELI) TITANIUM RESULTS

6.1.1 Plane-Strain Fracture Toughness

The plane-strain fracture toughness of 5Al-2.5Sn (ELI) titanium varies markedly with temperature. This is illustrated in Figure 31, which shows the range in K_{IC} values that were determined at each of the three test temperatures: room temperature, -320°F , and -423°F .

Only a single K_{IC} value of $116 \text{ ksi } \sqrt{\text{in.}}$ was determined for the titanium at room temperature. This K_{IC} value compared favorably with a K_{IC} of slightly over $120 \text{ ksi } \sqrt{\text{in.}}$ that was obtained in Frankfort Arsenal from a 1.5- by 0.5- by 0.6-inch single-edge-notched specimen (Ref. 21).

Certain specimens were disregarded in the computation of an average plane-strain fracture toughness of $61 \text{ ksi } \sqrt{\text{in.}}$ for 5Al-2.5Sn (ELI) titanium at -320°F . Statically tested specimen ST-1 and cyclically tested specimens CTO-7, CTO-19, CT5-7, and CT5-19 were tested at maximum net cyclic stresses that were greater than the uniaxial yield stress of the titanium. The theory that is used to analyze fracture specimens does not apply to specimens that go into general yielding; hence, fracture toughness values are not reported for the above specimens. Statically tested specimens CT5-5 and CT5-6 yielded calculated K_{IC} values of 53.5 and 45.6 $\text{ksi } \sqrt{\text{in.}}$, respectively. In both specimens, the area of the surface flaw was significantly greater than 10 percent of the gross specimen area. It is believed that this condition contributed to the apparent reduction in K_{IC} for these specimens. The K_{IC} values determined from the test results of specimens CT5-5 and CT5-6 are not considered valid and are not reported in Table V. In some other titanium tests at -320°F , Equation 4 was used to compute K_{IC} values for specimens with critical flaw depths as large as 77 percent of the thickness of the specimen, even though the equation is considered to be valid only for specimens with critical flaw depths less than 50 percent of the specimen thickness. Figure 69 shows that, in this particular test, the K_{IC} values computed for specimens with critical flaw depths greater than $0.5t$ agreed with K_{IC} values computed from specimens with critical flaw depths less than $0.5t$. For this reason, K_{IC} values for specimens with critical flaw depths greater than $0.5t$ were used in computing an average K_{IC} of $61 \text{ ksi } \sqrt{\text{in.}}$ for 5Al-2.5Sn (ELI) titanium at -320°F .

It is noted that, at -423°F , there was an apparent influence of fracture stress level on calculated K_{IC} for 5Al-2.5Sn (ELI) titanium. As the fracture stress level increased, K_{IC} also increased. A similar but less-marked correlation was noticed at -320°F . These observations indicate that Equation 4 may not properly account for the physical phenomena that contribute to resistance to fracture for 5Al-2.5Sn (ELI) titanium.

6.1.2 Cyclic Life — Stress-Intensity Relationships

The cyclic flaw-growth test results for 5Al-2.5Sn (ELI) titanium at room temperature, for a maximum cyclic stress of 88 ksi, and under each of the two loading profiles are represented well by the K_{II} versus cycles to grow through-the-thickness curves in Figure 32. Well defined K_{II} versus N curves were also obtained for both the 0-100-0 and 50-100-50 loading profiles at -320°F as shown in Figure 33. At -423°F , K_{II} versus N curves were not as well defined by the test data because of the relatively larger scatter in the data.

At -320°F , cyclic tests that were conducted at maximum cyclic stresses which varied from 117.5 to 158.3 ksi yielded cyclic life data that is represented well by single K_{II} versus N curves. However, four specimens that were tested at maximum cyclic stresses of 175 ksi (about 97 percent of the uniaxial yield strength of the material) yielded cyclic lives that were significantly shorter than were the lives of specimens cycled at the same K_I levels but at lower maximum cyclic stresses. These data indicate that the cyclic life curves and flaw growth rates in this report should not be applied at stress levels above the proportional limit of the material.

Notwithstanding the relatively large scatter in the flaw growth data for titanium at -423°F , average K_{II} versus N curves were drawn for both 0-100-0 and 50-100-50 loading profiles. This was done to derive reasonable flaw growth rates. Since flaw growth rates are proportional to the slope of the K_{II} versus N curve, average representatives with fairly steep slopes were drawn so that flaw growth rates would not be greatly underestimated.

The scatter in the -423°F cyclic flaw growth data for the 5Al-2.5Sn (ELI) titanium cannot be attributed to the existence of a unique relationship between flaw growth rate and stress intensity as implied by the crack growth criteria of Paris and Krafft. If flaw growth rates are a function of K_I and independent of the maximum cyclic stress, then the lives of specimens tested at identical K_I levels should be inversely proportional to the square of the maximum cyclic stress levels. Since the maximum cyclic stresses were varied from 100 to 175 ksi in the -423°F cyclic flaw growth tests, a reasonable amount of data scatter on a K_{II} versus N plot could be expected if the cyclic lives are indeed inversely proportional to the maximum cyclic stress. However, the longest relative lives were obtained from specimens tested at the highest maximum cyclic stress value of 175 ksi. Hence, the data scatter cannot be attributed to an inverse square dependence of cyclic life on maximum cyclic stress.

6.1.3 Flaw Growth Rates Computed from End-Point Analysis

End-point analysis flaw growth rates computed for particular K_I levels from given K_{II} versus N curves vary inversely as the square of the maximum cyclic stress. The cyclic flaw growth data obtained from a given material, test environment, and loading profile in these tests have been represented by unique K_{II} versus N

curves. Hence, end-point analysis flaw growth rates reported herein for given environments (air, LN₂, or LH₂) and loading profiles (0-100-0 or 50-100-50) will be given for a specified maximum cyclic stress level, say σ_0 . Flaw growth rates can be computed for other maximum cyclic stresses, say σ_1 , by multiplying the flaw growth rates for σ_0 by $(\sigma_0/\sigma_1)^2$. It is recommended that flaw growth rates not be computed for maximum cyclic stresses and K_I values which differ greatly from those σ_{\max} and K_I values for which test data are reported herein.

Flaw growth rates were computed at room temperature from 5Al-2.5Sn (ELI) titanium specimens in which the flaws grew through the thickness of the specimens before becoming unstable. To understand how the cyclic life data from such specimens can be evaluated, let it be assumed that two specimens of equal thickness have been tested under identical loading and environmental conditions. Specimen 1 has an initial surface flaw of known shape and a depth of $a_1 < 0.5t$. The flaw grew through the thickness of the specimen in A loading cycles. Specimen 2 had an initial flaw depth a_2 where $a_1 < a_2 < 0.5t$. Furthermore, the shape of the initial flaw in Specimen 2 was the same as the shape of the flaw in Specimen 1 after the flaw in Specimen 1 had grown to depth a_2 . The initial flaw in Specimen 2 grew through the thickness in B loading cycles. It is reasonable to assume that the flaw in Specimen 1 also required B loading cycles to grow from the depth a_2 through the thickness of the specimen. Hence, the number of loading cycles that were required to grow the flaw in Specimen 1 from depth a_1 to depth a_2 was A minus B cycles. Since both a_1 and a_2 were less than $0.5t$, the flaw was growing between depths a_1 and a_2 at K_{II} levels which can be computed from Equation 3. If the value of $a_2 - a_1$ is small, a flaw growth rate can be taken for this interval of growth as $(a_2/Q_2 - a_1/Q_1)/A - B$. This growth rate is simply an approximation of the slope of the $(a/Q)_i$ versus cycles to grow through the thickness curve that would represent the data from Specimens 1 and 2. If several specimens had been tested with varying initial flaw depths less than $0.5t$ and with similar flaw shapes at given flaw depths, an $(a/Q)_i$ versus cycles to grow through the thickness curve could be drawn through the test points. The flaw growth rates are given by the slope of this curve. Since all the initial flaw depths were less than $0.5t$, the $(a/Q)_i$ values can be converted to K_{II} values by means of Equation 3 and, hence, flaw growth rates can be determined from a K_{II} versus cycles to grow through the thickness curve for specimens.

In the cyclic tests of 5Al-2.5Sn (ELI) titanium conducted at room temperature, three specimens were tested at a maximum cyclic stress level of 88 ksi for each of the 0-100-0 and 50-100-50 loading profiles. The initial flaw depths were all less than $0.55t$ and the shapes of the flaws at given depths were reasonably similar. Hence, the K_{II} versus cycles to grow through the thickness curves for the above specimens were used to compute flaw growth rates over the K_{II}/K_{IC} range of $0.30 < K_{II}/K_{IC} < 0.41$. The computed flaw growth rates were extrapolated in Figure 39 to K_I values greater than K_I values at which flaw growth tests were conducted.

The computed room temperature flow growth rates for the 5Al-2.5Sn (ELI) titanium were linearly extrapolated on a $\log K_I$ versus $\log d(a/Q)/dN$ plot to the K_{IC} value of 116 ksi $\sqrt{\text{in.}}$ and the resulting curve was numerically integrated to derive K_{Ii} versus N curves for all K_{Ii} values less than K_{IC} . The resulting curves for 0-100-0 and 50-100-50 loading profiles are included in Figure 70. This extrapolation is not entirely valid since the flow growth rates actually tend to infinity as K_I approaches K_{IC} . However, the error involved in computing cyclic lives for K_I values near the K_{IC} level is small since the flow growth rates are very large at such K_I levels.

The ratio of end-point analysis flow growth rates for the 0-100-0 loading profile to those for the 50-100-50 loading profile was found to vary with both temperature and K_I . For example, at a K_I of 43 ksi $\sqrt{\text{in.}}$, the above ratio was 6.4 at room temperature, 3.0 at -320°F , and 4.8 at -423°F . At a K_I of 50 ksi $\sqrt{\text{in.}}$, the ratios were 10.8 at room temperature, 3.9 at -320°F , and 5.5 at -423°F . These results agree reasonably well at -320°F and -423°F with the corresponding ratio of 3.8 that is predicted by Krafft's equation for flow growth rates (Equation 9).

6.1.4 Microscopically Determined Flow Growth Rates

Room-temperature flow growth rates that were determined from measured striation spacings in room temperature titanium specimens agree reasonably well with the corresponding flow growth rates computed from the end-point analysis. For the 0-100-0 cyclic profile, some of the microscopically determined flow growth rates are equal to corresponding end-point analysis rates. On the average, however, the microscopic rates tend to be the greater of the two flow growth rates. For the 50-100-50 cyclic profile, the microscopically determined flow growth rates are approximately two times the computed end-point analysis flow growth rates.

The cyclic profile seemed to affect the relative magnitudes of microscopic and end-point analysis flow growth rates in titanium at -320°F . For the 0-100-0 cyclic profile, the microscopic flow growth rates were consistently smaller than the corresponding end-point analysis flow growth rates. For the 50-100-50 cyclic profile, the microscopic flow growth rates were consistently greater than the corresponding end-point analysis flow growth rates.

The microscopic flow growth rates determined for titanium at -320°F varied inversely with the test stress level. The effect of stress level on the flow growth rates is illustrated in Figure 49. In particular, the microscopic flow growth rates determined at 117.5 ksi and 138 ksi maximum cyclic stress levels for the 0-100-0 cyclic profile were inversely proportional to the square of the maximum cyclic stress. Thus, the representation of cyclic life test data obtained at several test stress levels by single K_{Ii} versus N curves appears to be reasonable.

Some slip lines were visible on the replicas taken from the fracture surfaces of the titanium specimens cyclically tested at -423°F . A study of the distribution of

the slip lines was conducted to see if there was a recurring slip line pattern which was indicative of flaw growth rates. The results of the study were inconclusive.

It is believed that some striations on the fracture surfaces of the titanium specimens resulted from the propagation of small flaws which formed ahead of the main crack front. Numerous grains in the fracture surfaces contained striations with monotonously increasing striation spacings. If small cracks did initiate ahead of the main flaw front and propagate in a striated mode, the stress intensity at the crack front would have rapidly increased as the main flaw front approached the advance crack. This explanation would account for the variable striation spacings observed in single grains. Any striations that were thought to be the result of advance cracking were not included in the determinations of microscopic flaw growth rates.

The method of interpretation of striation spacings used herein resulted in local flaw growth rates that agreed reasonably well with overall average flaw growth rates computed by end-point analysis. However, there were numerous striation spacings on the fracture surfaces that were presumably affected by grain boundaries, imperfections, or other physical discontinuities in the material. The spacings of many of these affected striations differed greatly from the spacings that were used to determine the microscopic flaw growth rates presented herein. Hence, it is possible that microscopic flaw growth rates determined from a very limited investigation of a fracture surface could be greatly in error.

6.1.5 Cylindrical Tank Results

The cyclic life data obtained from the 5Al-2.5Sn (ELI) titanium tank tests agree with the corresponding cyclic life data obtained from uniaxial test specimens at all three test temperatures. These results indicate that uniaxial plane-strain cyclic life data and flaw growth rates can be applied directly to the prediction of cyclic lives and flaw growth rates of flaws that grow under plane-strain conditions in cylindrical tank walls of 5Al-2.5Sn (ELI) titanium.

6.2 2219-T87 ALUMINUM TEST RESULTS

6.2.1 Effect of Laminations on Test Results

It was observed during the testing of the aluminum specimens that the 2219-T87 plate material from which the specimens were taken was layered. The planes of the layers were oriented parallel to the specimen surfaces so that the initial flaws had to propagate perpendicularly to the layering planes to reach critical size. Subsequent to the testing of some specimens, delaminations were noticed near the flaw front along the layering planes.

The possible effects of layering on flaw growth are illustrated by the fracture surface of the specimen shown in Figure 71. A delamination is visible at the tip of the initial flaw. At first, the delamination prevented the flaw from growing in

the depthwise direction and forced the flaw to grow laterally. The lateral growth shows in Figure 71 as a dark area adjacent to the light-colored initial fatigue extension. After a significant amount of lateral growth, the flaw tip traversed the split and began growing in the depthwise direction. The flaw continued to grow slowly along its entire periphery until it attained critical size and became unstable. In other specimens that were affected by delaminations, the crack growth in the depthwise direction was completely stopped (i.e. the crack was unable to traverse the split) and the flaw became critical at a point on the flaw periphery other than at the point of maximum depth.

Specimens that were considered to exhibit normal growth (i.e. not affected by layering or actual delaminations) typically had critical flaw shapes like that shown in Figures 72a. Figure 72b shows another example where layering was believed to have affected the flaw growth.

6.2.2 Plane-Strain Fracture Toughness

The room-temperature aluminum cyclic specimens were separated into two groups on the basis of the shape of the critical flaws. All specimens in group one had critical flaw shapes similar to the critical flaw shape illustrated in Figure 72a. Fracture toughness values computed for group one specimens agreed with the fracture toughness values computed for the statically tested specimens. All specimens in group two had critical flaw shapes similar to the critical flaw shape of Figure 72b. Fracture toughness values computed for group two specimens were consistently higher (about 15 percent) than were the fracture toughness values of the group one specimens. In view of the fact that the flaw growth in the group two specimens seemed to be affected by delaminations, it is possible that the computed toughness values were also affected. For example, an obstruction (such as a delamination) near the tip of the critical flaw could have prevented the flaw from becoming unstable at the maximum flaw depth. Fracture toughness values computed on the basis of the flaw becoming unstable at the maximum flaw depth would then be too high. It was felt that the K_{Ic} values obtained from the group one specimens were more representative of the fracture toughness of homogeneous 2219-T87 aluminum than were the group two K_{Ic} values.

The cyclic specimens that were tested at -320°F and -423°F were divided into groups in the same way as were the room-temperature specimens. The fracture toughness values were computed only for the specimens with critical flaw shapes similar to Figure 72a.

In an attempt to determine if the K_{Ic} values could be determined from the group two (layered) specimens, it was assumed that the flaws became critical at the points on the flaw peripheries where the amounts of cyclic growth were a maximum. The stress intensities were then calculated at these points of maximum flaw growth using the solution for stress intensity variation around flaw peripheries shown in

Figure 1. The results for the room temperature and -320°F specimens are shown in Figure 73. The solid bars indicate K_{Ic} values obtained from specimens that were not layered. The dashed-line bars indicate the apparent values in layered specimens using Equation 4 and the solid-line bars indicate the corrected K_{Ic} values for the same specimens. As can be seen from the figure, the corrected K_{Ic} values agree reasonably well with the K_{Ic} values obtained from nonlayered specimens.

6.2.3 Cyclic Life — Stress Intensity Relationships

The cyclic flaw growth data obtained for each loading profile in each of the three test environments is well represented by a single K_{Ii} versus N curve. Even though the depthwise flaw growth was inhibited in some specimens and not greatly inhibited in others, the same K_{Ii} versus N curves were found to represent the cyclic life results from both types of specimens that were tested in a given environment and under a given loading profile.

6.2.4 Flaw Growth Rates Computed by End-Point Analysis

Since the cyclic flaw growth data was well represented by unique K_{Ii} versus N curves for given test environments and loading profiles, it follows that end-point analysis flaw growth rates computed from the K_{Ii} versus N curves will also be representative of the overall average flaw growth rates in the specimens. The flaw growth rates given in Figure 62 are strictly valid only for unobstructed plane strain flaw growth. However, the agreement between cyclic life data obtained from specimen with obstructed flaw growth with data obtained from specimens with unobstructed growth implies that the cyclic lives for all 2219-T87 aluminum can be closely approximated by using the flaw growth rates in Figure 62.

The ratio of end-point analysis flaw growth rates for the 0-100-0 loading profile to flaw growth rates for the 50-100-50 loading profile was found to vary with both test temperature and K_I level. At a K_I of 30 ksi $\sqrt{\text{in.}}$, the ratio for the 2219-T87 aluminum was 3 at room temperature, 9 at -320°F, and 10 at -423°F. At a K_I of 25 ksi $\sqrt{\text{in.}}$, the ratio was 3 at room temperature, 5 at -320°F, and 5 at -423°F. Krafft's flaw growth rate, Equation 9, predicts a ratio of flaw growth rates for the two loading profiles of 3.8 at all three test temperatures and all K_I levels.

6.2.5 Microscopic Flaw Growth Rates

The majority of the microscopically determined flaw growth rates for the 2219-T87 aluminum specimens did not agree with corresponding flaw growth rates determined by end-point analysis. For the 0-100-0 loading profile at room temperature, the microscopically determined flaw growth rates were significantly greater than were the corresponding end-point analysis flaw growth rates. For the 50-100-50 loading profile at -423°F, some microscopic flaw growth rates were equal to the corresponding end-point analysis flaw growth rates. Under the same test condition, however, microscopic flaw growth rates were determined that were about ten times the corresponding end-point analysis flaw growth rates.

No recognizable striations were observed on the fracture of one uniaxial test specimen and one tank. For both, striation spacings needed to be about the grain size of the base material to be representative of the overall average flaw growth rate. Well-defined striations that were observed in this test program had spacings that were considerably smaller than the grain size of the base material. Hence, the fatigued fracture surfaces in 2219-T87 aluminum will not always contain recognizable striations.

In the 2219-T87 aluminum, evidence that cracking occurs ahead of the main flaw front was provided by striations that radiated with increasing spacing from inclusions. It appeared that small flaws originated at the inclusions and propagated under continually increasing stress intensities as the main flaw front approached the inclusions.

6.2.6 2219-T87 Aluminum Tank Tests

The major single difficulty encountered in the analysis of the preflawed aluminum tank cyclic data is the uncertainty as to the exact magnitude of the hoop stress applied to the tank walls at maximum cyclic pressure. As pointed out in Section 5.5, the first tank (Tank V) to be cyclically tested at room temperature was instrumented with strain gages on the outside surface. The strain measurements indicated maximum cyclic stresses of 40.4 ksi and 20.0 ksi in the hoop and longitudinal directions, respectively. These compare to hoop and longitudinal stresses of 44.3 ksi and 22.2 ksi, which were calculated using the measured tank pressures and the conventional membrane stress formulae, $\sigma_{\text{hoop}} = pR/t$ and $\sigma_{\text{long}} = pR/2t$.

In addition to the strain gage data, the results of the preflawed 2219-T87 aluminum tanks tested for the Saturn S-IC program (NAS8-5608) also tend to indicate that the calculated hoop stresses in the aluminum tanks tested in this program are somewhat high. Test tanks for the Saturn S-IC program were also 35 inches in diameter but of a configuration believed to be less susceptible to the restraining effects of weld land buildups and heavy heads. A comparison of the calculated K_{Ic} values (for the room-temperature and -320°F tanks tested on this program) with somewhat similar preflawed tanks tested on NAS8-5608 and with the uniaxial specimen data follows:

<u>Tank No.</u>	<u>Test Temp.</u>	<u>K_{Ic} Value</u>		<u>AV K_{Ic} From Uniaxial Data</u>	<u>NAS8-5608 Tank K_{Ic} Data</u>
		<u>Based On pR/t Stress</u>	<u>Based On 90% pR/t Stress</u>		
I	Room	38.2	34.4	33.5	---
V	Room	42.0	37.8	33.5	---
II	-320°F	43.6	39.4	37.2	39.2
VI	-320°F	45.8	41.2	37.2	40.6

It can be seen that the K_{Ic} values obtained using 90 percent of the calculated pR/t stress (i. e. , the approximate stress indicated by the strain gage data) compared quite favorably with the K_{Ic} values obtained from the tanks tested on NAS8-5608, but are still slightly higher than the values obtained from uniaxial specimens. The high apparent K_{Ic} values obtained with Tanks V and VI are believed to be due to material layering. As noted in Section 6.2.2, similar results were obtained on a number of uniaxial specimens.

While there are a number of possible reasons why the calculated pR/t stresses might be slightly in error, it has not yet been determined which of the two stresses (calculated or measured) are actually correct.

When comparing the tank cyclic life data with the uniaxial specimen data on a K_{Ii}/K_{Ic} versus cycles curve, the problem of lack of exact knowledge of the applied stresses can be circumvented if the flaw growth is normal and not affected by material layering or actual delaminations. At a given stress level, the stress intensity ratio is independent of the applied stress level and depends only upon the initial and critical flaw sizes as follows:

$$\frac{K_{Ii}}{K_{Ic}} = \frac{1.1 \sqrt{\pi} \sigma (a/Q)_i^{1/2}}{1.1 \sqrt{\pi} \sigma (a/Q)^{1/2}_{cr}} = \frac{(a/Q)_i^{1/2}}{(a/Q)_{cr}^{1/2}}$$

From the tank flaw size data shown in Table XX, the K_{Ii}/K_{Ic} ratios for Tanks I and II can be determined as follows:

<u>Tank</u>	<u>Test Temp.</u>	<u>$(a/Q)_i$</u>	<u>$(a/Q)_{cr}$</u>	<u>$\frac{(a/Q)_i}{(a/Q)_{cr}}$</u>	<u>$\frac{K_{Ii}}{K_{Ic}}$</u>	<u>Cycles</u>
I	Room	0.178	0.312	0.57	0.755	1285
II	-320°F	0.163	0.311	0.522	0.722	989

These data are plotted on the K_{Ii}/K_{Ic} versus cycle curves determined from the uniaxial specimens and shown in Figures 53 and 54. As can be seen from the figures, the correlation between the tank and uniaxial specimen data is quite good. However, if the K_{Ii}/K_{Ic} ratios are determined in the above manner for Tanks V and VI, the resulting data will have relatively poor correlation with the uniaxial data. It is believed that this can be explained by the abnormal flaw growth associated with material layering. As previously pointed out, if the crack front is retarded by a split in the material, the crack can become unstable at a point on the crack periphery other than at the point of maximum depth. In such a case, the calculated critical stress intensity, K_{Ic} , would be fictitiously high, as appears to be the case for both Tanks V and VI. This in turn causes the calculated K_{Ii}/K_{Ic} ratios to be fictitiously low.

To obtain a best estimate of the actual K_{II}/K_{IC} ratios, it was assumed that the flaws became critical at some unknown points on the flaw peripheries at stress intensities equal to the uniaxial K_{IC} values (i. e. , 33.5 ksi $\sqrt{\text{in.}}$ and 37.2 ksi $\sqrt{\text{in.}}$), and the initial stress intensities were calculated using the measured initial flaw sizes and the best estimate of the applied stress levels (i. e. , 90-percent pR/t). The resulting initial stress intensities for Tanks V and VI were 28.6 ksi $\sqrt{\text{in.}}$ and 31.6 ksi $\sqrt{\text{in.}}$, respectively, and the resulting K_{II}/K_{IC} ratios were 0.855 and 0.85. These data are plotted on Figures 53 and 54, and again the correlation with the uniaxial data is quite good.

Like the room-temperature and -320°F test tanks, the tanks tested in liquid hydrogen (Tanks III and IV) also exhibited calculated K_{IC} values in excess of those values obtained from uniaxial specimens. However, in both tanks, the presumed 10 percent error in the calculated hoop stress is insufficient to account for the discrepancy between uniaxial and biaxial data. A comparison of the apparent K_{IC} values computed from the tanks with the average K_{IC} values obtained from uniaxial specimens follows:

<u>Tank</u>	<u>Test Temp.</u>	<u>Based On PR/t Stress</u>	<u>Based On 90% PR/t Stress</u>	<u>Av. K_{IC} From Uniaxial Data</u>
III	-423°F	47.9	43	37.3
IV	-423°F	47.2	42.5	37.3

Upon examination of the fracture origins of these two tanks it became apparent that, in both tanks, the initial fatigue extension grew out of the plane of the initial EDM slot. This is illustrated in the photographs showing cross-sectional views of the flaws in Figures 74a and 75a. In Tank IV this out-of-plane growth also occurred during the pressure cycling at liquid-hydrogen temperature, but in Tank III the flaw growth with pressure cycles occurred in a plane normal to the applied load. However, the flaw growth in Tank III appeared to be affected by plate delaminations. One such delamination is readily evident in the photograph shown in Figure 74c.

Both the out-of-plane growth and delaminations would be expected to result in calculated K_{IC} values (using Equation 4) that are higher than the actual K_{IC} values of the material. The effect of delaminations on measured K_{IC} values was discussed previously in Section 6.2.2. The stress intensity for a surface flaw oriented at an angle α to the plane that is perpendicular to the applied load can be approximated as follows:

$$K = 1.1\sqrt{\pi}\sigma (a/Q)^{1/2} \cos^2 \alpha \quad (13)$$

For Tank IV the angle α appears to be approximately 15 degrees (see Figure 75a). If stress intensities are computed from Equation 13 using an applied stress equal to 90 percent pR/t, and the flaw size measurements shown in Table XX, the following initial and critical stress intensity values are obtained:

<u>Tank</u>	<u>Test Temp.</u>	<u>K_{Ii}</u>	<u>K_{Ic}</u>	<u>$\frac{K_{Ii}}{K_{Ic}}$</u>	<u>Cycles To Failure</u>
IV	-423°F	38	38.9	0.975	18

The K_{Ii}/K_{Ic} ratio of 0.975 is independent of the applied maximum cyclic stress and the angle α , i.e.,

$$\frac{K_{Ii}}{K_{Ic}} = \frac{(a/Q)_i^{1/2}}{(a/Q)_{cr}^{1/2}} = \left(\frac{0.147}{0.156} \right)^{1/2} = 0.975.$$

Hence, uncertainties in test stress and effect of the angle α do not affect calculation of this ratio. The cyclic life of Tank IV is related to the above K_{Ii}/K_{Ic} ratio in Figure 55.

As mentioned in Section 5.5, Tank III was deliberately burst after 80 pressure cycles because of suspected delamination problems which since have been confirmed by the fractographs shown in Figure 74. As a result, it is not possible to make a direct comparison of the tank cyclic life with cyclic lives obtained with the uniaxial specimens. However, it is of interest to determine if, in spite of the delaminations, the average flaw growth rate over the 80 cycles is at all comparable to that determined from the differentiation of the uniaxial specimen data. Using the measured initial and final flaw sizes shown in Table XX, the average flaw growth rate can be determined as follows:

$$\frac{d(a/Q)}{dN} = \frac{(a/Q)_{cr} - (a/Q)_i}{N} = \frac{0.179 - 0.159}{80} = 250 \text{ microinches per cycle.}$$

BLANK PAGE

7.0 APPLICATIONS AND LIMITATIONS

7.1 APPLICATIONS

The application of static and cyclic fracture toughness test data to such practical engineering problems as critical flaw size prediction, material selection, tank life estimates, and determination of nondestructive inspection limits has been previously discussed in References 14, 15, 17, 22, and 23. The data generated in this investigation can be applied to these types of problems as well as directly to the design of cryogenic tanks. An example that illustrates this design application is given in Appendix A of this report. Additionally, there are numerous useful comparisons that can be made with the data obtained. Some such comparisons are shown in Figures 76 through 80 and are discussed below.

Figure 76 shows the effect of temperature on the critical flaw depth at nominal operating stress in typical 2219-T87 aluminum and 5Al-2.5Sn (ELI) titanium pressure vessels. The operating stress was determined by dividing the tensile ultimate strength by 1.4, or the tensile yield strength by 1.1, whichever was lower. It was assumed that the flaw length was large, compared to the flaw depth, such that $Q=1.0$. As can be seen from Figure 76, the titanium alloy has large critical flaw depths at room temperature due to the high fracture toughness (K_{IC} value) and the relatively low operating stress level. With decrease in temperature, the critical flaw depth rapidly decreases due to the severe reduction in the K_{IC} value as well as the increase in nominal operating stress. The critical flaw depth for the 2219-T87 aluminum is relatively insensitive to temperature due to the compensating effects of increases in toughness and operating stress with reduction in temperature.

It is of interest to compare growth rates in the two materials and to show the effect of temperature on flaw growth rate by plotting flaw size versus growth rate at the operating stress level. Figures 77 and 78 show such growth rate comparisons for the two materials.

From Figure 77 it can be seen that, at a given flaw size, the cyclic growth rate in 5Al-2.5Sn (ELI) titanium increases by about a factor of 10 with a decrease in temperature from room temperature to -320°F , and by another factor of 10 with a further decrease in temperature from -320 to -423°F .

The effect of temperature on cyclic flaw growth rates in the aluminum alloy is much less pronounced than in the titanium. This is illustrated in Figure 78. At a given flaw size the flaw growth rate increases by about a factor of 3 with a reduction in temperature from room temperature to -320°F , and by another factor of 3 with a reduction in temperature from -320 to -423°F .

Assuming that the actual initial flaw sizes in a 2219-T87 aluminum and 5Al-2.5Sn (ELI) titanium LH_2 tanks are comparable, it is of interest to note that the growth rate in the titanium tank would be about 100 times the growth rate in the aluminum tank at the corresponding operating stress levels.

In addition to comparing flaw growth rates, it is of interest to compare the total number of cycles required to grow an initial flaw to critical size and cause fracture in two materials. Figure 79 shows a plot of initial flaw size versus cycles to failure for 5Al-2.5Sn (ELI) titanium at room temperature, -320°F , and -423°F when the tank is cycled from zero to a maximum stress level equal to the nominal operating stress level. A similar plot for the 2219-T87 aluminum is shown in Figure 80.

Assuming an arbitrary initial flaw size of 0.030 inch in a titanium tank, it can be seen from Figure 78 that the average cyclic life of the tank would be about 15 cycles at -423°F , 580 cycles at -320°F , and more than 8000 cycles at room temperature. For the same initial flaw size in a 2219-T87 aluminum tank, the average cyclic life would exceed 5000 cycles at all temperatures.

It is clear from these comparisons that both from the standpoints of critical flaw size and cyclic life, the 2219-T87 aluminum is superior to the 5Al-2.5Sn (ELI) titanium at cryogenic temperatures. In fact, at liquid hydrogen temperature it is expected that allowable flaw sizes in a titanium tank will be nearly impossible to detect. Initial flaw size depends on the required cyclic life and would probably be determined using lower bounds of the test data. The maximum allowable flaw size is equal to the critical flaw size minus the maximum anticipated subcritical flaw growth.

The question as to whether the titanium or the aluminum alloy should be used in flight-weight liquid-hydrogen tanks cannot be answered only from the results of this program. As pointed out in the following section, additional considerations enter into the picture before a specific assessment of the relative merits of the two materials can be made.

Costs must be considered when comparing materials for a given tankage application. Although the cost required to obtain a reliable 5Al-2.5Sn (ELI) titanium liquid-hydrogen tank would be significantly higher than for a 2219-T87 aluminum tank, it is conceivable that in some upper-stage and payload applications the cost effectiveness in terms of dollars per pound of payload could be low enough to justify its use.

7.2 LIMITATIONS

It is the opinion of the investigators that the two major limitations on the application of the data obtained in this program are:

- 1) The present lack of data on sustained stress and combined sustained stress and cyclic flaw growth for the two materials;
- 2) The present lack of data on fracture toughness and subcritical flaw growth in weldments and heat-affected zones.

The problem of sustained-stress flaw growth and combined sustained-stress and cyclic flaw growth have been discussed previously in Section 2.1.2 of this report.

Without adequate quantitative data on the two materials, it must presently be assumed that the cyclic life data presented in this report is unconservative when applied to pressure vessels where the maximum cyclic stress is held for prolonged periods of time. The work presently being performed on NASA Contract NAS3-6290 should eliminate present deficiencies and thus allow more general application of the cyclic flaw growth data obtained.

The need for weldment- and heat-affected zone toughness and flaw growth data is obvious when it is recognized that most large tanks do contain relatively high stressed welds. It is in these areas that the probability of flaw occurrence is generally the highest. At present there has been some fracture toughness and subcritical flaw growth data generated on as-welded 2219-T87 aluminum at -320°F in support of the NASA Saturn 5-IC program (Ref. 17). However, to the authors' knowledge, there is virtually no valid data for weldments and heat affected zones in the 5Al-2.5Sn (ELI) titanium. As discussed previously in this report, there were several titanium weldment failures encountered during the course of this program. As a result, some effort was made to determine cyclic flaw growth rates in GTA weldments using electron fractography. The results indicated growth rates in the weldments at room temperature about eight times higher than those in the parent metal at comparable stress intensity levels.

8.0 CONCLUSIONS

The total cyclic lives, plane strain flaw growth rates, and critical flaw sizes in both uniaxial and biaxial stress fields appear to be essentially the same. Therefore, it is concluded that uniaxial fracture specimen data can be safely used to predict flaw growth and critical flaw sizes in thick-walled pressure vessels.

Plane strain flaw growth rate and total cyclic life curves can be obtained with a single surface-flawed specimen tested in fatigue using electron fractography to obtain the growth rate data or by testing a number of surface-flawed specimens and using the end-point analysis procedure presented herein. Because of the uncertainties involved in the interpretation of striation spacings, it is concluded that the electron fractography procedure is less reliable.

From the standpoints of parent metal critical flaw sizes and subcritical flaw growth characteristics, the 2219-T87 aluminum alloy shows clear advantages over the 5Al-2.5 Sn (ELI) titanium alloy for cryogenic tankage application.

REFERENCES

1. Green, A. E., and I. N. Sneddon, "The Distribution of Stress in the Neighbourhood of a Flat Elliptical Crack in an Elastic Solid," Proc. Cambridge Phil. Soc 46, 1959 (1950)
2. Irwin, G. R., "Crack Extension Force for a Part-Through Crack in a Plate," Journal of Applied Mechanics, Vol. 84E, No. 4, December 1962.
3. Irwin, G. R., "Analysis of Stresses and Strains Near the End of a Crack Traversing a Plate," Journal of Applied Mechanics, Vol. 24, September 1957.
4. Westergaard, H. M., "Bearing Pressures and Cracks," Trans. ASME, Vol. 61, 1939, pp A-49 - A-53.
5. Kobayashi, A. K., R. D. Cherepy, and W. C. Kinsell, "A Numerical Procedure for Estimating the Stress Intensity Factor of a Crack in a Finite Plate," Journal of Basic Engineering, Vol. 86, No. 4, December 1964.
6. Paris, P. C., and G. C. Sih, "Stress Analysis of Cracks," Proc. of ASTM Fracture Toughness Testing and Its Application, ASTM Special Technical Publication No. 381, 1965, pp 30-81.
7. Kobayashi, A. K., M. Ziv, and L. R. Hall, "Approximate Stress Intensity Factor for an Embedded Elliptical Crack Near a Free Surface," International Journal of Fracture Mechanics, Vol. 2, No. 1, 1965.
8. "Fracture Testing of High-Strength Sheet Materials," ASTM Special Committee of Fracture Testing of High Strength Metallic Materials, ASTM Bulletin 243, January 1960, pp 29-40.
9. Boyle, R. W., A. M. Sullivan, and J. M. Krafft, "Determination of Plane Strain Fracture Toughness with Sharply Notched Sheets," Welding Journal (Research Supplement), Vol. 41, No. 9, September 1962, pp 428s-432s.
10. Paris, P., "The Growth of Cracks Due to Variation in Load," Ph.D dissertation, Lehigh University, September 1962.
11. Anderson, W. E., and D. R. Donaldson, "Crack Propagation Behavior of Some Airframe Metals," Boeing Document D6-7888, September 1961.
12. Davis, R. A., "Fracture Toughness and Tear Tests - Exhibit C," Second Quarterly Progress Report on Contract AF33(657)-11461, January 1964.
13. Krafft, J. M., "A Comparison of Cyclic Fatigue Crack Propagation with Single Cycle Crack Toughness and Plastic Flow," Report to ASTM Fracture Toughness of High-Strength-Materials Special Committee, September 1964.
14. Tiffany, C. F., and P. M. Lorenz, "An Investigation of Low-Cycle Fatigue Failures Using Applied Fracture Mechanics," ML-TDR-64-53, May 1964.

15. Tiffany, C. F., and F. A. Pall, "An Approach to the Pressure Vessel Minimum Fatigue Life Based Upon Applied Fracture Mechanics," Boeing Document D2-22437, March 1963.
16. Johnson, H. H., and A. M. Millner, "Environment and Fracture of High Strength Steel," Cornell University Report, Ithica, New York, October 1963.
17. Tiffany, C. F., and P. M. Lorenz, "Fracture Toughness and Subcritical Flaw Growth Characteristics of Saturn S-IC Tankage Materials," Boeing Document D2-22802, October 1963.
18. Forsyth, P. J. E., and D. A. Ryder, "Fatigue Fracture: Some Results Derived from the Microscopic Examination of Crack Surfaces," Aircraft Engineering, Vol. 32, 1960, p. 96.
19. Beachem, C. D., and R. M. N. Pelloux, "Electron Fractographs," ASTM Special Technical Publication No. 381, April 1965.
20. "Fracture Testing of High-Strength Sheet Materials," ASTM Special Committee of Fracture Testing of High Strength Metallic Materials, ASTM Bulletin, May 1961.
21. Carmen, C. M., J. W. Forney, and J. M. Catlin, "Plane Strain Fracture Toughness and Mechanical Properties of 5Al-2.5Sn (ELI) Titanium at Room and Cryogenic Temperatures," NASA CR54296.
22. Tiffany, C. F., and J. N. Masters, "Applied Fracture Mechanics," ASTM Proceedings of the Symposium on Fracture Toughness Testing and its Applications, STP 381, March 1965.
23. "Progress in the Measurement of Fracture Toughness and the Application of Fracture Mechanics to Engineering Problems," ASTM Special Committee on Fracture Testing of High-Strength Metallic Materials, Materials Research and Standards, Vol. 4, No. 3, March 1964, p. 107.

APPENDIX

ILLUSTRATIVE TANK DESIGNS USING CYCLIC-LIFE AND FRACTURE-TOUGHNESS DATA

1.0 INTRODUCTION

The body of this report contains cyclic life and fracture toughness data that can be useful in the design of cryogenic tanks fabricated from either 5Al-2.5Sn (ELI) titanium or 2219-T87 aluminum. To illustrate possible ways in which the data can be used, two illustrative tank designs are included in this appendix. One 2219-T87 aluminum tank and one 5Al-2.5Sn (ELI) titanium tank are designed to satisfy a given set of hypothetical design requirements. The designs are carried only as far as required to illustrate the use of cyclic life and fracture toughness data.

2.0 DESIGN INFORMATION

2.1 OPERATING CONDITIONS

A minimum-weight pressure vessel is to contain helium gas at a maximum operating pressure of 4000 psig. The vessel is to be stored in a liquid-hydrogen-propellant tank. Installation and mounting conditions require that the tank be cylindrical in shape, with a maximum outside diameter of 20 inches.

2.2 LOADING CONDITIONS

The pressure vessel must be able to withstand the following loadings:

- 1) 300 loading cycles in which the pressure changes from 50 to 100 to 50 percent of operating pressure.
- 2) 150 loading cycles in which the pressure varies from 0 to 90 to 0 percent of maximum operating pressure.
- 3) 50 loading cycles in which the pressure varies from 0 to 95 to 0 percent of the maximum operating pressure.
- 4) 8 days at 100 percent of the maximum operating pressure.

2.3 MATERIAL PROPERTIES

<u>Material</u>	<u>Temp.</u>	<u>Yield Stress (ksi)</u>	<u>Ultimate Stress (ksi)</u>
5Al-2.5Sn (ELI) Ti	-423°F	170	195**
2219-T87 Al	-423°F	70.5*	87*

* Firm design allowables from Boeing Design Manual

** Preliminary design allowables from Boeing Design Manual

Maximum Allowable Proof Stress — The maximum allowable proof stress will be the yield stress of the material. Proof tests will be assumed to be conducted at -423°F.

3.0 REQUIRED INFORMATION

The following items are required for one 2219-T87 aluminum and one 5Al-2.5Sn (ELI) titanium pressure vessel that have been designed to meet the foregoing requirements:

- 1) Operating pressure;
- 2) Factor of safety with respect to burst;
- 3) Proof test factor;
- 4) Weight per linear foot of cylindrical portion of tank.

4.0 ASSUMPTIONS

The following assumptions will be made:

- 1) The apparent threshold K_{Ic} values are equal to 0.90 K_{Ic} .
- 2) The welds are sufficiently well designed to prevent failures originating at the welds.
- 3) There are no significant secondary stresses in the pressure vessels.

5.0 USE OF CYCLIC LIFE AND FRACTURE TOUGHNESS DATA

Cyclic life curves, which are considered to be lower bounds for the data included in this report, will be used in the illustrative design to follow. The lower-bound curves, as drawn, are not statistical lower limits and it is not possible to determine the probability of failure associated with their use. The limited number of data points that are available for a given material and test conditions are not sufficient to permit a statistical analysis.

5.1 5Al-2.5Sn (ELI) TITANIUM

Fracture toughness values ranging from 45 to 58 ksi $\sqrt{\text{in.}}$ were computed for the 5Al-2.5Sn (ELI) titanium at -423°F. In drawing a lower-bound normalized cyclic life curve to be used in designing the 5Al-2.5Sn (ELI) titanium tank, a K_{Ic} of 58 ksi $\sqrt{\text{in.}}$ was used to normalize the data of Figure 37 in the main body of the report. The resulting normalized data and lower-bound design curves for the 0-100-0 and 50-100-50 loading profiles are included in Figure A1. The use of a high K_{Ic} to normalize the test data results in lower bound cyclic life curves that are conservative. This result is schematically illustrated in Figure A2. It can be seen that the curve derived by using the higher K_{Ic} value is the more conservative, both from the standpoint of cyclic life for given K_{Ii}/K_{Ic} values and the standpoint of flaw growth rates which are proportional to the slope of the K_{Ii}/K_{Ic} versus N curve.

5.2 2219-T87 ALUMINUM

The cyclic life data obtained for a given loading profile in the 2219-T87 aluminum tests did not vary greatly with temperature. Cyclic life data for the 2219-T87 aluminum at three different test temperatures and under two different loading profiles are plotted in Figure A3. Lower-bound curves have been drawn for each loading profile to bound the data obtained at all three test temperatures. The lower-bound curves in Figure A3 will be used to design the 2219-T87 aluminum tank in this appendix.

6.0 TANK DESIGNS

6.1 5Al-2.5Sn (ELI) TITANIUM TANK

The lower-bound cyclic life curves in Figure A1 for 5Al-2.5Sn (ELI) titanium at -423°F have been reproduced in Figure A4. The change in K_{Ii}/K_{Ic} throughout the life of the titanium tank is graphically illustrated in Figure A4 and was determined by the following procedure:

- 1) Since the apparent threshold stress intensity is 0.90 K_{Ic} , the allowable K_{Ii}/K_{Ic} at the beginning of the 8-day hold period is 0.90. This requirement is illustrated by point A in Figure A4.
- 2) The tank wall stress is raised by 5 percent at the end of the 50 loading cycles of from 0 to 95 to 0 percent of the operating stress. The flaw size remains the same during the stress increase. Therefore, the increase in K_{Ii}/K_{Ic} is proportional to σ since

$$\frac{K_{Ii}}{K_{Ic}} = \frac{1.1 \sqrt{\pi} \sigma \left(\frac{a}{Q}\right)_i^{\frac{1}{2}}}{K_{Ic}} \quad (A1)$$

Hence, the allowable K_{Ii}/K_{Ic} ratio at the end of the 50 loading cycles is $0.95 \times 0.90 = 0.855$. This K_{Ii}/K_{Ic} ratio is given by point B in Figure A4.

- 3) The 50 loading cycles from 0 to 95 to 0 percent of operating pressure changes the K_{Ii}/K_{Ic} ratio from point B to point C in Figure A4. Point C is 50 cycles to the right of point B with the cycles being measured along the abscissa of the plot. Hence, the allowable K_{Ii}/K_{Ic} ratio at the beginning of the 50 loading cycles is 0.75.
- 4) The stress is increased by 5 percent at the end of the 150 loading cycles of from 0 to 90 to 0 percent of operating pressure. Hence, the allowable K_{Ii}/K_{Ic} ratio at the end of the 150 loading cycles is $0.90/0.95 \times 0.77 = 0.71$. (See Step 2.) This K_{Ii}/K_{Ic} ratio is given by point D in Figure A4.
- 5) The 150 loading cycles of 0 to 90 to 0 percent of the operating stress change the K_{Ii}/K_{Ic} ratio from that given by point D in Figure A4 to that given by point E. Point E is located 150 cycles to the right of point D as measured along the abscissa of the plot. Hence, the allowable K_{Ii}/K_{Ic} ratio at the end of the 150 loading cycles is 0.615.
- 6) At the end of the 300 loading cycles of 50 to 100 to 50 percent of the operating pressure, the stress is decreased by 10 percent. Hence, the allowable K_{Ii}/K_{Ic} ratio at the end of the 300 loading cycles is $100/0.90 \times 0.615 = 0.68$. This allowable K_{Ii}/K_{Ic} ratio is given by point F in Figure A4. After an increase in pressure, the K_{Ii}/K_{Ic} ratio must not exceed the 0.90 apparent threshold level.
- 7) At the beginning of the 300 loading cycles of 50 to 100 to 0 percent of the operating stress, the allowable K_{Ii}/K_{Ic} ratio is given by point G as 0.66. Point G is located 300 cycles to the right of point F along the cyclic life curve for the 50-100-50 loading profile.
- 8) After the tank is proof tested to the yield stress, there can be no flaws in the tank greater than the critical flaw size at the proof test stress σ_y , i.e.,

$$\left(\frac{a}{Q}\right)_{\max.}^{1/2} \leq \frac{1}{1.1\sqrt{\pi}} \cdot \frac{K_{Ic}}{\sigma_y} \quad (A2)$$

To prevent the K_{Ii}/K_{Ic} ratio from increasing to a value greater than 0.90 at the beginning of the 8-day hold period for the tank, it has been shown in Steps 1 through 7 that the K_{Ii}/K_{Ic} ratio must be no greater than 0.66, i.e.,

$$\frac{K_{Ii}}{K_{Ic}} \leq 0.66 \leq \frac{1.1\sqrt{\pi}\sigma_{op} \left(\frac{a}{Q}\right)_{\max.}^{1/2}}{K_{Ic}} \quad (A3)$$

The proof test establishes a maximum value of (a/Q) given by Equation A2. The substitution of Equation A2 into Equation A3 permits the calculation of an operating stress that satisfies the requirement expressed by Equation A3. Hence,

$$0.66 < \frac{1.1\sqrt{\pi} \sigma_{op}}{K_{Ic}} \cdot \frac{1}{1.1\sqrt{\pi}} \cdot \frac{K_{Ic}}{\sigma_y}$$

or
$$\sigma_{op} \leq 0.66 \sigma_y$$

- 9) The required thickness of the cylindrical tank wall can be computed from the conventional formula for the hoop membrane stresses in cylindrical tanks, i.e.,

$$t = \frac{pD}{2\sigma_{op}} = \frac{4000 \times 20}{2 \times 112} = 0.35 \text{ in.}$$

From the standpoint of tank fabrication, it is desirable to know how large the largest flaw in the tank can be before that flaw will become unstable at the proof stress. For this computation, a low value of $K_{Ic} = 45 \text{ ksi}\sqrt{\text{in.}}$ will be used in conjunction with Equation A2 since a low value of K_{Ic} places the most restrictive requirements on the manufacturing process. Then,

$$\begin{aligned} (a/Q) \text{ allowable} &= \frac{1}{1.21\sqrt{\pi}} \left(\frac{K_{Ic}}{\sigma_y} \right)^2 \\ &= \frac{1}{1.21\sqrt{\pi}} \left(\frac{45}{170} \right)^2 = 0.018 \text{ in.} \end{aligned}$$

6.2 2219-T87 ALUMINUM TANK

The change in the maximum allowable value of K_{Ii}/K_{Ic} throughout the required life (Section A2) of the aluminum tank is graphically in Figure A5. This plot was constructed by following exactly the same procedure used in the titanium tank design. The cyclic life curves in Figure A5 are the same as the lower bound cyclic life curves in Figure A3.

The maximum allowable K_{Ii}/K_{Ic} ratio at the beginning of the 300 cycles of 50 percent σ_{op} to 100 percent σ_{op} to 50 percent σ_{op} is 0.84 (Figure A5). As outlined in Step 8 of the titanium tank design, it follows that the allowable operating stress is $0.84 \sigma_y$ or $0.84 (70.5) = 59 \text{ ksi}$.

The maximum flaw size that could exist in an aluminum tank after being tested to a proof test stress of σ_y at -423°F can be computed from Equation A2. Taking the appropriate minimum K_{Ic} that was measured in the test program described in the main body of the report of $32.8 \text{ ksi}\sqrt{\text{in.}}$,

$$(a/Q) \text{ allowable} = \frac{1}{1.21\sqrt{\pi}} \left(\frac{K_{Ic}}{\sigma_y} \right)^2 = \frac{1}{1.21\sqrt{\pi}} \left(\frac{32.8}{70.5} \right)^2 = 0.057 \text{ in.}$$

7.0 SUMMARY OF RESULTS

Material	σ_{op} ksi	$\frac{\sigma_y}{\sigma_{op}}$	$\frac{\sigma_{ult}}{\sigma_{op}}$	t in.	(a/Q) cr @ Proof Stress	Weight lb/ft
5Al-2.5Sn (ELI) Ti	112	1.5	1.7	0.35	0.018	35.6
2219-T87 Al	59	1.2	1.5	0.68	0.057	43.5

8.0 COMMENTS

The titanium tank was the lighter of the two tanks. However, the allowable maximum flaw size at proof stress is only 0.018-inch (or only one third of the allowable maximum flaw size at proof stress for the aluminum tank). It would be very difficult to fabricate titanium tanks and ensure by nondestructive inspection that there were no flaws greater than 0.018 in. A number of titanium tanks could be expected to fail during proof test. The allowable flaw size in the aluminum tank is larger, and it would be easier to fabricate acceptable aluminum tanks than to fabricate acceptable titanium tanks.

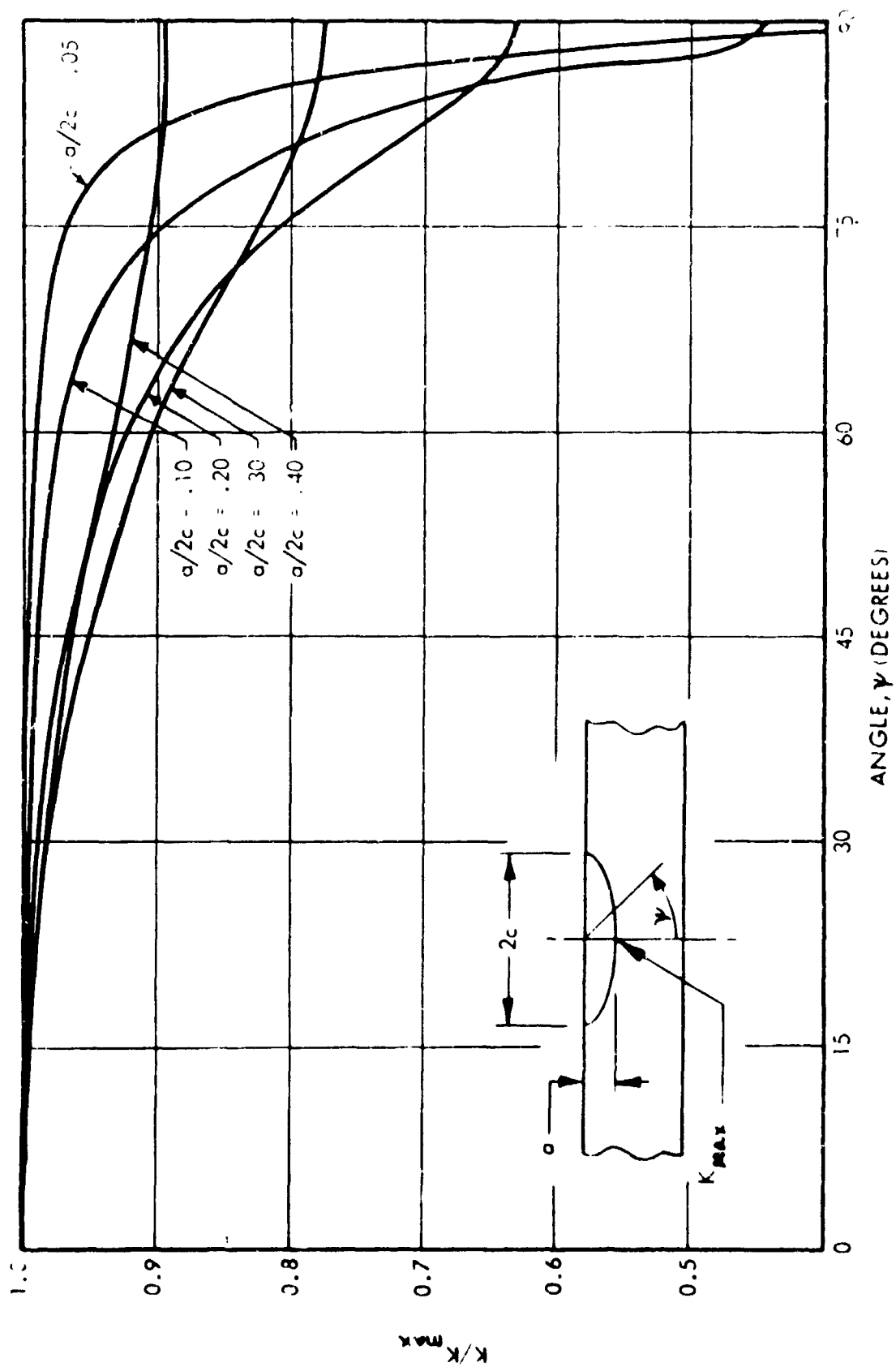


Figure 1: VARIATION OF STRESS INTENSITY ALONG FLAW PERIPHERY

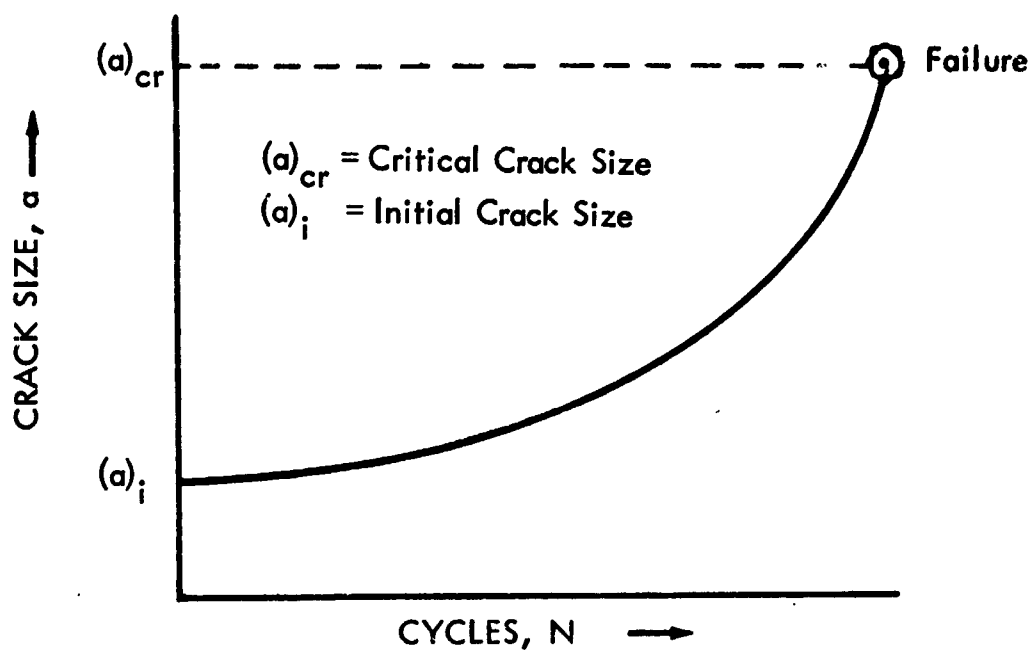


Figure 2a: BASIC CRACK GROWTH CURVE
Schematic Representation

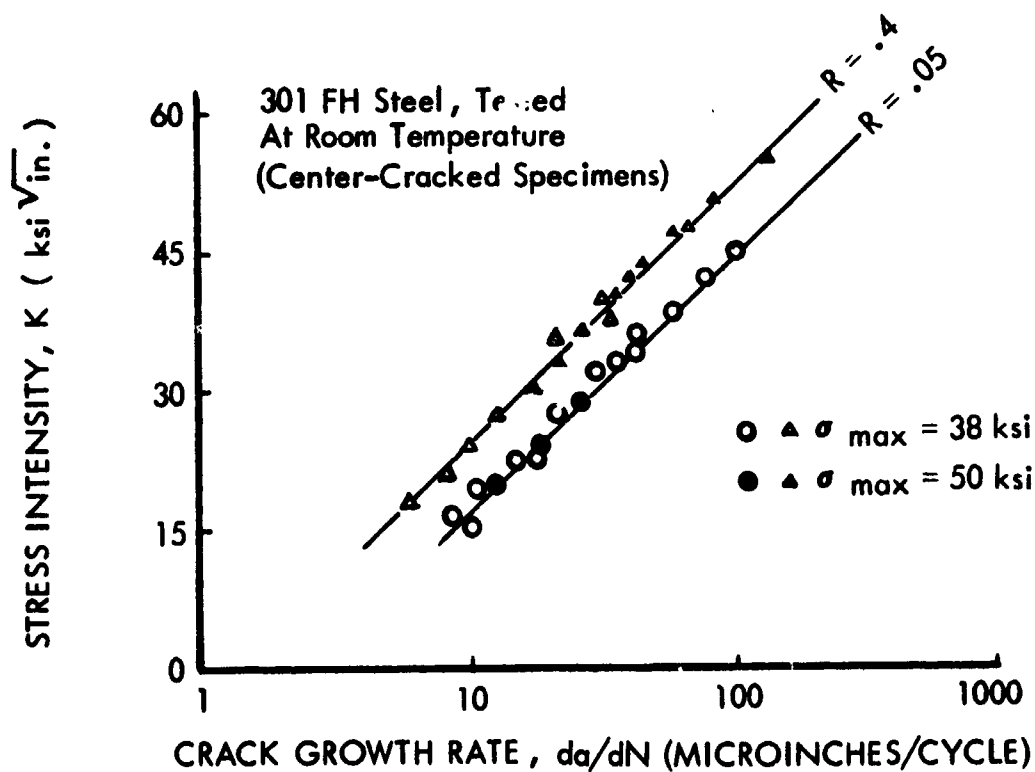


Figure 2b: CRACK GROWTH-RATE DATA
Actual Sample

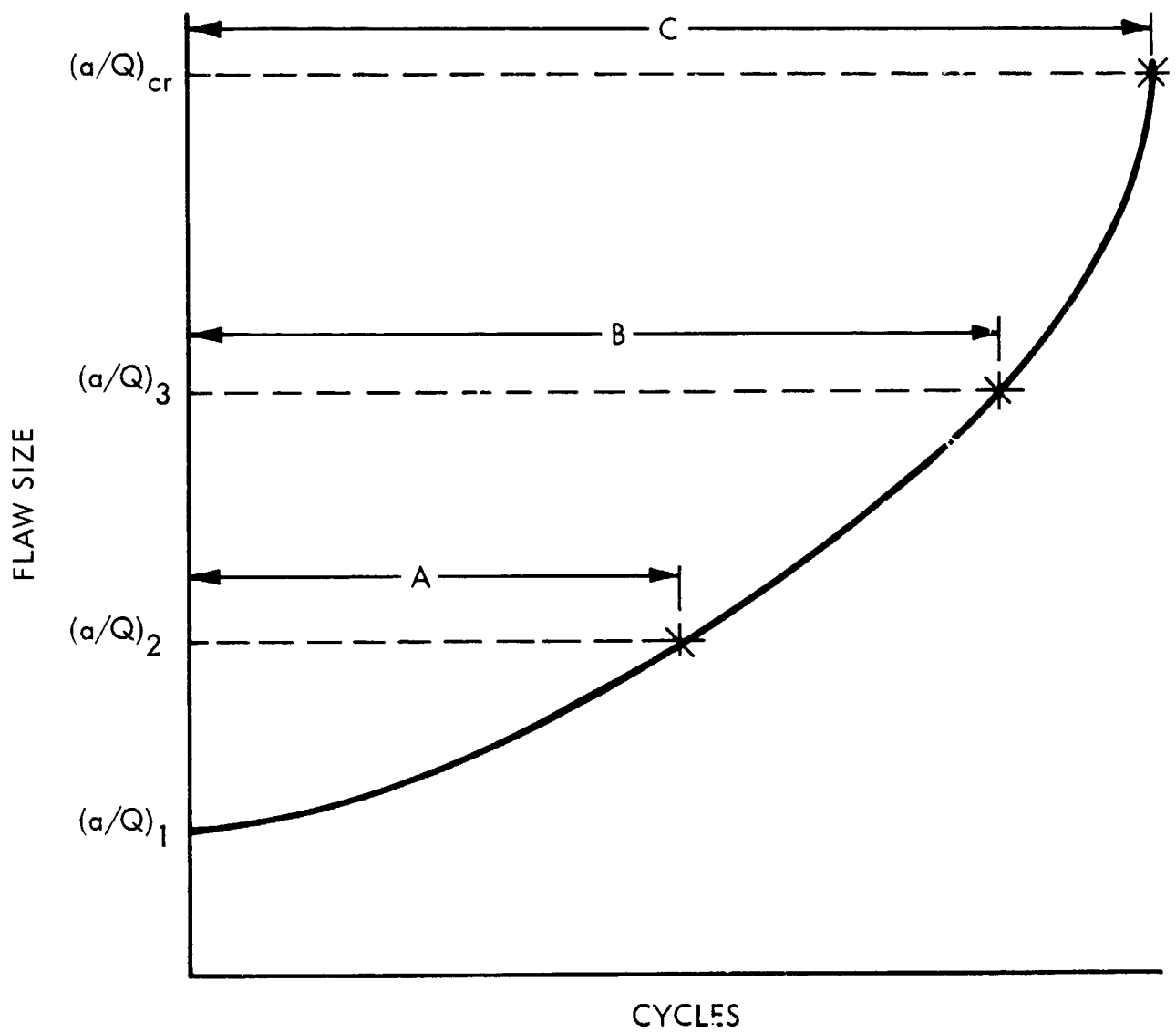


Figure 3: FLAW-GROWTH MEASUREMENT FROM A SINGLE SPECIMEN

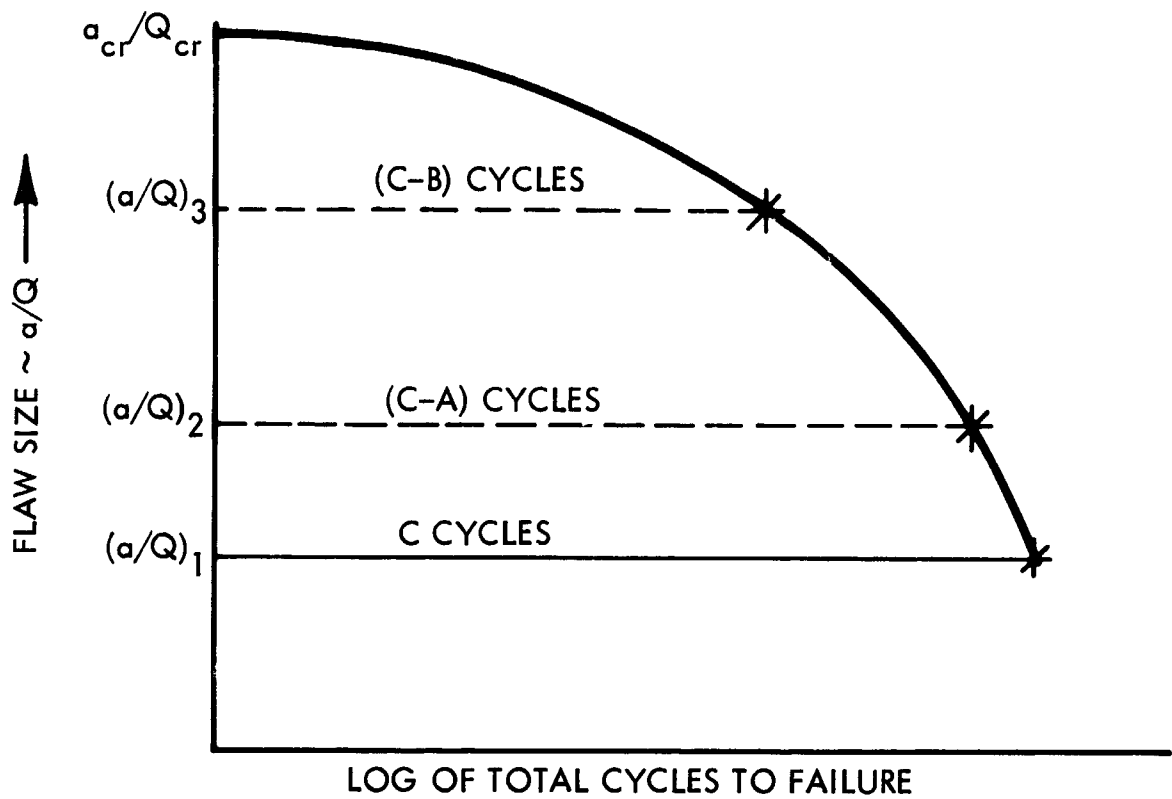


Figure 4a: INITIAL FLAW SIZE VS LIFE SPAN (SCHEMATIC REPRESENTATION)

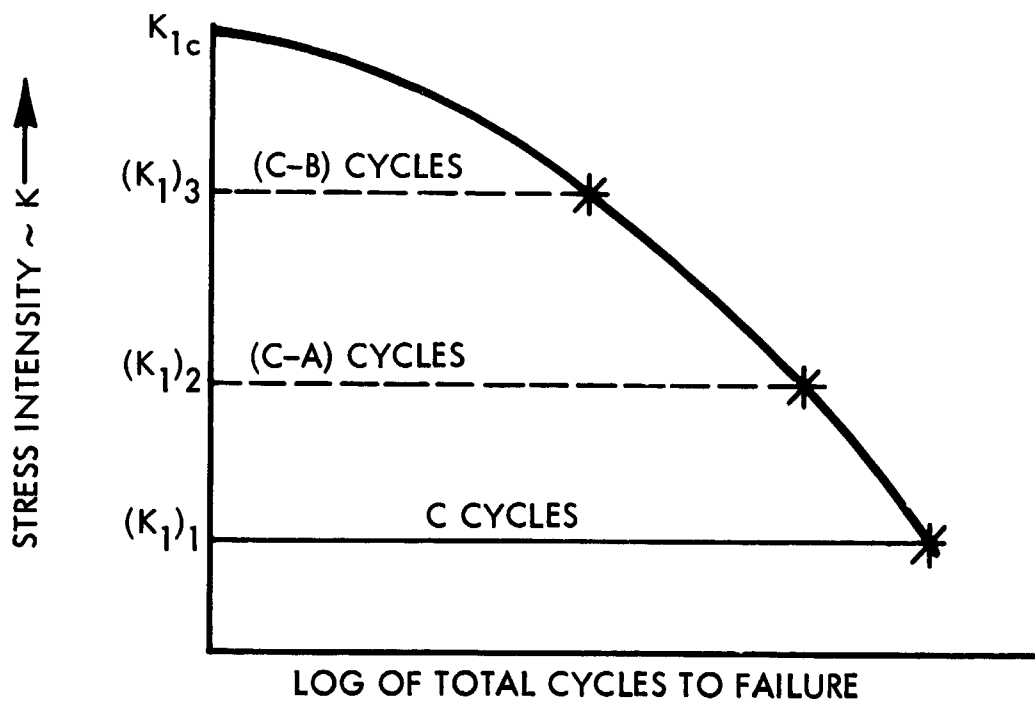


Figure 4b: K-N CURVE DESCRIBING CYCLIC LIFE SPAN (SCHEMATIC REPRESENTATION)

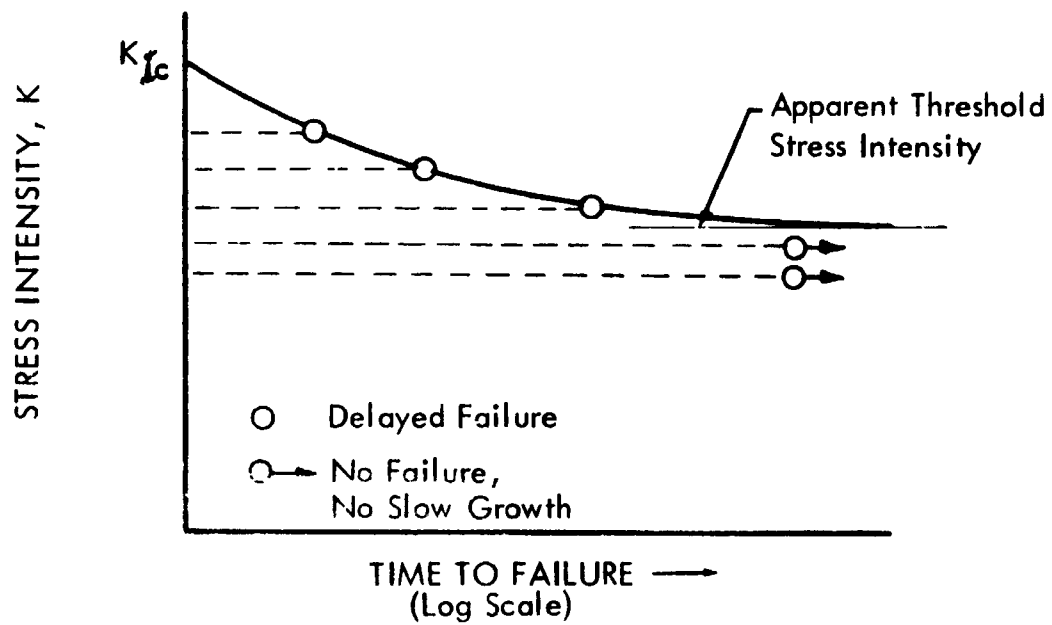


Figure 5: SUSTAINED FLAW GROWTH
Schematic Representation

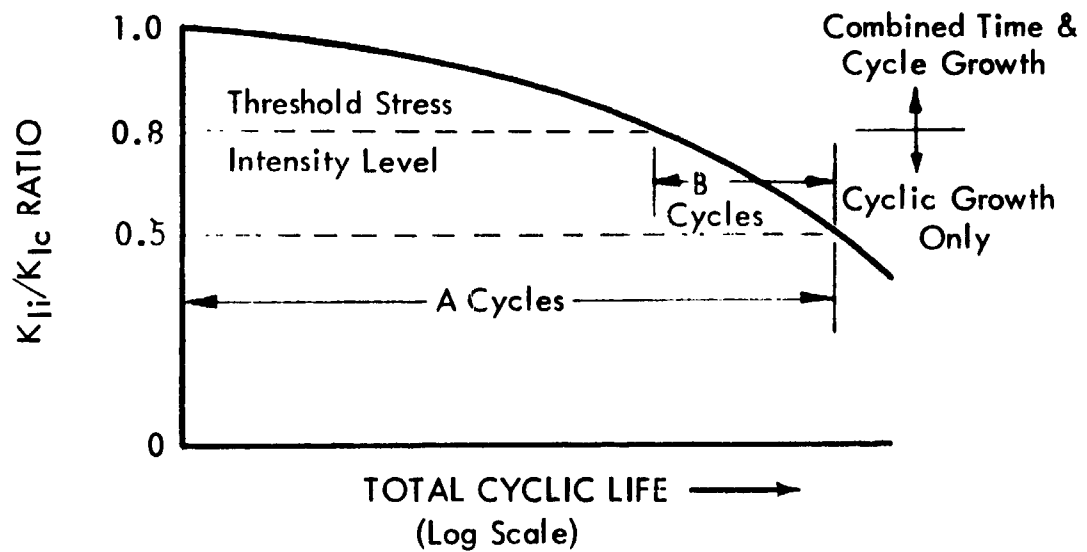


Figure 6: COMBINED CYCLIC AND SUSTAINED-STRESS FLAW GROWTH
Schematic Interpretation



Figure 7a: ELECTRON FRACTOGRAPH OF CYCLIC CRACK GROWTH
IN 2219-T87 ALUMINUM

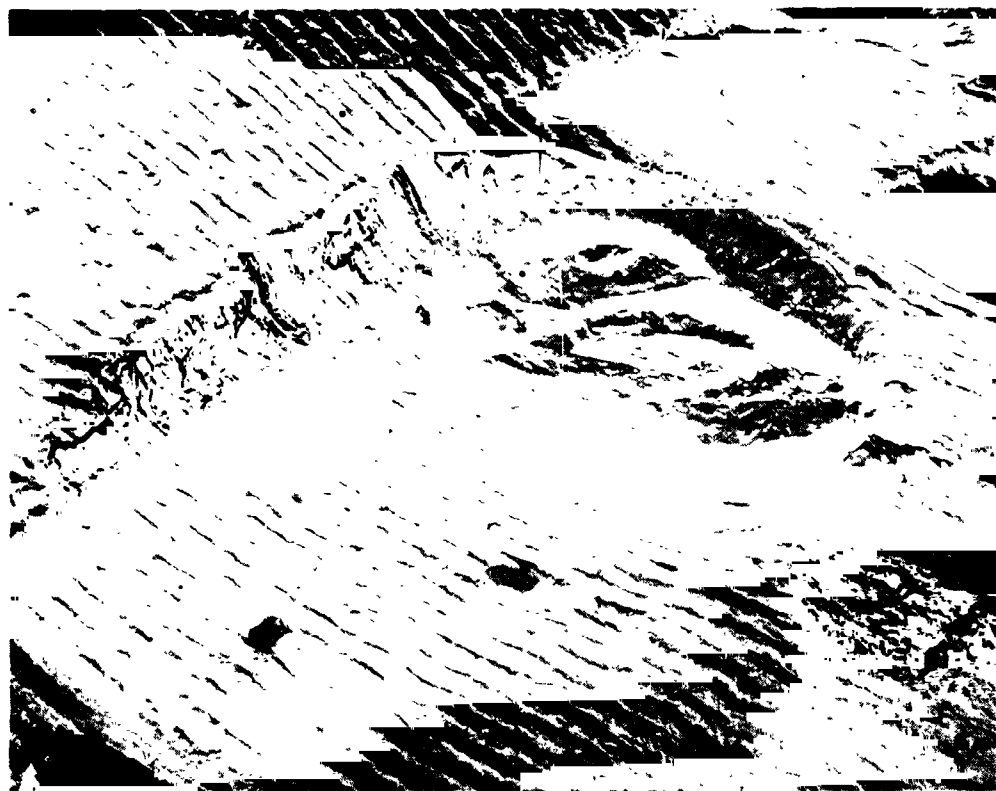


Figure 7b: ELECTRON FRACTOGRAPH OF CYCLIC CRACK GROWTH
IN 6AL-4V TITANIUM

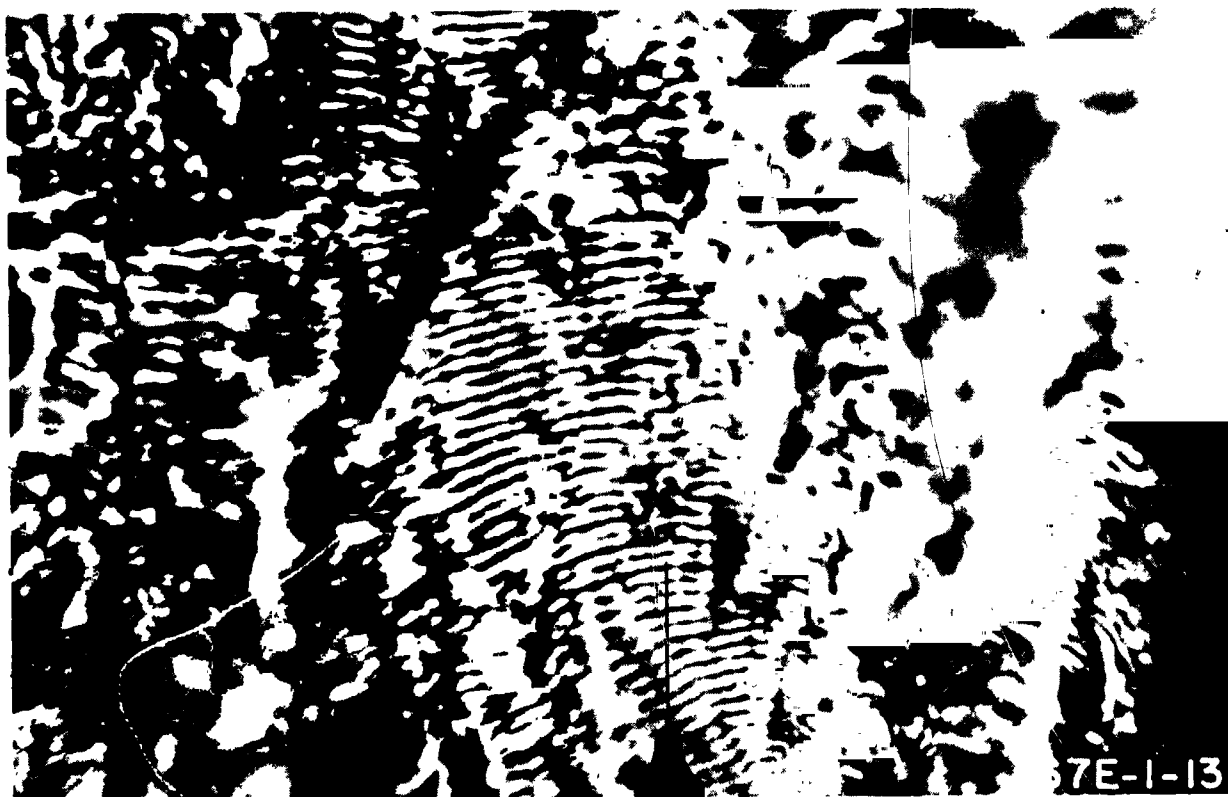


Figure 8a: OPTICAL MICROGRAPH OF CYCLIC CRACK GROWTH IN 7075-T6 ALUMINUM

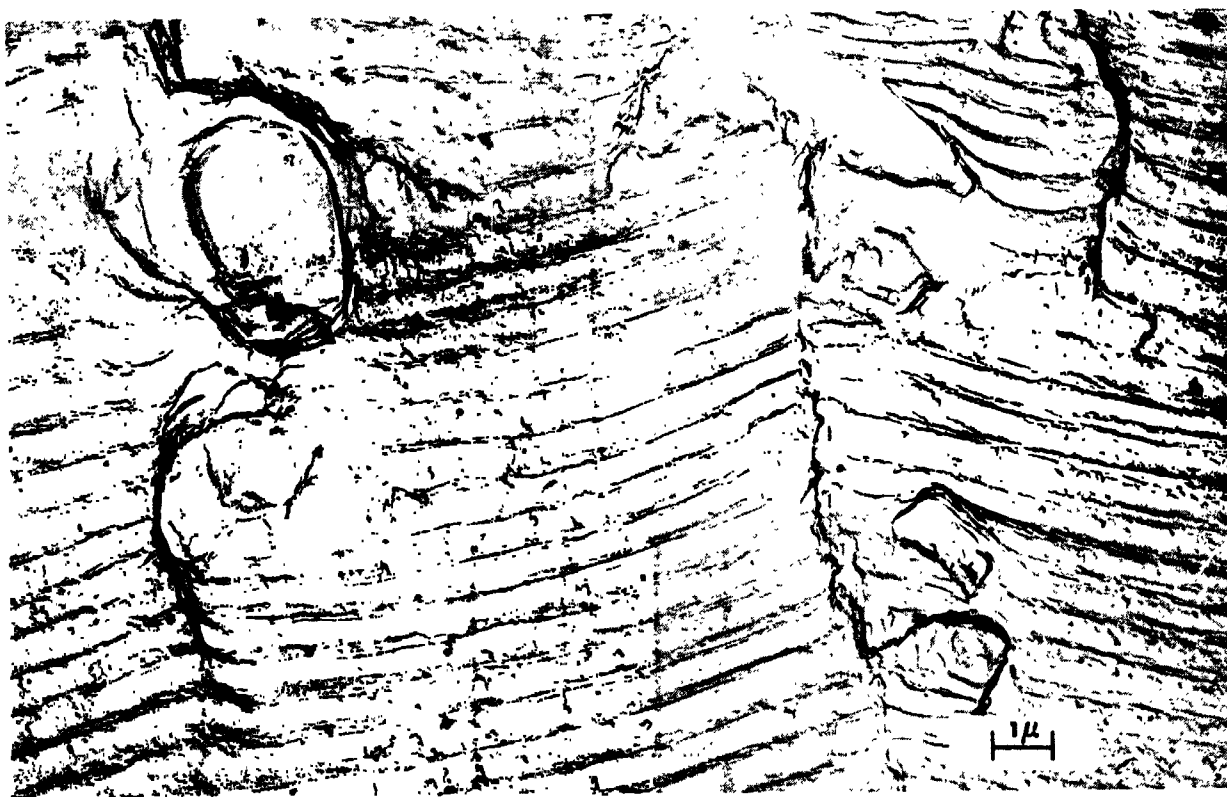


Figure 8b: ELECTRON MICROGRAPH OF CYCLIC CRACK GROWTH IN 7075-T6 ALUMINUM

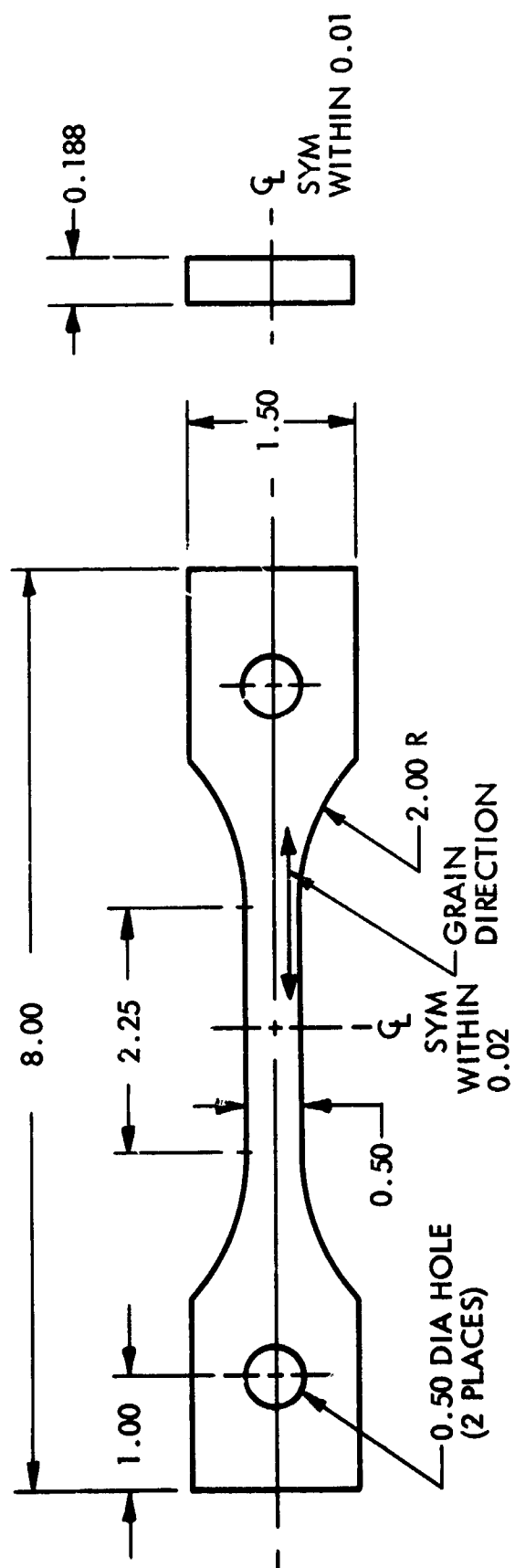


Figure 9: TENSILE SPECIMEN (TITANIUM)

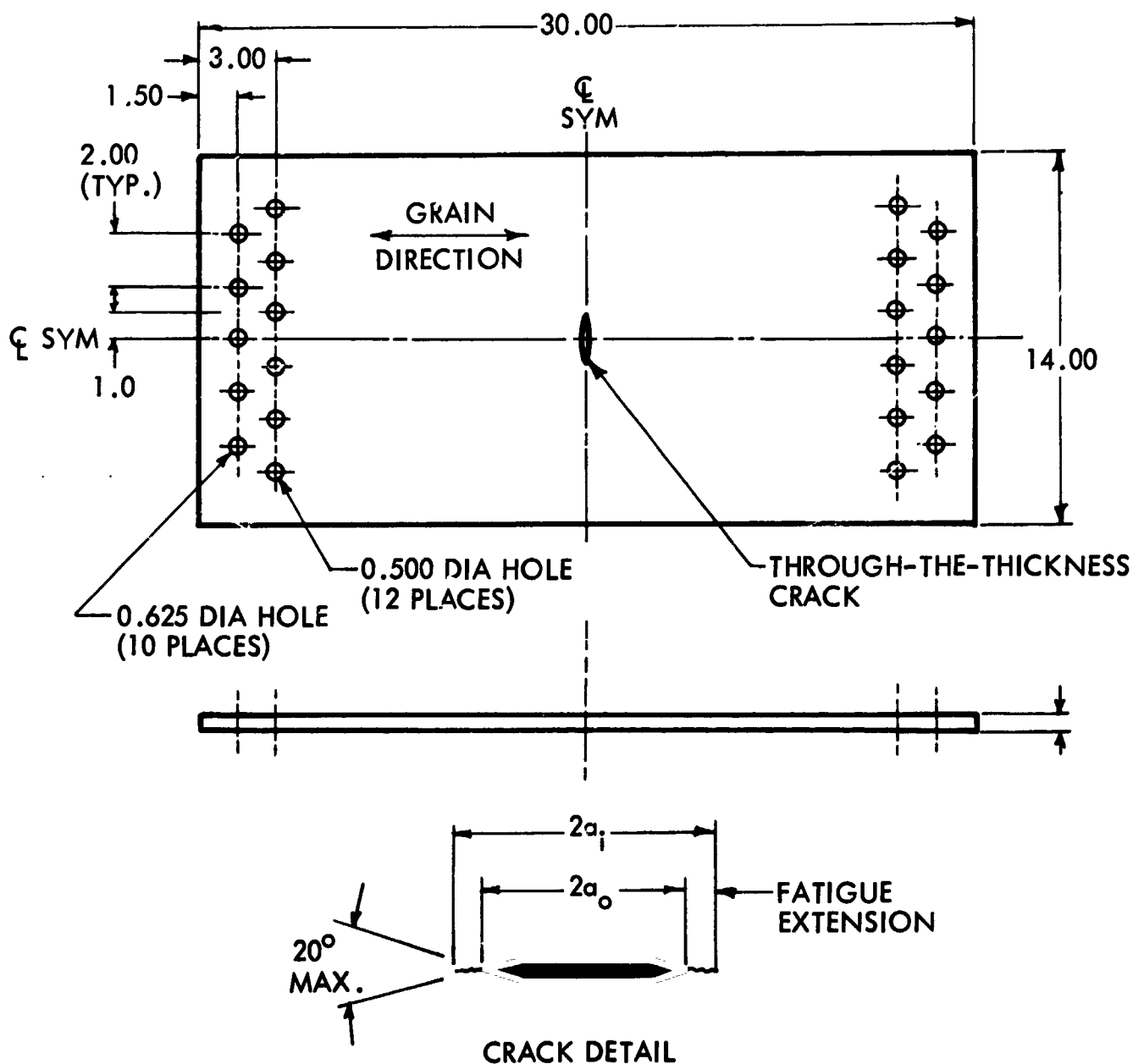


Figure 10: THROUGH-THE-THICKNESS CENTRALLY CRACKED FRACTURE TOUGHNESS SPECIMEN

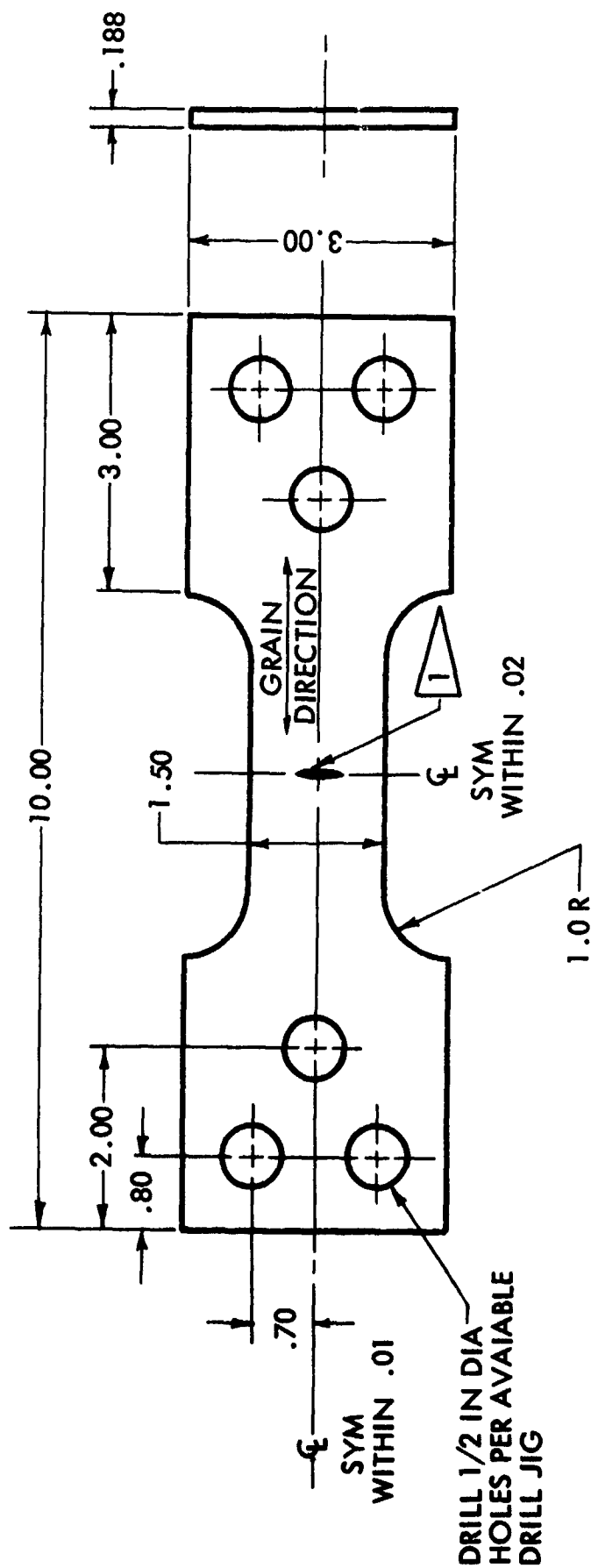


Figure 11: SURFACE-FLAWED TITANIUM SPECIMEN

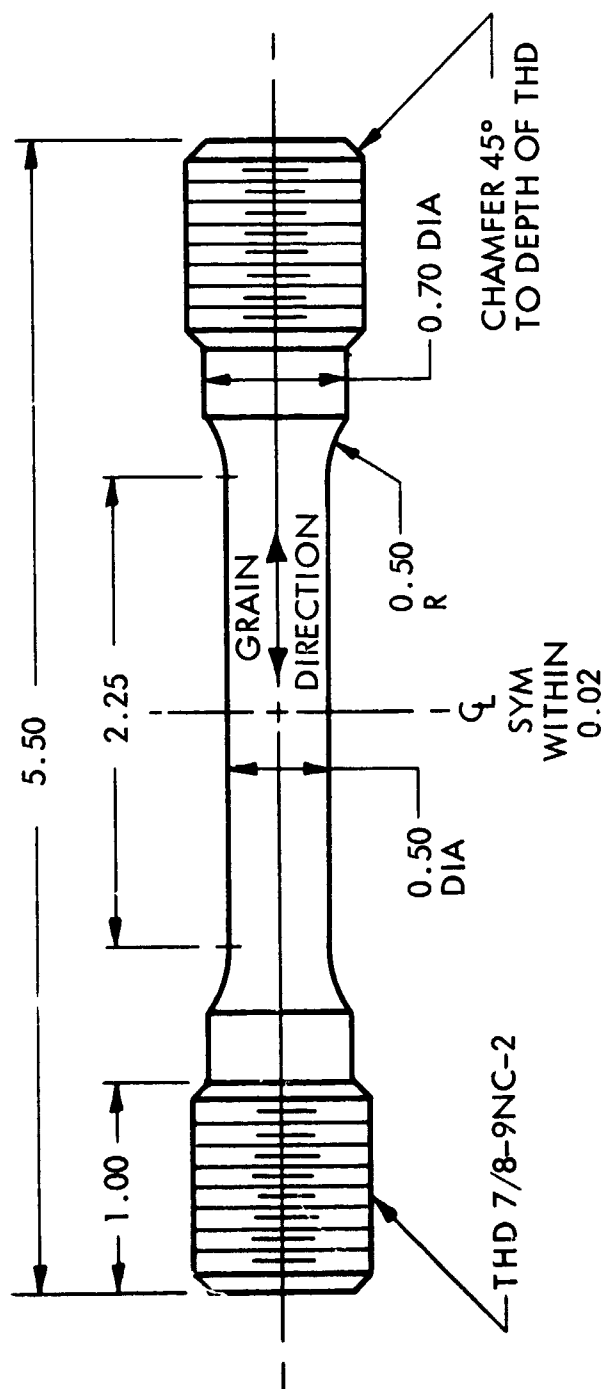


Figure 12: TENSILE SPECIMEN (ALUMINUM)

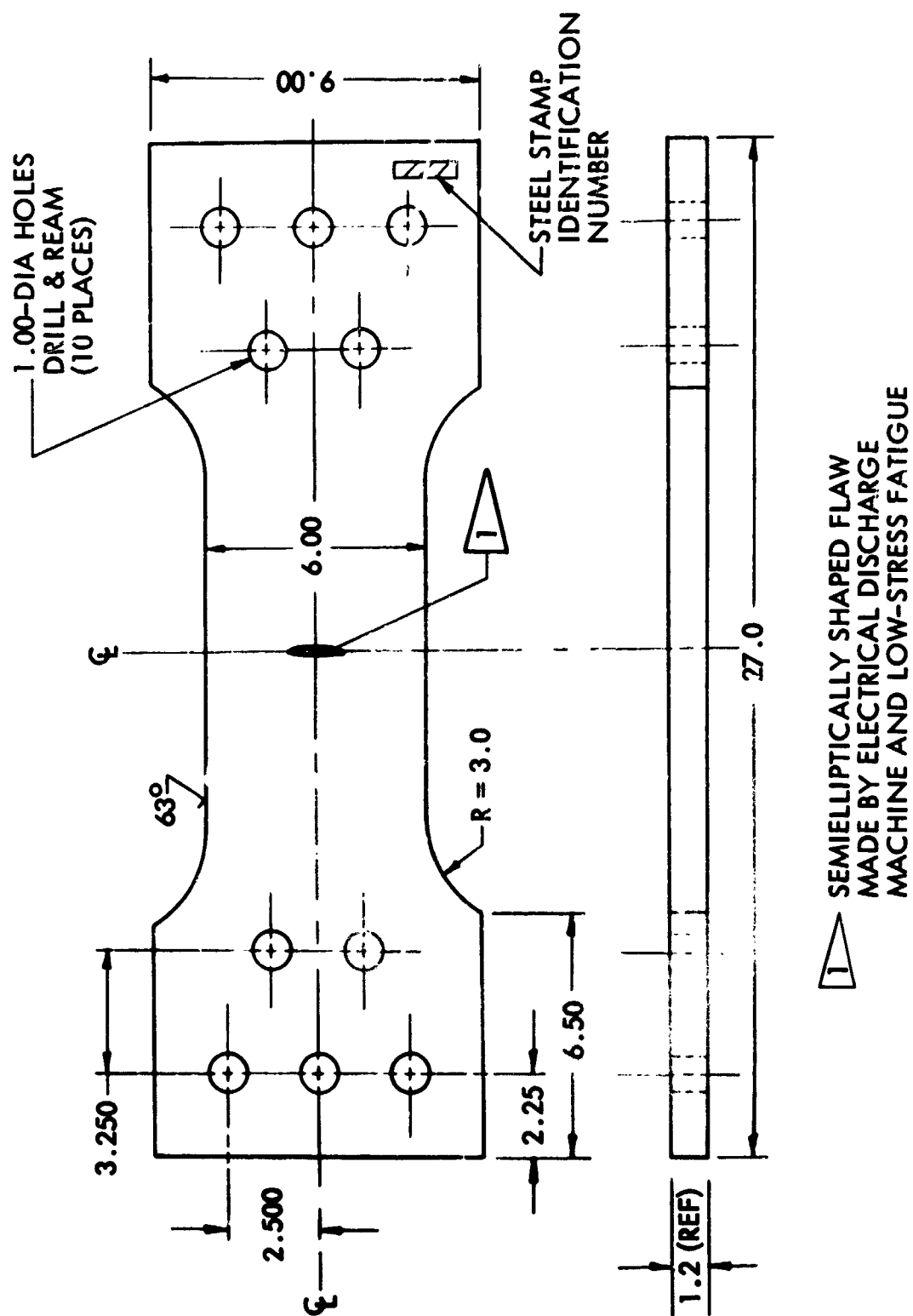
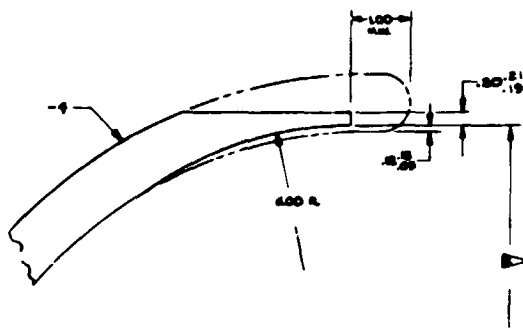
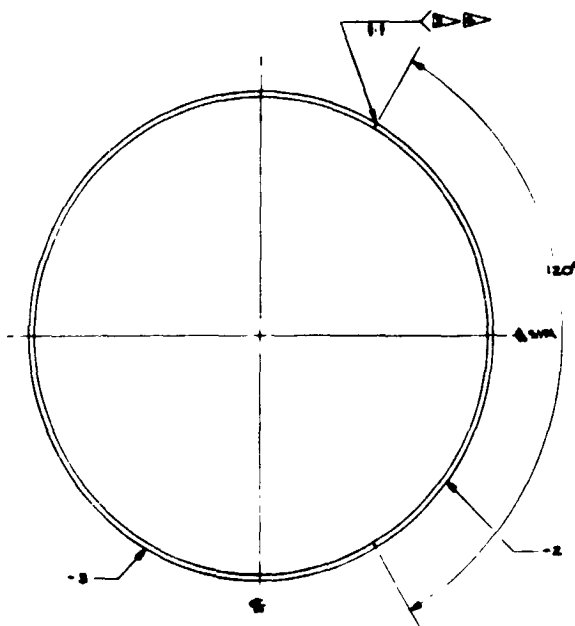


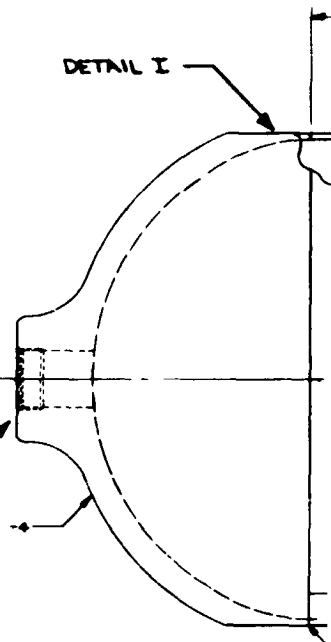
Figure 13: SURFACE-FLAWED SPECIMEN FOR 1.2 IN. ALUMINUM



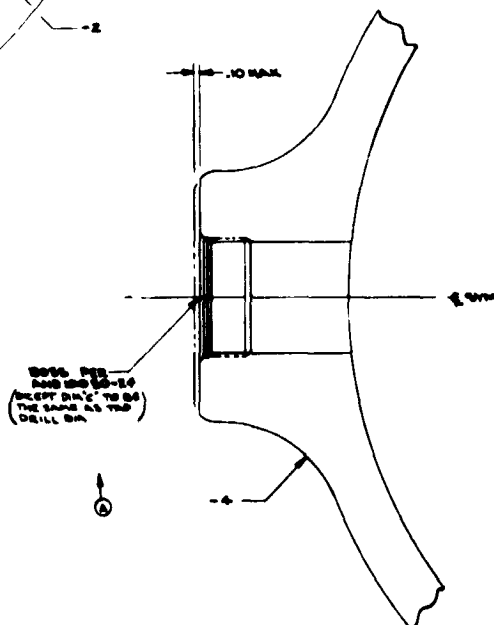
DETAIL I
FULL SIZE



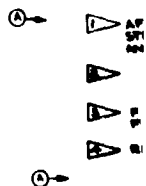
SECTION A-A
1/2" SIZE



DETAIL II

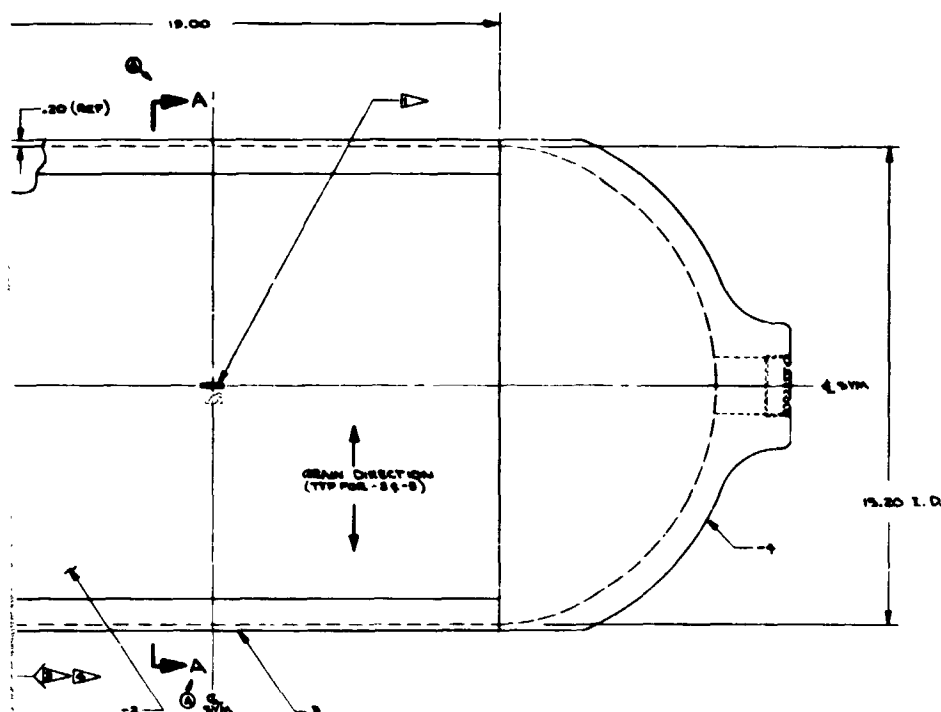


DETAIL II
FULL SIZE



69
①

REVISION		DATE	BY
1	A	1/10/68	WLB



0753-1 TITANIUM TEST TANK ASSY

SECTION OF -1 ASSY, ONE SEMI-ELLIPTICAL PLAIN MADE BY TEST UNIT USING ELECTRICAL DISCHARGE MACHINE CYCLE PATRIQUE.

TO MATCH INSIDE DIA OF -2-3 SHELL WITHIN .010

LD EDGE AND YELD IN ACCORDANCE WITH INSTRUCTIONS MANUFACTURING DEVELOPMENT UNIT.

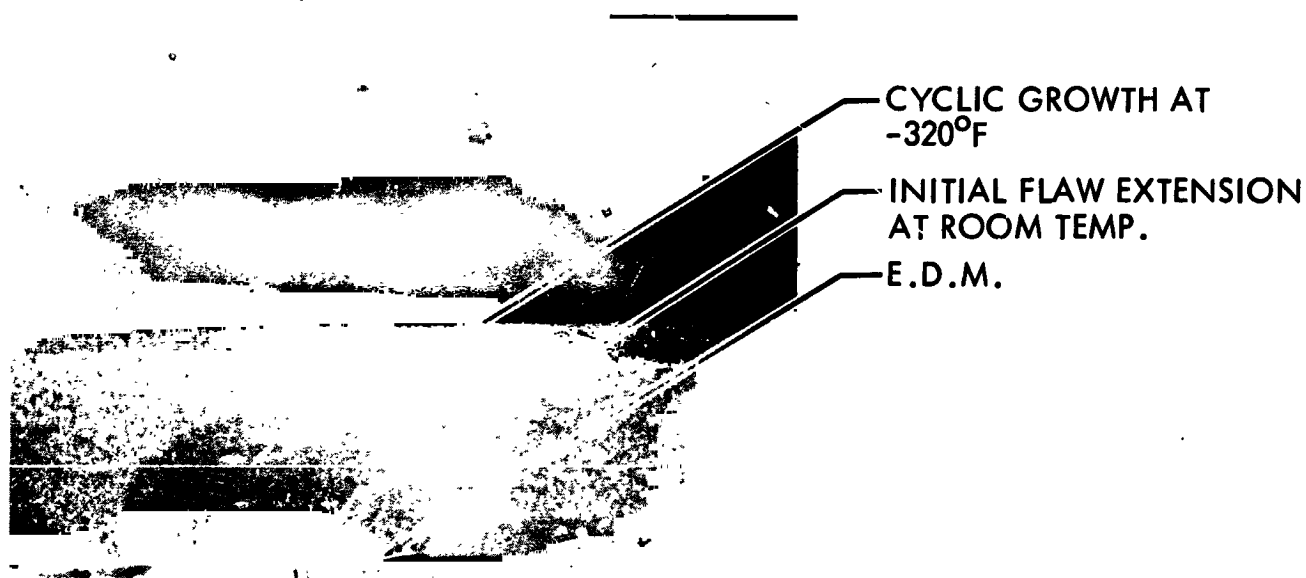
MIC INSPECT PER S-5-501

QTY	PART NO.	DESCRIPTION	UNIT	QTY	UNIT	QTY	UNIT	QTY	UNIT
✓ 2	-4	HEAD							
✓ 1	-5	SHELL SEGMENT							
✓ 1	-2	SHELL TEST SECTION							
-	-1	TITANIUM TEST TANK BODY							
-1	QTY	PART NO.	DESCRIPTION	UNIT	QTY	UNIT	QTY	UNIT	QTY

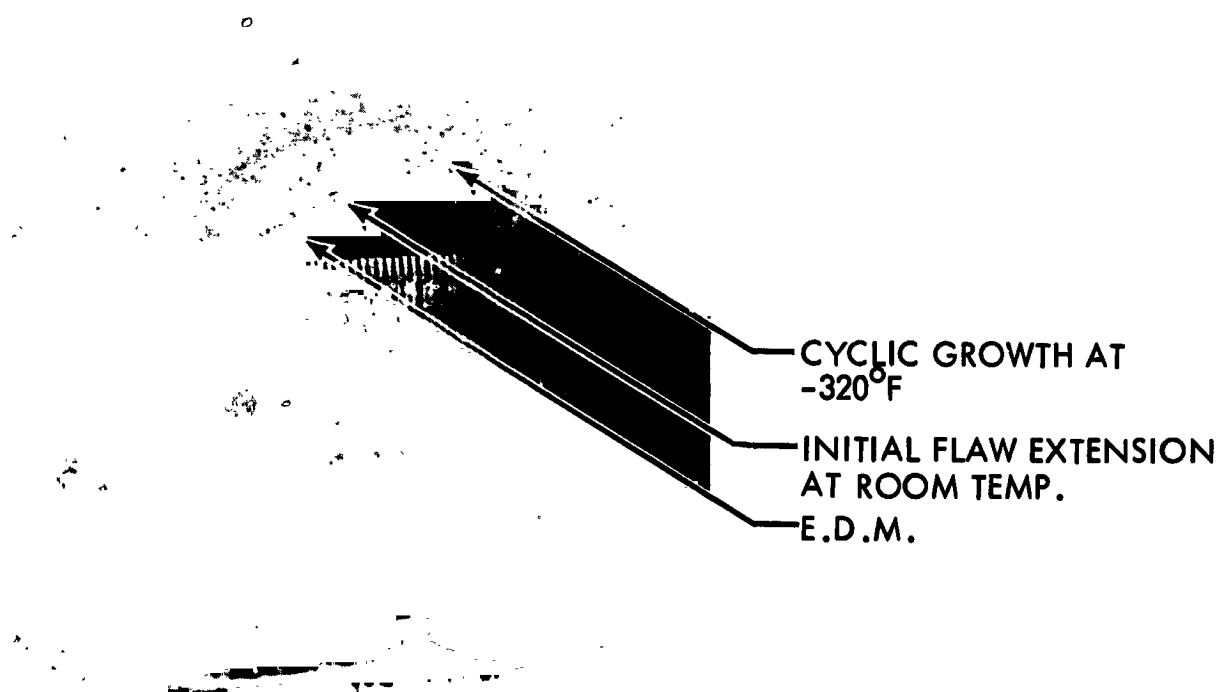
<p>Des. Group PA 1000-2</p> <p>1/10/68</p> <p>WLB</p>	<p>THE BOEING COMPANY</p> <p>PA 1000-2</p> <p>1/10/68</p> <p>WLB</p>	<p>TITANIUM TEST TANK ASSY (TEST ONLY)</p> <p>29-40753</p>
---	--	--

Figure 15: 5Al-2.5 Sn (ELI) TITANIUM TEST CYLINDER (ROOM TEMP. -320°F & -423°F TESTS)

(2)

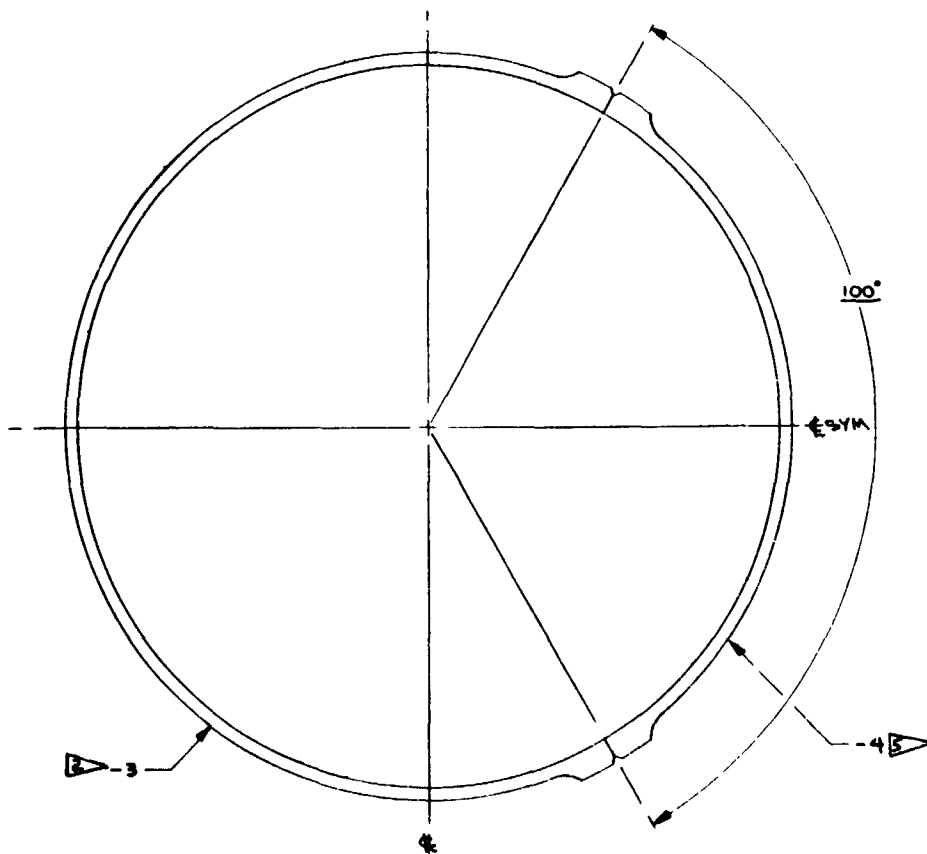
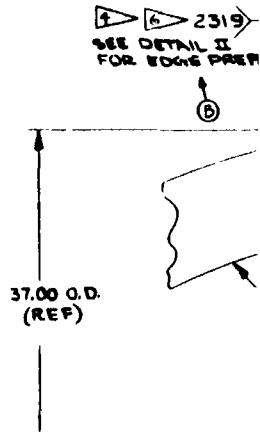
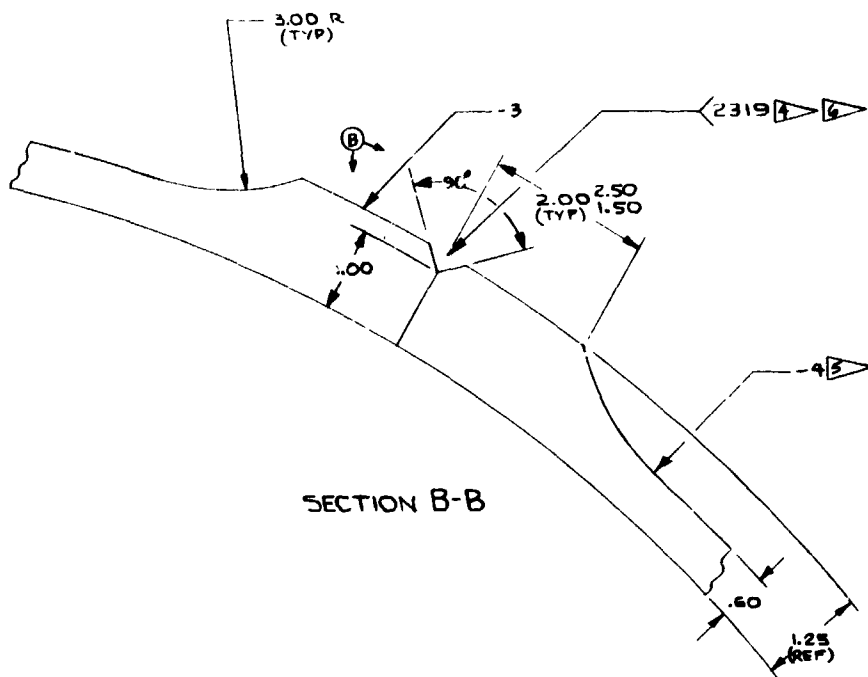


INITIAL FLAW EXTENSION ACCOMPLISHED BY
CYCLIC UNIAXIAL TENSION IN 5Al.-2.5 Sn (ELI)
TITANIUM SPECIMEN TESTED AT -320°F .

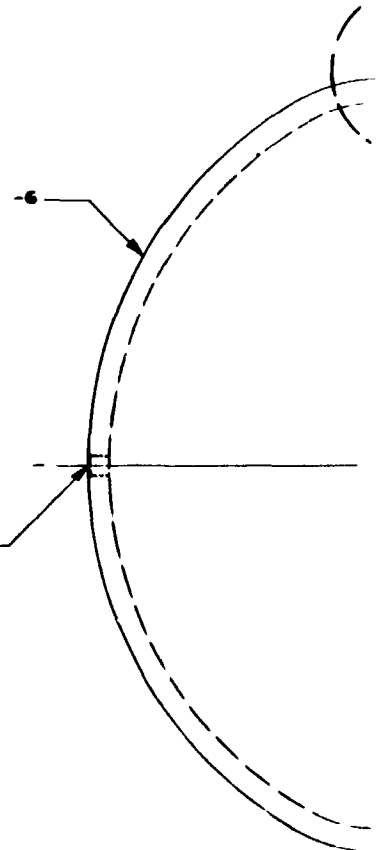


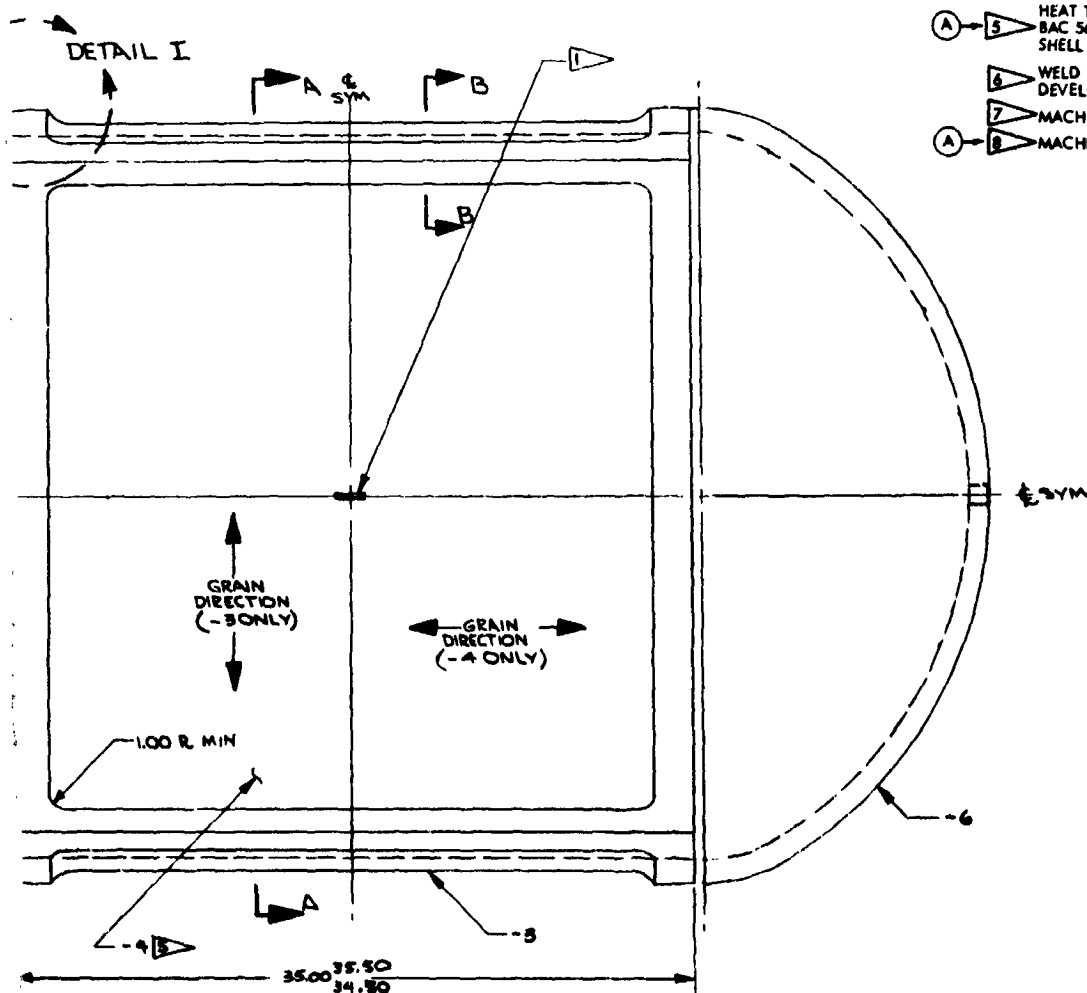
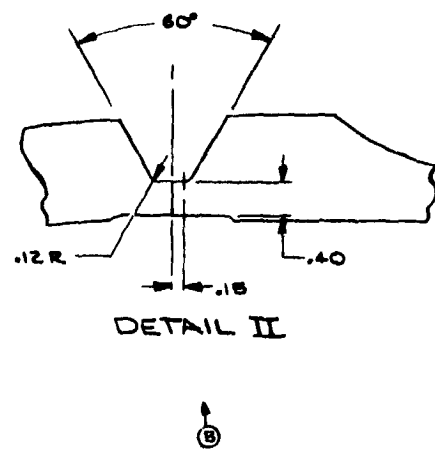
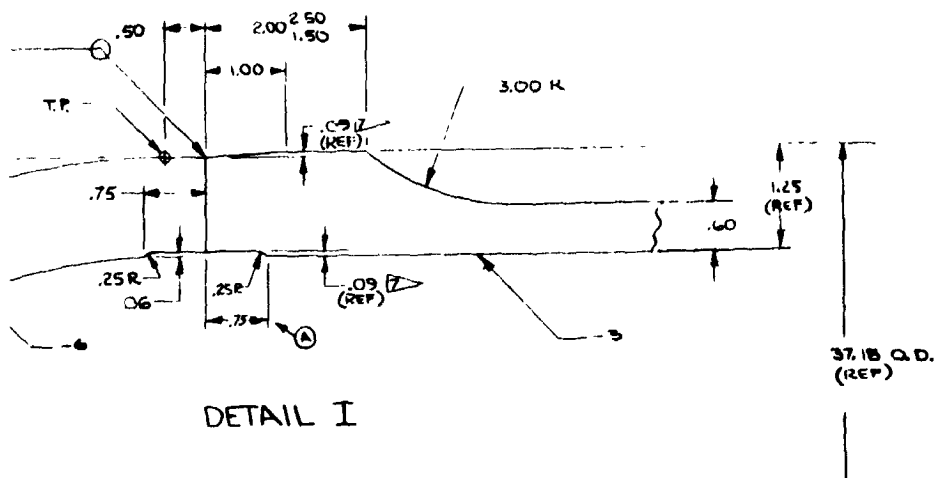
INITIAL FLAW EXTENSION ACCOMPLISHED BY
CYCLIC PRESSURE IN 5Al.-2.5 Sn
(ELI) TITANIUM TANK TESTED AT -320°F .

Figure 16: FRACTOGRAPHS SHOWING TYPICAL INITIAL FLAW
EXTENSION IN TITANIUM SPECIMENS AND TANKS



BOSS PER
AND 10050-12

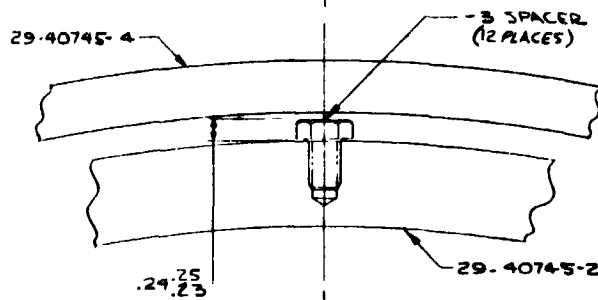




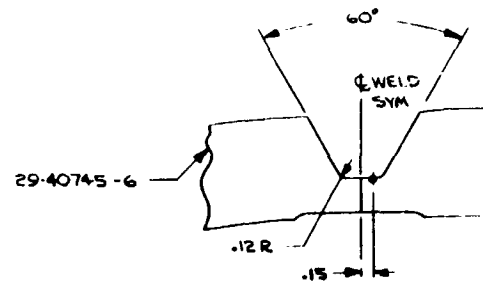
- 1 ONE SEMI-ELLIPTICAL FLAW MADE BY STRUCTURAL TEST UNIT USING ELECTRICAL DISCHARGE MACHINE AND LOW CYCLE FATIGUE
- (A) 2 HEAT TREAT TO T62 PER BAC 5602 PRIOR TO MACHINING
- 3 HEAT TREAT TO T87 PER BAC 5602 AFTER ROLLING
- 4 RADIOGRAPHIC INSPECT PER BAC 5-6401
- (A) 5 HEAT TREAT ALL -4 TEST SHELL SEGMENTS IN ONE BATCH, TO T87 BAC 5602, PRIOR TO MACHINING AFTER WELDING -3 TO -4, SUBMIT SHELL ASSY TO STRUCTURAL TEST UNIT FOR PREPARATION OF SURF
- 6 WELD IN ACCORDANCE WITH INSTRUCTIONS FROM MANUFACTURING DEVELOPMENT UNIT
- 7 MACHINE TO MATCH -6 HEAD
- (A) 8 MACHINE -7 TO MATCH I.D. OF -5

29-40745-1 TEST TANK ASSY

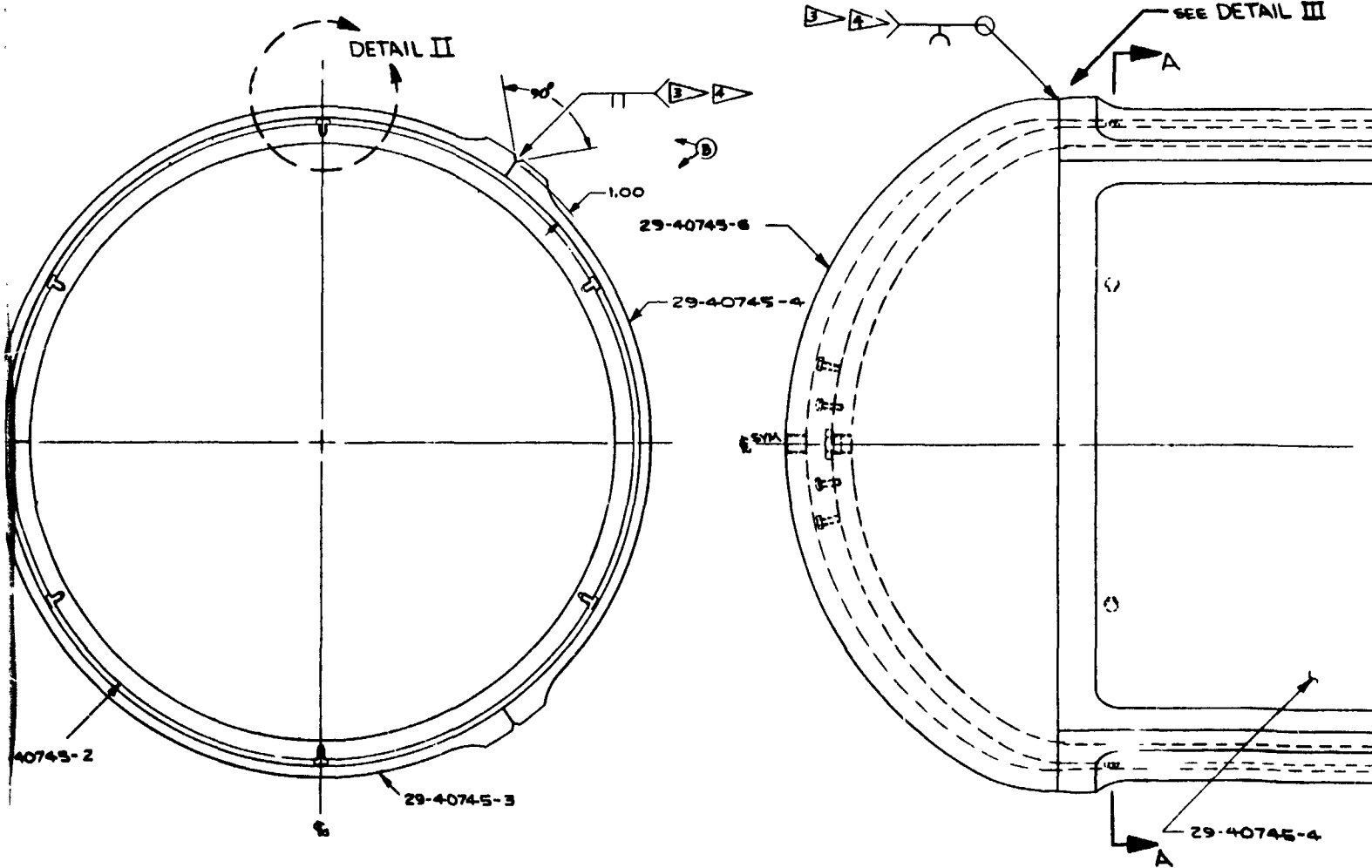
Figure 17: 2219-T87 ALUMINUM TEST TANK ROOM TEMP. AND -320°F TEST I.



DETAIL II



DETAIL III

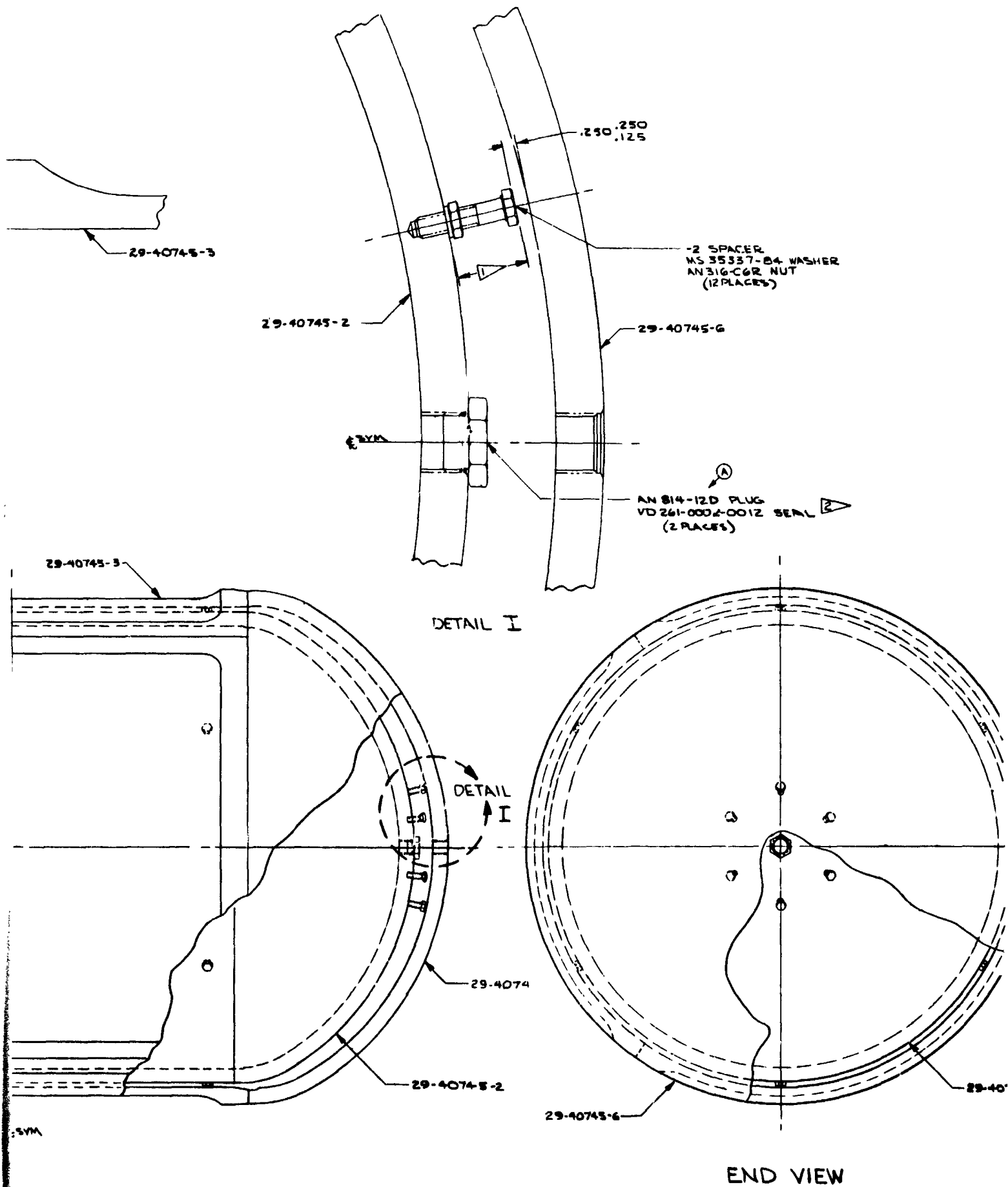


SECTION A-A

- THIS DISTANCE TO BE UNIFORM WITHIN ± 0.010 ON ALL BOLTS
- USE BMS 8-388 POLYURETHANE TYPE I, GRADE N FOAM PER 5434, CLASS V TO FILL 29-40745-2 FILLER TANK, PRIOR TO INSTALLING PLUG & SEAL.
- RADIOGRAPHIC INSPECT PER BAC 5-8401
- WELD IN ACCORDANCE WITH INSTRUCTIONS FROM MANUFACTURING DEVELOPMENT UNIT
- TO BE FURNISHED BY ENGINEERING

29-40746-

75(1)



LH₂ TEST TANK ASSY

Figure 18: 2219-T87 ALUMINUM TEST TANK FOR -423⁰F TEST

(2)



Figure 19: INITIAL FLAW EXTENSION IN ALUMINUM SHELL

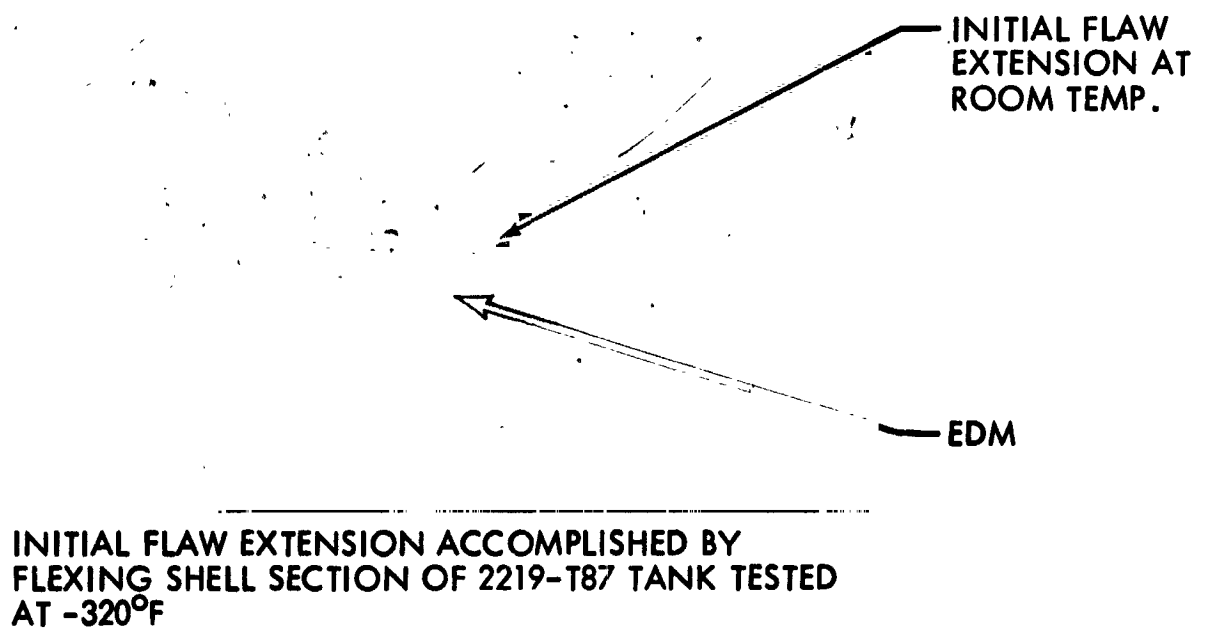
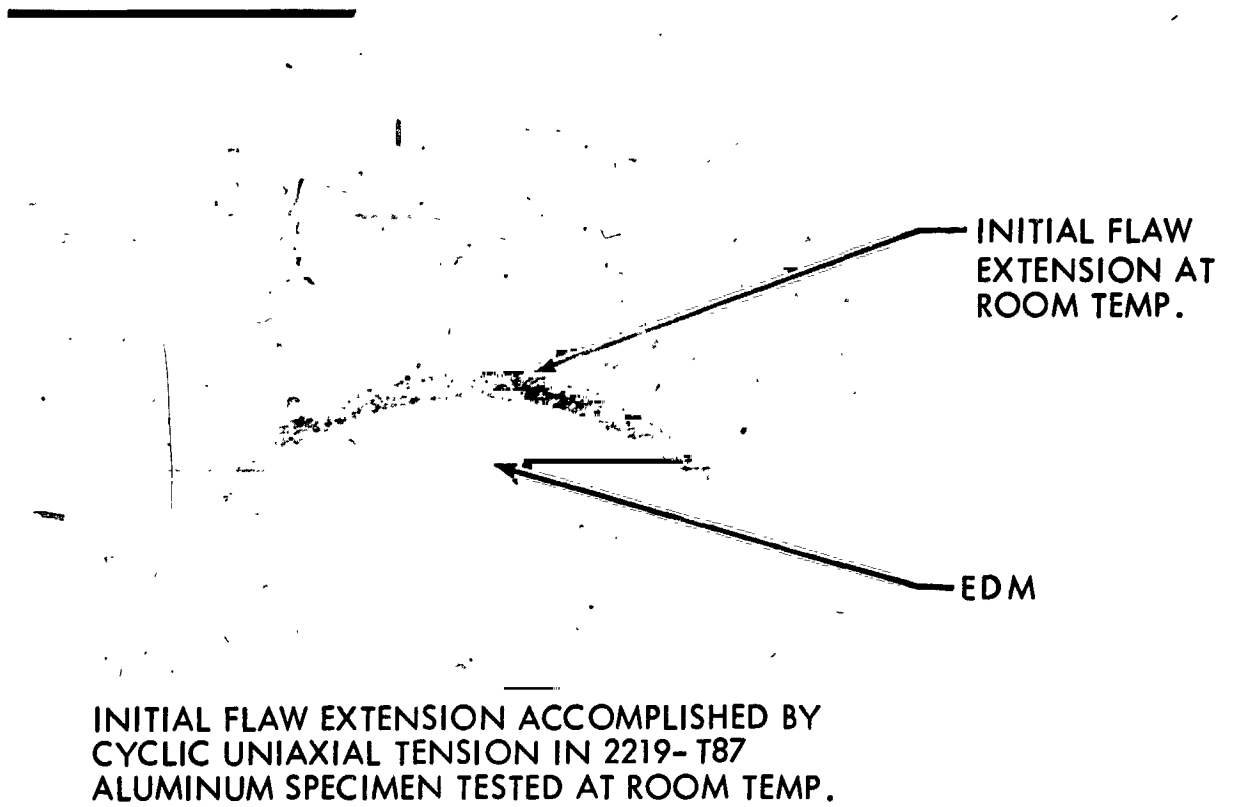
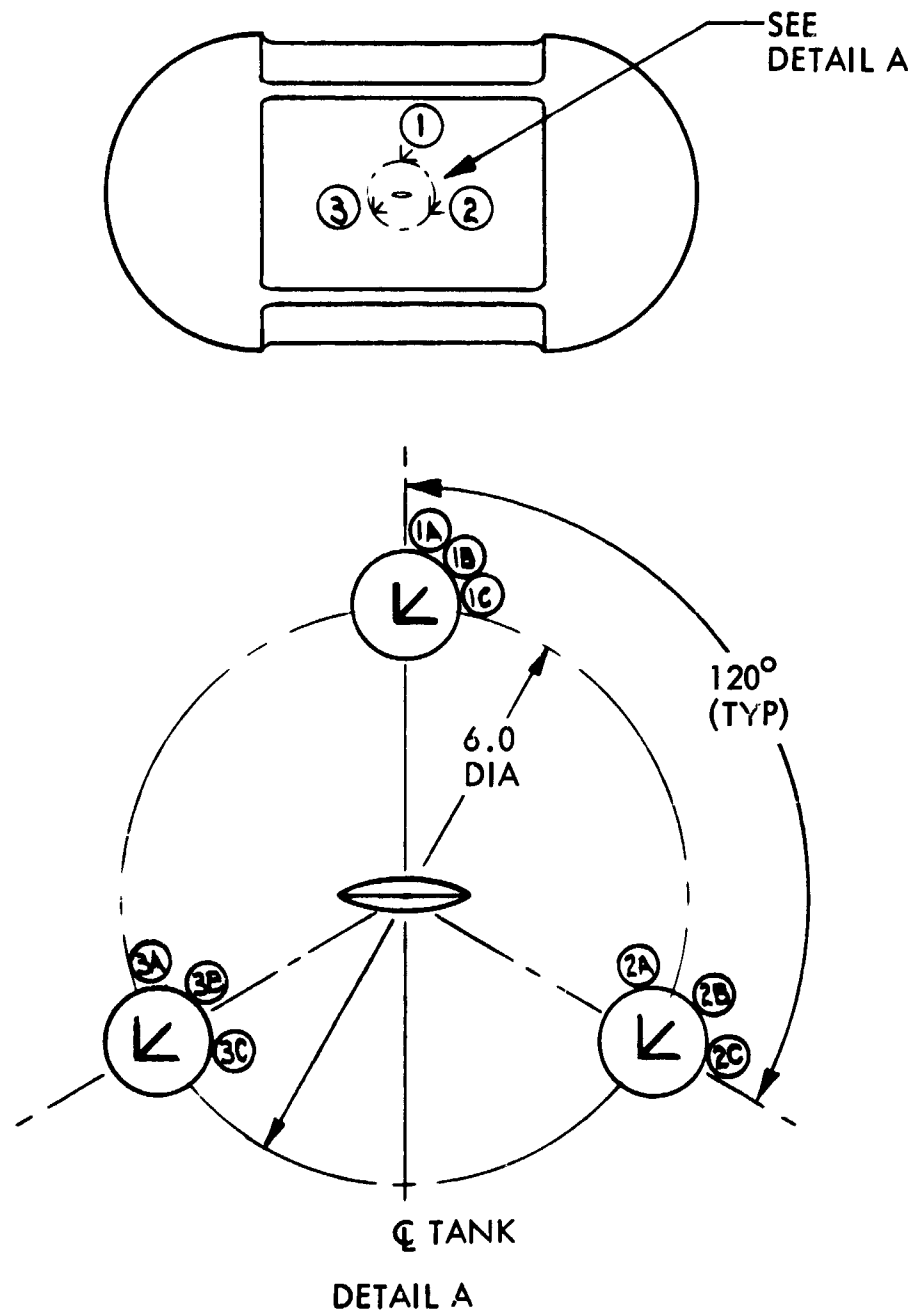


Figure 20: FRACTOGRAPHS SHOWING TYPICAL INITIAL FLAW EXTENSION IN ALUMINUM SPECIMENS AND TANKS



STRAIN-GAGE INFORMATION

TYPE: FABR-12-12 S13H

RES: $120 \pm .5 \Omega$

GF: $2.12 \pm 1.7\%$

LOT: 35

CEMENT: EPY 150 (150°F CURE)

Figure 21: LOCATION OF STRAIN GAGES ON 2219-T87 TEST TANK



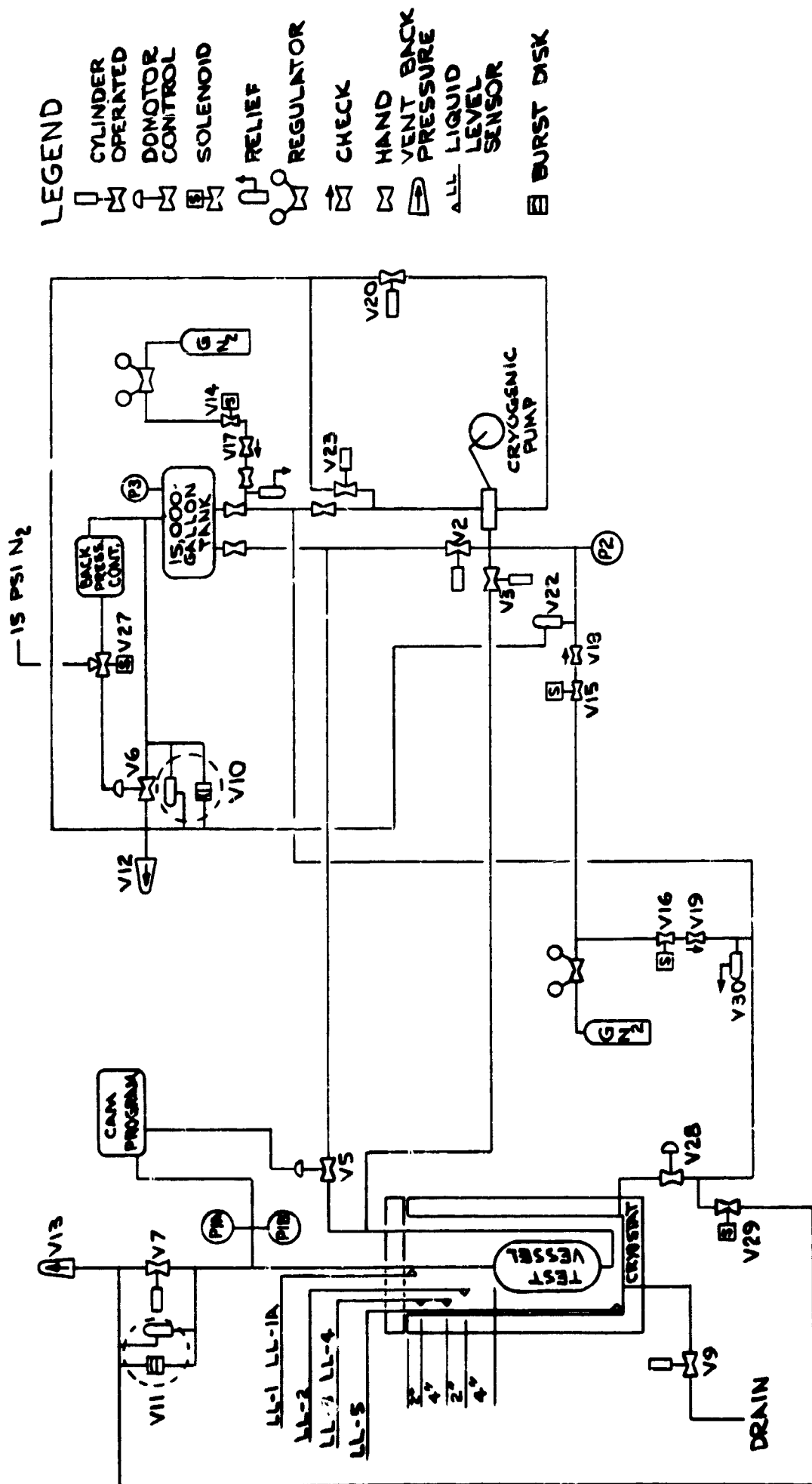


Figure 23: SCHEMATIC DIAGRAM OF PRESSURE AND CONTROL SYSTEM USED FOR -320°F TANK TESTS

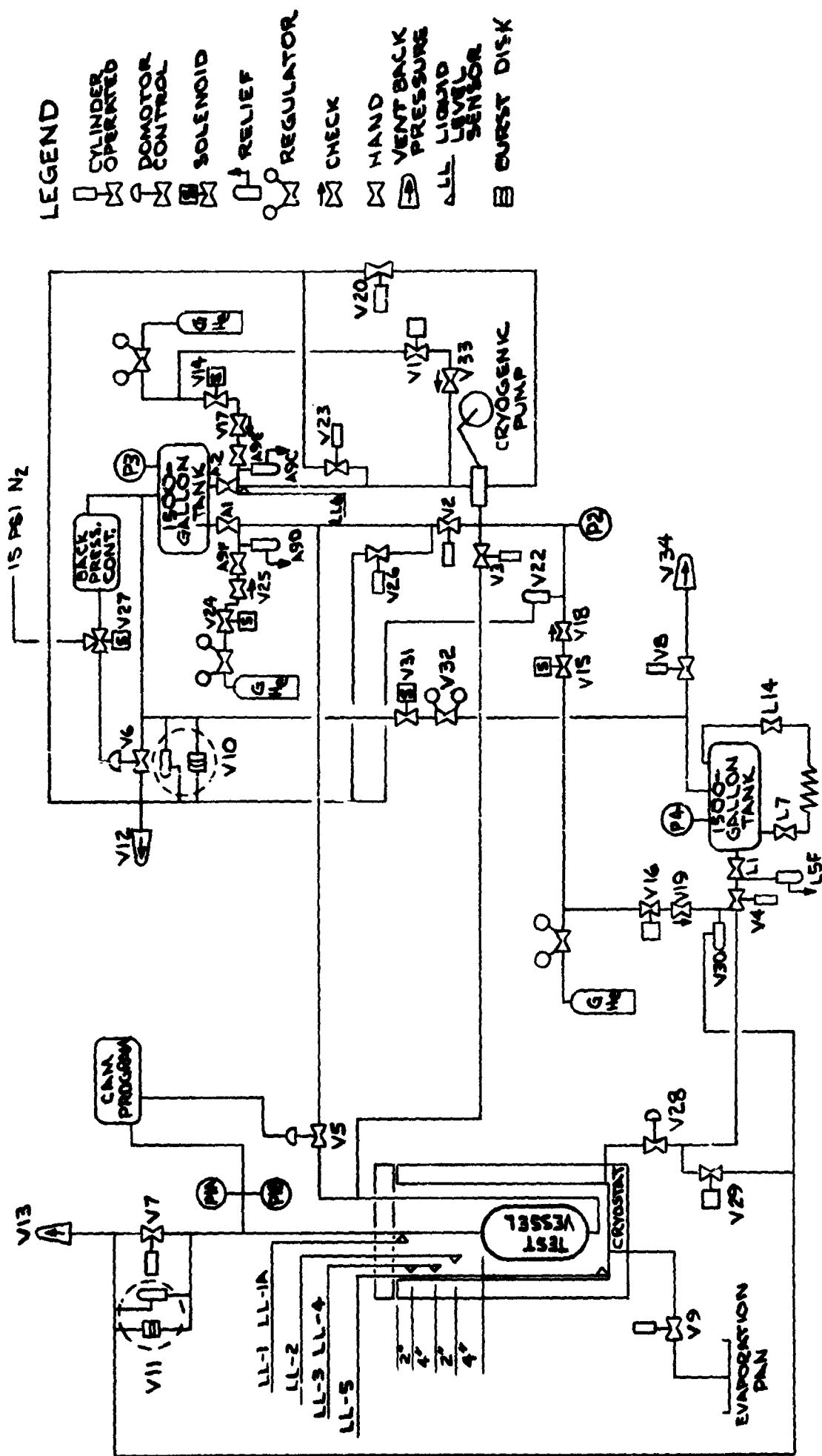


Figure 24: SCHEMATIC DIAGRAM OF PRESSURE AND CONTROL SYSTEM USED FOR -423°F TEST TANKS

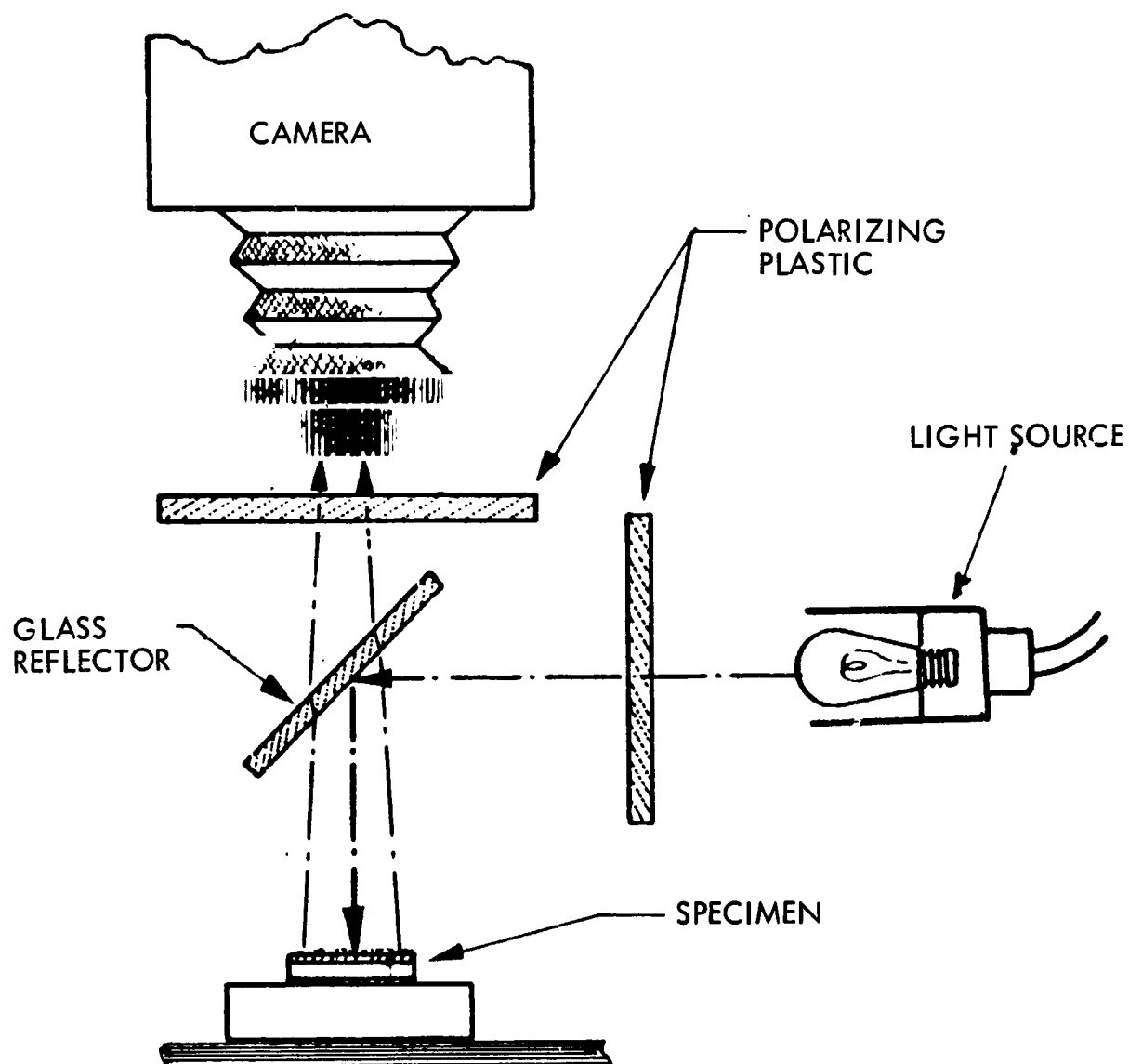


Figure 25: SCHEMATIC ILLUSTRATION OF FRACTOGRAPHIC SETUP

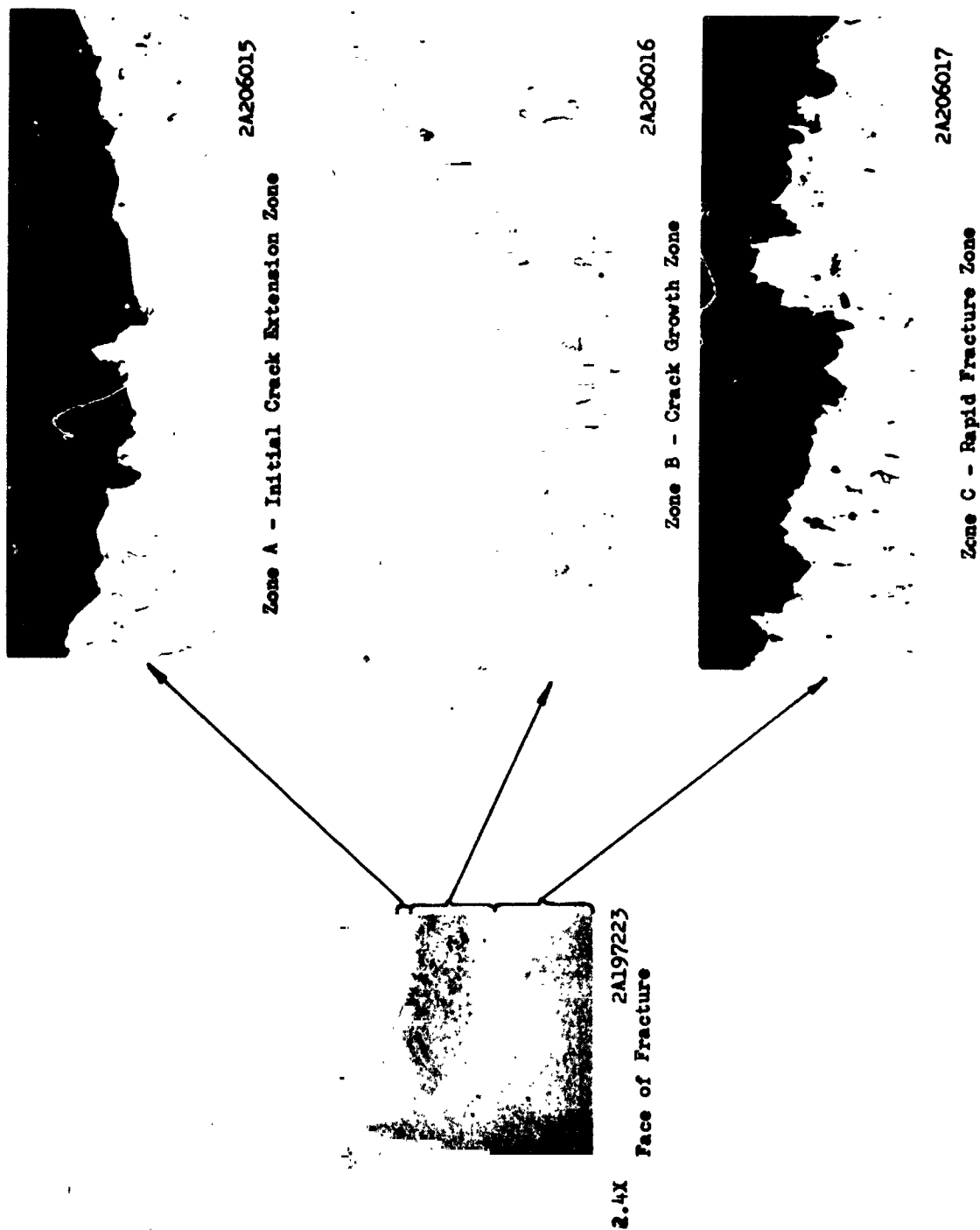
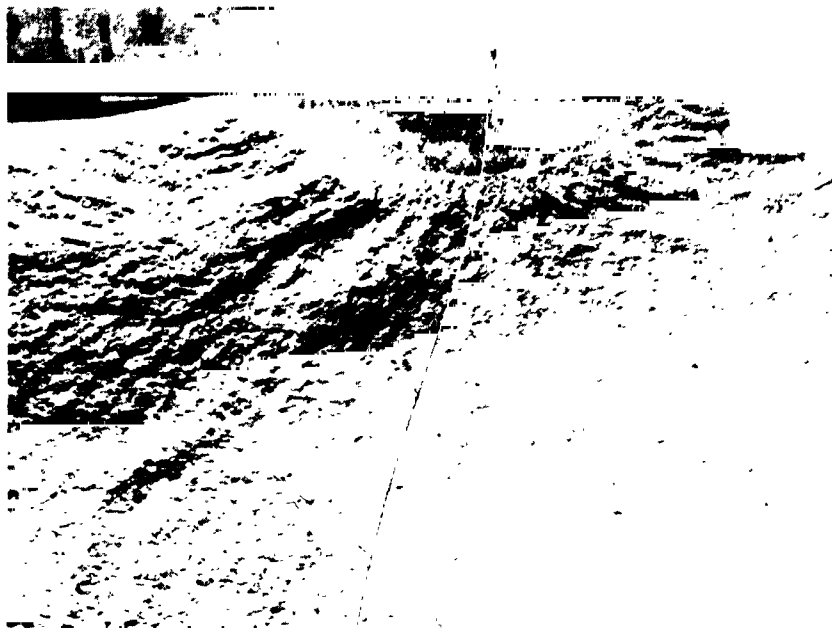


Figure 26: CROSS-SECTIONS OF PHOTOGRAPHICALLY DISCRETE ZONES (300X)
IN CYCLICALLY TESTED 2219-T87 ALUMINUM SPECIMEN



NO POLARIZATION (REFLECTED WHITE LIGHT)



LIGHT POLARIZED BY CROSSED POLARS

Figure 27: 2219 ALUMINUM FATIGUE SPECIMEN

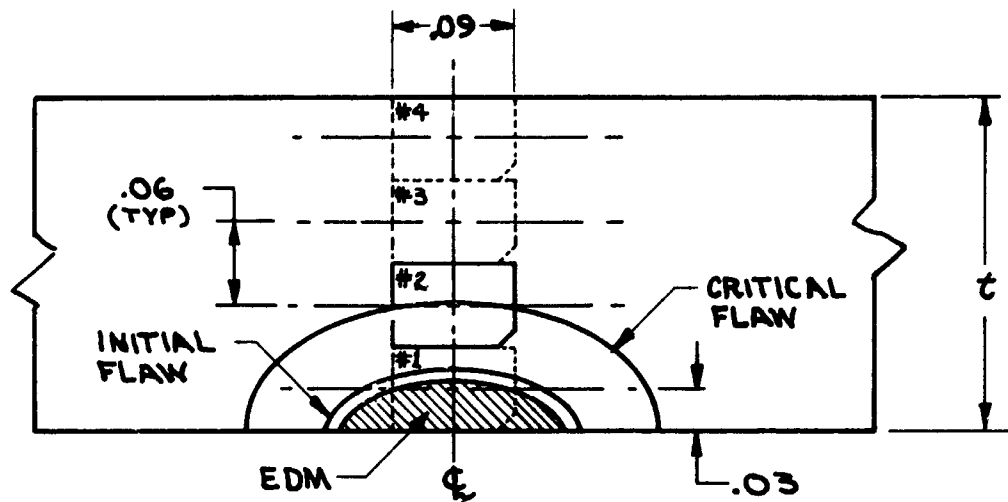


Figure 28a: SCHEMATIC ILLUSTRATION OF GRID AND REPLICA LOCATION ON FRACTURE FACE OF TEST SPECIMEN

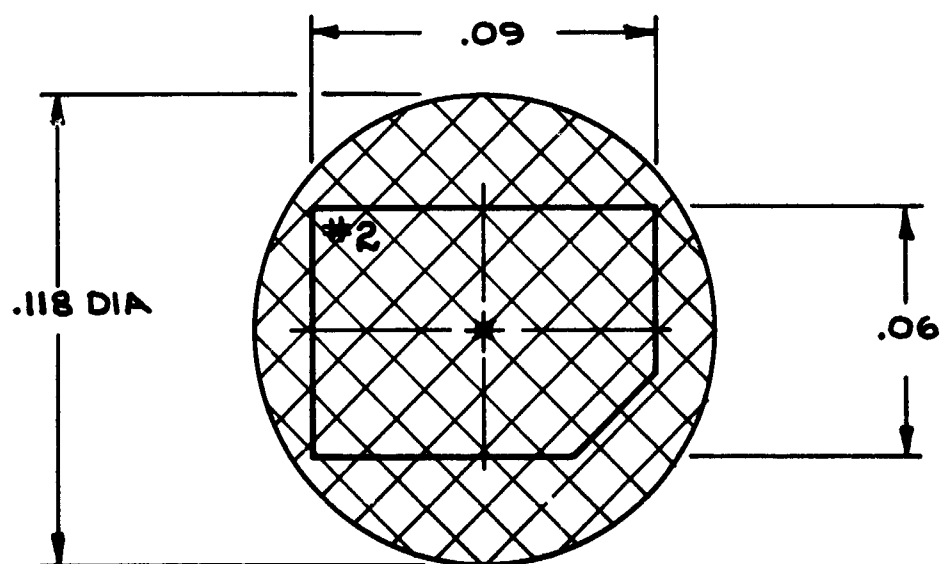


Figure 28b: SCHEMATIC ILLUSTRATION OF SAMPLE GRID WITH TYPICAL REPLICA

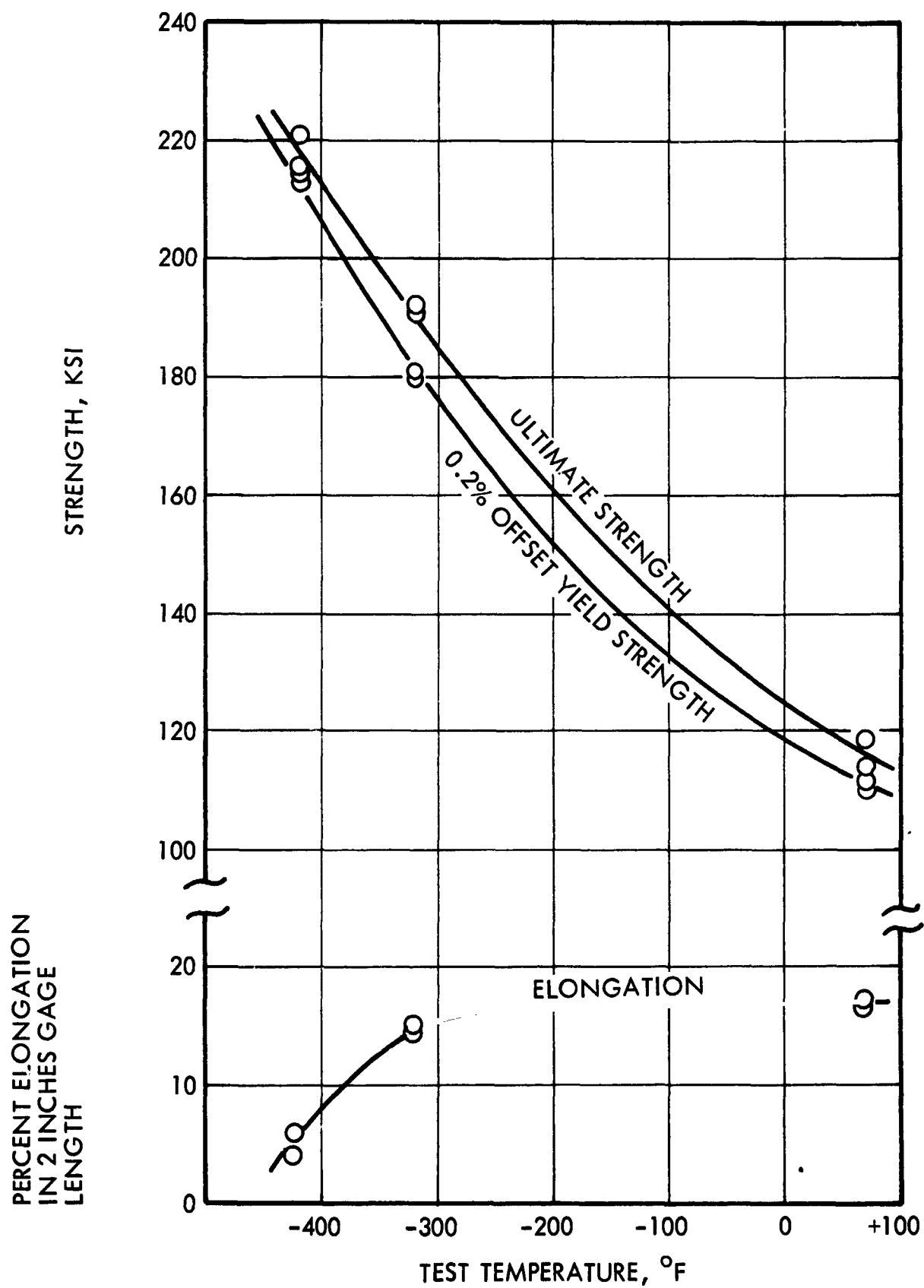


Figure 29: MECHANICAL PROPERTIES OF 5Al-2.5 Sn (ELI) TITANIUM PLATE

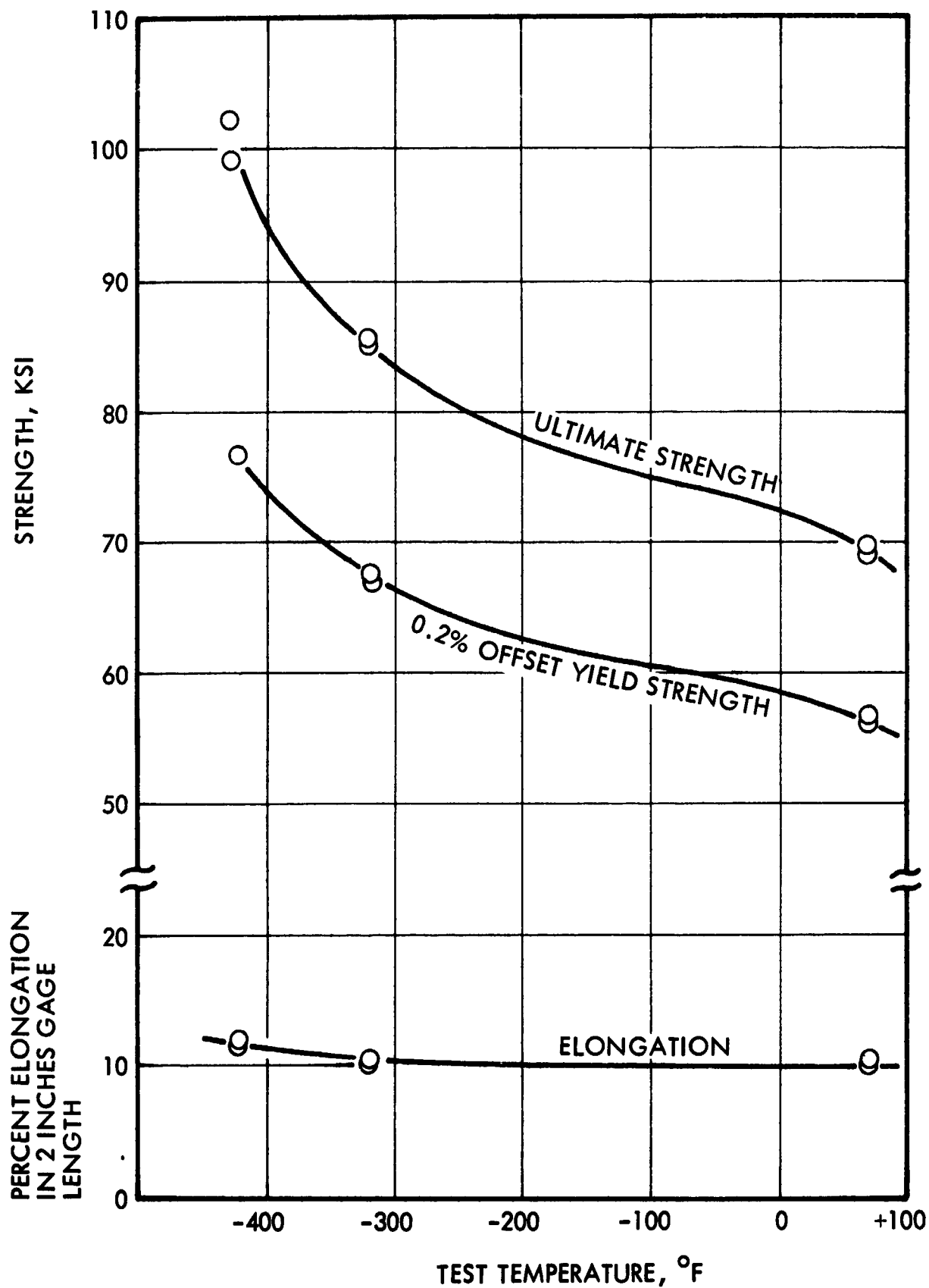


Figure 30: MECHANICAL PROPERTIES OF 2219-T87 ALUMINUM PLATE

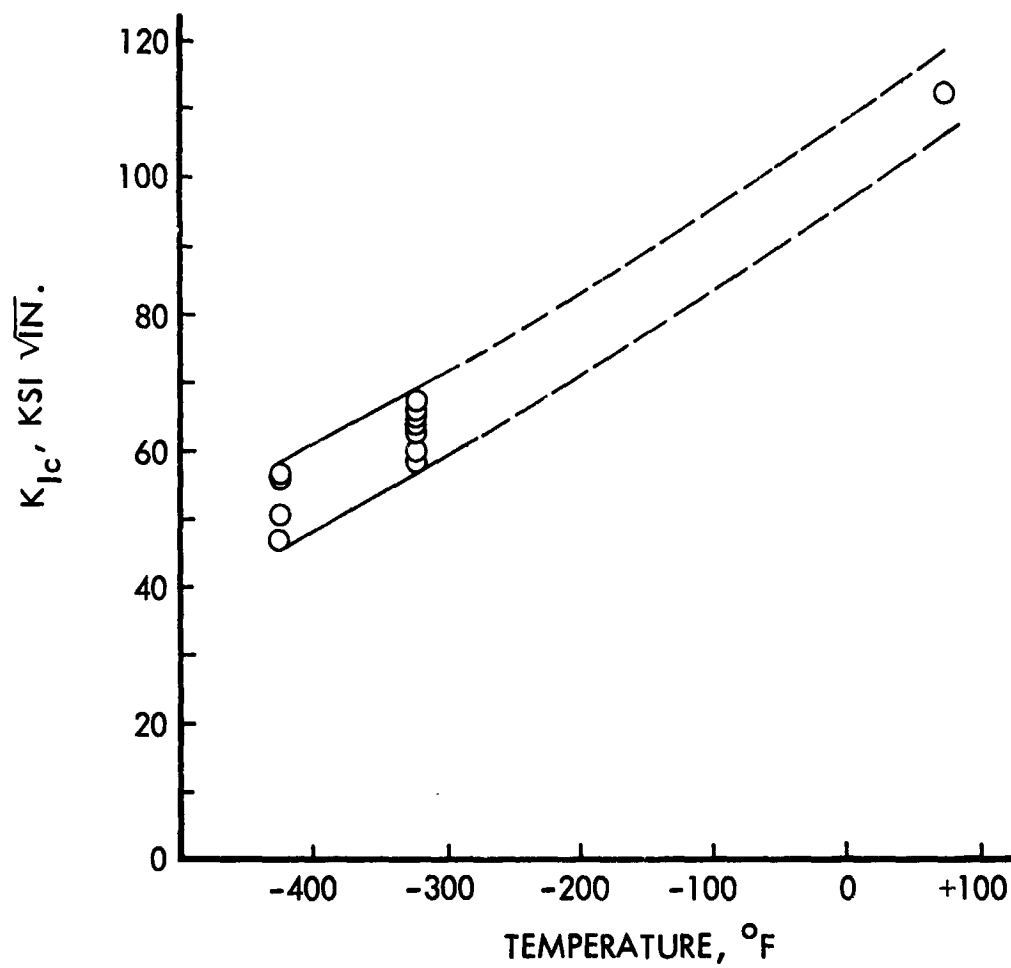


Figure 31: PLANE STRAIN FRACTURE TOUGHNESS OF 5Al-2.5 Sn (ELI) TITANIUM

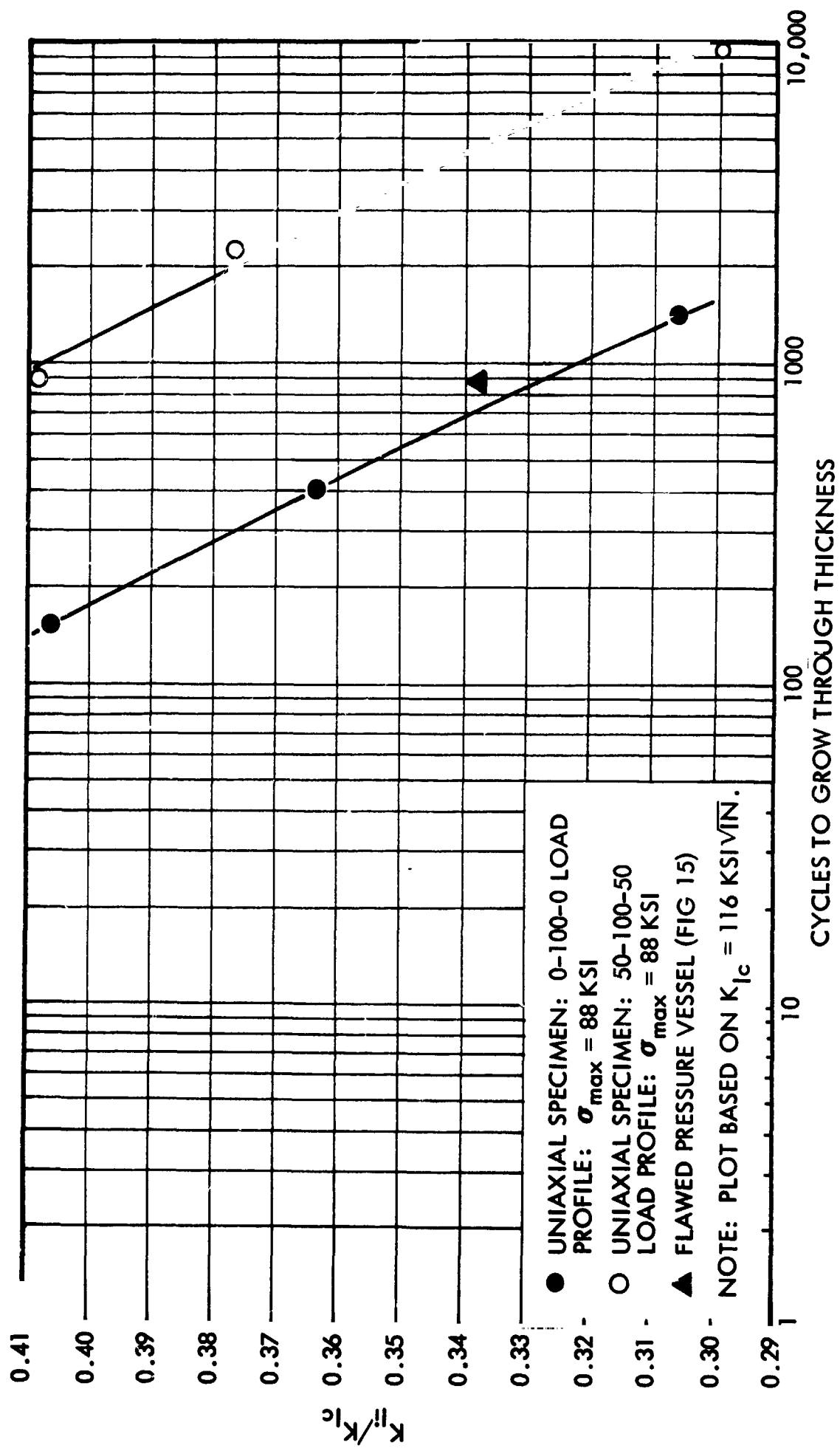


Figure 32: STRESS INTENSITY VS CYCLES-TO-FAILURE CORRELATION FOR 5Al -2.5 Sn (ELI) TITANIUM AT ROOM TEMPERATURE

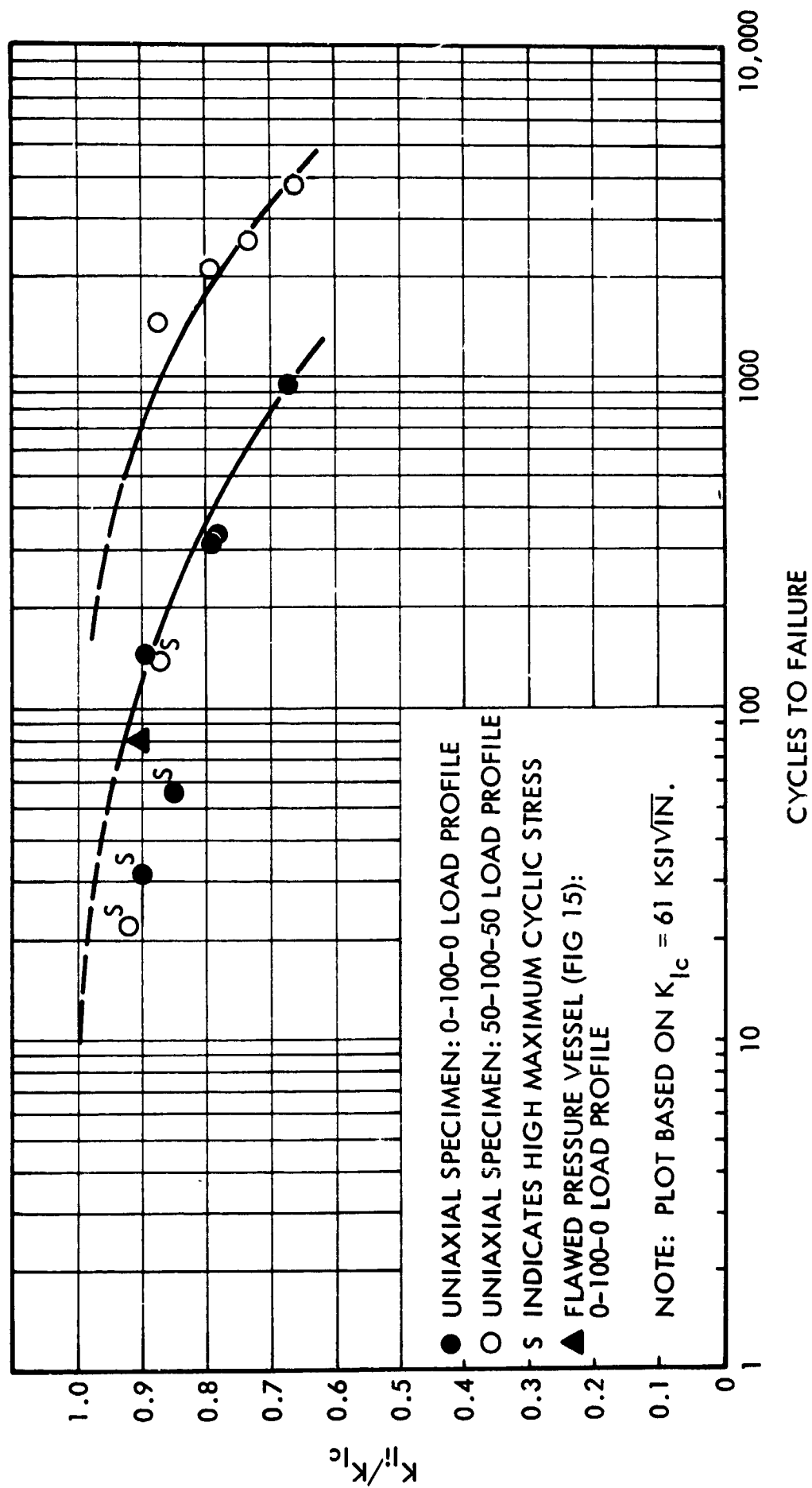


Figure 33: STRESS INTENSITY VS CYCLES-TO-FAILURE CORRELATION FOR 5Al -2.5 Sn (ELI) TITANIUM AT -320°F

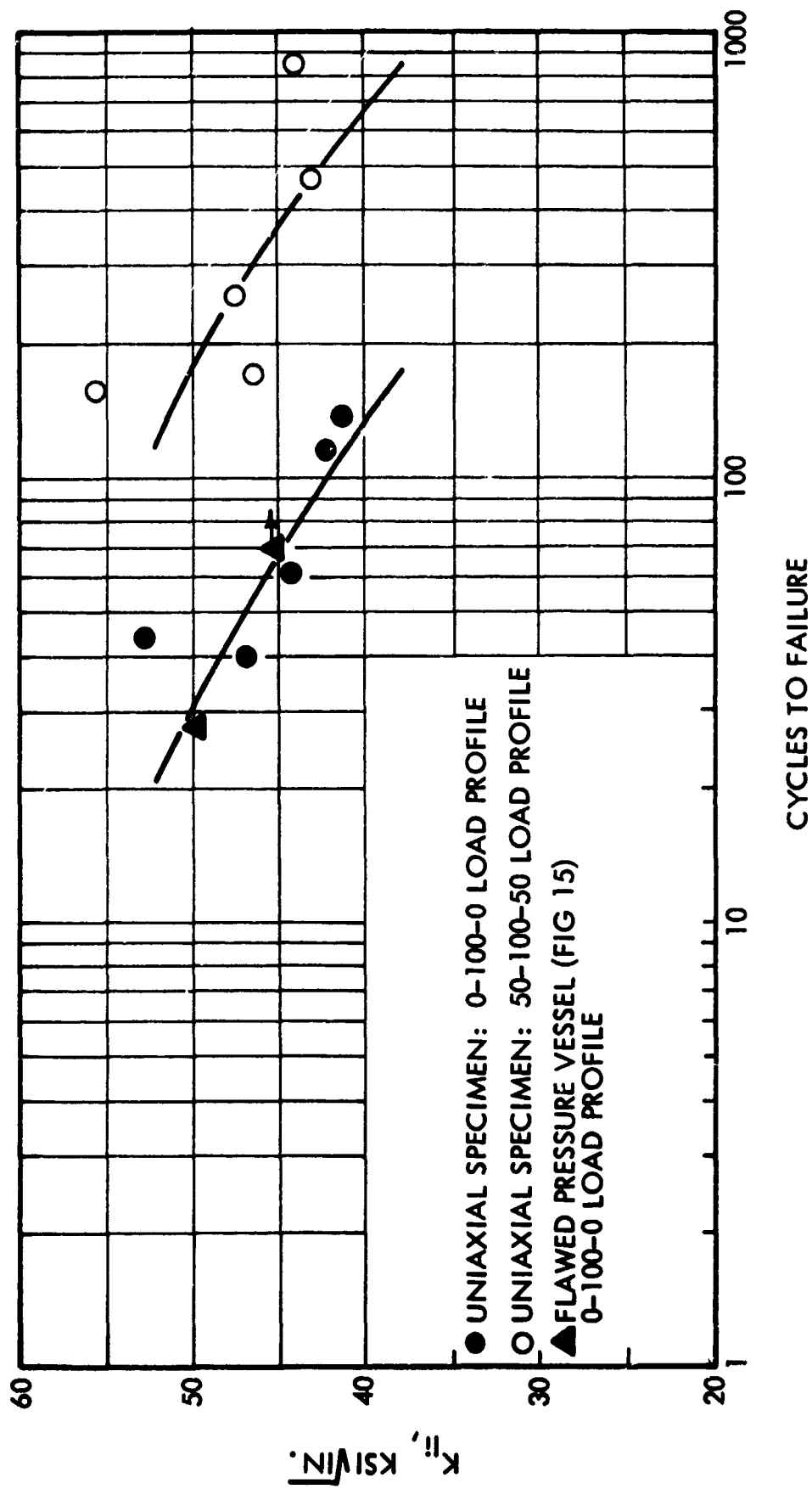


Figure 34: STRESS INTENSITY VS CYCLES-TO-FAILURE CORRELATION FOR 5Al-2.5 Sn (ELI) TITANIUM AT-423°F

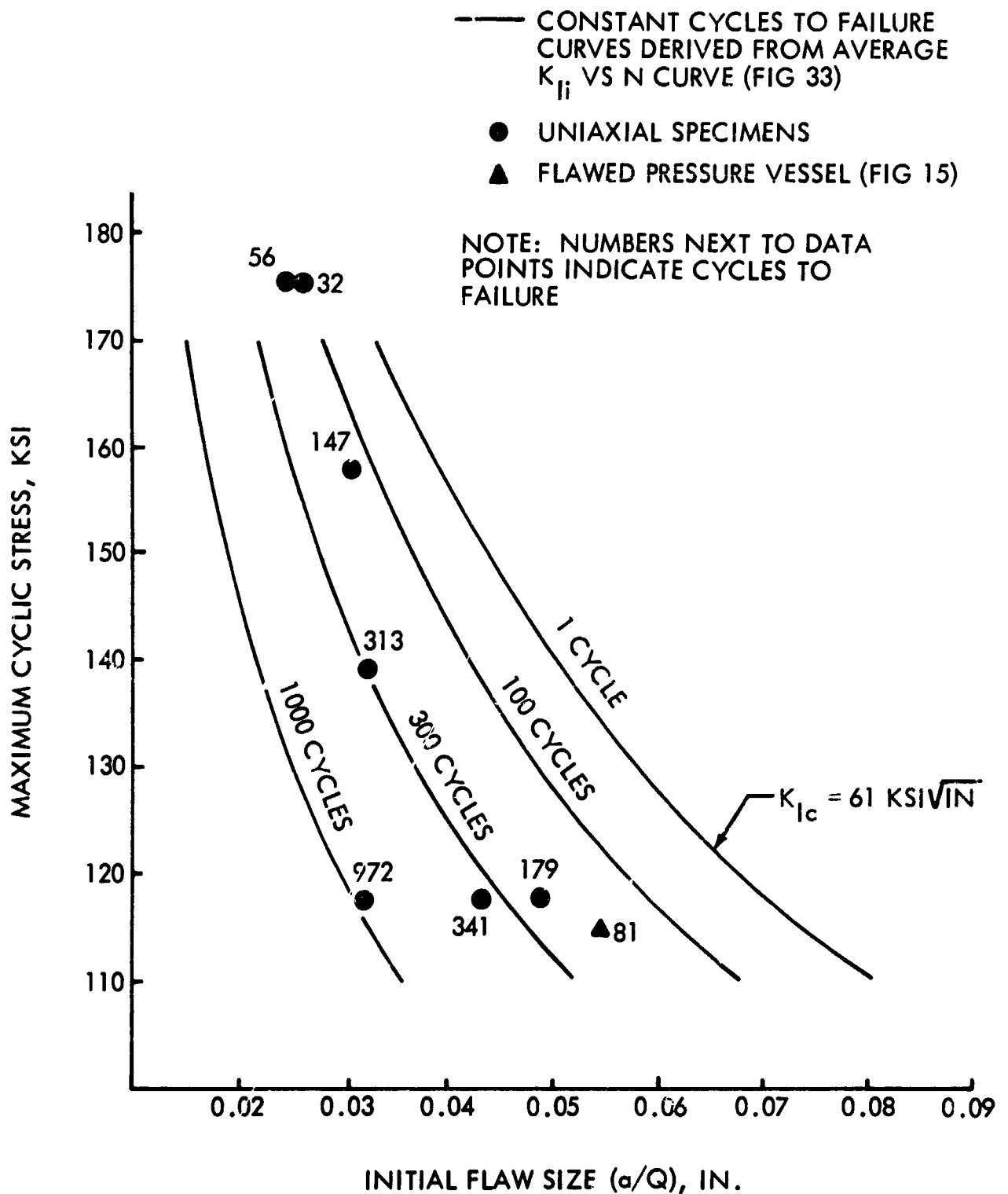


Figure 35: CYCLIC FLAW GROWTH DATA FOR 5Al -2.5 Sn (ELI) TITANIUM AT -320°F (0-100-0 LOAD PROFILE)

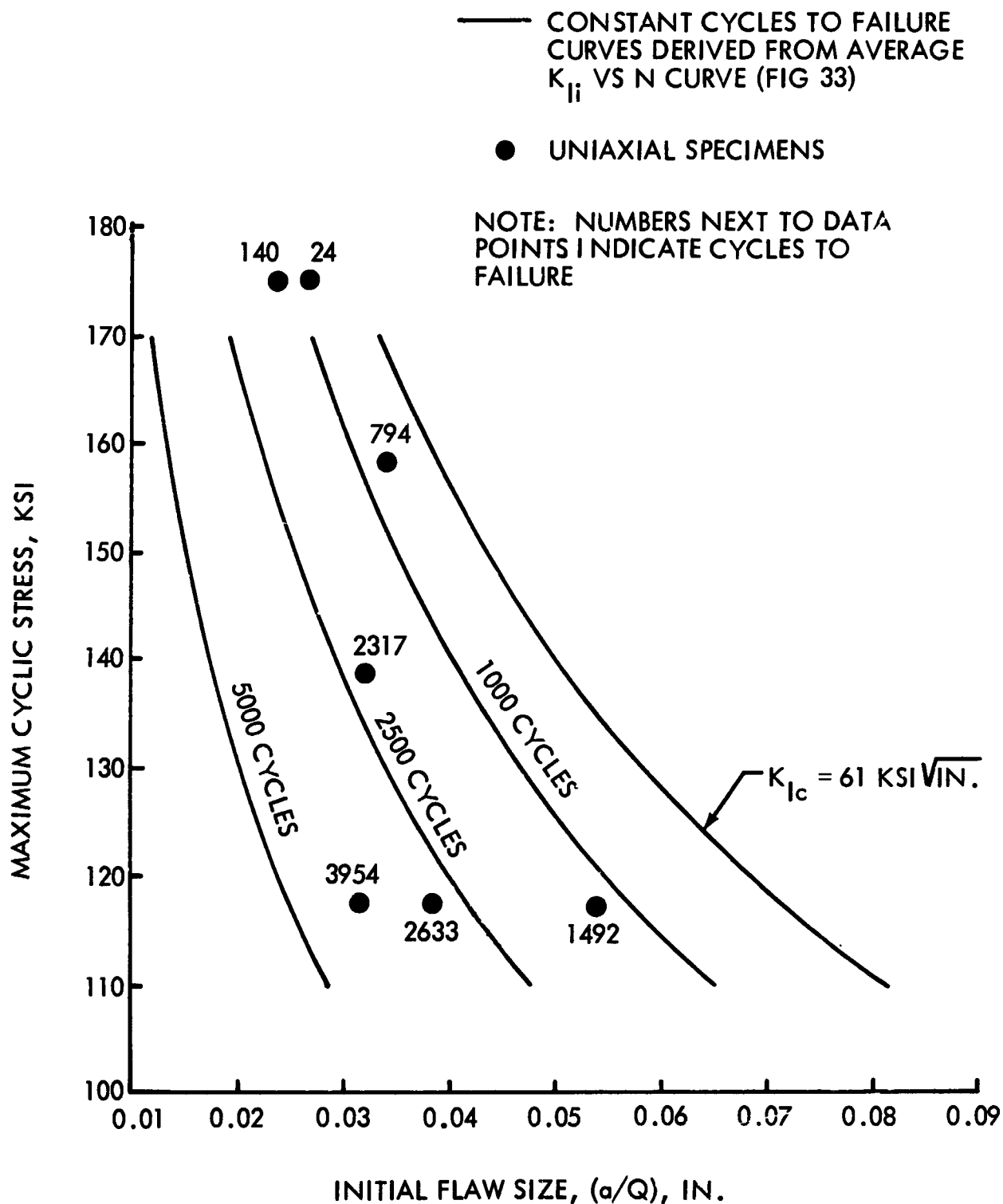


Figure 36: CYCLIC FLAW GROWTH DATA FOR 5Al -2.5 Sn (ELI)
TITANIUM AT -320°F (50-100-50 LOAD PROFILE)

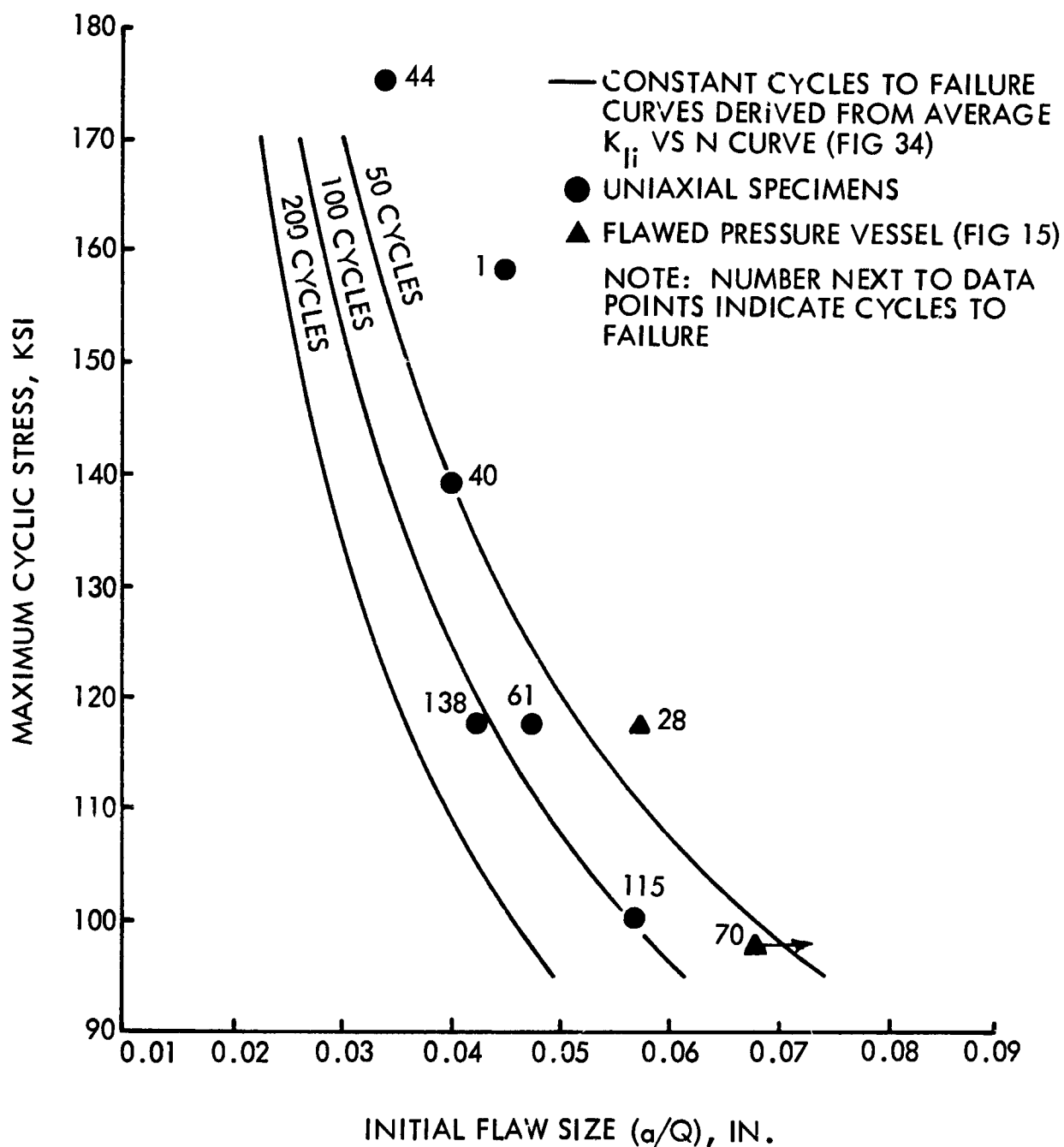


Figure 37: CYCLIC FLAW GROWTH DATA FOR 5Al -2.5 Sn (ELI) TITANIUM AT -423°F (0-100-0 LOAD PROFILE)

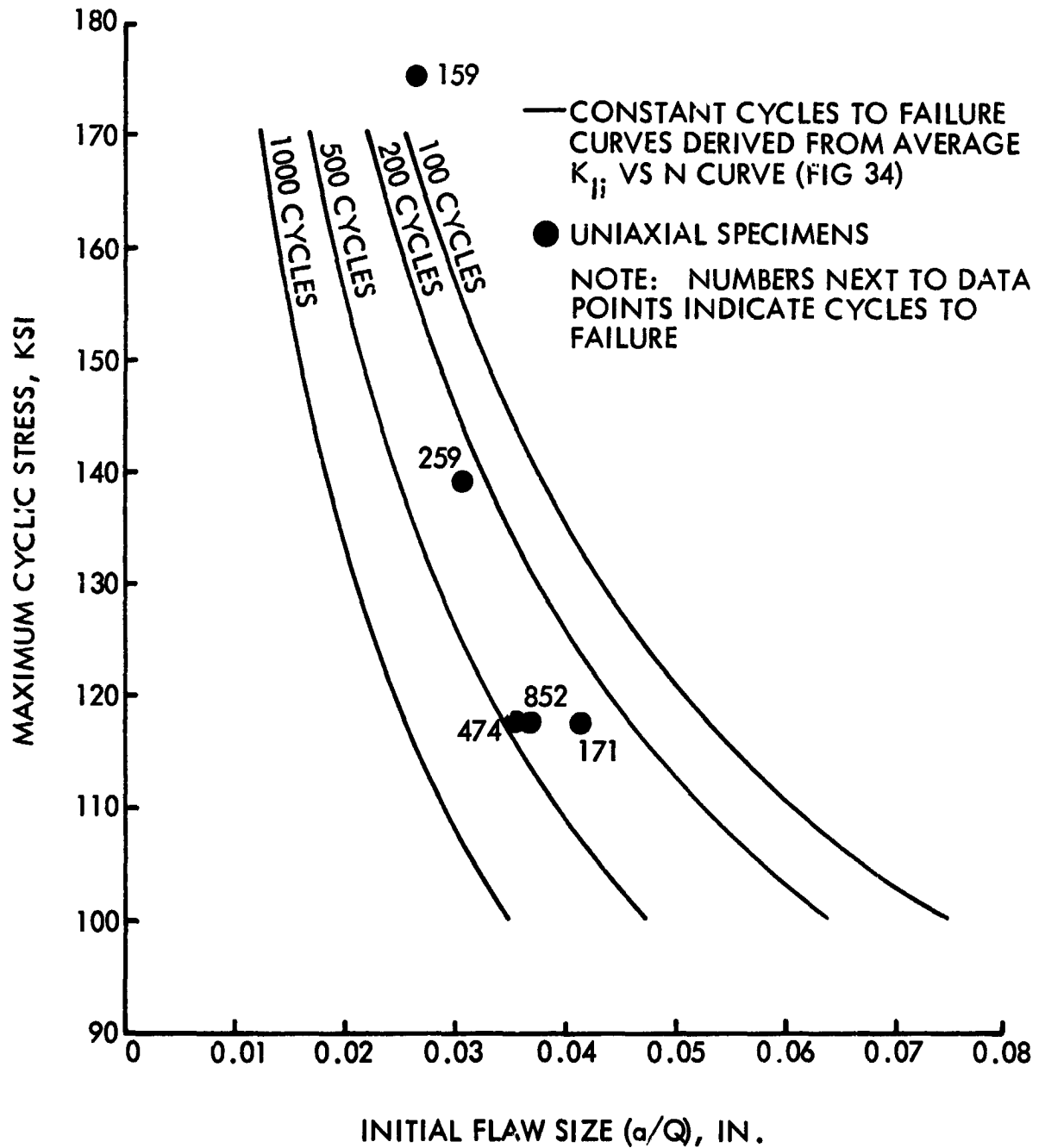


Figure 38: CYCLIC FLAW GROWTH DATA FOR 5Al -2.5 Sn (ELI) TITANIUM AT -423°F (50-100-50 LOAD PROFILE)

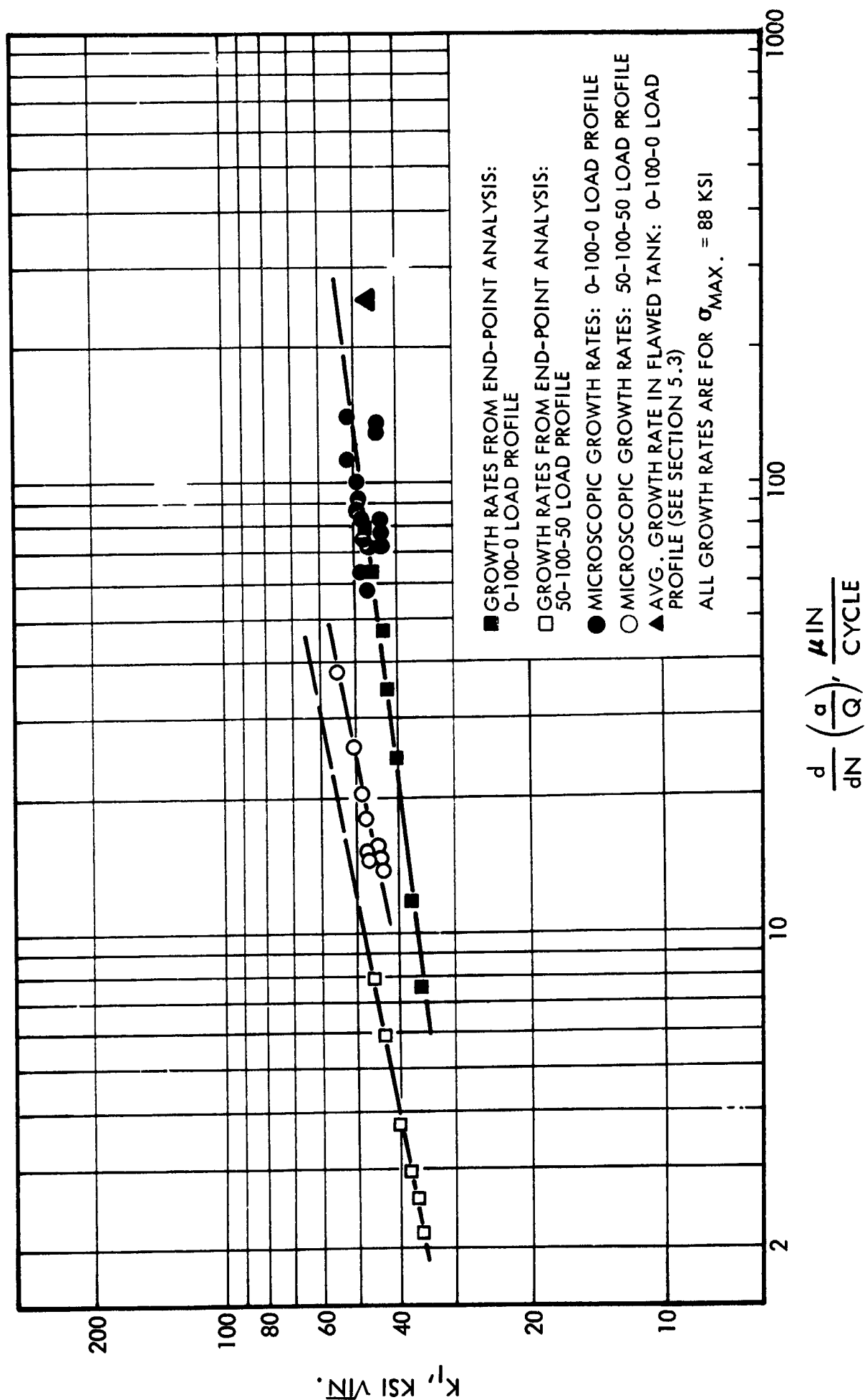


Figure 39: FLAW GROWTH RATES FOR 5Al -2.5 Sn (ELI) TITANIUM AT ROOM TEMPERATURE

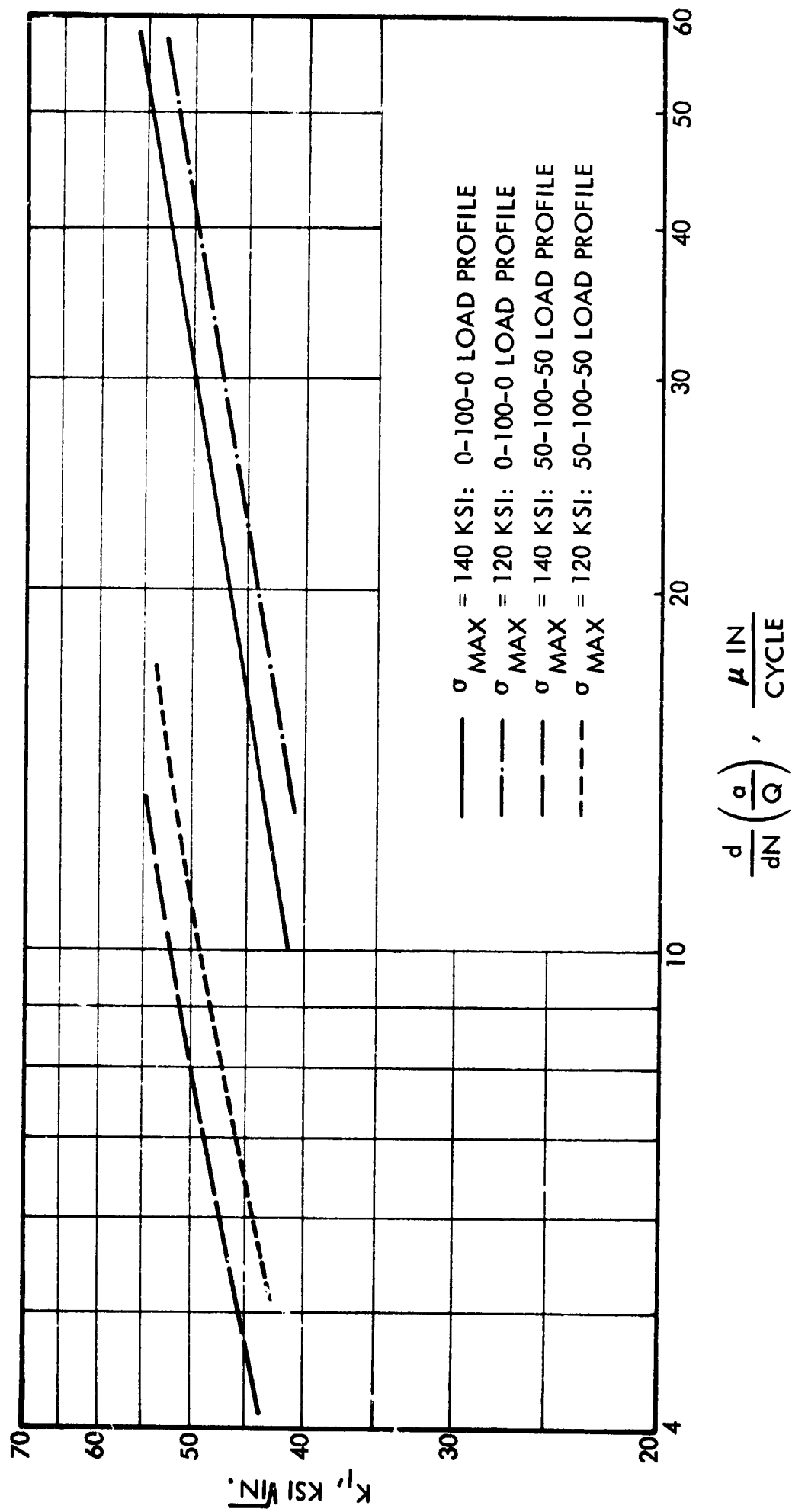


Figure 40: FLAW GROWTH RATES COMPUTED FROM END POINT ANALYSES
FOR 5A1 -2.5 Sn (ELI) TITANIUM AT -320°F

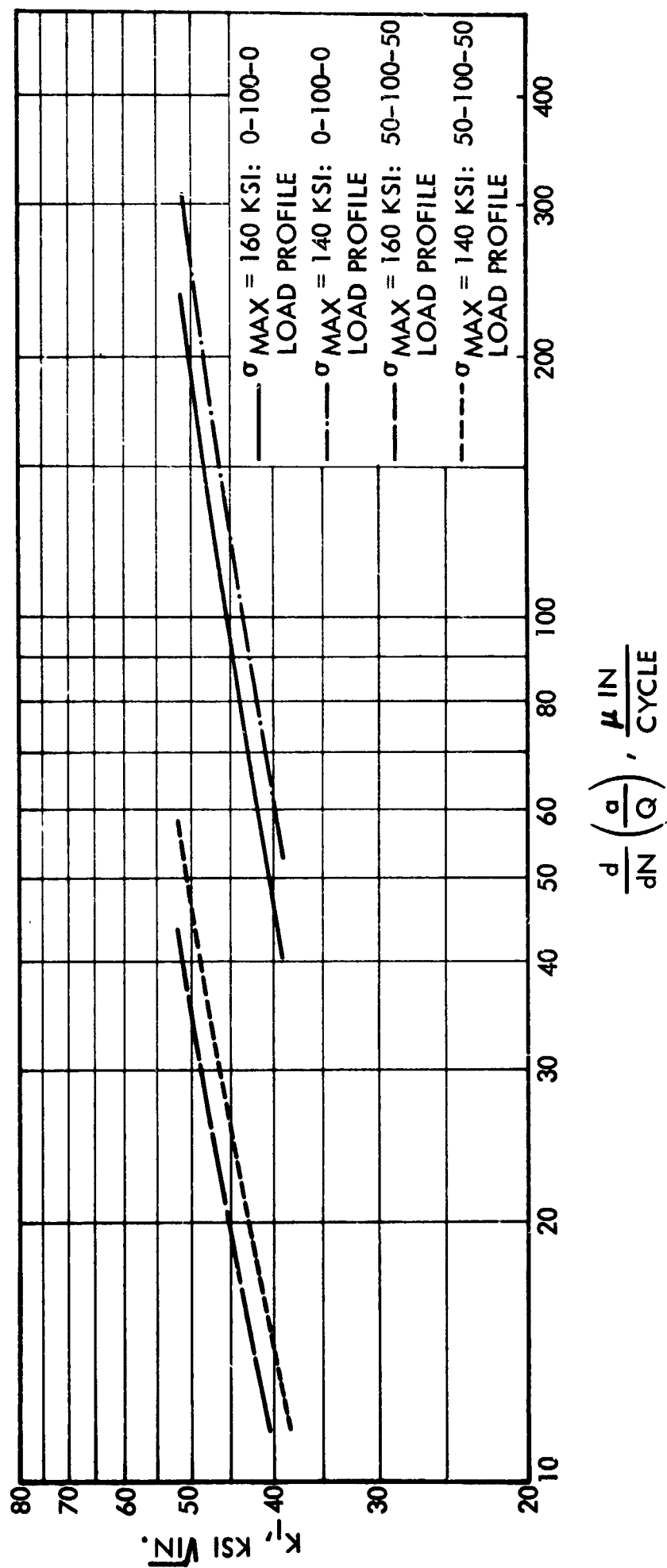
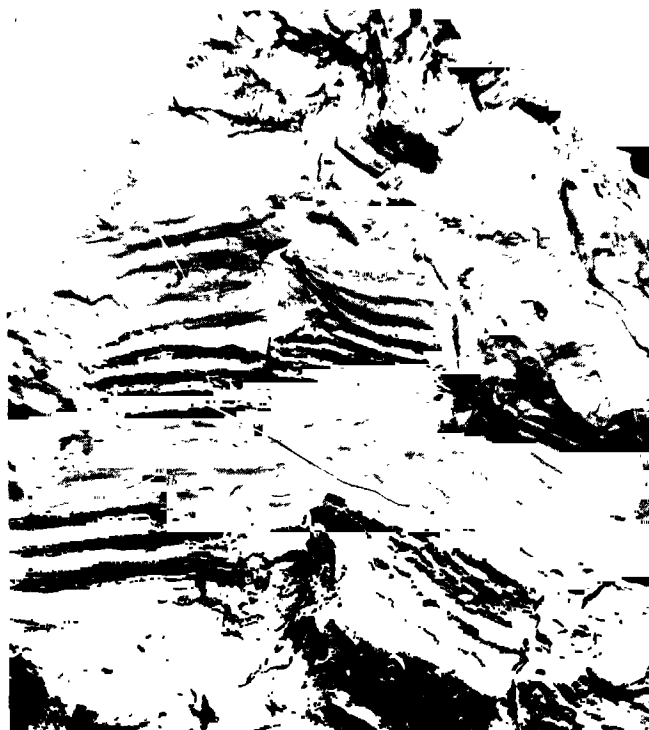


Figure 41: FLAW GROWTH RATES COMPUTED FROM END POINT ANALYSES
FOR 5Al-2.5 Sn (ELI) TITANIUM AT -423°F



ROOM TEMPERATURE



-320°F



-423°F

Figure 42: FRACTOGRAPHS OF STRIATED REGIONS
5Al-2.5 Sn (ELI) TITANIUM

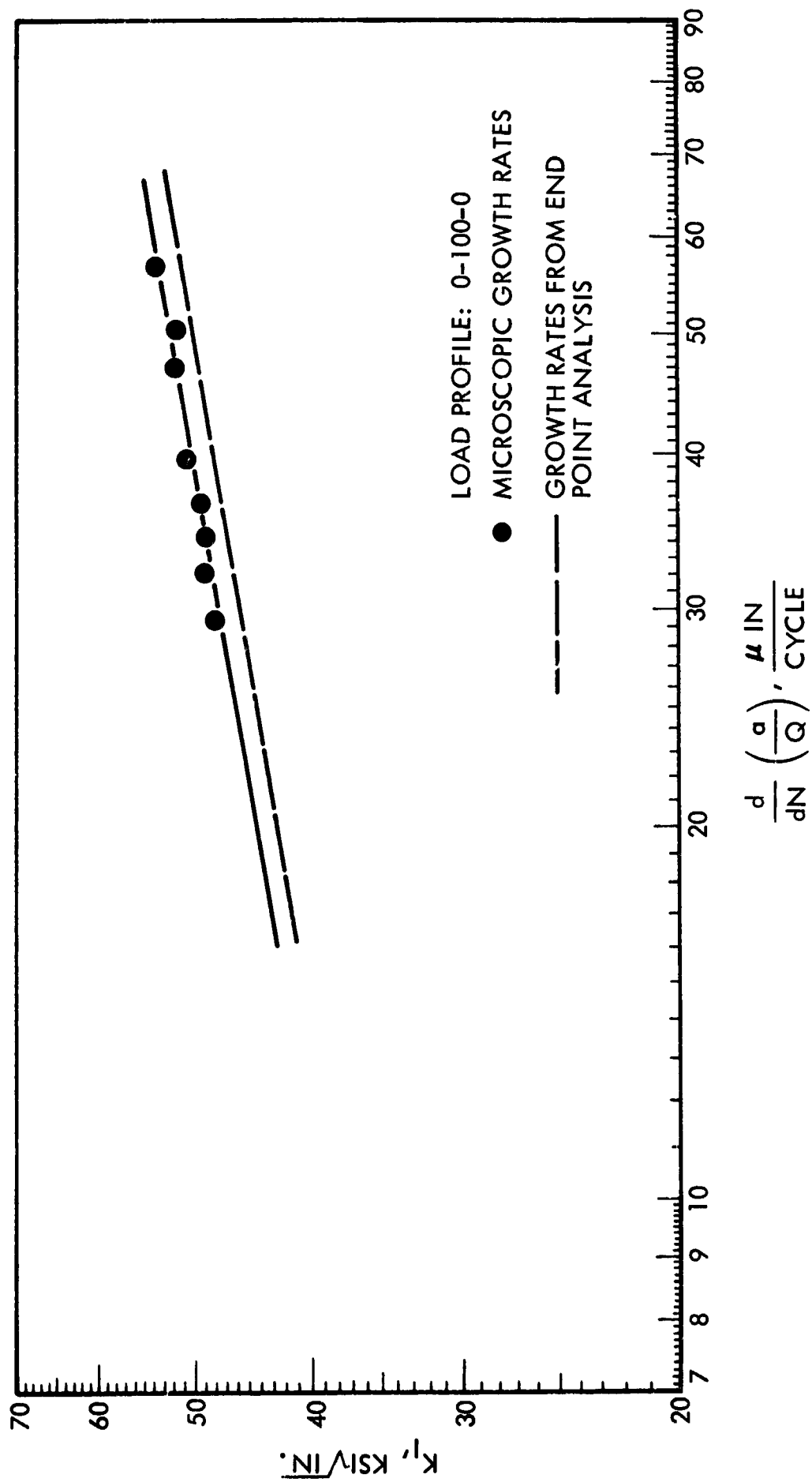


Figure 43: FLAW GROWTH RATES FOR 5Al -2.5 Sn (ELI) TITANIUM
AT -320°F (MAX. CYCLIC STRESS = 117.5 KSI)

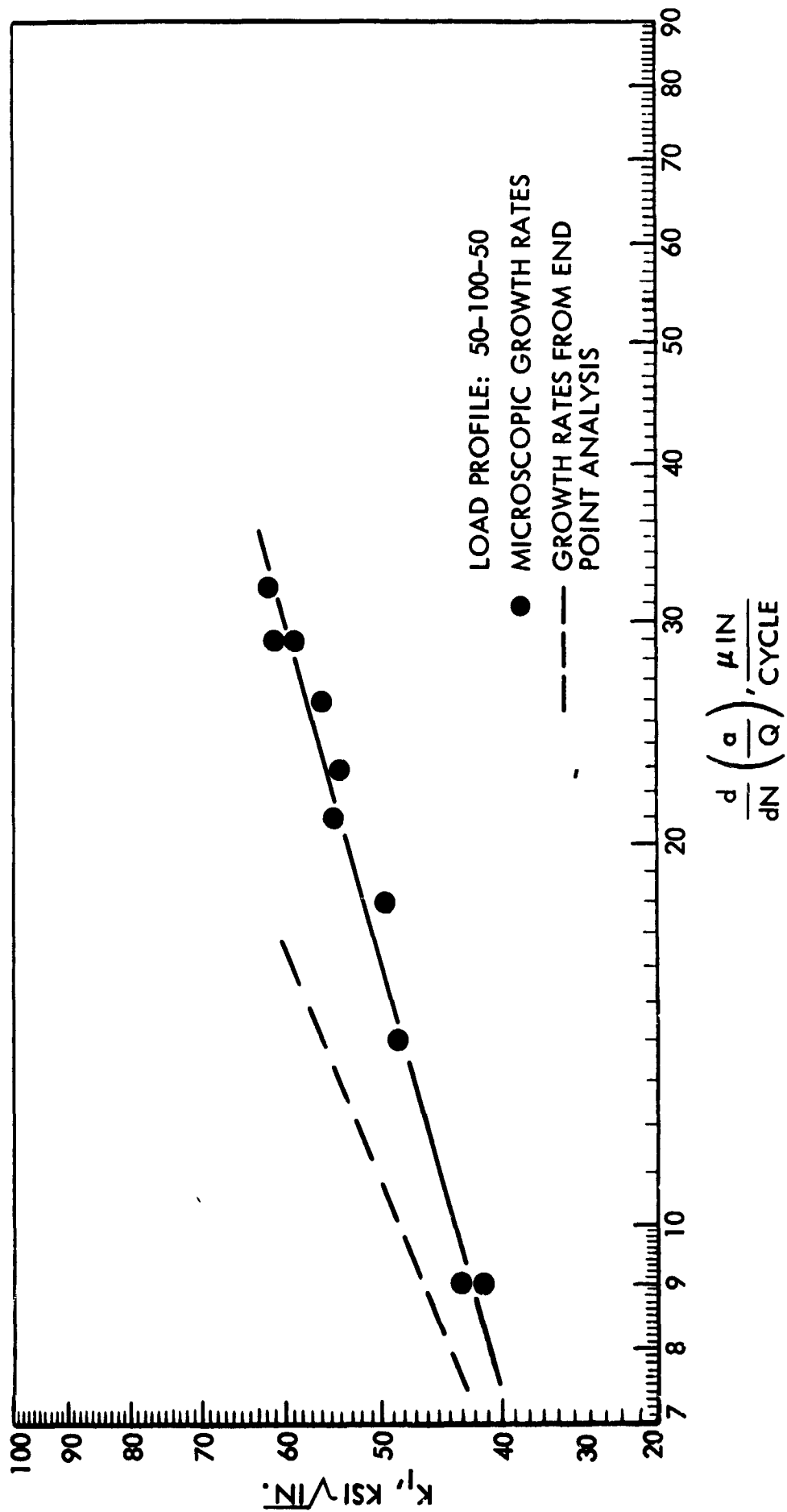


Figure 44: FLAW GROWTH RATES FOR 5Al -2.5 Sn (ELI) TITANIUM
AT -320°F (MAX. CYCLIC STRESS = 117.5 KSI)

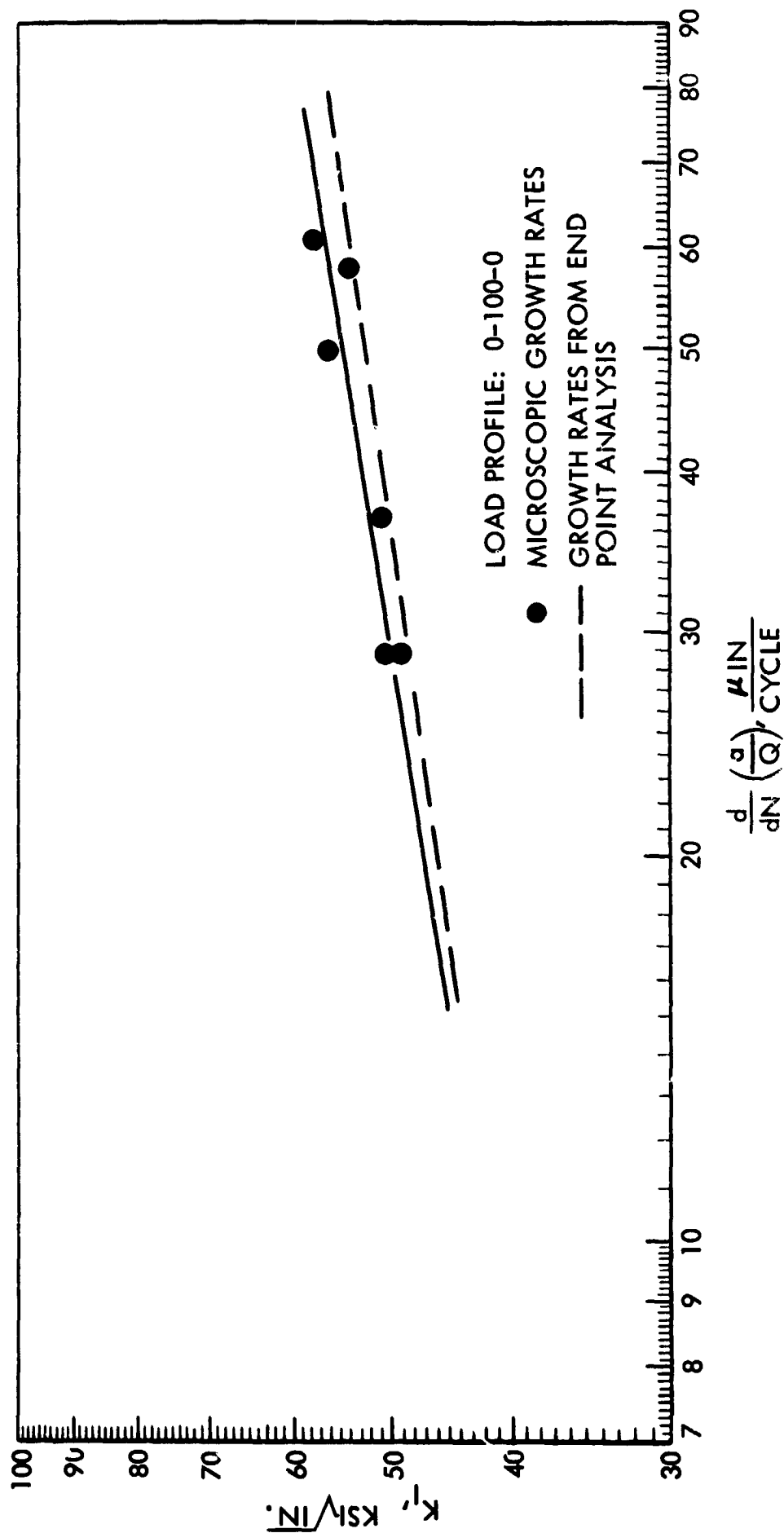


Figure 45: FLAW GROWTH RATES FOR 5 Al - 2.5 Sn (ELI) TITANIUM
AT -320°F (MAX. CYCLIC STRESS = 139 KSI)

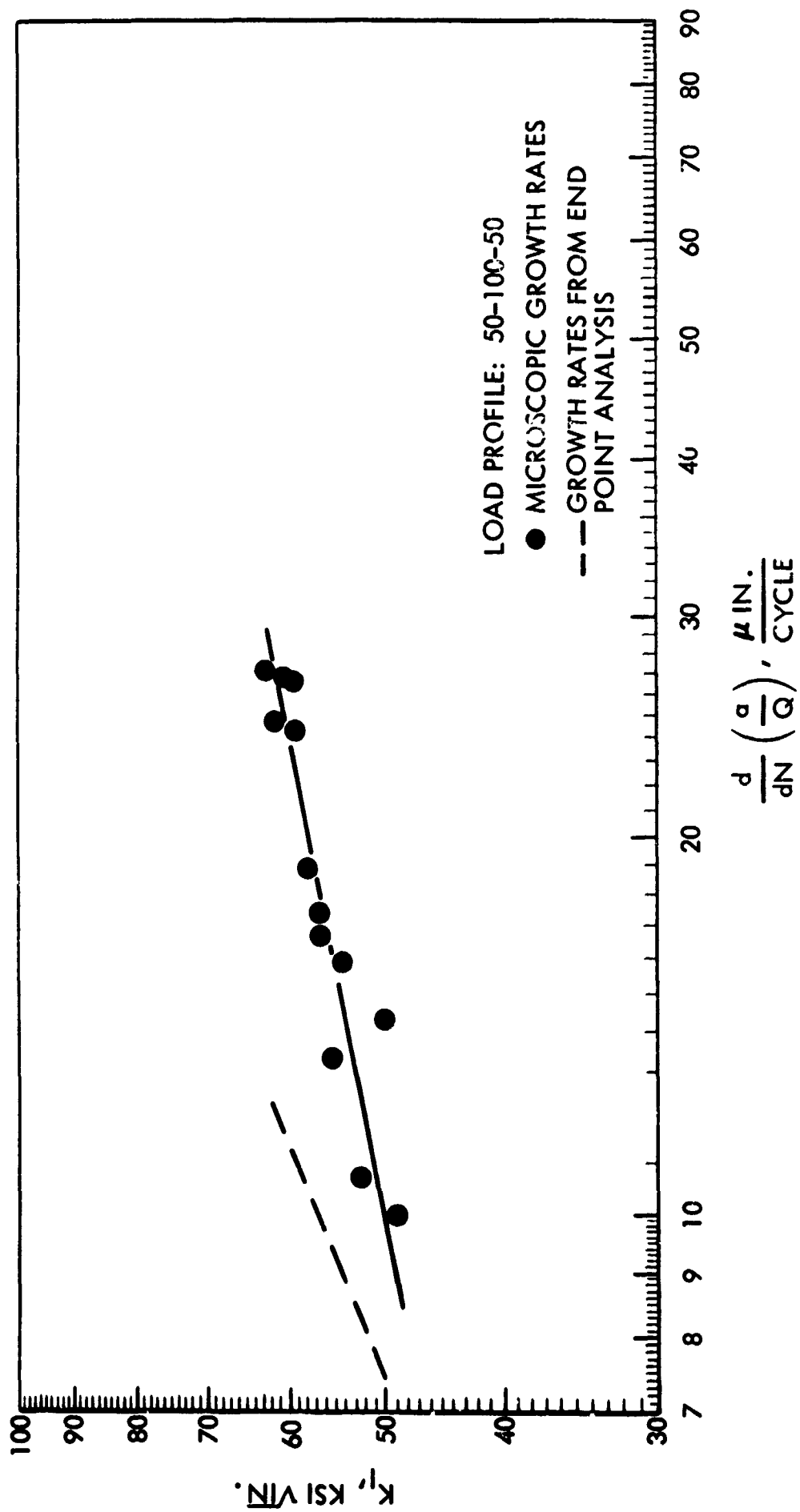


Figure 46: FLAW GROWTH RATES FOR 5Al-2.5Sn (ELI) TITANIUM
AT -320°F (MAX. CYCLIC STRESS = 139 KSI)

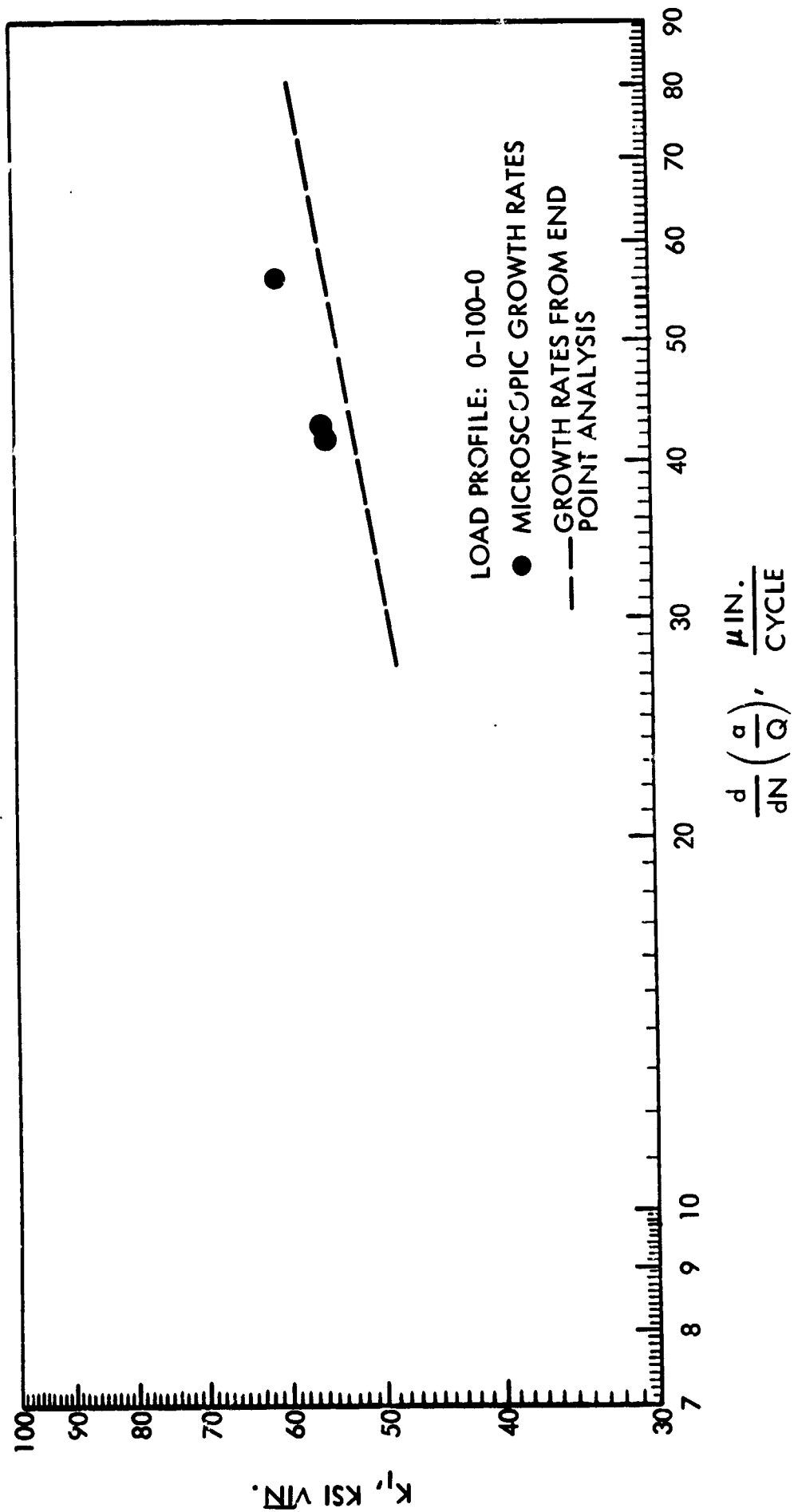


Figure 47: FLAW GROWTH RATES FOR 5Al - 2.5 Sn (ELI) TITANIUM AT -320°F
(MAX. CYCLIC STRESS = 158 KSI)

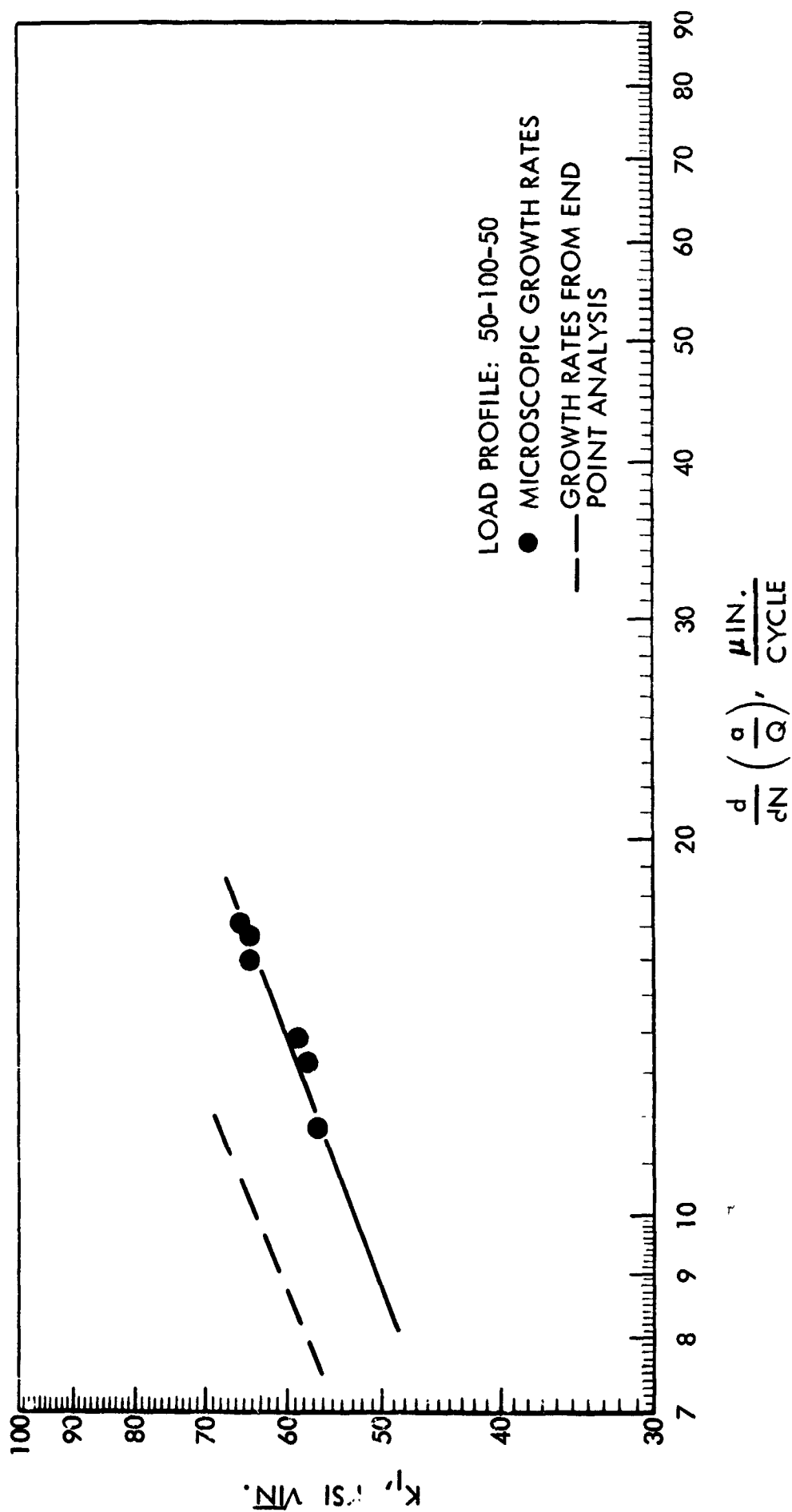


Figure 48: FLAW GROWTH RATES FOR 5Al -2.5 Sn (ELI) TITANIUM AT -320°F
(MAX. CYCLIC STRESS = 158 KSI)

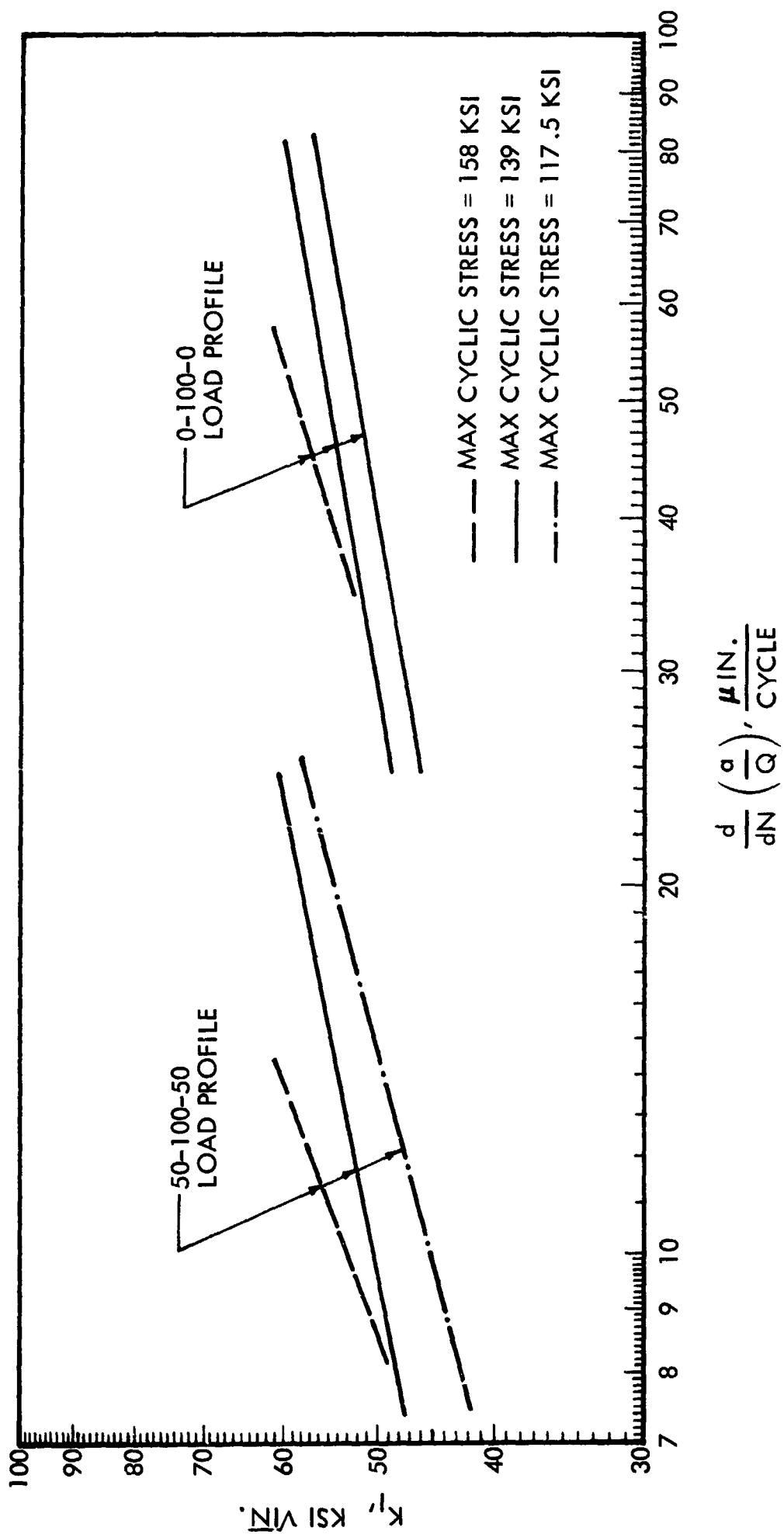
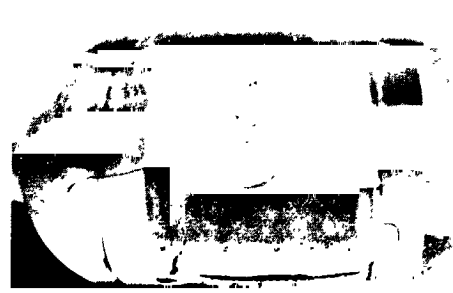


Figure 49: COMPARISON OF MICROSCOPIC FLAW GROWTH RATES AT THREE DIFFERENT
MAXIMUM CYCLIC STRESSES: 5A1 -2.5 Sn (ELI) TITANIUM AT -320°F



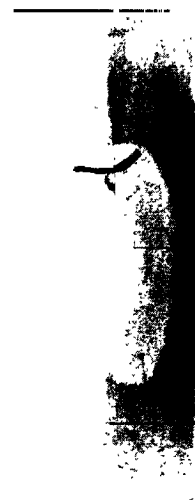
TANK 0013

5 AL 2.5 Sn (ELI)
TITANIUM TANK
TESTED AT -423°F
HOOP STRESS: 98 KSI
CYCLES TO FAILURE: 70

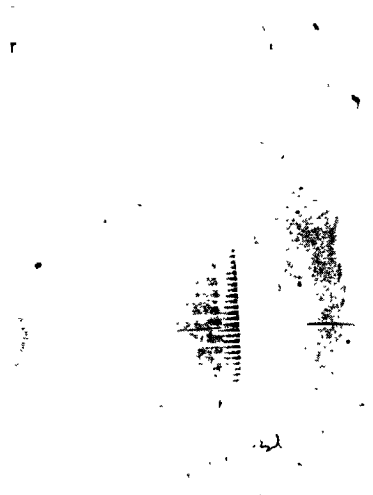


TANK 0012

5 AL 2.5 Sn (ELI)
TITANIUM TANK
TESTED AT -320°F
HOOP STRESS:
1ST RUN 80.4 KSI
2ND RUN 114.9 KSI
CYCLES TO FAILURE:
 $315 + 81 = 396$



50b



50a

Figure 50: FRACTURE APPEARANCE OF 5Al -2.5 Sn (ELI) TITANIUM TANKS

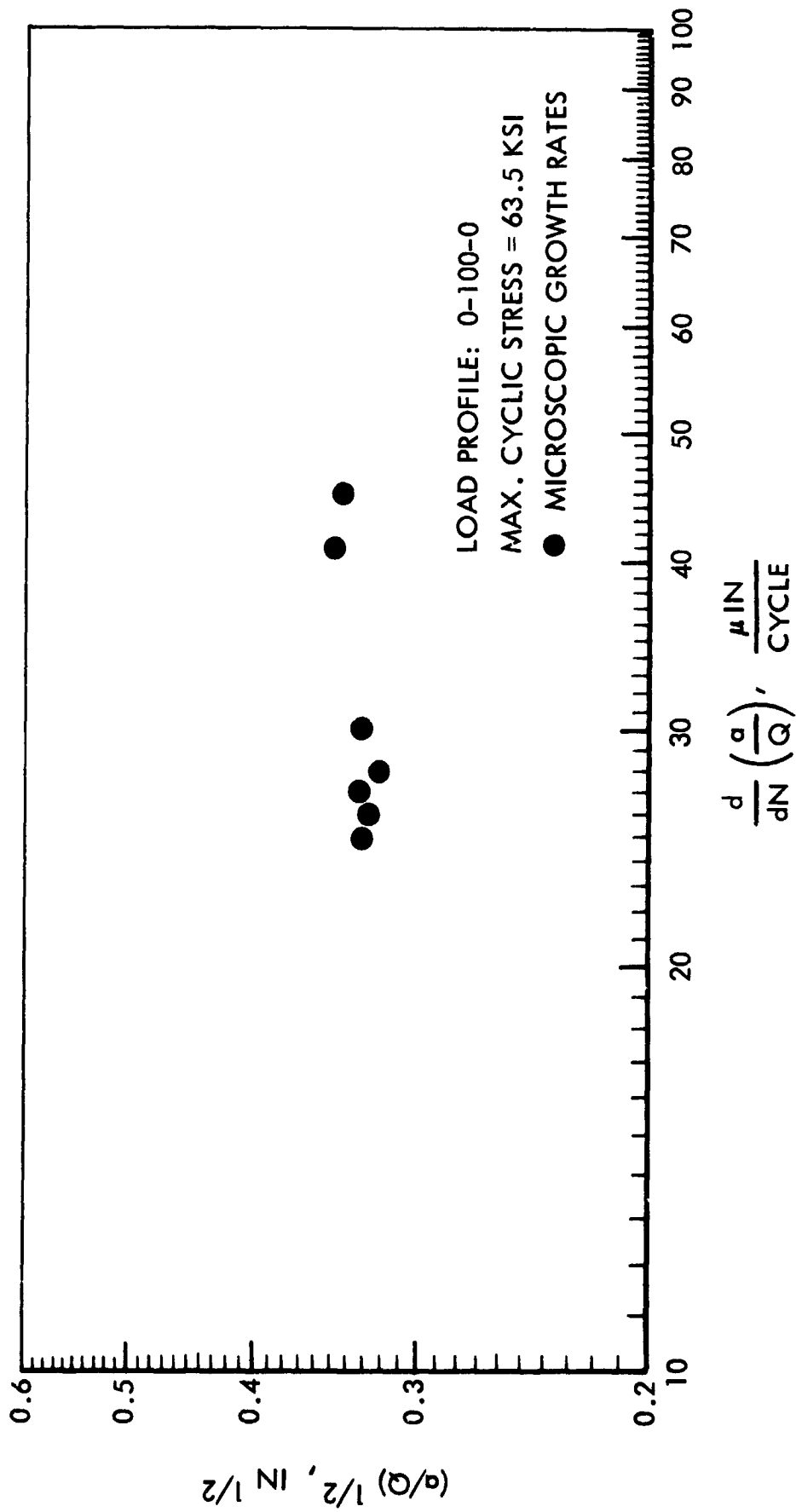


Figure 51: MICROSCOPIC FLAW GROWTH RATES FOR 5Al -2.5 Sn (ELI)
 TITANIUM TANK 0009 TESTED AT ROOM TEMPERATURE

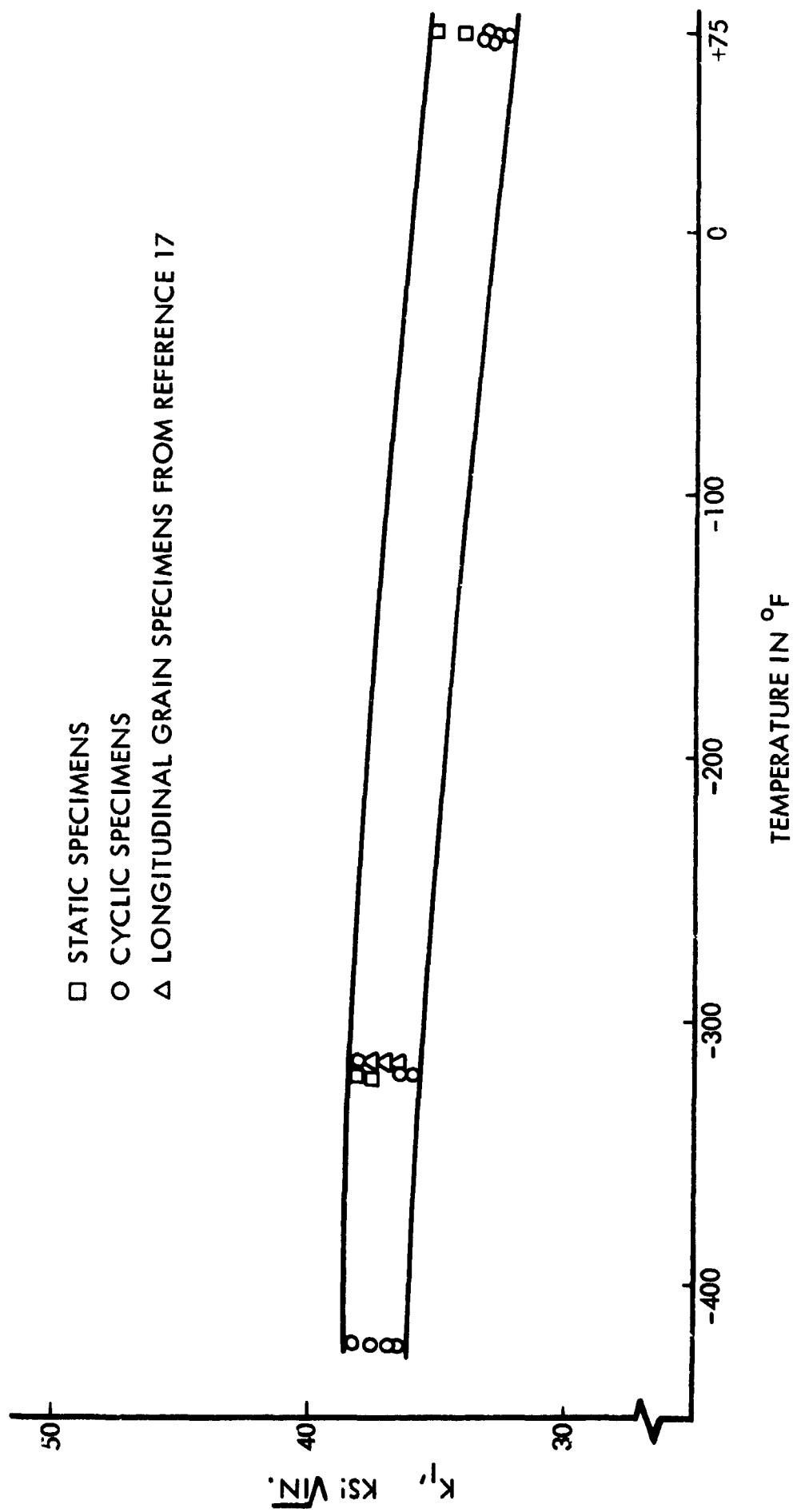


Figure 52: PLANE STRAIN FRACTURE TOUGHNESS OF 2219-T87 ALUMINUM
(LONG TRANSVERSE GRAIN AS A FUNCTION OF TEMPERATURE)

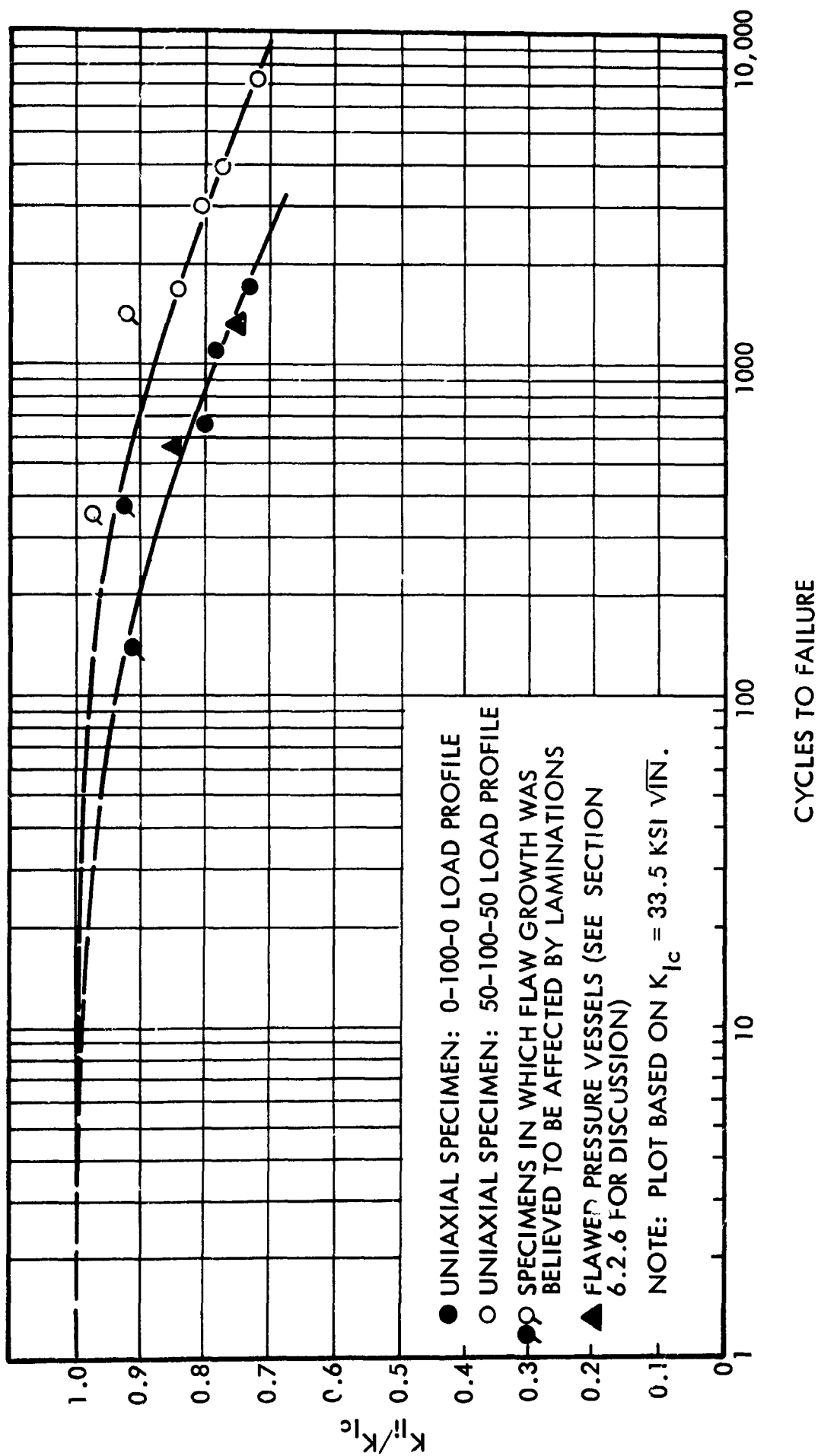


Figure 53: STRESS INTENSITY VS CYCLES TO FAILURE CORRELATION
FOR 2219-T87 ALUMINUM AT ROOM TEMPERATURE

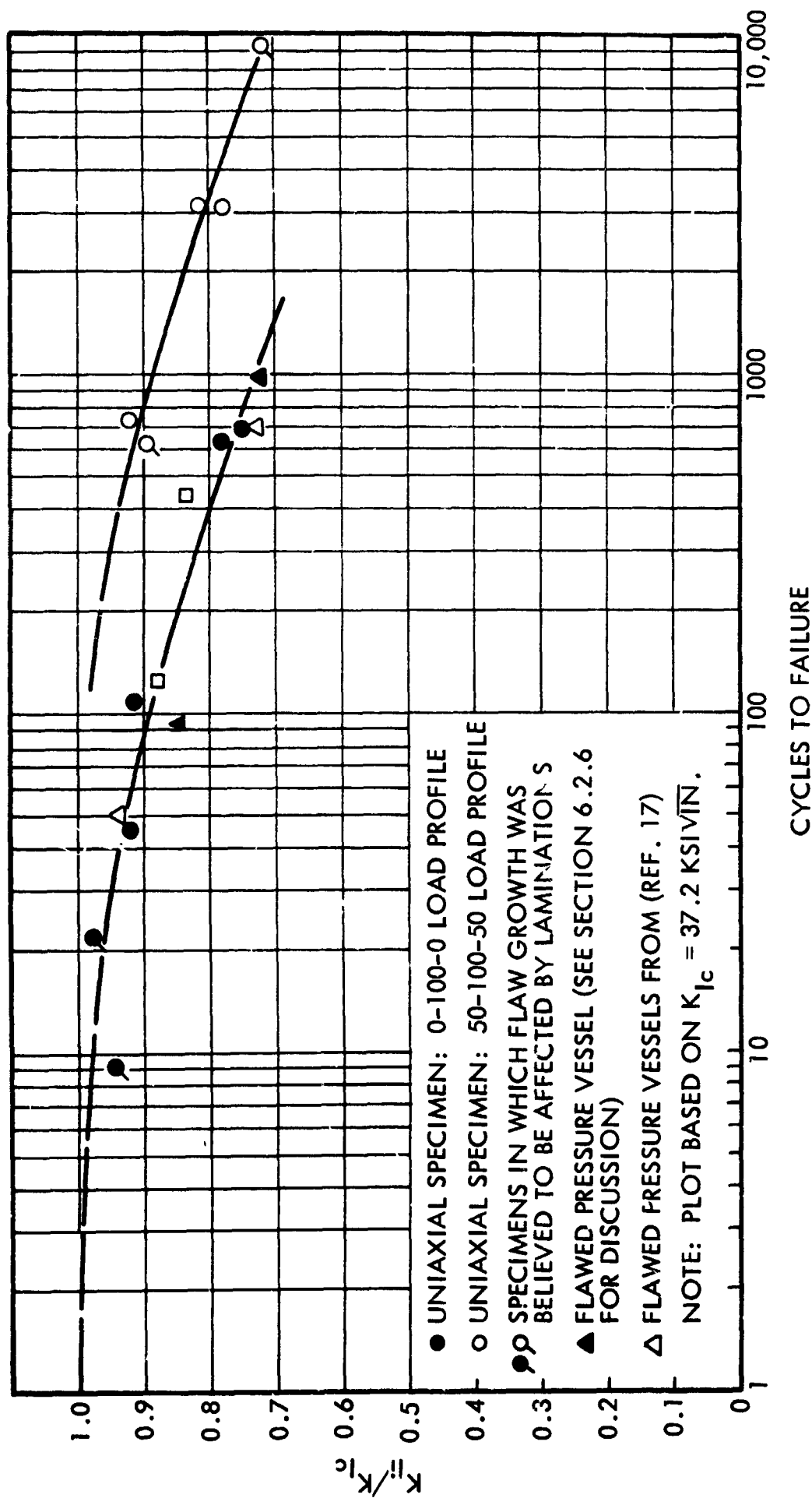


Figure 54: STRESS INTENSITY VS CYCLES TO FAILURE CORRELATION FOR 2219-T87 ALUMINUM AT -320°F

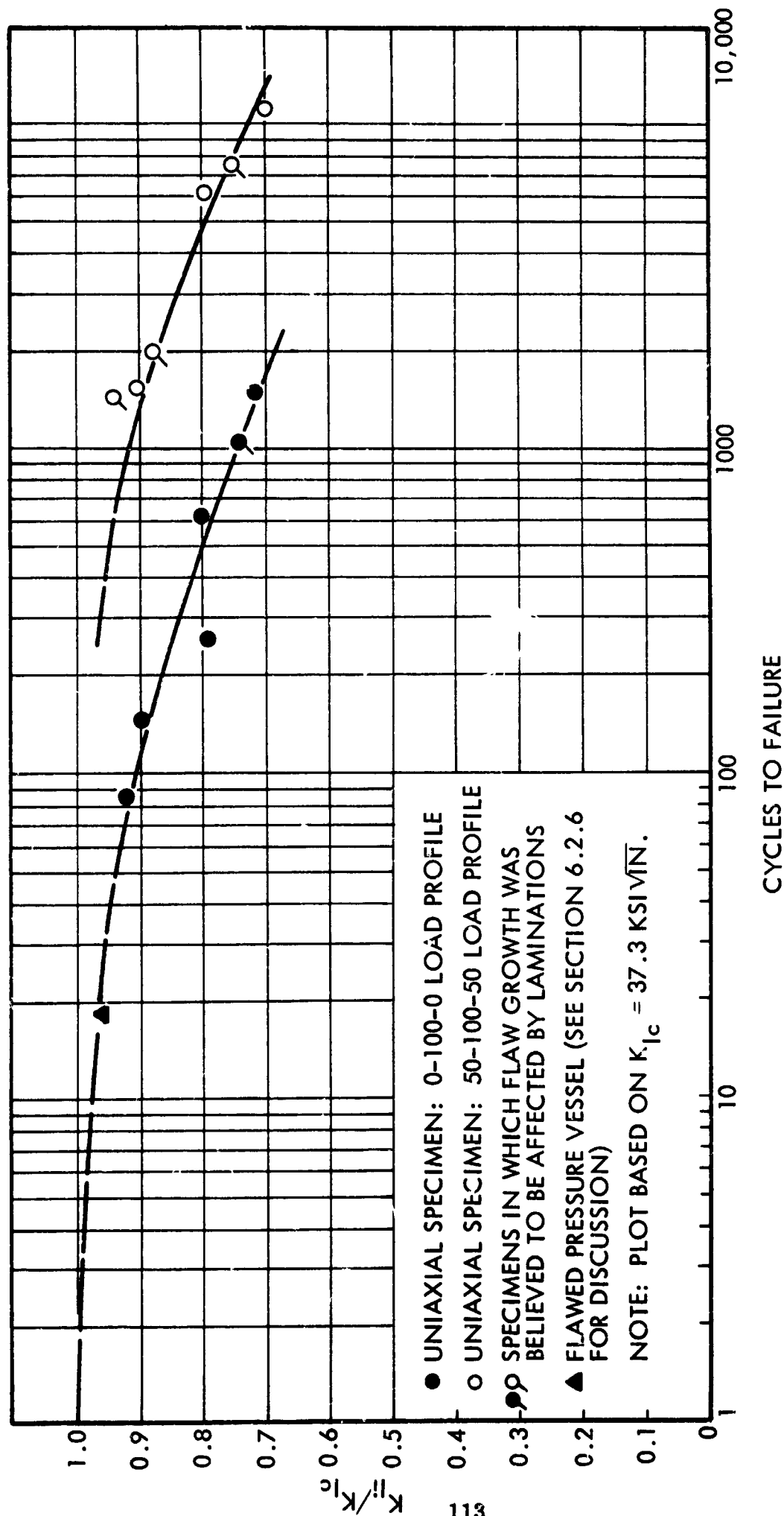


Figure 55: STRESS INTENSITY VS CYCLES-TO-FAILURE CORRELATION
FOR 2219-T87 ALUMINUM AT -423°F

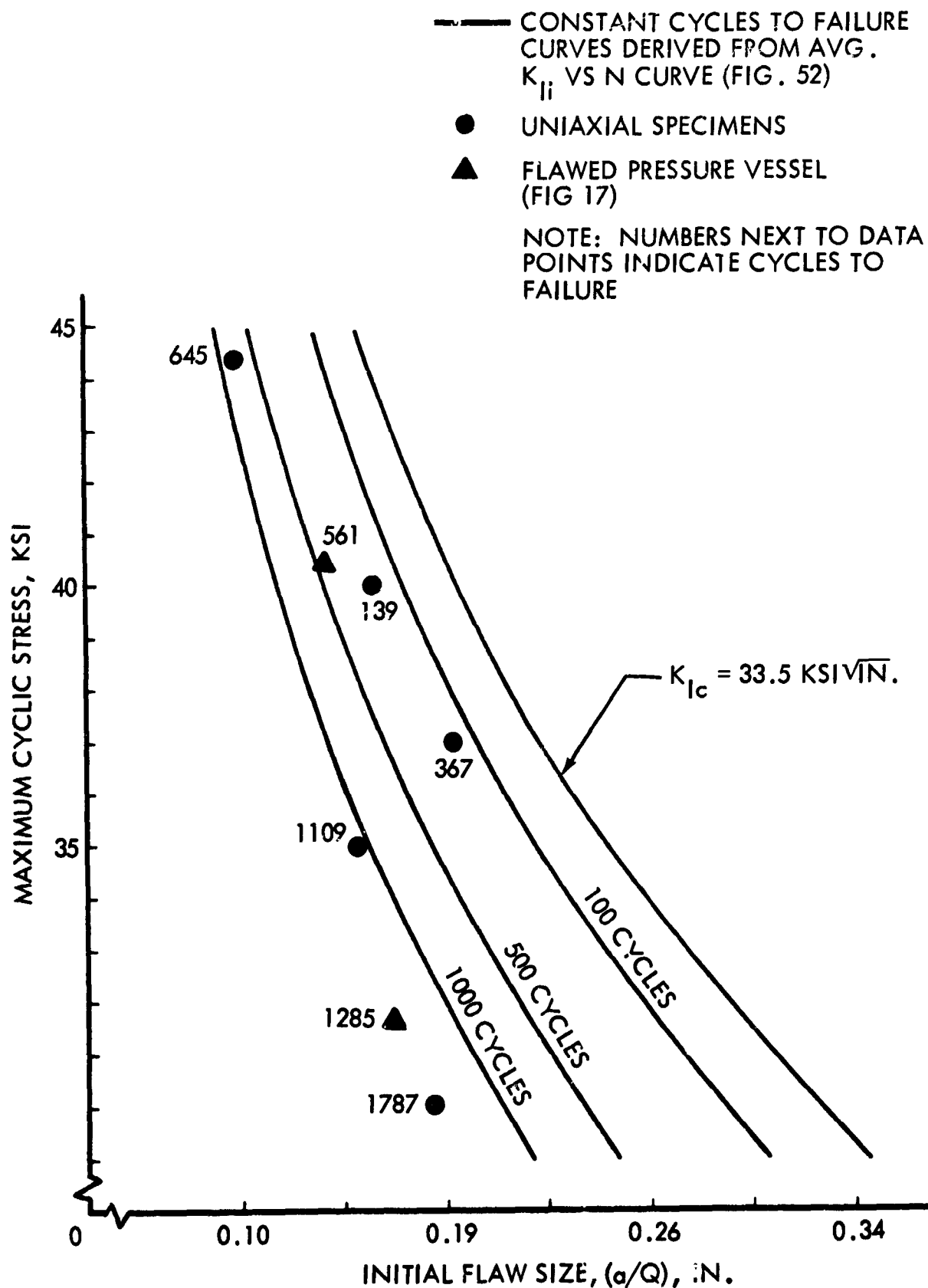


Figure 56: CYCLIC FLAW GROWTH DATA FOR 2219-T87 ALUMINUM AT ROOM TEMP. (0-100-0 LOAD PROFILE)

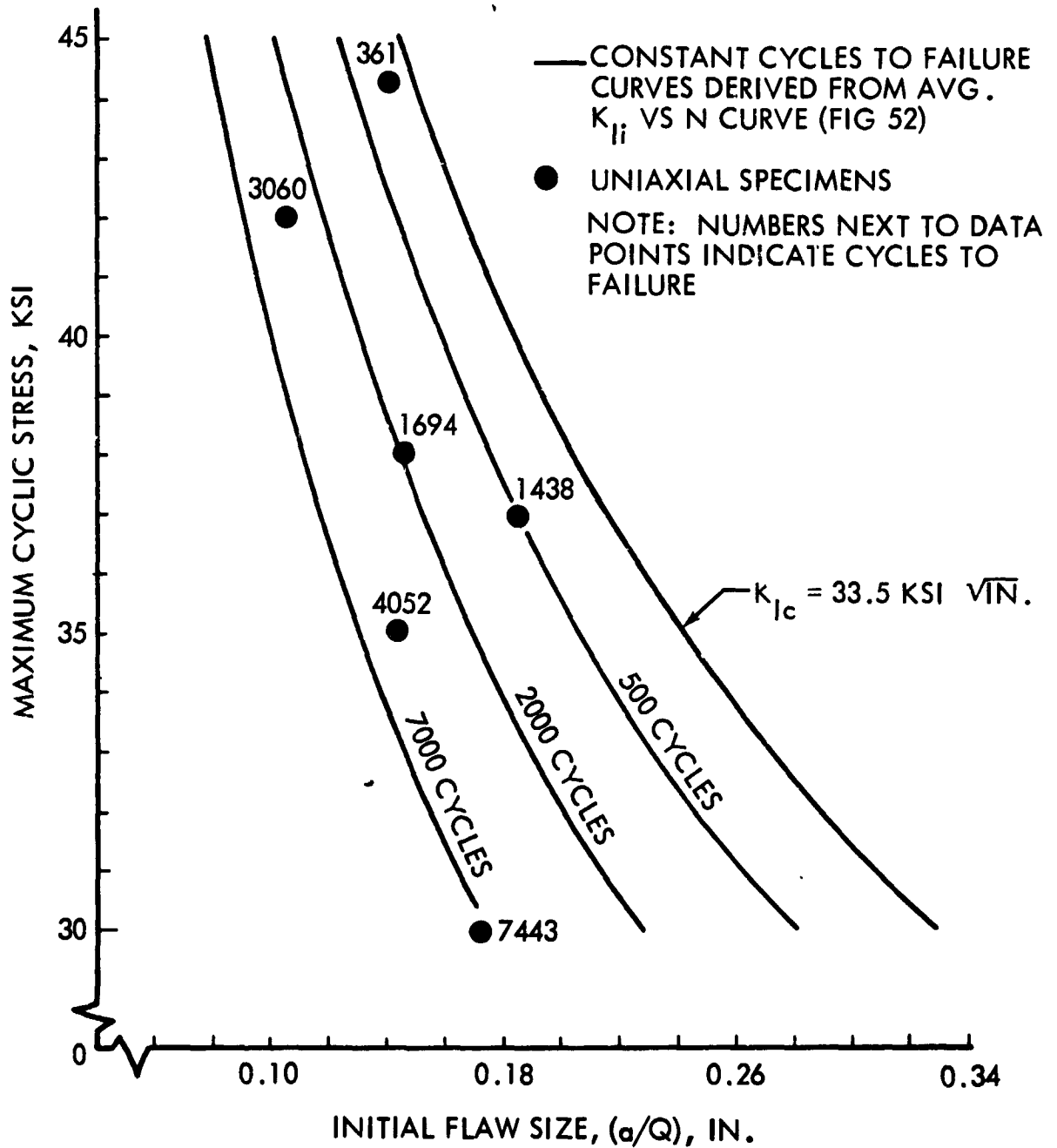


Figure 57: CYCLIC FLAW GROWTH DATA FOR 2219-T87 ALUMINUM AT ROOM TEMP. (50-100-50 LOAD PROFILE)

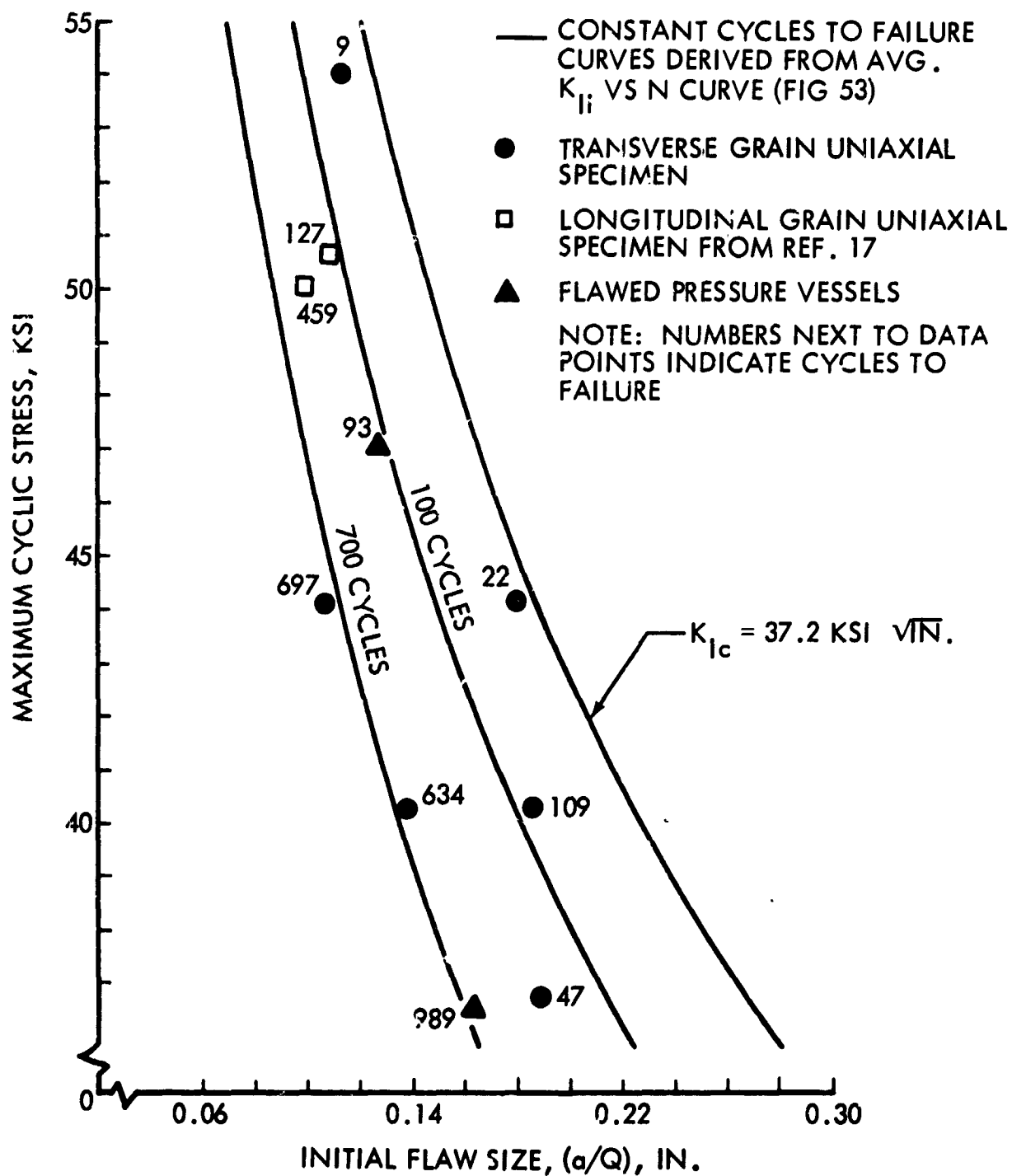


Figure 58: CYCLIC FLAW GROWTH DATA FOR 2219-T87 ALUMINUM AT -320°F (0-100-0 LOAD PROFILE)

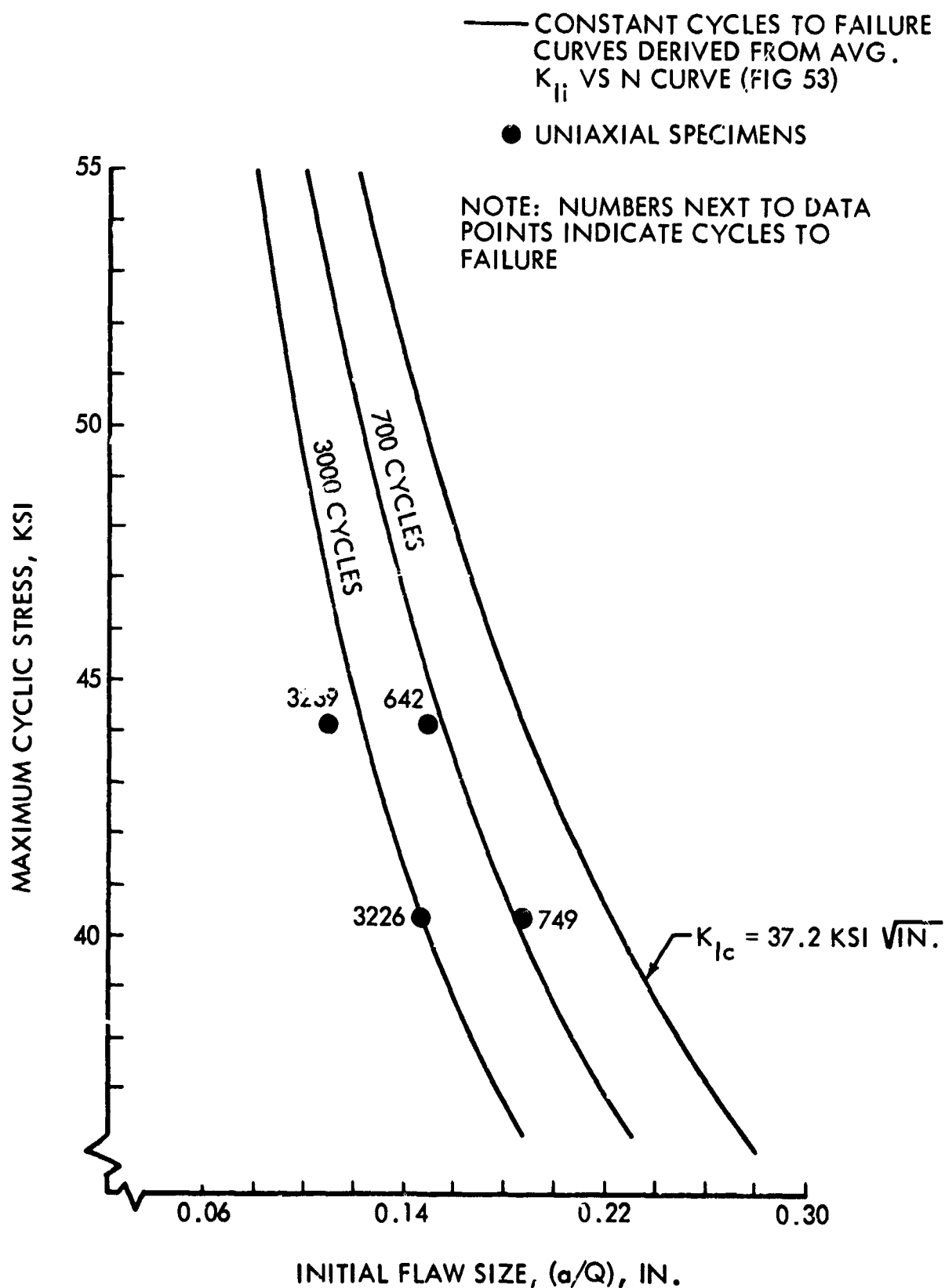


Figure 59: CYCLIC FLAW GROWTH DATA FOR 2219-T87 ALUMINUM
AT -320°F (50-100-50 LOAD PROFILE)

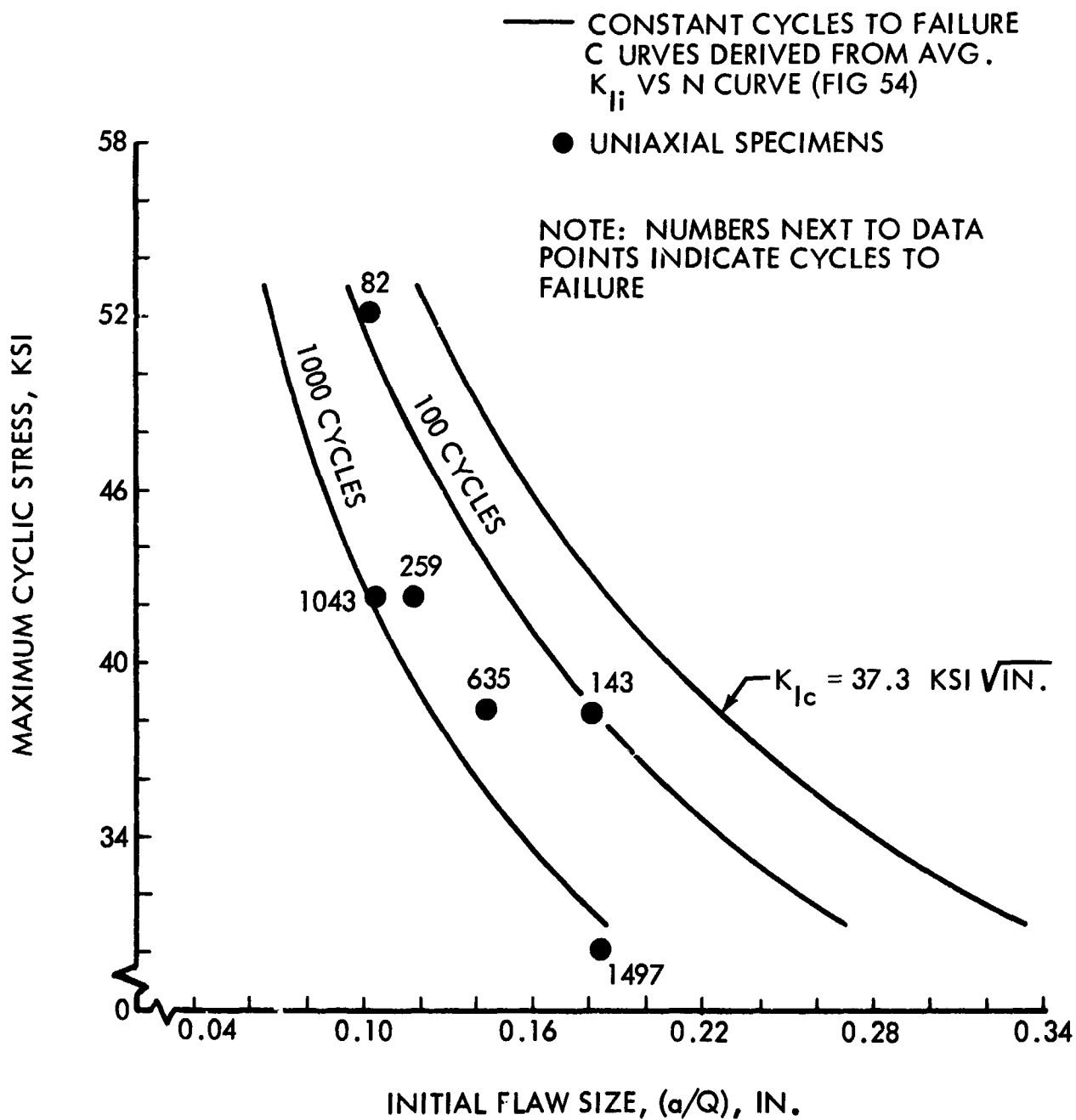


Figure 60: CYCLIC FLAW GROWTH DATA FOR 2219-T87 ALUMINUM AT -423°F (0-100-0 LOAD PROFILE)

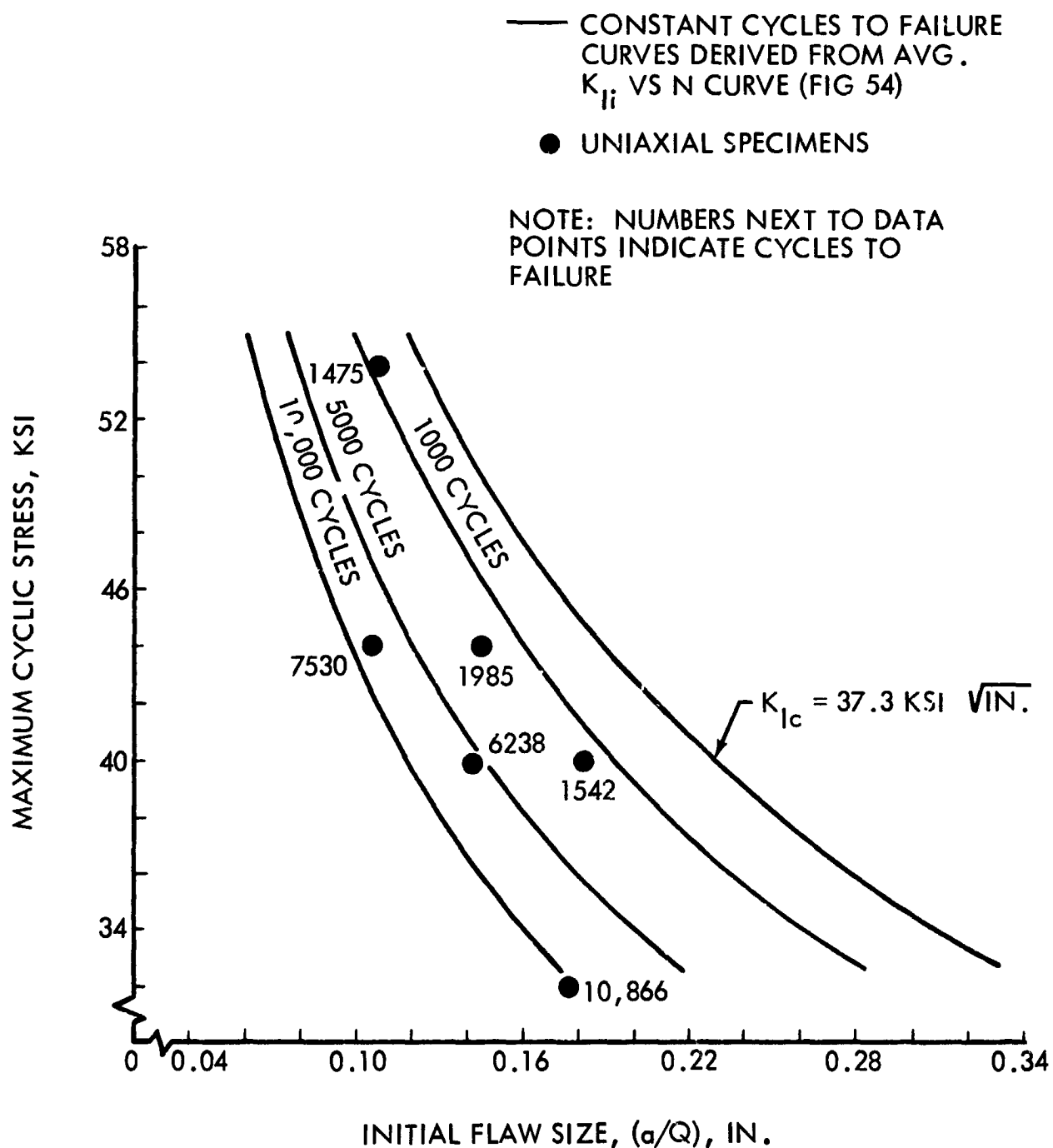


Figure 61: CYCLIC FLAW GROWTH DATA FOR 2219-T87 ALUMINUM
AT -423°F (50-100-50 LOAD PROFILE)

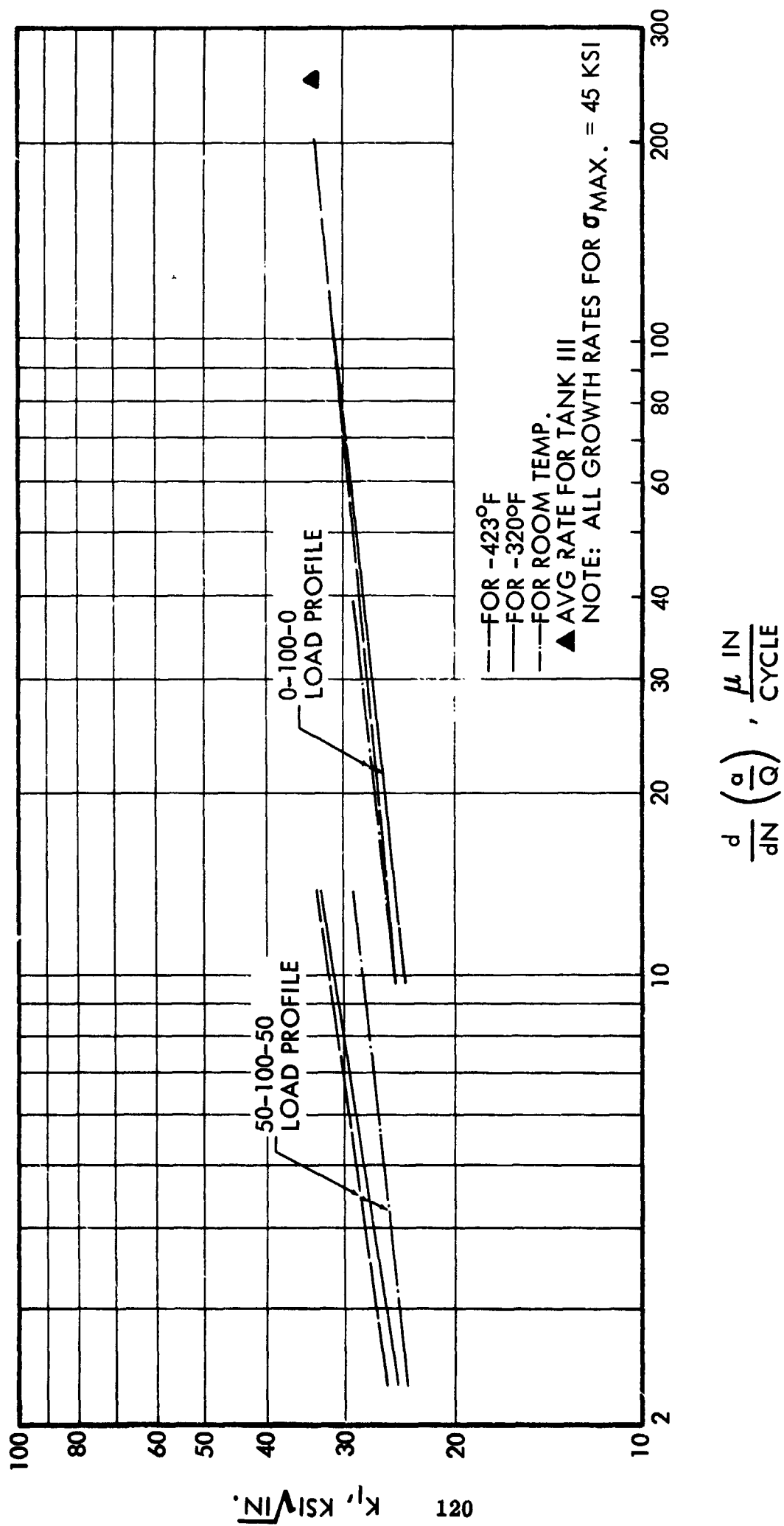
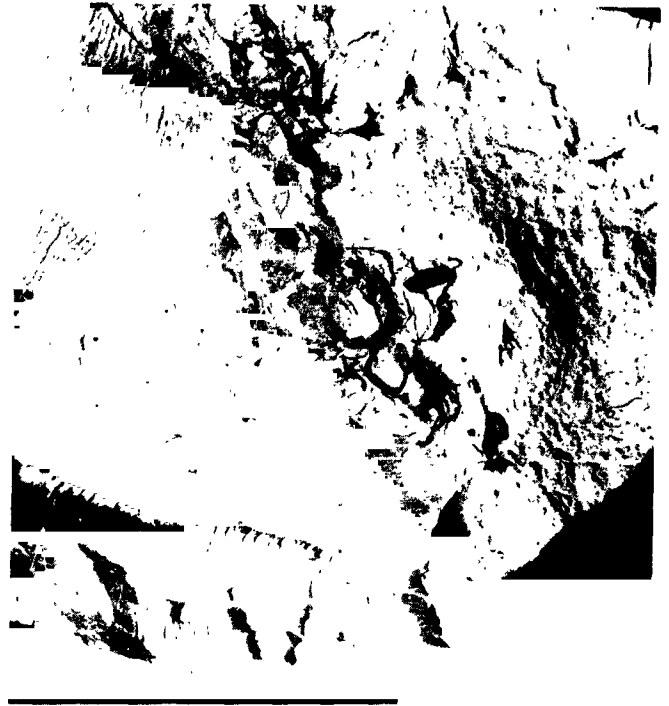


Figure 62: FLAW GROWTH RATES COMPUTED FROM END POINT ANALYSES FOR 2219-T87 ALUMINUM



ROOM TEMPERATURE



-320°F



-423°F

Figure 63:
FRACTOGRAPHS OF STRIATED REGIONS 2219-T87 ALUMINUM

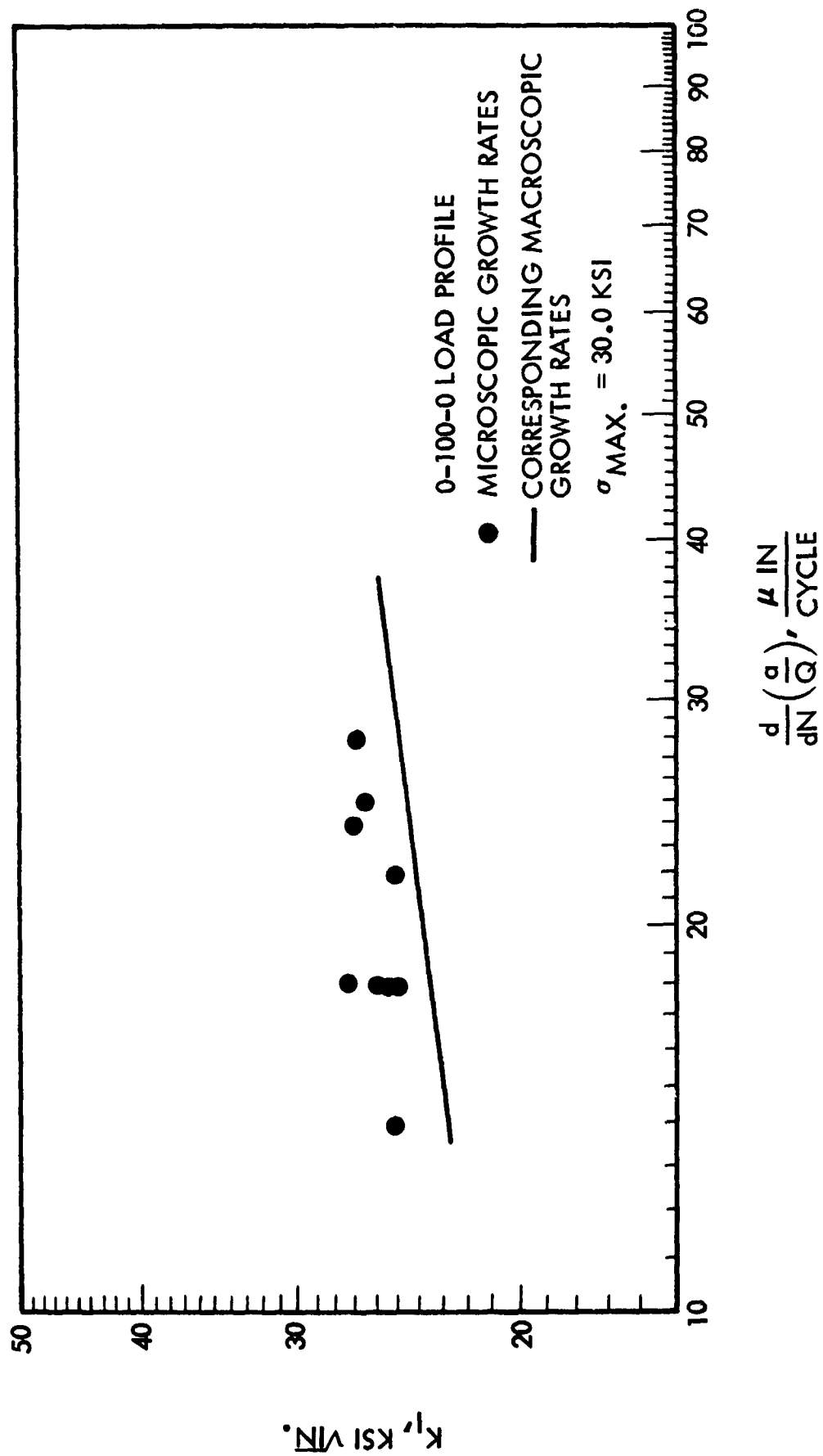


Figure 64: MICROSCOPIC FLAW GROWTH RATES FOR 2219-T87 ALUMINUM AT ROOM TEMP.

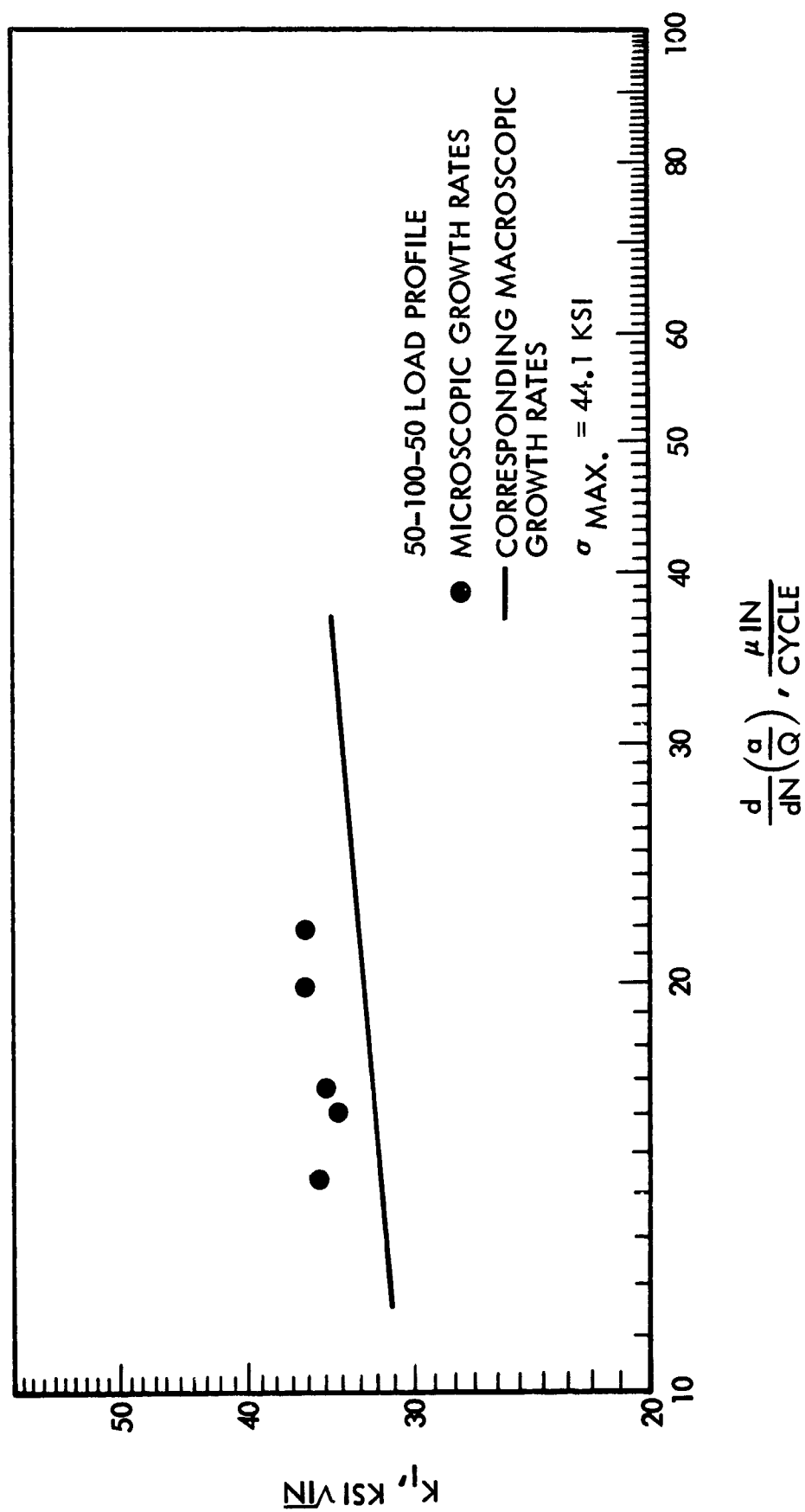


Figure 65: MICROSCOPIC FLAW GROWTH RATES FOR 2219-T87 ALUMINUM AT -320°F

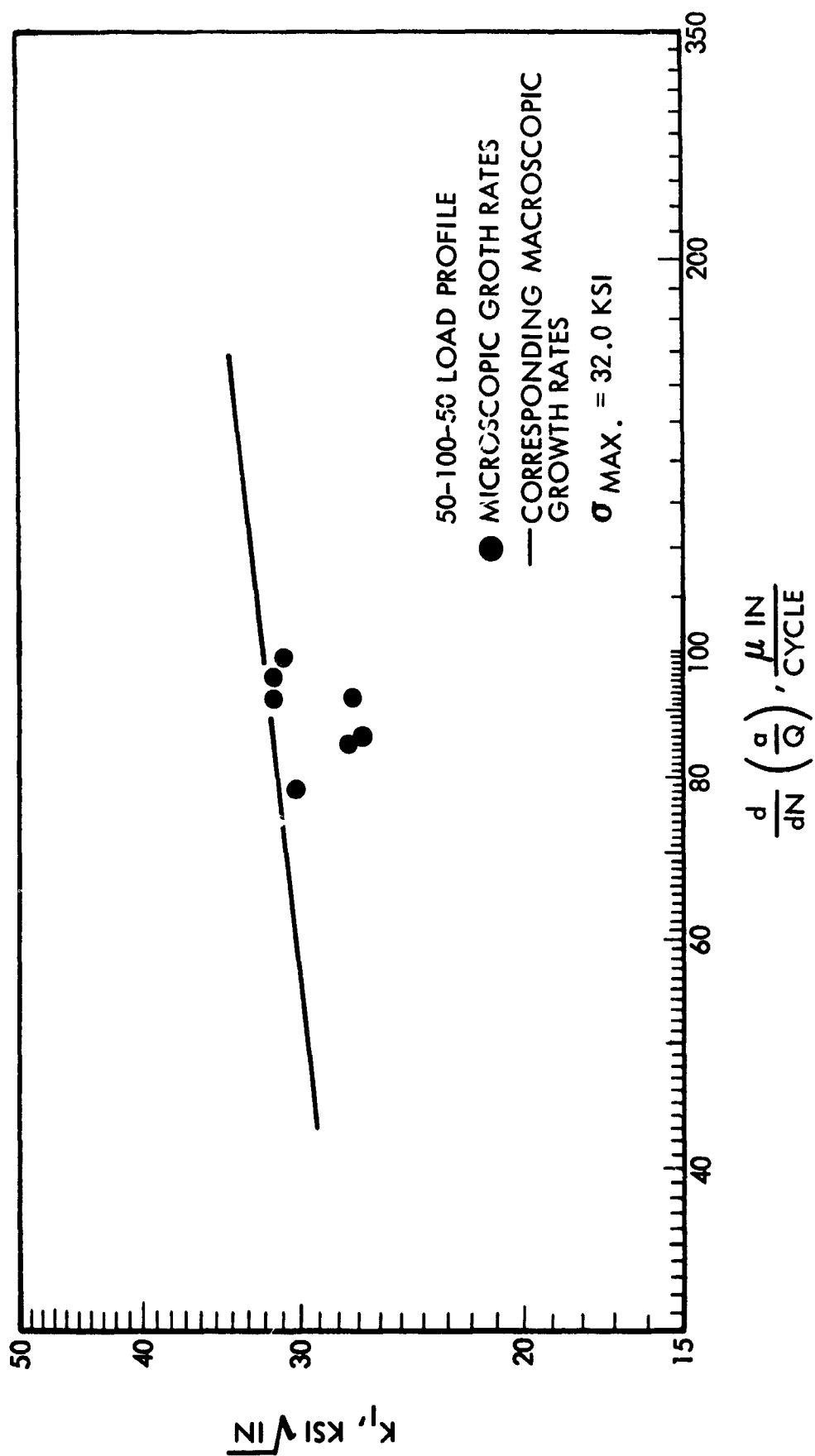


Figure 66: MICROSCOPIC FLAW GROWTH RATES FOR
2219-T87 ALUMINUM AT -423°F



2219-T87 AL TANK
TESTED AT ROOM TEMP.
HOOP STRESS: 44.3 KSI
CYCLES TO FAILURE: 561

TANK V



2219-T87 AL TANK
TESTED AT -320°F
HOOP STRESS: 51.7 KSI
CYCLES TO FAILURE: 93

TANK VI

Figure 67: PHOTOGRAPHS OF FRACTURED 2219-T87 TANKS

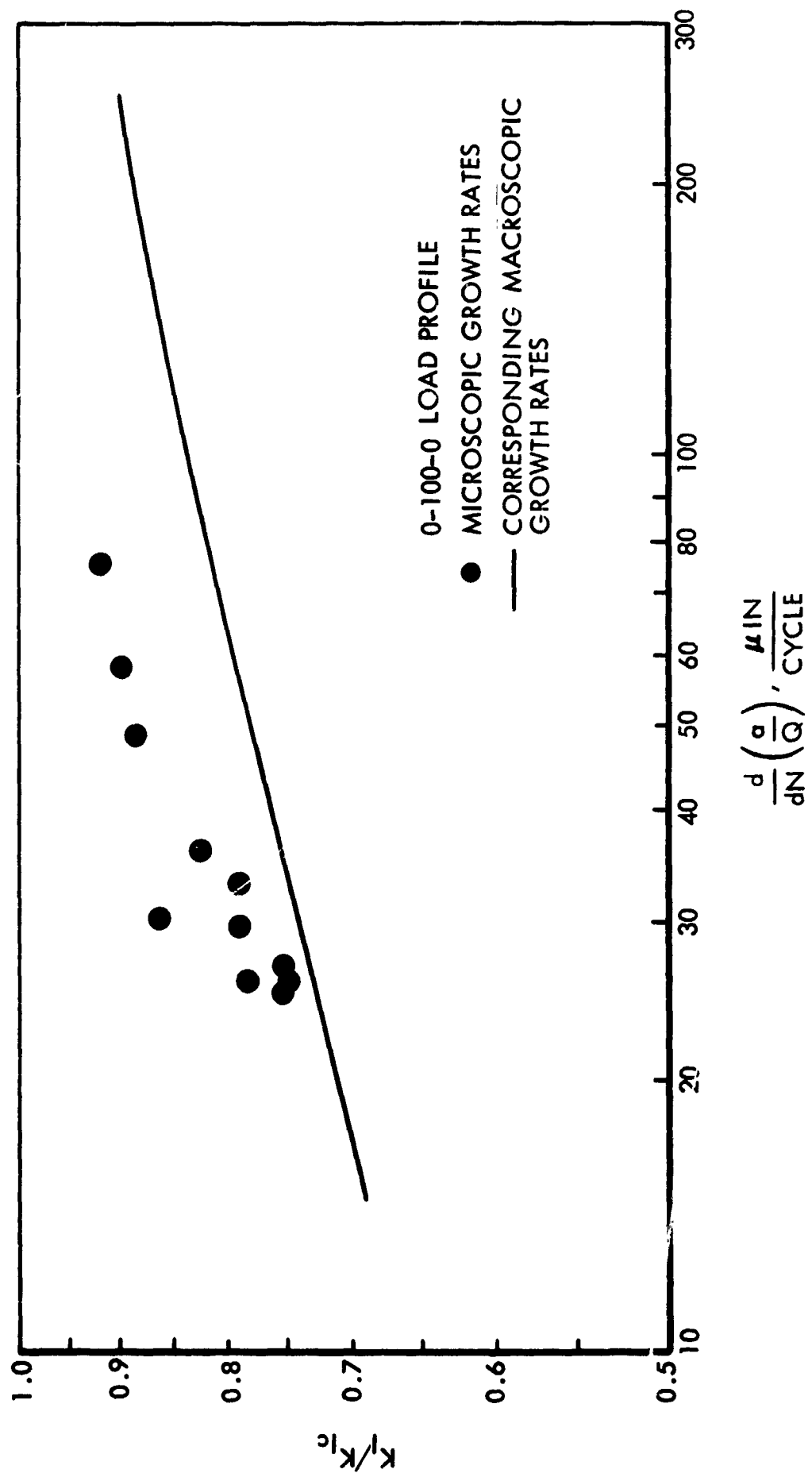


Figure 68: MICROSCOPIC FLAW GROWTH RATES FOR 2219-T87 ALUMINUM TANK II AT -320°F

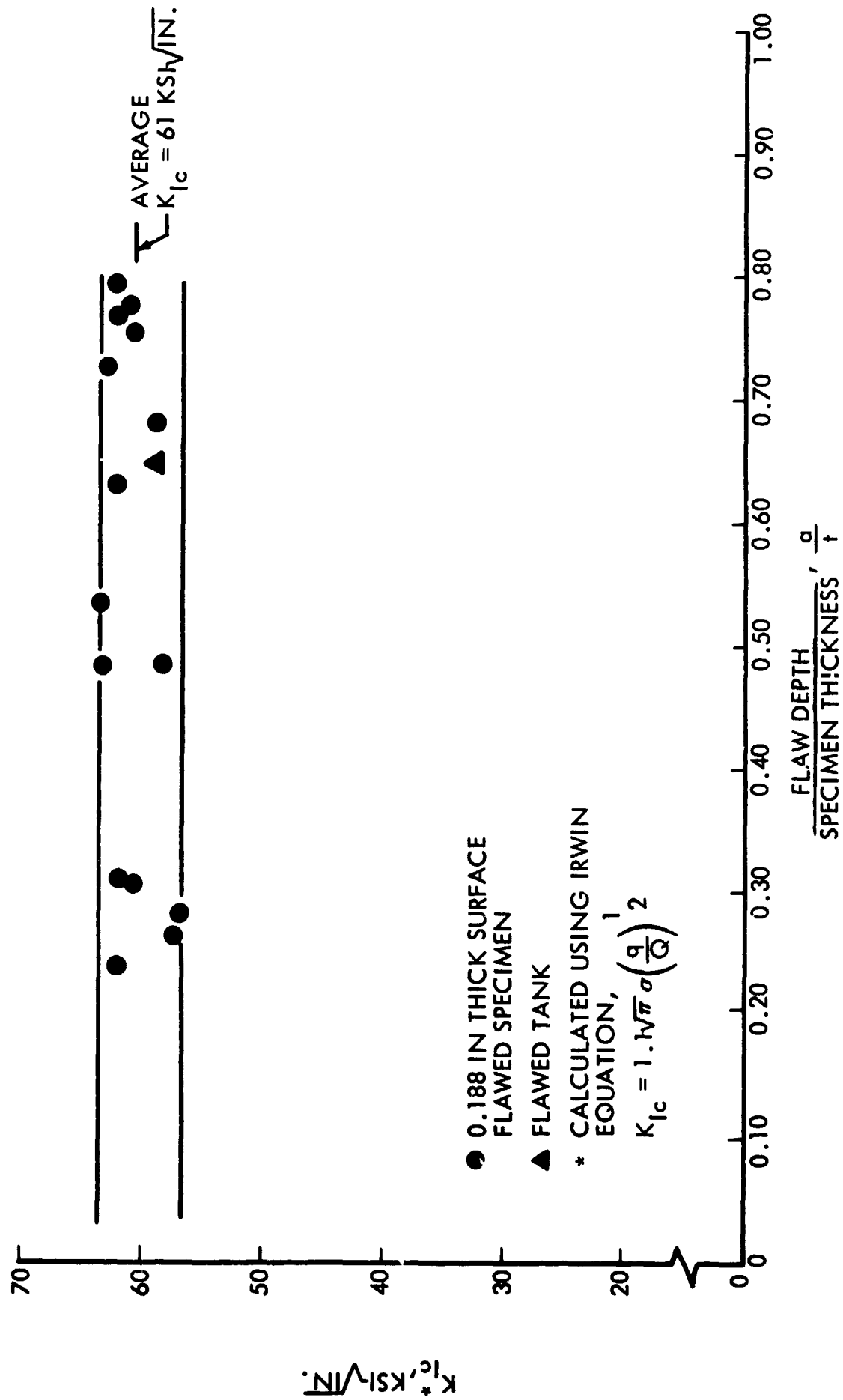


Figure 69: EFFECT OF RELATIVE FLAW DEPTH ON CALCULATED K_{Ic} VALUES FOR 5A1 -2.5 Sn (ELI) TITANIUM AT -320°F

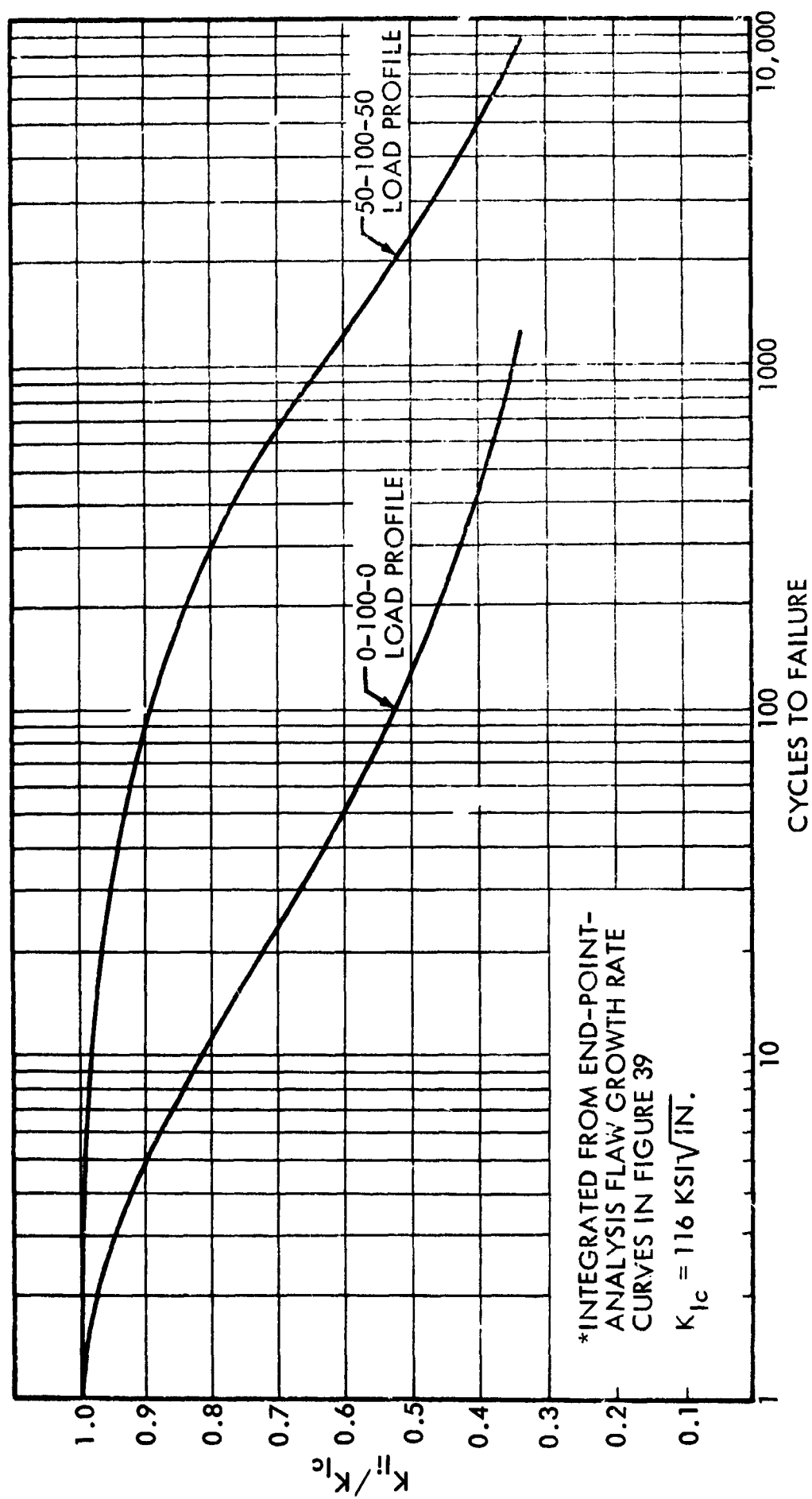


Figure 70: ESTIMATED* CYCLIC LIFE CURVES FOR 5Al -2.5 Sn (ELI) TITANIUM AT ROOM TEMPERATURE

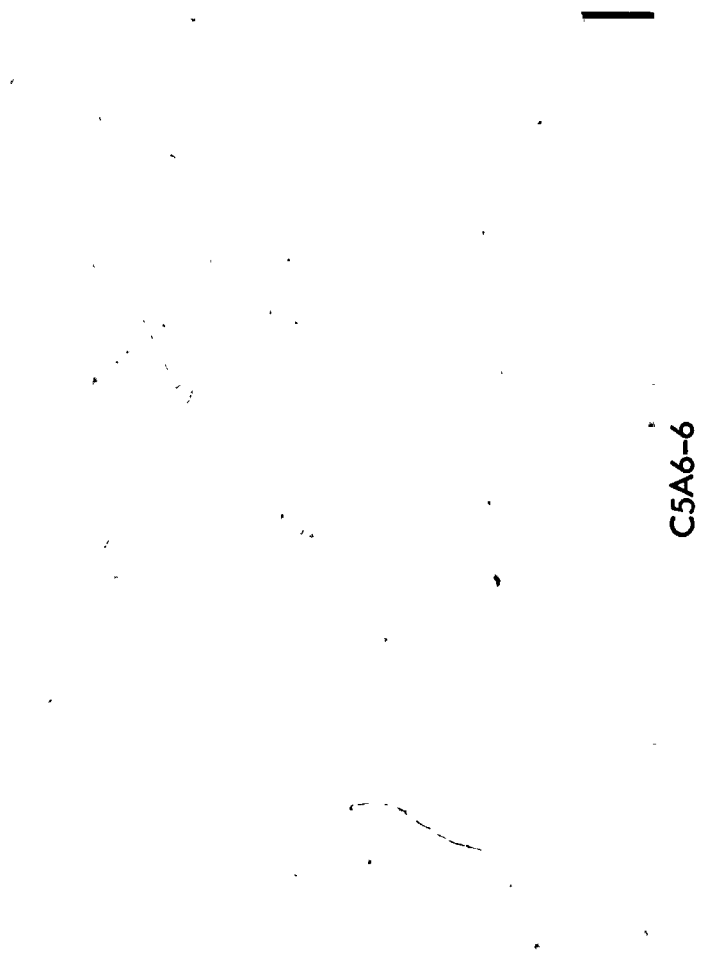


Figure 71: FRACTURE SURFACE WITH VISIBLE DELAMINATION IN 2219-T87 ALUMINUM

FLAW GROWTH NOT SIGNIFICANTLY
AFFECTED BY LAMINATIONS



COA12-1

FLAW GROWTH THAT IS SIGNIFICANTLY
AFFECTED BY LAMINATIONS



COA6-2

Figure 72: EFFECT OF LAMINATIONS ON FLAW GROWTH IN 2219-T87 ALUMINUM

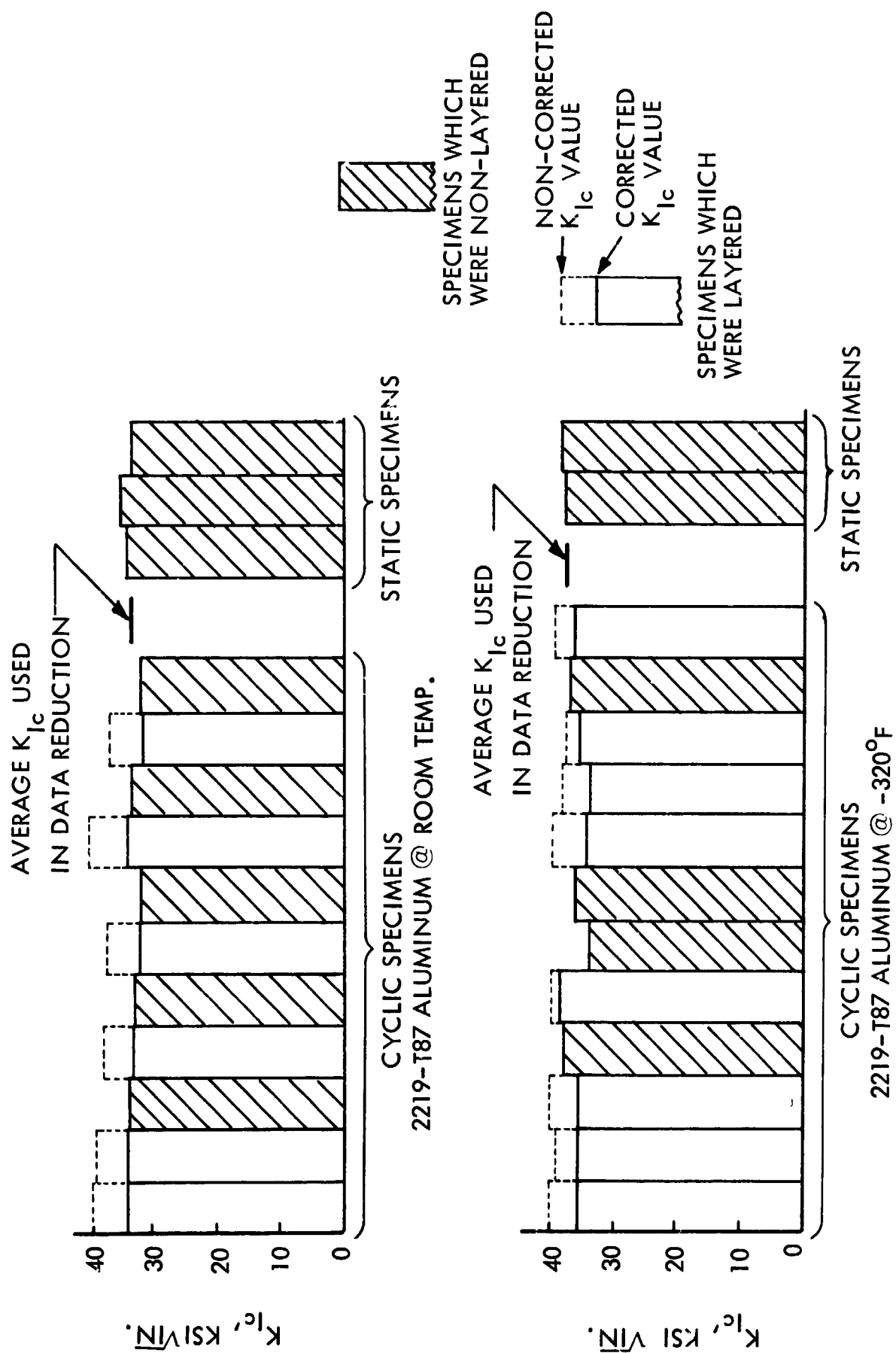


Figure 73: COMPARISONS OF K_{Ic} VALUES IN LAYERED & NONLAYERED 2219-T87 ALUMINUM

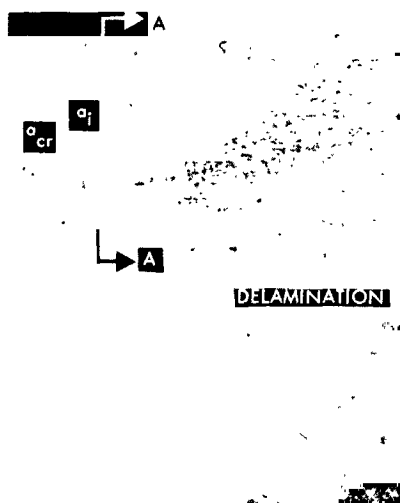


Figure 74b:
FRACTURE FACE

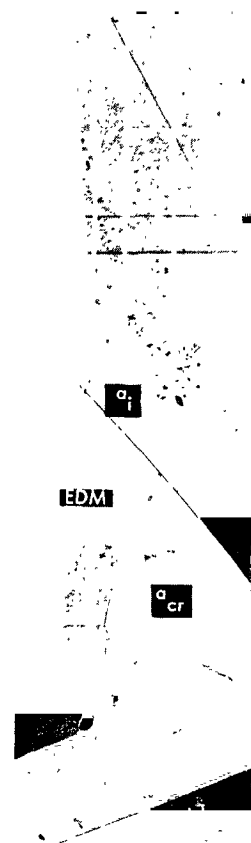


Figure 74a:
ENLARGED VIEW
OF SECTION A - A

Figure 74: FAILURE ORIGIN OF 2219-T87 ALUMINUM TANK NO. III
(CYCLIC TESTED @ -423°F)

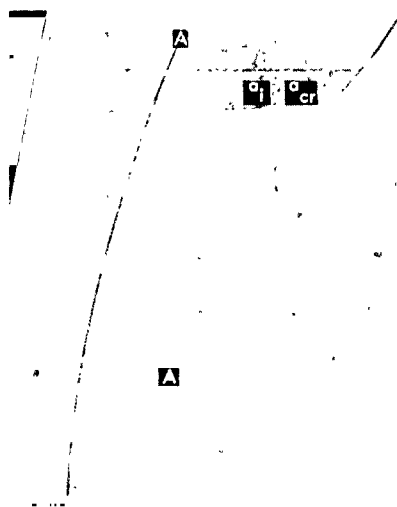


Figure 75b:
FRACTURE FACE

6.3X



Figure 75a:
ENLARGED VIEW
OF SECTION A-A

25X

Figure 75: FAILURE ORIGIN OF 2219-T87 ALUMINUM TANK NO. IV
(CYCLIC TESTED @ -423°F)

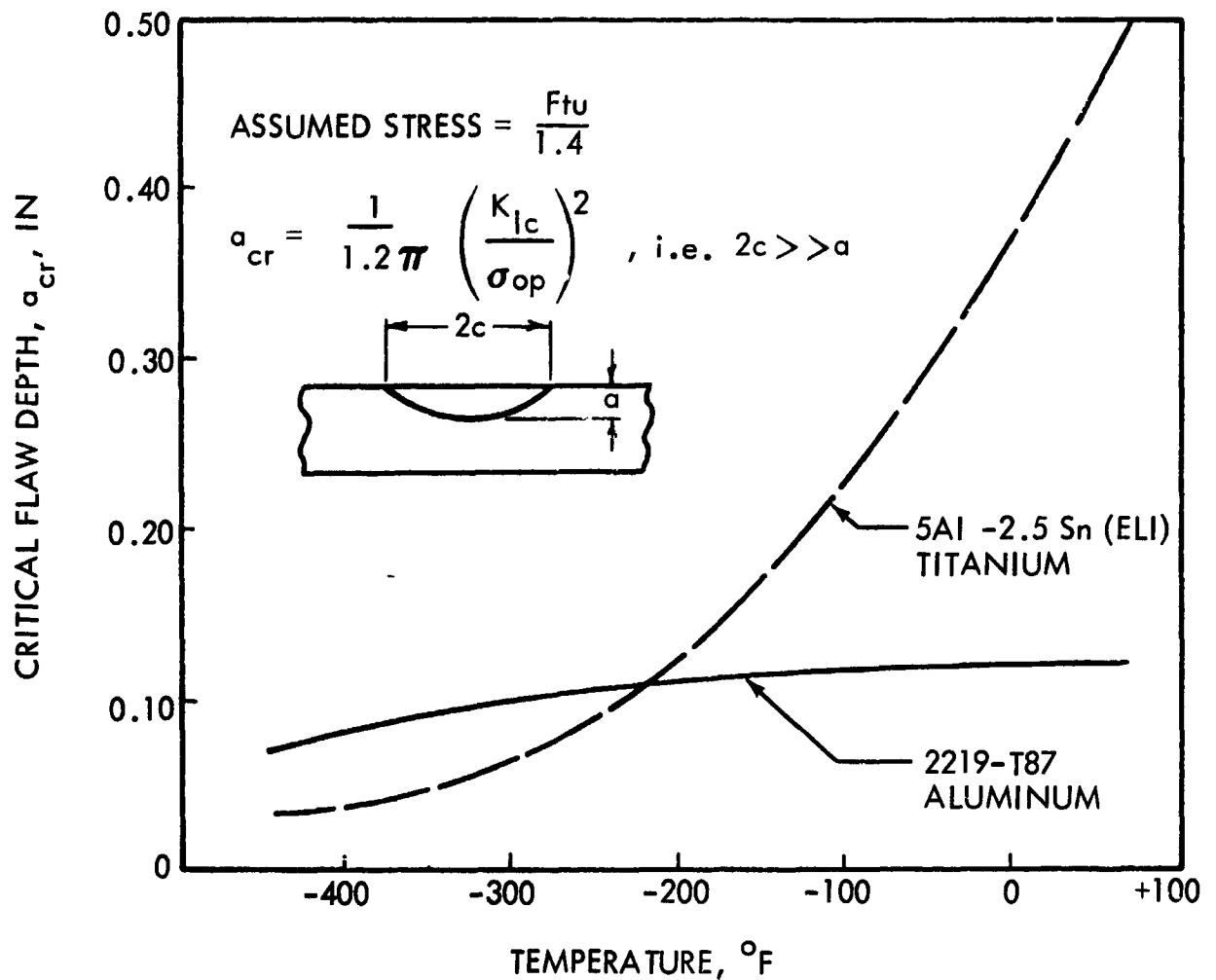


Figure 76: CRITICAL FLAW SIZES AT OPERATING STRESS FOR 5Al -2.5 Sn (ELI) TITANIUM AND 2219-T87 ALUMINUM VS TEMPERATURE

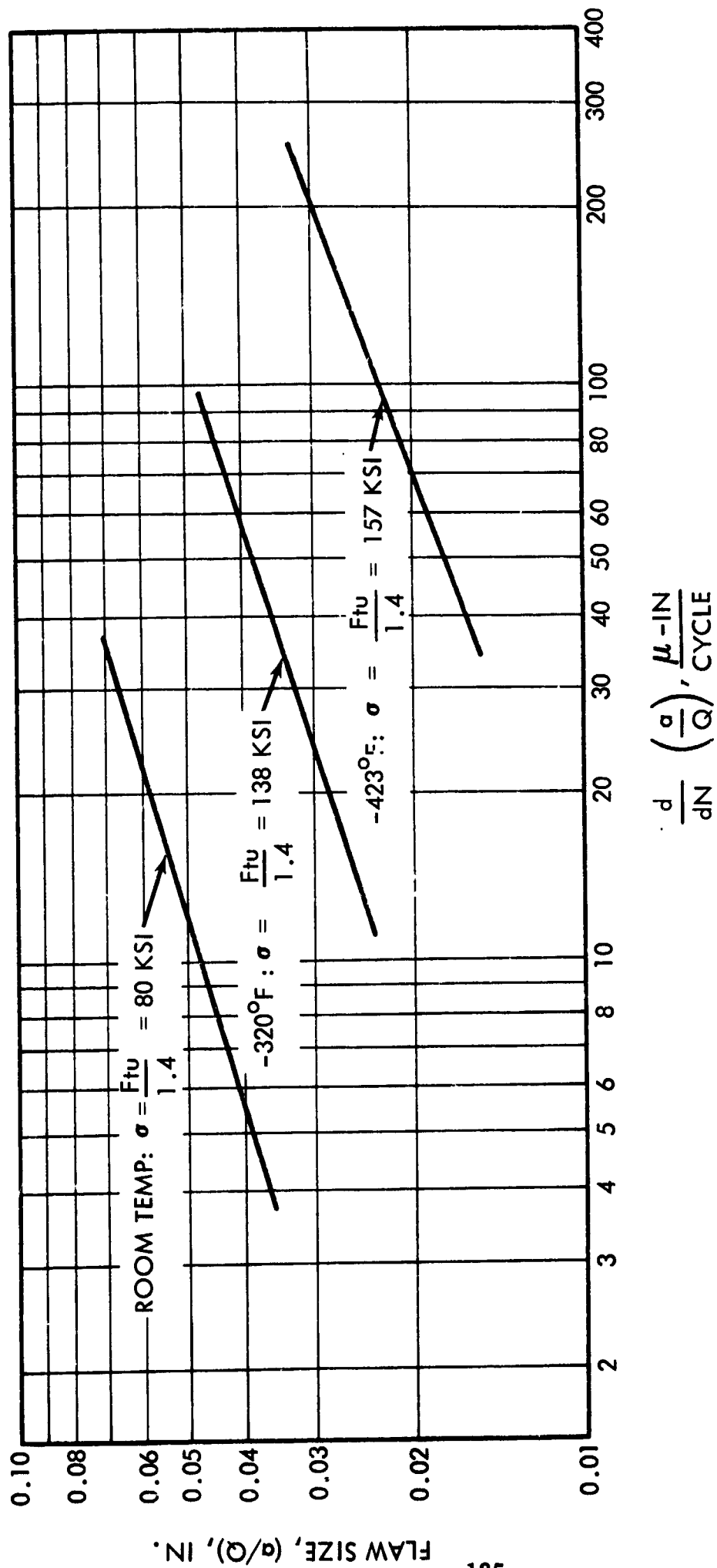


Figure 77: FLAW GROWTH RATES AT OPERATING STRESS VS FLAW SIZE FOR 5A1 -2.5 Sn (ELI) TITANIUM (0-100-0 LOAD PROFILE)

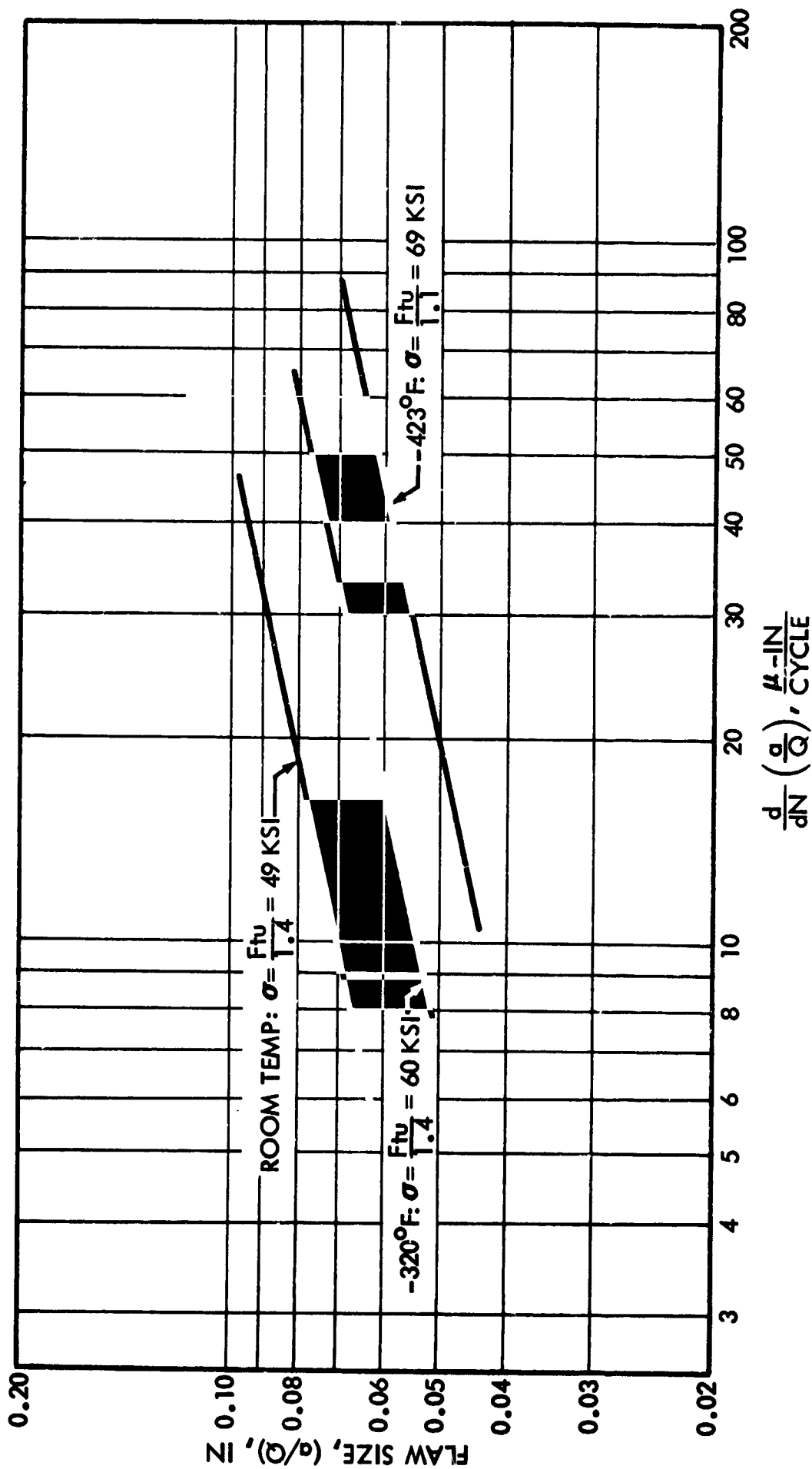


Figure 78: FLAW GROWTH RATES AT OPERATING STRESS VS. FLAW SIZE
FOR 2219-T87 ALUMINUM (0-100-0 LOAD PROFILE)

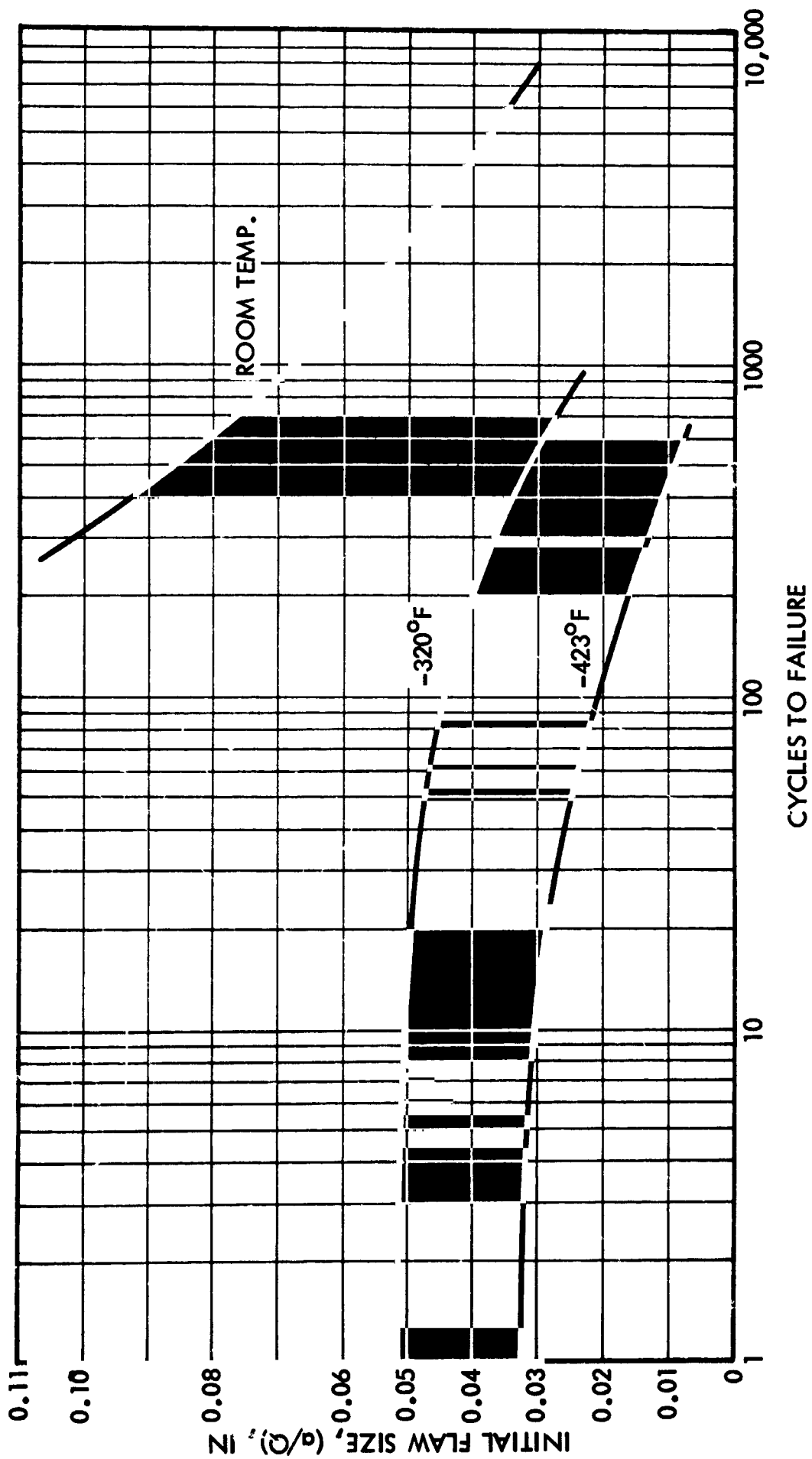


Figure 79: CYCLES TO FAILURE AT OPERATING STRESS VS INITIAL FLAW SIZE FOR 5Al -2.5 Sn (ELI) TITANIUM (0-100-0 LOAD PROFILE)

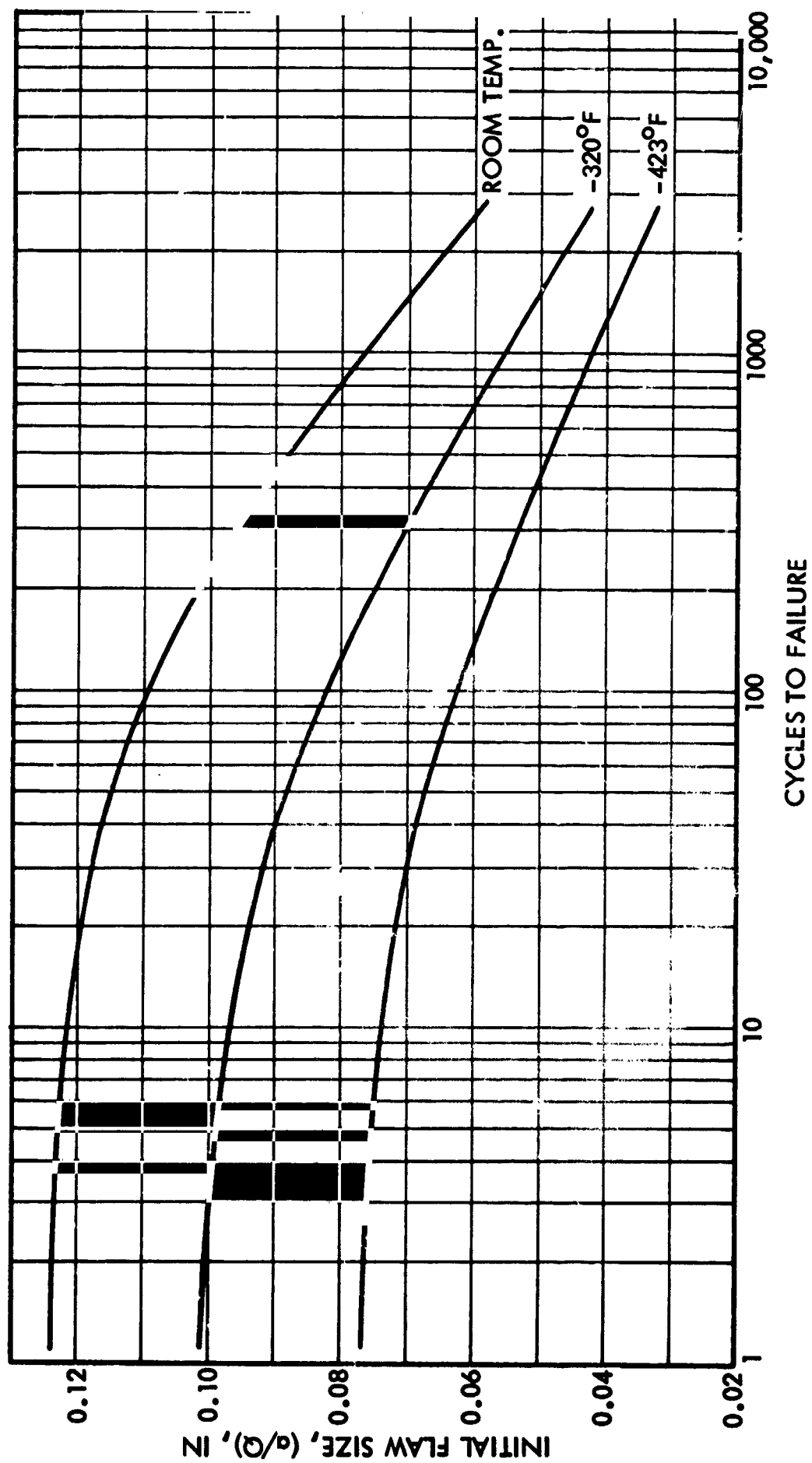


Figure 80: CYCLES TO FAILURE AT OPERATING STRESS VS. INITIAL FLAW SIZE FOR 2219-T87 ALUMINUM (0-100-0 LOAD PROFILE)

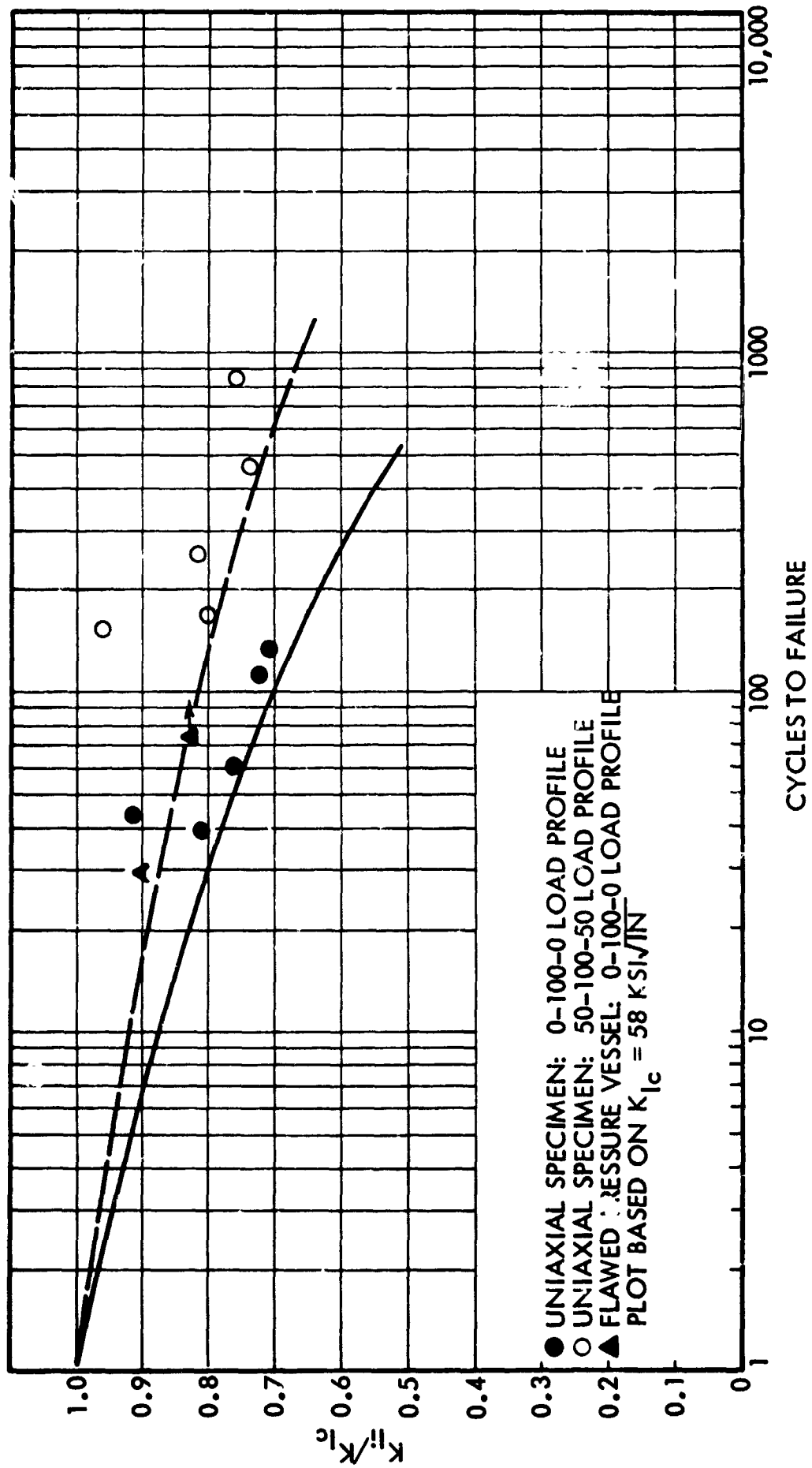


Figure A1: LOWER BOUND STRESS INTENSITY —CYCLIC LIFE CURVES AT -423°F FOR ILLUSTRATIVE DESIGN OF TITANIUM TANK

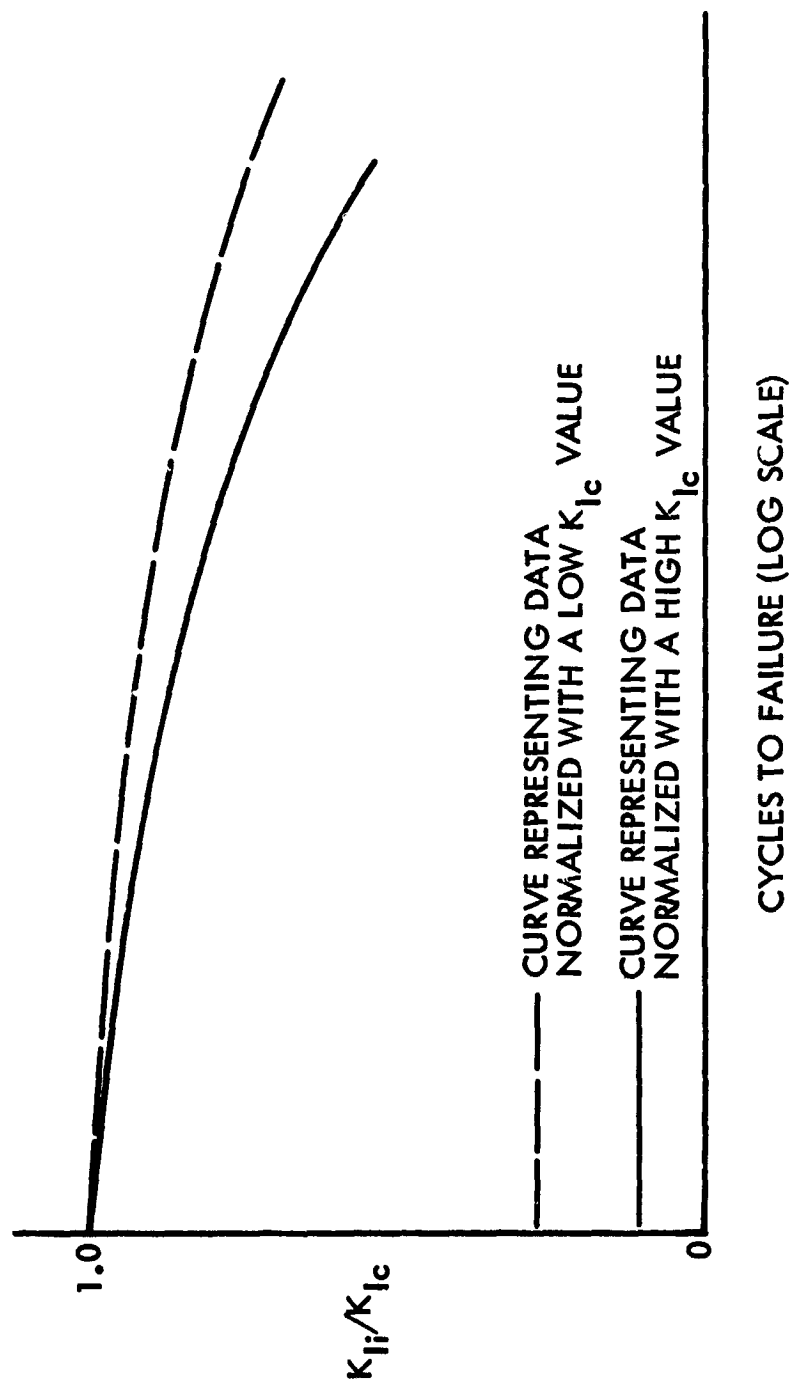


Figure A2: SCHEMATIC REPRESENTATION OF THE EFFECT OF K_{Ic} ON NORMALIZED CYCLIC-LIFE CURVES

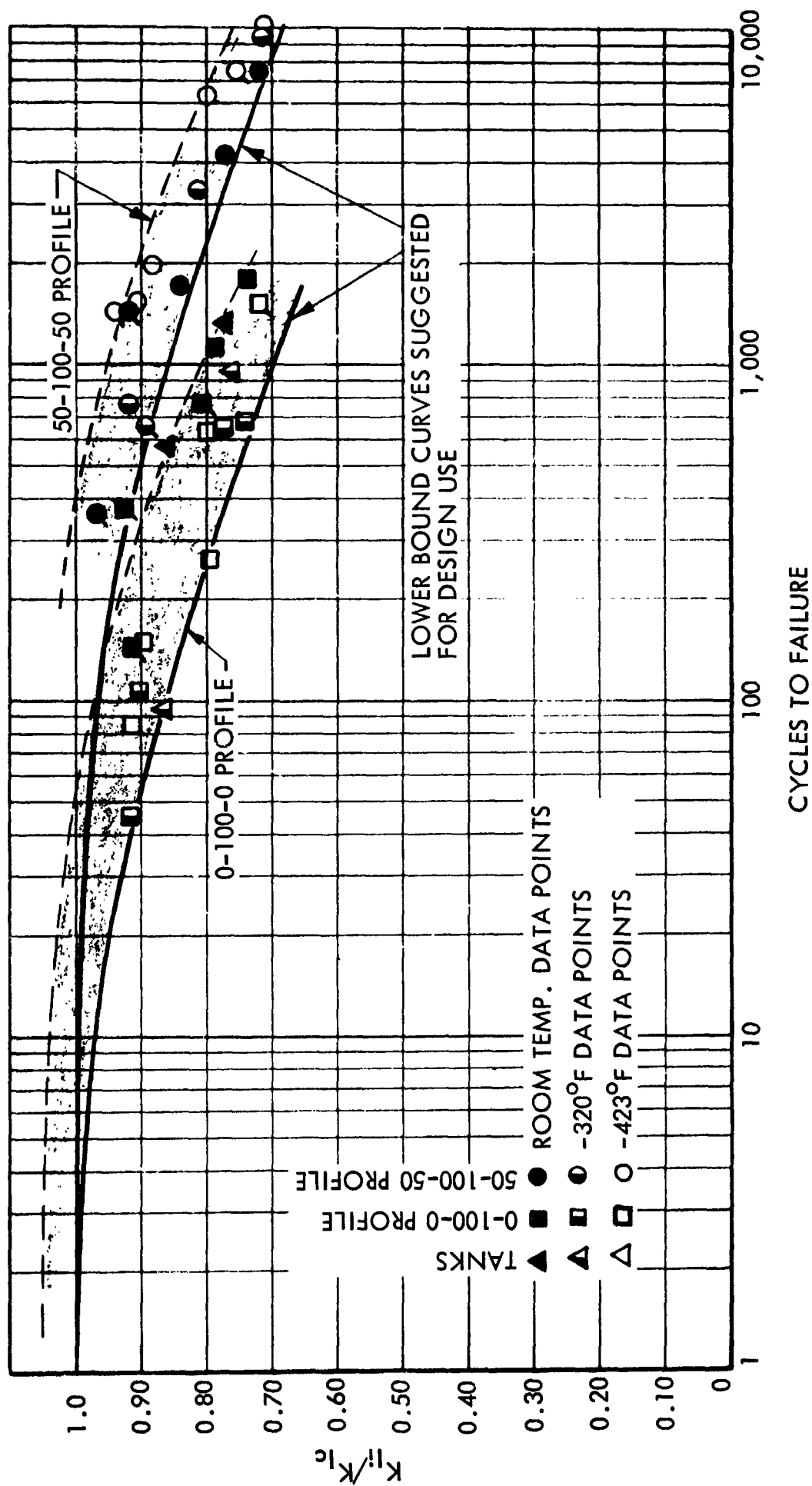


Figure A3: COMPOSITE CYCLIC FLAW GROWTH DATA
2219-T87 ALUMINUM @ ROOM TEMPERATURE,
-320°F & -423°F

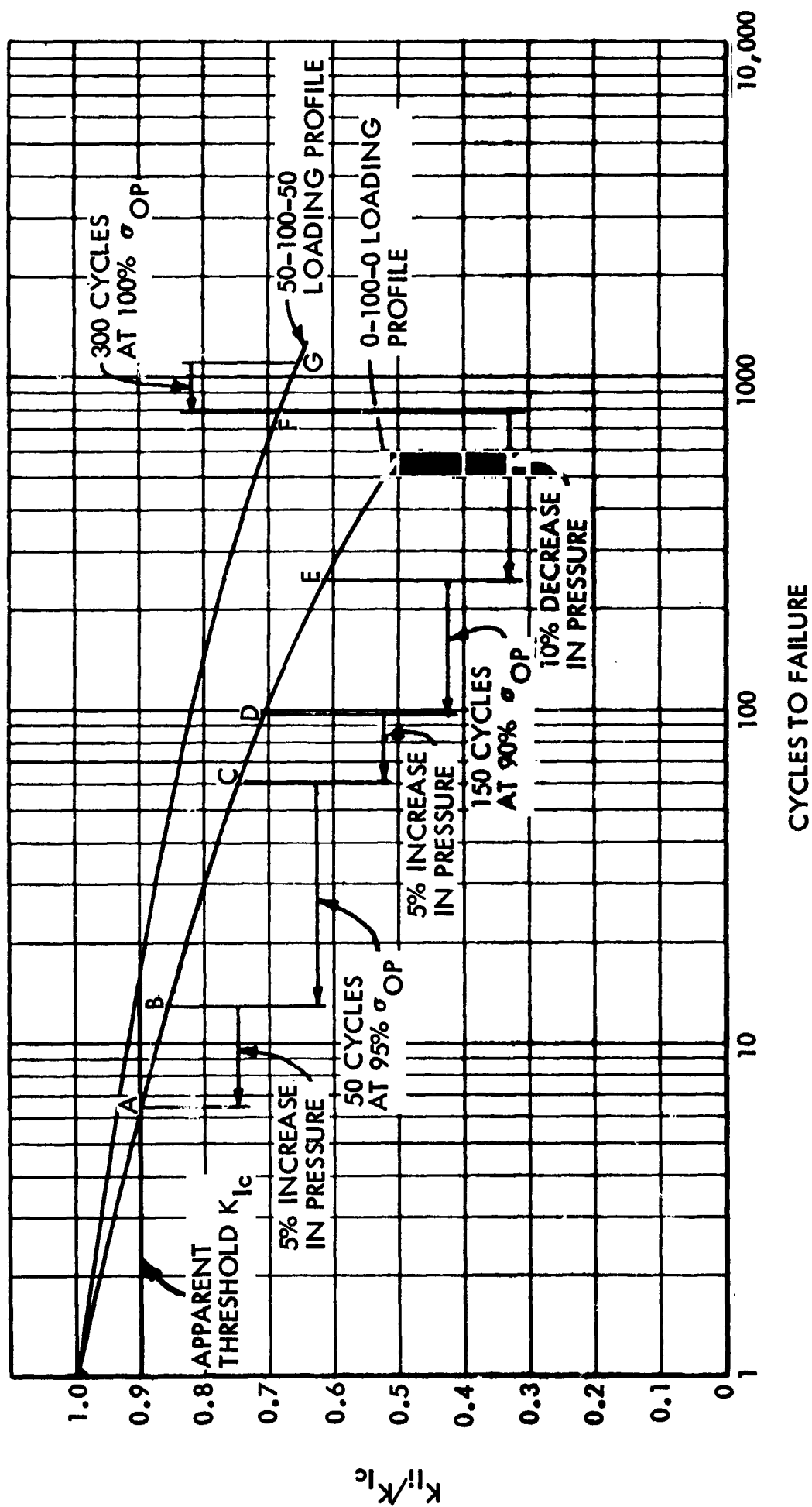


Figure A4: ILLUSTRATIVE DESIGN OF 5Al-2.5Sn (ELI) TITANIUM TANK

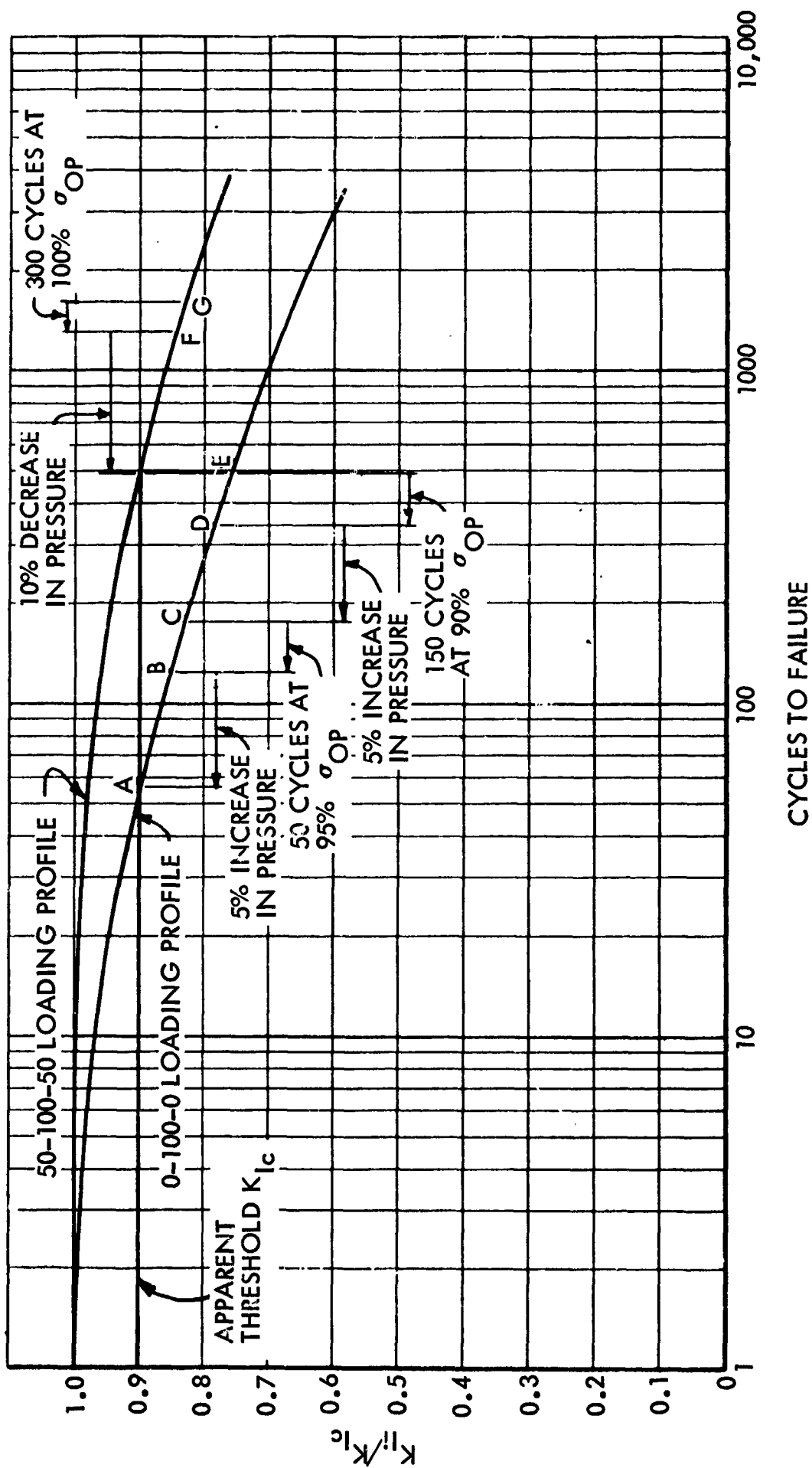


Figure A5: ILLUSTRATIVE DESIGN OF 2219-T87 ALUMINUM TANK

BLANK PAGE

Table I: CHEMICAL COMPOSITION OF THE MATERIALS USED
TO FABRICATE SPECIMENS AND TANKS

Material	Chemical Composition (% By Weight)											
	C	Mn	Si	Al	V	Zr	Sn	Cu	Mg	Zn	Ti	Fe
2219 Aluminum Plate 1.25 Inches Thick	--	.20-.40	.20 Max	Bal.	.05-.15	.10-.25	--	5.8-6.8	.02 Max	.10 Max	.10-.20	.30 Max
2319 Weld Wire, .062 Dia	--	.20-.40	.20 Max	Bal.	.05-.15	.10-.25	--	5.8-6.8	.02 Max	.10 Max	.10-.20	.30 Max
5 Al-2.5Sn (ELI) Titanium. .188 in. Thick Plate Ht. No. D-5907 N ₂ = .016 O ₂ = .07 H ₂ = .005	.025	.002	--	5.2	--	.007	2.5	--	--	--	Bal.	.16
5 Al-2.5Sn (ELI) Titanium Weld Wire, .062 Dia Ht. No. 2936 N ₂ = .007 O ₂ = .063 H ₂ =.0028	--	--	--	5.16	--	--	2.59	--	--	--	Bal.	.09

Table II: WELD SETTINGS USED FOR FABRICATION OF
ALUMINUM AND TITANIUM TANKS

Designation	Plate Thickness	Edge Configuration	Weld Position	Filler Wire		Filler Wire Feed (in./min.)	Inert Gas			Voltage (volts)	Current (amps)	Travel Speed (in./min.)
				Type	Dia (in.)		Torch	Trailing Cup	Back-Up			
<u>2219-T87 Aluminum</u>												
Long. Shell Weld 1st Pass	1.25	90°B-V	V	--	--	--	He	--	--	12-13	470	2.4
2nd Pass	1.25	90°B-V	V	--	--	--	He	--	--	12-13	450	2.4
Filler Pass	1.25	V	V	2319	.062	50	He	--	--	15-16	225	4.0
Shell to Head Weld												
Fusion Pass	1.00	J	D	--	--	--	He	--	--	13	210	7.0
1st Pass	1.00	J	3 o'clock	--	--	--	He	--	--	12.5	280	3.75
2nd Pass	1.00	J	D	2319	.062	50	He	--	--	14	240	10.0
Filler Pass	1.00	J	D	2319	.062	50-100	He	--	--	14	240	10.0
<u>5Al-2.5Sn (ELD) Titanium</u>												
Long. Shell Weld 1st Pass	0.20	90°B	D	--	--	--	He	He	He	9-10	225	9.0
2nd Pass	0.20	90 B	D	5Al-2.5Sn	.062	30	A ₂	A ₂	A ₂	9-10	225	9.0
Shell to Head Weld												
1st Pass	0.20	90°B	D	--	--	--	He	He	He	9-10	235	9.0
2nd Pass	0.20	90°B	D	5Al-2.5Sn	.062	30	A ₂	A ₂	A ₂	11	225	9.0

V = Vertical

D = Downhand

Table III: MECHANICAL PROPERTIES OF 5 Al-2.5Sn (ELI) TITANIUM PLATE
0.188-INCH THICK, AT R. T., -320°F, AND -423°F TEST TEMPERATURES

Specimen Identification	Test Temperature (°F)	Grain Orientation	Specimen Size		Ultimate Strength (ksi)	Yield Strength (ksi)		Elongation (% in. Gage Length Shown)	
			Gage Thickness (in.)	Area (in. ²)		Offset 0.2%	Offset 0.02%	1-inch Gage Length	2-inch Gage Length
TT-1	R. T.	L	.2009	.1005	118.8	111.6	110.0	26.0	17.0
TT-2	R. T.	L	.1962	.0983	114.0	109.8	108.7	25.0	16.5
TT-3	-320	L	.1942	.0973	191.3	180.4	176.5	19.0	15.0
TT-4	-320	L	.1951	.0977	191.6	180.1	175.9	19.0	14.0
T-5	-423	L	.1945	.0973	212.7	212.7	--	10.0	6.0
T-6	-423	L	.1950	.0973	220.9	214.7	--	9.0	4.0

Table IV: MECHANICAL PROPERTIES OF 2219-T87 ALUMINUM PLATE
1.25 INCHES THICK, AT R. T., -320°F AND -423°F TEST TEMPERATURE

Specimen Identification	Test Temperature (°F)	Grain Orientation	Specimen Size		Ultimate Strength (ksi)	Yield Strength (ksi)		Elongation (% in Gage Length Shown)	
			Dia (in.)	Area (in. ²)		Offset 0.2%	Offset 0.02%	1-inch Gage Length	2-inch Gage Length
TA-1	R. T.	T	.4995	.1960	69.4	56.2	43.5	15	10.5
TA-2	R. T.	T	.4991	.1956	69.6	56.8	46.7	15	10.0
TA-3	-320	T	.4997	.1961	85.9	67.7	57.1	12	10.5
TA-4	-320	T	.4992	.1957	85.7	67.8	57.9	13	10.0
TA-5	-423	T	.5030	.1987	99.0	69.4	51.1	17	13
AT-1	-423	T	.4994	.1963	103.1	76.9	70.4	15	12

Table V: STATIC FRACTURE TOUGHNESS TEST RESULTS — 5Al-2.5Sn (ELI) TITANIUM

Specimen Identification	Specimen Size (in.)		Test Temperature (°F)	Flaw Size (in.)			Fracture Stress (ksi)	$K_{Ic} \sim \text{ksi} \sqrt{\text{in.}}$	$K_{Ic} \sim \text{ksi} \sqrt{\text{in.}}$	Remarks
	Thickness (t)	Width (w)		Flaw Depth (a)	Flaw Length (2c)	Flaw Size (a/q)				
C-1*	.204	13.88	R. T.	---	4.91	---	39.5**	116.1		* Through-the-thickness cracked specimen
C-2*	.202	13.88	R. T.	---	4.55	---	68.7	192.5		** Stress at "pop-in"
ST-1	.171	1.516	-320	.041	.168	.033	175.0		***	*** Valid fracture toughness not obtained
ST-2	.185	1.500	-320	.090	.334	.063	117.5		57.7	
CT5-5	.188	1.502	-320	.102	.418	.074	100.9		***	
CT5-6	.183	1.501	-320	.138	.599	.101	73.5		***	
ST-4	.184	1.502	-423	.081	.330	.058	96.7		45.4	
ST-5	.193	1.515	-423	.042	.188	.033	161.4		57.4	

Table VI: CYCLIC FLAW GROWTH DATA FOR 5Al-2.5Sn (ELI) TITANIUM,
0-100-0 LOAD PROFILE AT ROOM TEMPERATURE

Specimen Identification	Specimen Size		Cyclic Gross Stress		Initial Flaw Size			K_{II} , ksi $\sqrt{\text{in.}}$	K_{IC}^\dagger , ksi $\sqrt{\text{in.}}$	$K_{II}/(K_{IC})_{\text{avg.}}^{**}$ Ratio	Cycles to Failure
	Thickness (in.)	Width (in.)	Maximum (ksi)	Minimum (ksi)	Flaw Depth (a) _i (in.)	Flaw Length* (2c) _i (in.)	Flaw Shape Parameter (Q) _i				
CTO-1	.177	1.500	88.0	0	.061	.221	1.410	35.5	---	.306	1,489
CTO-2	.186	1.497	88.0	0	.086	.315	1.396	42.4	---	.365	423
CTO-3	.192	1.497	88.0	0	.104	.399	1.364	47.4	---	.408	152
CTO-4	.180	1.499	74.0	0	.096	.424	1.302	39.2	---	.338	775
CTO-5	.197	1.501	63.0	0	.078	.312	1.398	29.1	---	.251	1,709
CTO-6	.183	1.502	63.0	0	.137	.562	1.377	38.7	---	.348	313

* Calculated

** $K_{IC} = 116.0$

† No valid K_{IC} 's obtained

Table VII: CYCLIC FLAW GROWTH DATA FOR 5Al-2.5Sn (ELI) TITANIUM,
50-100-50 LOAD PROFILE AT ROOM TEMPERATURE

Specimen Identification	Specimen Size		Cyclic Gross Stress		Initial Flaw Size			K_{II} , ksi $\sqrt{\text{in.}}$	K_{IC}^{\dagger} , ksi $\sqrt{\text{in.}}$	$K_{II}/(K_{IC})_{\text{avr.}}^{**}$ Ratio	Cycles to Failure
	Thickness (in.)	Width (in.)	Maximum (ksi)	Minimum (ksi)	Flaw Depth (a) _i (in.)	Flaw Length* (2c) _i (in.)	Flaw Shape Parameter ((c) _i)				
CT5-1	.192	1.501	88.0	44.0	.054	.216	1.337	34.7	---	.299	9,655
CT5-2	.191	1.513	88.0	44.0	.092	.335	1.410	43.8	---	.377	2,244
CT5-3	.188	1.500	88.0	44.0	.106	.398	1.379	47.5	---	.409	896

* Calculated

** $K_{IC} = 116.0$

† No valid K_{IC} obtained

Table VIII: CYCLIC FLAW GROWTH DATA FOR 5Al-2.5Sn (ELI) TITANIUM,
0-100-0 LOAD PROFILE AT -320°F

Specimen Identification	Specimen Size		Cyclic Gross Stress		Initial Flaw Size			Critical Flaw Size			K_{II} , ksi $\sqrt{\text{in.}}$	K_{IC} , ksi $\sqrt{\text{in.}}$	$K_{II}/(K_{IC})_{\text{avg.}}^{**}$ Ratio	Cycles to Failure
	Thickness (in.)	Width (in.)	Maximum (ksi)	Minimum (ksi)	Flaw Depth (a) _I (in.)	Flaw Length* (2c) _I (in.)	Flaw Shape Parameter (Q) _I	Flaw Depth (a) _{cr} (in.)	Flaw Length* (2c) _{cr} (in.)	Flaw Shape Parameter (Q) _{cr}				
CTO-7	.180	1.501	175.0	0	.033	.127	1.294	.052	.122	1.924	54.9	---	0.90	32
CTO-8	.178	1.501	158.3	0	.042	.158	1.348	.086	.191	2.024	54.3	63.3	0.89	147
CTO-9	.170	1.515	138.9	0	.045	.167	1.399	.107	.252	1.993	48.4	62.7	0.79	313
CTO-10	.190	1.499	117.5	0	.046	.169	1.443	.147	.342	2.049	41.0	61.3	0.67	972
CTO-11	.188	1.497	117.5	0	.068	.215	1.595	.145	.356	1.950	47.4	62.2	0.78	341
CTO-12	.186	1.500	117.5	0	.070	.256	1.446	.127	.313	1.946	50.2	58.5	0.82	179
CTO-19	.188	1.499	175.0	0	.029	.119	1.246	.050	.127	1.786	51.9	---	0.85	56

* Calculated

** $(K_{IC})_{\text{avg.}} = 61.0$

Table IX: CYCLIC FLAW GROWTH DATA FOR 5Al-2.5Sn (ELI) TITANIUM,
50-100-50 LOAD PROFILE AT -320°F

Specimen Identification	Specimen Size		Cyclic Gross Stress		Initial Flaw Size			Critical Flaw Size			K_{II} , ksi $\sqrt{\text{in.}}$	K_{Ic} , ksi $\sqrt{\text{in.}}$	$K_{II}/(K_{Ic})_{\text{avg.}}^{**}$ Ratio	Cycles to Failure
	Thickness (in.)	Width (in.)	Maximum (ksi)	Minimum (ksi)	Flaw Depth $(a)_I$ (in.)	Flaw Length* $(2c)_I$ (in.)	Flaw Shape Parameter $(Q)_I$	Flaw Depth $(a)_{cr}$ (in.)	Flaw Length* $(2c)_{cr}$ (in.)	Flaw Shape Parameter $(Q)_{cr}$				
CT5-7	.195	1.500	175.0	87.5	.036	.131	1.343	.061	.148	1.860	56.0	---	0.92	24
CT5-8	.201	1.497	158.3	79.2	.045	.173	1.331	.087	.209	1.911	56.8	66.0	0.93	794
CT5-9	.192	1.502	138.9	69.5	.042	.176	1.305	.103	.261	1.863	48.5	63.6	0.80	2,317
CT5-10	.184	1.502	117.5	58.8	.042	.170	1.365	.139	.353	1.896	40.3	61.9	0.66	3,954
CT5-11	.176	1.500	117.5	58.8	.052	.208	1.375	.139	.356	1.880	44.7	62.4	0.73	2,633
CT5-12	.191	1.498	117.5	58.8	.085	.274	1.574	.139	.375	1.805	53.1	63.5	0.87	1,492
CT5-19	.191	1.503	175.0	87.5	.026	.142	1.080	.058	.143	1.834	52.9	---	0.87	140

* Calculated
** $(K_{Ic})_{\text{avg.}} = 61.0$

Table X: CYCLIC FLAW GROWTH DATA FOR 5Al-2.5Sn (ELI) TITANIUM,
0-100-0 LOAD PROFILE AT -423°F

Specimen Identification	Specimen Size		Cyclic Gross Stress		Initial Flaw Size			K_{II} , ksi $\sqrt{\text{in.}}$	K_{IC} , ksi $\sqrt{\text{in.}}$	$K_{II}/(K_{IC})_{\text{avg.}}^{**}$ Ratio	Cycles to Failure
	Thickness (in.)	Width (in.)	Maximum (ksi)	Minimum (ksi)	Flaw Depth (a) _i (in.)	Flaw Length* (2c) _i (in.)	Flaw Shape Parameter (Q) _i				
CTO-13	.195	1.501	175.0	0	.032	.123	1.35	52.6	57.4		44
CTO-14	.193	1.499	158.3	0	.049	.180	1.41	57.4			1
CTO-15	.182	1.499	138.9	0	.043	.160	1.43	46.9			40
CTO-16	.189	1.501	117.5	0	.044	.185	1.36	41.2			138
CTO-17	.186	1.500	117.5	0	.055	.198	1.47	44.1			61
CTO-18-1	.195	1.499	100.0	0	.068	.265	1.45	42.1			115

* Calculated

Table XI: CYCLIC FLAW GROWTH DATA FOR 5Al-2.5Sn (ELI) TITANIUM,
50-100-50 LOAD PROFILE AT -423°F

Specimen Identification	Specimen Size		Cyclic Gross Stress		Initial Flaw Size			K_{II} , ksi $\sqrt{\text{in.}}$	K_{Ic} , ksi $\sqrt{\text{in.}}$	$K_{II}/(K_{Ic})_{\text{avg.}}^{**}$ Ratio	Cycles to Failure
	Thickness (in.)	Width (in.)	Maximum (ksi)	Minimum (ksi)	Flaw Depth (a) _i (in.)	Flaw Length* (2c) _i (in.)	Flaw Shape Parameter (Q) _i				
CT5-13	.188	1.499	175.0	87.5	.035	.140	1.32	55.6			159
CT5-15	.178	1.497	138.9	69.5	.041	.168	1.34	47.3			259
CT5-16	.182	1.500	117.5	58.8	.053	.205	1.42	44.0			852
CT5-17	.182	1.501	117.5	58.8	.059	.230	1.42	46.7			171
CT5-18	.186	1.499	116.1	58.8	.069	.247	1.43	49.6	49.6		1
CT5-14-1	.197	1.515	117.5	58.8	.052	.184	1.51	43.6			474

* Calculated

Table XII: TITANIUM TANK TEST RESULTS

Tank Identification	Tank Size		Test Temperature (°F)	Cyclic Gross Stress		Initial Flaw Size			Critical Flaw Size			K_{II} , ksi $\sqrt{\text{in.}}$	K_{IC} , ksi $\sqrt{\text{in.}}$	$K_{II}/(K_{IC})_{\text{avg.}}$ Ratio	Cycles to Failure
	Shell Thickness (in.)	Shell I. D. (in.)		Maximum (ksi)	Minimum (ksi)	Flaw Depth (a) _I (in.)	Flaw Length * (2c) _I (in.)	Flaw Shape Parameter (Q) _I	Flaw Depth (a) _{cr} (in.)	Flaw Length * (2c) _{cr} (in.)	Flaw Shape Parameter (Q) _{cr}				
0008	.200	15.0	R. T.	88.0	0	.078	.370	1.22	.082**	.370**	1.24**	39.2			5**
0009	.196	15.0	R. T.	63.5	0	.120	.600	1.19							898***
0011	Broke at longitudinal weldment														
0012	.198	15.0	-320	80.4	0	.065	.265	1.40	.099	.275	1.81	33.7			315†
				114.9	0	.099	.275	1.81	.130	.335	1.88	52.9	59.0	0.90	81
0010	.194	15.0	-423	117.3	0	.072	.250	1.53	.093	.280	1.67	49.8			28
0013	.200	15.0	-423	98.0	0	.077	.350	1.33	.140	.470	1.59	45.8	56.5		70

* Calculated

** Did not fail at flaw

*** Cycles to grow flaw through thickness

† Did not fail

Table XIII: STATIC FRACTURE TOUGHNESS TEST RESULTS — 2219-T87 ALUMINUM

Specimen Identification	Specimen Size (in.)		Test Temperature (°F)	Flaw Size (in.)			Fracture Stress (ksi)	$K_{Ic} \sim \text{ksi} \sqrt{\text{in.}}$	$K_{Ic} \sim \text{ksi} \sqrt{\text{in.}}$	Remarks
	Thickness (t)	Width (w)		Flaw Depth (a)	Flaw Length (2c)	Flaw Size (a/Q)				
SA6-1	0.608	6.00	R. T.	.257	0.944	.181	40.8	33.8		
SA12-1	1.240	6.00	R. T.	.364	1.370	.255	35.6	35.0		
SA6-2	0.608	6.00	-320	.274	1.016	.191	44.1	37.6		
SA12-2	1.231	6.00	-320	.342	1.341	.233	40.3	37.9		
SA6-3	0.607	6.00	-423	.283	0.999	.193	48.5			Specimens delaminated at tip of flaw
SA12-3	1.239	6.00	-423	.348	1.287	.242	43.7			

Table XIV: CYCLIC FLAW GROWTH DATA FOR 2219-T87 ALUMINUM,
0-100-0 LOAD PROFILE AT ROOM TEMPERATURE

Specimen Identification	Specimen Size		Cyclic Gross Stress		Initial Flaw Size			Critical Flaw Size			K_{II} , ksi $\sqrt{\text{in.}}$	K_{IC} , ksi $\sqrt{\text{in.}}$	$K_{II}/(K_{IC})_{\text{avg.}}$ **	Cycles to Failure
	Thickness (in.)	Width (in.)	Maximum (ksi)	Minimum (ksi)	Flaw Depth (a) _i (in.)	Flaw Length* (2c) _i (in.)	Flaw Shape Parameter (Q) _i	Flaw Depth (a) _{cr} (in.)	Flaw Length* (2c) _{cr} (in.)	Flaw Shape Parameter (Q) _{cr}				
COA6-1	.608	6.01	44.3	0	.125	.524	1.303	.295	1.091	1.398	26.8	---	0.80	645
COA6-2	.608	6.00	40.0	0	.225	.795	1.465	.363	1.290	1.455	30.6	---	0.91	139
COA6-3	.612	6.01	44.3	0	.208	.760	1.412	---	---	---	33.1	33.1	---	1
COA12-1	1.239	6.00	35.0	0	.202	.804	1.387	.460	1.147	1.933	26.1	33.3	0.78	1,109
COA12-2	1.239	6.00	37.0	0	.254	1.007	1.378	.443	1.426	1.576	31.0	---	0.92	367
COA12-3	1.238	6.00	30.0	0	.254	.976	1.435	.549	1.567	1.751	24.6	32.8	0.73	1,787

* Calculated

** $(K_{IC})_{\text{avg.}} = 33.5$

Table XV: CYCLIC FLAW GROWTH DATA FOR 2219-T87 ALUMINUM,
50-100-50 LOAD PROFILE AT ROOM TEMPERATURE

Specimen Identification	Specimen Size		Cyclic Gross Stress		Initial Flaw Size			Critical Flaw Size			K_{II} , ksi $\sqrt{\text{in.}}$	K_{IC} , ksi $\sqrt{\text{in.}}$	$K_{II}/(K_{IC})_{\text{avg.}}^{**}$ Ratio	Cycles to Failure
	Thickness (in.)	Width (in.)	Maximum (ksi)	Minimum (ksi)	Flaw Depth (a) _I (in.)	Flaw Length* (2c) _I (in.)	Flaw Shape Parameter (Q) _I	Flaw Depth (a) _{cr} (in.)	Flaw Length* (2c) _{cr} (in.)	Flaw Shape Parameter (Q) _{cr}				
C5A6-1	.609	6.00	42.1	21.1	.151	.546	1.430	.302	1.035	1.480	26.8	---	0.80	3,060
C5A6-2	.607	6.00	38.0	19.0	.205	.768	1.425	.304	1.221	1.367	28.1	34.9	0.84	1,694
C5A6-3	.607	6.00	44.3	22.2	.201	.751	1.393	.300	1.154	1.362	32.7	---	0.98	361
C5A12-1	1.239	6.00	35.0	17.5	.203	.771	1.427	.420	1.142	1.800	25.7	33.0	0.77	4,052
C5A12-2	1.242	6.00	37.0	18.5	.260	.998	1.406	.393	1.288	1.473	31.0	---	0.93	1,438
C5A12-3	1.240	6.00	30.0	15.0	.262	.923	1.515	.600	1.529	1.687	24.3	32.2	0.73	7,443

* Calculated

** $(K_{IC})_{\text{avg.}} = 33.5$

Table XVI: CYCLIC FLAW GROWTH DATA FOR 2219-T87 ALUMINUM,
0-100-0 LOAD PROFILE AT -320°F

Specimen Identification	Specimen Size		Cyclic Gross Stress		Initial Flaw Size			Critical Flaw Size			K_{II} , ksi $\sqrt{\text{in.}}$	K_{IC} , ksi $\sqrt{\text{in.}}$	$K_{II}/(K_{IC})_{\text{avg.}}^{**}$ Ratio	Cycles to Failure
	Thickness (in.)	Width (in.)	Maximum (ksi)	Minimum (ksi)	Flaw Depth (a) _i (in.)	Flaw Length* (2c) _i (in.)	Flaw Shape Parameter (Q) _i	Flaw Depth (a) _{cr} (in.)	Flaw Length* (2c) _{cr} (in.)	Flaw Shape Parameter (Q) _{cr}				
COA6-4	.604	6.01	54.0	0	.160	.567	1.438	.232	.706	1.597	35.1	---	0.94	9
COA6-5	.602	6.01	44.1	0	.157	.549	1.490	.342	1.034	1.650	27.9	39.1	0.75	697
COA6-6	.614	6.00	44.1	0	.245	1.002	1.359	.316	1.122	1.476	36.4	---	0.98	22
COA12-4	1.240	6.00	40.3	0	.197	.740	1.438	.446	1.125	1.921	29.1	37.9	0.78	634
COA12-5	1.242	6.00	40.3	0	.257	1.028	1.388	.473	1.265	1.831	33.8	---	0.91	109
COA12-6	1.240	6.00	36.8	0	.276	1.002	1.481	.380	1.092	1.738	30.9	33.6	0.83 [†]	47

* Calculated

** $(K_{IC})_{\text{avg.}} = 37.2$

† Based on $K_{IC} = 33.6$

Table XVII: CYCLIC FLAW GROWTH DATA FOR 2219-T87 ALUMINUM,
50-100-50 LOAD PROFILE AT -320°F

Specimen Identification	Specimen Size		Cyclic Gross Stress		Initial Flaw Size			Critical Flaw Size			K_{II} , ksi $\sqrt{\text{in.}}$	K_{Ic} , ksi $\sqrt{\text{in.}}$	$K_{II}/(K_{Ic})_{\text{avg.}}^{**}$ Ratio	Cycles to Failure
	Thickness (in.)	Width (in.)	Maximum (ksi)	Minimum (ksi)	Flaw Depth (a) _I (in.)	Flaw Length* (2c) _I (in.)	Flaw Shape Parameter (Q) _I	Flaw Depth (a) _{cr} (in.)	Flaw Length* (2c) _{cr} (in.)	Flaw Shape Parameter (Q) _{cr}				
C5A6-4	.608	6.01	54.0	27.0	.171	.581	1.473	----	----	----	35.9	35.9	----	1
C5A6-5	.609	6.01	44.1	22.1	.161	.578	1.467	.303	1.142	1.421	28.6	----	0.77	3,239
C5A6-6	.609	6.00	44.1	22.1	.220	.772	1.486	.295	1.219	1.510	33.1	38.0	0.89	642
C5A12-4	1.236	6.00	40.3	20.2	.205	.776	1.402	.438	1.090	1.940	30.0	37.3	0.81	3,226
C5A12-5	1.240	6.00	40.3	20.2	.270	1.037	1.419	.345	1.105	1.595	34.3	36.5	0.92	749
C5A12-6	1.259	6.00	32.0	16.0	.268	1.028	1.449	.699	1.914	1.823	26.8	38.6	0.72	9,468

* Calculated

** $(K_{Ic})_{\text{avg.}} = 37.2$

Table XVIII: CYCLIC FLAW GROWTH DATA FOR 2219-T87 ALUMINUM,
0-100-0 LOAD PROFILE AT -423°F

Specimen Identification	Specimen Size		Cyclic Gross Stress		Initial Flaw Size			Critical Flaw Size			K_{II} , ksi $\sqrt{\text{in.}}$	K_{IC} , ksi $\sqrt{\text{in.}}$	$K_{II}/(K_{IC})_{\text{avg.}}^{**}$ Ratio	Cycles to Failure
	Thickness (in.)	Width (in.)	Maximum (ksi)	Minimum (ksi)	Flaw Depth $(a)_i$ (in.)	Flaw Length* $(2c)_i$ (in.)	Flaw Shape Parameter $(Q)_i$	Flaw Depth $(a)_{cr}$ (in.)	Flaw Length* $(2c)_{cr}$ (in.)	Flaw Shape Parameter $(Q)_{cr}$				
COA6-7	.608	6.006	54.0	0	.152	.522	1.468	.188	.640	1.474	33.8	37.5	0.91	82
COA6-8	.609	6.007	44.1	0	.153	.536	1.485	.392	1.296	1.545	27.6	---	0.74	1,043
COA6-9	.608	6.008	44.1	0	.172	.603	1.488	.319	.875	1.783	29.3	36.4	0.79	259
COA12-7	1.240	6.001	40.3	0	.211	.776	1.462	.558	1.294	2.071	29.8	40.8	0.80	635
COA12-8	1.246	5.999	40.3	0	.266	.971	1.470	.456	1.213	1.841	33.4	39.1	0.90	143
COA12-9	1.237	5.997	32.0	0	.273	1.017	1.478	.665	2.308	1.585	26.8	---	0.72	1,497

* Calculated


** $(K_{IC})_{\text{avg.}} = 37.3$

Table XIX: CYCLIC FLAW GROWTH DATA FOR 2219-T87 ALUMINUM,
50-100-50 LOAD PROFILE AT -423°F

Specimen Identification	Specimen Size		Cyclic Gross Stress		Initial Flaw Size			Critical Flaw Size			K_{II} , ksi $\sqrt{\text{in.}}$	K_{Ic} , ksi $\sqrt{\text{in.}}$	$K_{II}/(K_{Ic})_{\text{avg.}}^{**}$ Ratio	Cycles to Failure
	Thickness (in.)	Width (in.)	Maximum (ksi)	Minimum (ksi)	Flaw Depth (a) _i (in.)	Flaw Length* (2c) _i (in.)	Flaw Shape Parameter (Q) _i	Flaw Depth (a) _{cr} (in.)	Flaw Length* (2c) _{cr} (in.)	Flaw Shape Parameter (Q) _{cr}				
C5A6-7	.606	6.013	54.0	27.0	.152	.570	1.385	.274	.924	1.487	35.0	---	0.94	1,475
C5A6-8	.607	6.003	44.1	22.1	.159	.546	1.510	.334	1.056	1.600	27.9	---	0.75	7,530
C5A6-9	.606	5.998	44.1	22.1	.216	.761	1.486	.392	1.301	1.545	32.8	---	0.88	1,985
C5A12-7	1.240	6.001	40.3	20.1	.201	.785	1.416	.427	1.063	1.947	29.6	36.2	0.79	6,238
C5A12-8	1.239	5.997	40.3	20.1	.265	.988	1.452	.389	1.203	1.642	33.6	38.3	0.90	1,542
C5A12-9	1.239	5.997	32.0	16.0	.261	.967	1.483	.469	1.417	1.696	26.2	32.8	0.76	10,866

* Calculated
 $(K_{Ic})_{\text{avg.}} = 37.3$

Table XX: ALUMINUM TANK TEST RESULTS

Tank Number	Tank Size		Test Temperature (°F)	Cyclic Gross Stress		Initial Flaw Size				Critical Flaw Size				K_{II} , ksi $\sqrt{\text{in.}}$	K_{Ic} , ksi $\sqrt{\text{in.}}$	K_{II}/K_{Ic}	Cycles to Failure
	Shell Thickness (in.)	Shell I. D. (in.)		Maximum 	Minimum	Flaw Depth (a) _i (in.)	Flaw Length (2c) _i (in.)	Flaw Shape Parameter (Q) _i	Flaw Size (a/Q) _i	Flaw Depth (a) _{cr} (in.)	Flaw Length (2c) _{cr} (in.)	Flaw Shape Parameter (Q) _{cr}	Flaw Size (a/Q) _{cr}				
I	.612	35.0	R. T.	35.0	0	.210	1.19	1.18	.178	.437	1.71	1.40	.312				1,285
V	.608	35.0	R. T.	44.3 (40.4)*	0	.180	.71	1.34	.135	.350	1.18	1.48	.236				561
II	.607	35.0	-320	40.0	0	.215	.94	1.32	.163	.460	1.65	1.48	.311				989
VI	.604	35.0	-320	51.7	0	.158	.69	1.28	.123	.307	1.03	1.49	.205				93
III	.602	35.0	-423	46.4	0	.194	.99	1.22	.159	.240	1.00	1.34	.179				** 80
IV	.608	35.0	-423	60.4	0	.186	.80	1.25	.147	.218	.80	1.40	.156				18

 Calculated hoop stress — see Section 6.2.6 for discussion on discrepancy between calculated and measured stresses

* Stress indicated by strain gages

** Deliberate burst after 80 cycles.
Calculated hoop stress at burst = 58 ksi